Upgrading polyetherimide-derived carbon molecular sieve membrane via co-pyrolysis for gas separation applications

A thesis submitted in the fulfilment of the requirements for the degree of

Doctor of Philosophy

by

Yi-Chen Lin

Supervisor: Dr. David Wang

School of Chemical and Biomolecular Engineering

University of Sydney

July 2025

this research reported in this thesis was supported by the award of Taiwan-University of Sydney scholarship to the PhD Candidate.

Statement of originality

I hereby declare that, to the best of my knowledge, the work presented in this thesis is authentic and original, except where explicit acknowledgment has been made. This thesis has not been submitted, either wholly or substantially, for the award of any other degree or diploma at any other educational institution.

Throughout the thesis, I have duly acknowledged the contributions of others, including assistance with experimental design and setup, data analysis, characterization processes, and the review of manuscripts and thesis drafts. This document reflects the work undertaken during my candidature and does not contain any significant portion of work previously submitted for any other qualification.

I recognise the copyright ownership of all materials, procedures, and data included in this thesis. Where applicable, I have obtained permission to reproduce any copyrighted material.

Additionally, I acknowledge that I used Paperpal, an AI tool, to assist with academic writing improvements and to correct grammatical errors during the preparation of this work. All AI-assisted content has been thoroughly reviewed and edited by me, and I take full responsibility for the final content of this thesis.

Yi-Chen Lin
05/Aug/2025

Authorship attribution statement

Page 50-52, 64-65, 69-70, Fig. 3-1, Fig. 3-6, and entire Chapter 4 of this thesis has been published as [Yi-Chen Lin, Thanh Tam Dang, Cheng-Han Lee, Clara Tran, Marcela Bilek, Hui-Hsin Tseng, Dianne E. Wiley, David K. Wang, Polishing effect on the alpha- alumina tubes for membrane separation performance, Separation and Purification Technology, Volume 375, 2025, 133753, ISSN 1383-5866, https://doi.org/10.1016/j.seppur.2025.133753.]. I investigated the entire study and drafted the manuscript.

Page 52-53, 60-63, 66-68, and entire Chapter 5-1 has been submitted to Separation and Purification Technology and is under revision and has the potential to be published in that journal. I designed, analysed, and wrote the draft and the data included in the chapter.

Page 54-55, 68-69, and entire Chapter 7-1 has been submitted to Carbon and revised in the journal system. I designed, analysed, and wrote the draft and the data included in the chapter.

Besides the authorship attribution statements mentioned earlier, in cases where I am not the corresponding author of a published work, I have obtained permission from the corresponding author to include the published material.

Yi-Chen Lin
05/Aug/2025

Dr David Wang, MRACI CChem
05/Aug/2025

Acknowledgement

While this thesis may not be flawless, it reflects my personal and scientific journey in membrane science, beginning with foundational experiments on gas separation membranes and culminating in more advanced explorations. Firstly, I appreciate the financial support from the Australian Research Council (DP 190101734) and the Taiwan-Sydney Scholarship, which covered research expenses, tuition and living costs. Moreover, I am deeply grateful to my principal supervisor, Dr. David Wang, for his invaluable academic guidance, as well as his unwavering mental and financial support, which kept me on track throughout this PhD journey. I would also like to sincerely thank my co-supervisors, Prof. Dianne Wiley and Prof. Hui-Hsin Tseng, for their insightful advice and for their generous support in providing recommendation letters during my job search. Special thanks go to the research teams at NCHU and KAUST for their instrumental support in facilitating my experiments. I am especially thankful to Prof. Ingo Pinnau for his critical guidance on proper gas separation measurements for polymeric membranes, which greatly strengthened the foundation of this work.

I am truly grateful to Po-Han Huang, whose continued concern for my mental well-being provided me with comfort and encouragement during difficult times. I also thank Dr. Xinpeng (Sean) Li for his valuable insights and support throughout my Ph.D. To my lab members and colleagues, thank you for creating a collaborative, engaging, and supportive environment that fostered both intellectual growth and scientific discovery. There are many others who helped me along the way, too many to mention individually. but each of your contributions is important to me. Finally, I thank my family for supporting me in studying in a foreign country and both the university and the scholarship provider from the Taiwanese government that made this work possible through their financial support, enabling me to pursue this research in the field of membrane science.

Publication list

Publications in this thesis

1. **Yi-Chen Lin,** Thanh Tam Dang, Cheng-Han Lee, Clara Tran, Marcela Bilek, Hui-Hsin Tseng, Dianne Wiley, David K. Wang, Polishing effect on the alpha- alumina tubes for membrane separation performance, Separation and Purification Technology, Vol 375(2025), 133753.

   Status: Published; Chapter 4

2. **Yi-Chen Lin**, Jing-Yi Li, Cara M. Doherty, Durga Acharya, Paul Fitzgerald, Hui-Hsin Tseng, Dianne Wiley, David K. Wang, The polyetherimide composite alumina membranes for carbon dioxide and methane separations

   Status: Under Review, SEPPUR-D-25-04700 (2025); Chapter 5.1.

3. **Yi-Chen Lin**, Cheng-Han Lee, Hui-Hsin Tseng, Dianne Wiley, David K. Wang, Discerning the effect of n-methyl pyrrolidone solvent residue on the polyetherimide composite membranes for carbon dioxide separations.

   Status: Will be submitted to Journal of Membrane Science; Chapter 5.2.

4. **Yi-Chen Lin**, John Zheng, Ruth Knibbe, Ching-Yi Li, Hui-Hsin Tseng, Dianne Wiley, David K. Wang, Ultramicroporous carbon molecular sieve membranes via biomimetic and polyetherimide co-pyrolysis for enhanced gas separations.

   Status: Under Review, CARBON-S-25-03223 (2025); Chapter 7.1.

5. **Yi-Chen Lin**, John Zheng, Ruth Knibbe, Cheng-Han Lee, Hui-Hsin Tseng, Dianne Wiley, David K. Wang, Novel metal based biomimetic materials carbon molecular sieve membranes for humidified CO_2 separation.

   Status: Will be submitted to Journal of Membrane Science; Chapter 7.2.

Abstract

Composite membrane technology offers a scalable and efficient approach for fabricating membranes suitable for large-scale production. It involves a selective thin film supported by a porous substrate, enabling highly efficient separation processes. However, achieving a uniformly coated selective layer on porous substrates remains a major challenge in developing high-performance gas separation membranes. Therefore, establishing strong interfacial compatibility between the selective layer and the substrate is essential for improving coating quality. An important yet often overlooked step in composite membrane preparation is polishing the inorganic substrate layer. This process effectively removes surface impurities and modifies surface roughness preparing the substrate for subsequent layer deposition. The resulting surface characteristics may also contribute to the formation of an asymmetric substrate, enhancing adhesion and coating performance, particularly for molecular sieving gas separation membranes.

Carbon molecular sieve membranes (CMSM) have been extensively studied as promising candidates for industrial gas separation and purification owing to their molecular sieving mechanism, which enables high gas permeance, tailored selectivity, and stability under corrosive and high-temperature conditions. Polyetherimide (PEI) is commonly used as a carbon precursor due to its low cost, thermal stability, and industrial compatibility. However, the relatively low gas permeability of PEI-derived CMS membranes limits their industrial application. To enhance the porous structure of PEI-based carbon membranes, thermally stable dopants—metal-based 2,6-bis(2-benzimidazolyl) pyridine (MtBBP)—have been introduced. These metal–ligand complexes incorporate gas-facilitating moieties, acting as functional dopants within the PEI matrix to improve gas transport and membrane porosity.

This thesis consists of eight chapters, including four main research chapters focused on the development, modifications, characterisations, and performance of PEI and CMS membranes for gas separation.

Chapter 1 introduces the project background and outlines the thesis structure.

Chapter 2 presents a literature review of membrane separation theory, followed by discussions on CMSM precursors and pyrolysis conditions. A critical review of advance modification technologies, such as composite and mixed matrix membranes, identifies effective strategies and research gaps in membrane fabrication.

Chapter 3 describes the methodology for synthesising PEI-based composite membranes, and the modification techniques employed. This section details membrane fabrication, characterisation methods, techniques, experimental setups, and key parameters used throughout the study.

Chapter 4 investigates the effects of polishing alumina substrates on the formation of an effective gutter layer for polymeric composite membranes. A customised automatic polishing machine was designed and evaluated, showing that polishing with 7000-grit sandpaper for 2.3 s at 1600 rpm, followed by partial sintering at 1200 °C, achieved a comparable surface pore diameter of 0.2 μm, porosity of 43.4 %, and an average pure water flux of 28.2 ± 1.4 LMH/bar. Under these conditions, the PEI-coated membrane reached a CO_2/N_2 permselectivity of 21.9.

Chapter 5 presents a detailed study of vacuum-assisted dip-coating for PEI-based composite membranes fabrication. The first part examines the optimal conditions for the formation of uniform selective layers. Membranes fabricated using a 12 wt.% PEI solution and low vacuum pressure (> -1 bar), followed by drying at 110 °C, exhibited an improved morphology. The second part evaluates the effects of drying temperature, focusing on solvent residue from N-methyl pyrrolidone (NMP). The membrane dried at 195 °C achieved the highest H_2 permeability of $(2.1\pm 0.22) \times 10^{-11}$ mol m^{-2} s^{-1} Pa^{-1}, along with H_2/CH_4 and CO_2/CH_4 permselectivities of 243 ± 23 and 31.9 ± 3.1, respectively. A strong correlation was found between residual NMP concentration and gas separation performance, providing insights for improving membrane efficiency.

Chapter 6 explores the incorporation of biomimetic materials into PEI membranes by investigating the concentration-dependent effects of cobalt-based 2,6-bis(2-benzimidazolyl)pyridine

(CoBBP). Doping 1 wt.% CoBBP increased H_2 permeability by 20% (from 7.7 to 9.4 Barrer) and improved H_2/CH_4 permselectivity from 62.9 to 102.2. Under humid conditions (80 ℃, 100% RH), CO_2/CH_4 separation showed a twofold increase in CO_2 permeability during the initial four hours, with stable selectivity over 24 hours. Various MtBBP complexes were also evaluated to assess their influence on gas separation with 1wt.% doped in PEI membranes. Iron-based 2,6-bis(2-benzimidazolyl)pyridine (FeBBP)- and zinc-based 2,6-bis(2-benzimidazolyl)pyridine (ZnBBP)-doped membranes exhibited enhanced CO_2 permeance due to preferential CO_2 coordination, suggesting a carbonic anhydrase–like mechanism. ZnBBP provided the best balance between selectivity and stability, though further PEI matrix modification is needed to increase gas permeability.

Chapter 7 focuses on developing CMSMs derived from MtBBP-doped PEI membranes via co-pyrolysis. CoBBP-doped CMS membranes (CoB_CM) were fabricated with concentrations ranging from 0 to 10 wt.% and pyrolysed at 600 ℃. The 1 wt.% CoB_CM membrane exhibited the highest H_2 permeability (3280 ± 490 Barrer) and H_2/CH_4 permselectivity (259 ± 7), which can be attributed to tailored ultramicropores. These membranes exceeded the 2015 and 2019 revisited Robeson upper bounds. Additionally, FeBBP- and ZnBBP-modified CMSMs also performed well: 1 wt.% FeB_CM yielded H_2 permeability of 3560 ± 30 Barrer and ZnB_CM reached 2800 ± 64 Barrer with a H_2/CH_4 permselectivities of 184 ± 3 and 270 ± 20, respectively. These findings confirm that MtBBP doping significantly improves CMS membrane.

Chapter 8 summarises the findings from Chapters 4-7, highlighting fabrication and performance improvements of PEI-based and CMS membranes. Recommendations for future research are provided to guide the ongoing advancement in membrane science and technology.

Table of Contents

Figure list

Table list

Abbreviation list

Abbreviation	Definition
CMS	Carbon molecular sieve
CMSMs	Carbon molecular sieve membranes
SDGs	Sustainable Development Goals
CO_2	Carbon dioxide
SO_2	
PEI	polyetherimide
BMM	Biomimetic materials
$F_{Knudsen}$	gas Knudsen flow
P_f	Partial feed pressure
P_p	Partial permeate pressure
L	pore length
M	molecular weight
P	Permeability coefficient
D	Diffusion coefficient
S	Solubility coefficient
FTM	Facilitated transport membrane
PBI	polybenzimidazole
PVA	Poly(vinyl alcohol
PIM	Polymers of intrinsic microporosity
Dc	Molecule dimension
d_λ	Jump length dimension
dTV	Negligible window thickness dimension
Tm	Melt temperature
Tg	Glass transition temperature
PVDC	Poly(vinylidene chloride)
PFA	Polyfurfuryl alcohol
PR	Phenolic resin
BTDA	3,3',4,4'-benzophenone tetracarboxylic dianhydride
6FDA	4,4'-(hexafluoroisopropylidene)diphthalic anhydride
PAN	polyacrylonitrile
CE	cellulose
Td	Degradation temperature
DAPI	5(6)-amino-1-(4′-aminophenyl-1,3-trimethylindane
DETDA	diethyltoluenediamine
DABA	3,5-diaminobenzoic acid
PA	Polyamide/imide
PVP	polyvinylpyrrolidone
PPO	Poly(p-phenylene oxide)
PEG	Polyethylene glycol
β-CD	β-cyclodextrin
MMM	*Mixed matrix membranes*
MWCNTs	*Multi-wall carbon nanotubes*
SBFDA	spirobifluorene-based dianhydride
DMN	3,3′-dimethylnaphthidine
TGA	Thermogravimetric analysis
NCC	
FFV	Free fraction volume
PDMS	polydimethylsiloxane

Teflon	polytetrafluoroethylene
PTMSP	Poly(trimethylsilyl-propyne)
MOF	Metal organic frameworks
PEGDMA	Polyethylene glycol dimethacrylate
CAP	Continuous assembly of polymers
TiO_2	Titanium dioxide
Al_2O_3	Alumina oxide
ZiFs	Zeolitic imidazolate frameworks
MIL	Materials of Institute Lavoisier
COF	Covalent organic frameworks
Tp	Triformylphloroglucinol
FTM	Facilitate transportation membranes
SLM	Supported liquid membranes
ILM	Immobilized liquid membranes
CA	Carbonic anhydrase
PVA	polyvinylamine
PEIm	Polyethylenimine
PVAm	Polyvinyl amine
PSf	polysulfone
BBP	2,6-bis(2-benzimidazolyl)pyridine
MtBBP	Metal-based 2,6-bis(2-benzimidazolyl)pyridine
CoBBP	Cobalt-based 2,6-bis(2-benzimidazolyl)pyridine
CuBBP	Copper-based 2,6-bis(2-benzimidazolyl)pyridine
FeBBP	Iron-based 2,6-bis(2-benzimidazolyl)pyridine
NiBBP	Nickel-based 2,6-bis(2-benzimidazolyl)pyridine
ZnBBP	Zinc-based 2,6-bis(2-benzimidazolyl)pyridine
He	Helium
H_2	Hydrogen
CO_2	Carbon dioxide
Ar	Argon
O_2	Oxygen
N_2	Nitrogen
CH_4	Methane
SEM	Scanning electron microscopy
EDS	Energy-dispersive X-ray spectroscopy
XRD	X-ray diffraction
DSC	Differential scanning calorimetry
BET	Physisorption
DFT	Density functional theory
XPS	X-ray photoelectron spectroscopy
ATR-FTIR	Attenuated total reflectance Fourier transform infrared spectroscopy
NMR	Nuclear magnetic resonance
STA-FTIR	TGA coupling with FTIR
TEM	Transmission electron microscopy
PALS	Positron annihilation lifetime spectroscopy
UF	Ultrafiltration
MF	Microfiltration
NF	nanofiltration
RO	Reverse osmosis

Chapter 1 Introduction

Developing energy-efficient separation processes for applications ranging from petroleum refining and water treatment to (petro-)chemicals production and carbon capture will yield long-term benefits across the energy, gas, water, food, and pharmaceutical industries, while contributing to environment. As global population growth continues alongside rising living standards, emerging environmental challenges and stricter emission regulations have intensified pressure on the chemical process industry to urgently reimagine sustainable chemical production. This includes aligning with the Sustainable Development Goals (SDGs) within the energy-water-food nexus.

Thermally driven separation processes, such as distillations and cryogenic separations, account for approximately 10-15% of global energy consumption, with more than 50% of that energy being lost as waste heat [1]. Estimates suggest that improving chemical separation efficiency in the petroleum, chemical, and paper manufacturing sectors could save approximately US$4 billion in energy costs and prevent 100 million tonnes of carbon dioxide emissions annually [2]. Achieving energy-efficient separation without relying on heat, while cutting greenhouse gas emission by 26%-28% below 2005 levels by 2025-2030 [3], could be transformative for the global chemical process industry. Such technologies would enable multiple sustainable innovations in service delivery and open new pathways for resource recovery.

Membrane technologies offer a promising alternative to conventional separation methods by significantly reducing energy consumption— up to 90% less than distillation [4-6]. These systems operate near thermodynamic equilibrium, driven by a concentration gradient across the membrane, with minimal external work required. However, the industrial-scale deployment of gas separation membrane present challenges. Thicker, denser membranes introduce high resistance, reduce gas permeance, while thinner membranes may lack sufficient mechanical strength to endure high operating pressures. To overcome these issues, composite membrane fabrication has been developed. This approach integrates a thin selective layer for separation with a porous support layer that ensures structural stability under operational conditions. Among these methods, thin film composite (TFC) membranes have emerged as a scalable and adaptable solution [7, 8]. TFC membranes offer key advantages to manufacturers, including enhanced gas permeance, reduced material consumption, and lower production costs due to the use of ultrathin selective layers [9, 10].

Carbon molecular sieves (CMSs) are considered promising membrane materials for gas separation due to their bimodal microporous structures and narrow pore size distribution, which enhance gas permeance and selectivity for various gas pairs, including H_2/CH_4, CO_2/N_2, CO_2/CH_4, and O_2/N_2 [11, 12]. Genduso et al. [12] provided a comprehensive review of CMS membrane fabrication strategies and gas separation performance over the past three decades, establishing an important benchmark that has guided subsequent developments in CMS membrane design. More recently, Feng et al. [13] successfully synthesized a thin-film Tröger's base polymer (TB)/poly(styrene sulfonic acid) (PSS) composite CMS membrane supported on anodic aluminium oxide (AAO) substrates, achieving an exceptional H_2 permeance exceeding 1000 GPU and an H_2/CH_4 selectivity of 149. Notably, their work demonstrated precise control over the CMS layer thickness, which was maintained below 500 nm. Among CMS precursors, polyetherimide (PEI) stands out as a thermally stable polymer with industrial maturity, ease of processing and low production cost characteristics that make it particularly attractive for membrane manufacturing. However, compared with the latest high-performance CMS membranes, PEI-derived CMS membranes still require improvements in both gas permeability and selectivity to meet the demands of large-scale industrial applications.

The development of high-performance CMS-based TFC membranes is currently constrained by four principal challenges: (1) substrate resistance, (2) infiltration of the selective layer into the substrate, (3) defects within ultrathin selective layers, and (4) doping of functional materials into the selective layers [8]. These challenges are often interdependent. For instance, efforts to reduce substrate resistance may unintentionally alter the substrate's surface morphology and chemistry, reducing coating efficiency and increasing the risk of interfacial defects and precursor infiltration into the substrate pores. To address this issue, a gutter layer, which serves as an intermediate layer between the selective layer (carbon precursor) and the porous substrate, can be applied to minimise both infiltration and surface defects [14]. This strategy supports the formation of an ultrathin selective layer while improving interfacial adhesion. The effectiveness of the gutter layer can be enhanced using materials with high compatibility or affinity for the selective layer. However, this approach may also increase the overall membrane resistance and complicate the manufacturing process, thereby raising production costs [15]. The dip-coating technique is widely used in both academia and industry due to its simplicity and cost-effectiveness [8, 16]. However, it is prone to issues such as polymer precursor infiltration into the porous substrate, which results in microdefects that reduce membrane selectivity and performance [17]. Therefore, a comprehensive investigation is essential to identify the key parameters that influence the quality of polymeric membrane coatings.

To address these limitations, this thesis introduces a new strategy to prime the inorganic substrates for improved polymer coating. A custom-designed polishing rig and methodology were developed for tubular substrates to modify surface roughness and enhance polymer–substrate interfacial adhesion. This modification supports the formation of defect-free PEI based membranes. In addition, a systematic investigation of the vacuum-assisted dip-coating process was conducted to identify the key parameters for fabricating well-coated PEI composite membranes that are free from both defect- and solvent- residues.

Building on these foundational investigations, a novel coordination complex based on 2,6-bis(2-benzimidazolyl)pyridine (BBP) was synthesised and incorporated into the PEI composite membranes to enhance CO_2 separation performance, particularly under humid conditions. Subsequently, a co-pyrolysis approach using metal-BBP-doped PEI membranes to fabricate mixed matrix carbon molecular sieve membranes (CMSMs). This method enables the integration of various metal-BBP complexes into the PEI network during pyrolysis, resulting in a unique ultramicroporous structure within the membrane matrix. This work explores advanced CMS composite membrane fabrication via co-pyrolysis, aiming to enhance the gas separation performance of PEI-based membranes.

As shown in Fig. 1-1, the thesis flowchart outlines the membrane modification strategies and provides an overview of the thesis structure. The blue section corresponds to the investigation of polishing effects on alumina substrates to optimise the interface for PEI membrane coating, followed by the determination of optimal dip-coating parameters (Chapter 4-5). The orange section focuses on the incorporation of biomimetic additives (CoBBP and MtBBP) into PEI membranes and their influence on gas separation performance (Chapter 6). Finally, the green section illustrates the carbonisation of both pure PEI and additive doped membranes to evaluate the performance of the resulting CMSMs (Chapter 7). This research focuses on membrane design and gas separation processes through four primary investigations:

- **Alumina tubular substrate modification:** Chapter 4 discusses the optimization of polishing parameters to control the surface finish and macroporous morphology of alumina tubes, thereby enhancing the dip-coating performance of the PEI polymer dope solution. Water permeation tests on the polished substrates and gas permeation tests on the PEI-coated substrates were performed to determine the optimal polishing conditions and procedures for preparing defect-free, gas-selective PEI membranes.

- **Dip-coating parameters for PEI membrane fabrication:** Chapter 5 presents a detailed study on the vacuum-assisted dip-coating methodology used to create uniform PEI thin films on optimally polished alumina substrates. Dip-coating parameters were systematically evaluated to establish the relationship between the properties of the thin film and single gas permeation performance.
- **Biomimetic material (BMM) modification of PEI thin films:** Chapter 6 introduces a series of metal-coordinated BMMs synthesised and incorporated into optimised PEI thin films to form mixed matrix membranes. The doping parameters for these BMMs were thoroughly investigated to assess their effects on both single and mixed gas permeation performance.
- **Carbonisation of PEI and PEI/BMM thin films:** Chapter 7 explores the use of BMMs as thermally stable dopants for tuning the pore structure of PEI-based CMS membranes. A series of characterisation and gas permeation tests were conducted on carbonised PEI/BMM membranes to evaluate the influence of pore structure modifications on gas separation performance.

Chapter 8 concludes the thesis and provides a future outlook on the modification strategies applied to mixed matrix carbon membranes within composite membrane systems. The final chapter compares the membrane performance achieved in this study with recent literature to evaluate the overall effectiveness of the approach.

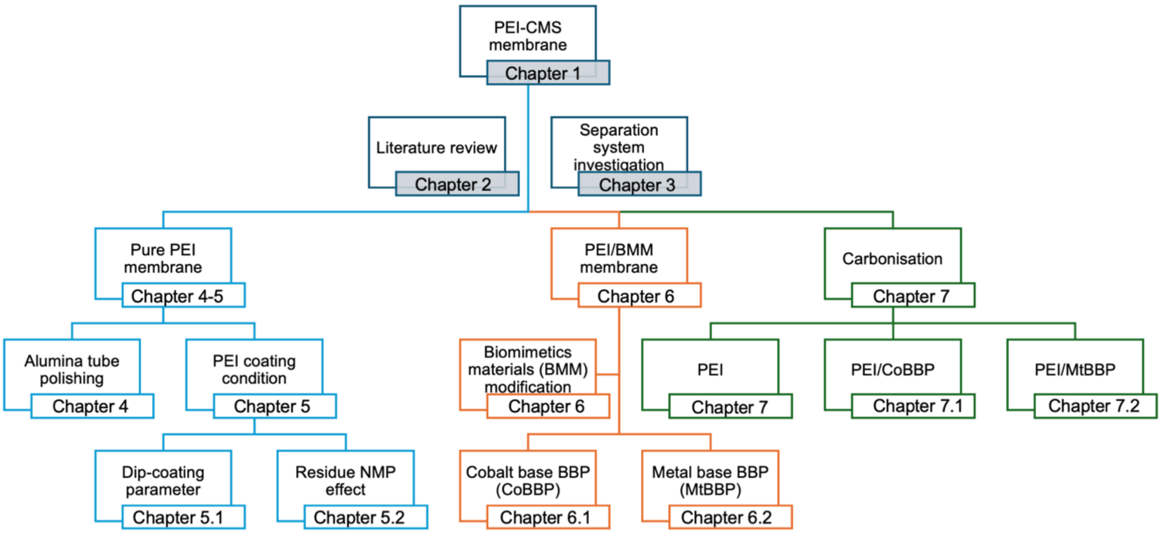

Fig. 1-1. Flow chart outlining the structure and key research components of the thesis.

Chapter 2 Literature Review

For over half a century, gas separation membranes have been developed and have demonstrated outstanding performance in separating various gas pairs, such as nitrogen from air, carbon dioxide from natural gas, and hydrogen from refinery and petrochemical streams [9]. In recent decades, a variety of advanced polymeric materials, including polymers of intrinsic microporosity (PIMs) [18-20] and thermally rearranged (TR) polymers [21-23], have been proposed as promising candidates for industrial gas separation. However, despite their high separation performance, these materials often suffer from rapid physical ageing and high synthesis costs, which limit their commercial viability [24].

Carbon molecular sieve membranes (CMSMs), which are produced through the pyrolysis of polymer precursors, have emerged as strong alternatives due to their superior permeability-selectivity trade-off when compared to their parent polymer membranes. Furthermore, CMSMs can operate under extreme conditions, including high temperatures (500-900°C) and chemically aggressive, non-oxidising environments, making them attractive for advanced gas separation applications [25-27]. Despite these advantages, CMSMs are brittle and costly to manufacture [28]. To address these limitations, composite membranes fabricated on porous inorganic supports have gained attention as a potential solution [29]. However, the weak interfacial interaction between the selective carbon layer and the inorganic substrate can lead to structural defects that compromise membrane performance [29, 30]. To improve interfacial adhesion and reduce coating defects, previous studies have introduced polymeric or inorganic gutter layers as interfacial modifiers [31-33]. While effective during the coating stage, these gutter layers may introduce complications during pyrolysis, including thermally induced delamination and pore blockage, which hinder the formation of high-quality CMSMs. As a result, alternative fabrication strategies must be explored to eliminate the need for gutter layers while still achieving defect-free, high-performance CMSMs.

This chapter provides a comprehensive review of CMSMs, with an emphasis on the membrane fabrication parameters that guide the design of methodology strategy of this thesis. The chapter begins with an overview of gas separation mechanisms, covering dense membrane transport (Section 2.1.1) and porous membrane transport (Section 2.1.3), to establish the theoretical foundation of gas separation. The classical Robeson upper bound (section 2.1.2) is also discussed to illustrate the trade-off between permeability and selectivity in polymeric membranes. This includes a review of the polymeric precursor materials used in the fabrication of CMSM from two key perspectives: the selection of polymeric precursors (Section 2.2.1) and pyrolysis conditions (Section 2.2.2). These discussions aim to identify existing limitations and research gaps that must be addressed to achieve high-performance CMSMs. Finally, the chapter explores various membrane material compositions and microstructures, including thin-film composite membranes (Section 2.3.1) and mixed matrix membranes (Section 2.3.2), to broaden the understanding of membrane design strategies relevant to CMSM development.

2.1. Gas Separation Theory

Gas separation in membranes is driven by differences in the partial pressure across the membrane surface, enabling the selective transport of specific gas components from a gas mixture [34]. As shown in Fig. 2-1, the incorporation of materials with varying pore sizes or functional properties into the membrane structure influences gas separation performance by targeting specific gas species. Typically, gas separation membranes can be categorized into porous and dense membranes, which define their gas separation mechanisms.

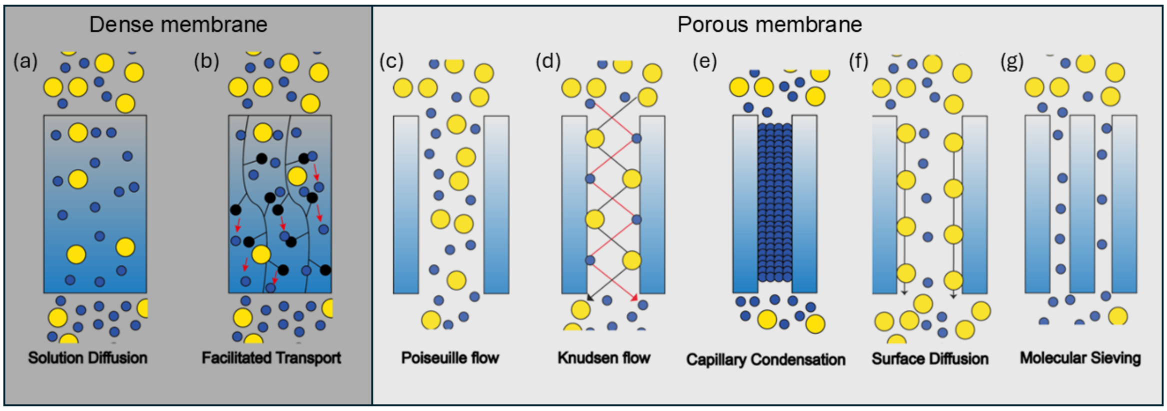

Fig. 2-1. Schematic illustration of gas transport mechanisms in dense and porous membranes.

2.1.1. Dense Membranes

Dense membranes, are also referred to as non-porous membrane or sub-nanometre pore size membrane [35], operate based on the classical solution-diffusion mechanism for gas separation processes (Fig. 2-1(a)). In this mechanism, gas molecules are driven by a transmembrane pressure gradient and permeate through the membrane bulk due to differences in their diffusivity and solubility, enabling the selective separation of different gas species [36]. Two critical parameters that influence membrane performance are the fractional free volume (FFV) and the gas affinity of the polymeric material used [37].

The solution-diffusion mechanism in polymeric membranes comprises three sequential (Fig. 2-2): (1) Adsorption: On the upstream (feed) side, gas molecules interact with the membrane surface and dissolve into the membrane material based on their molecular interactions. (2) Diffusion: Driven by the chemical potential and solvent activity gradient, gas molecules diffuse through the bulk of the membrane. During this stage, the internal membrane pressure is typically assumed to be equal to the upstream pressure [38]. (3) Desorption: On the downstream (permeate) side, gas molecules desorb due to differences in thermodynamic activity and concentration between the feed and permeate sides. This disparity facilitates the movement of gas molecules across the membrane. The overall driving force of this mechanism is the chemical potential gradient, which aligns with the concentration gradient. While surface adsorption and downstream desorption tend to reach equilibrium rapidly, the diffusion of gas molecules through the bulk membrane is generally slower, thereby governing the overall gas transport rate. The gas permeation rate of a membrane is quantified by its permeability coefficient (P), which is the product of the diffusion coefficient (D) and the solubility coefficient (S), as defined by the following equation:

$$P = DS \tag{1}$$

where P, D, S is the permeability, diffusion and solubility coefficient, respectively.

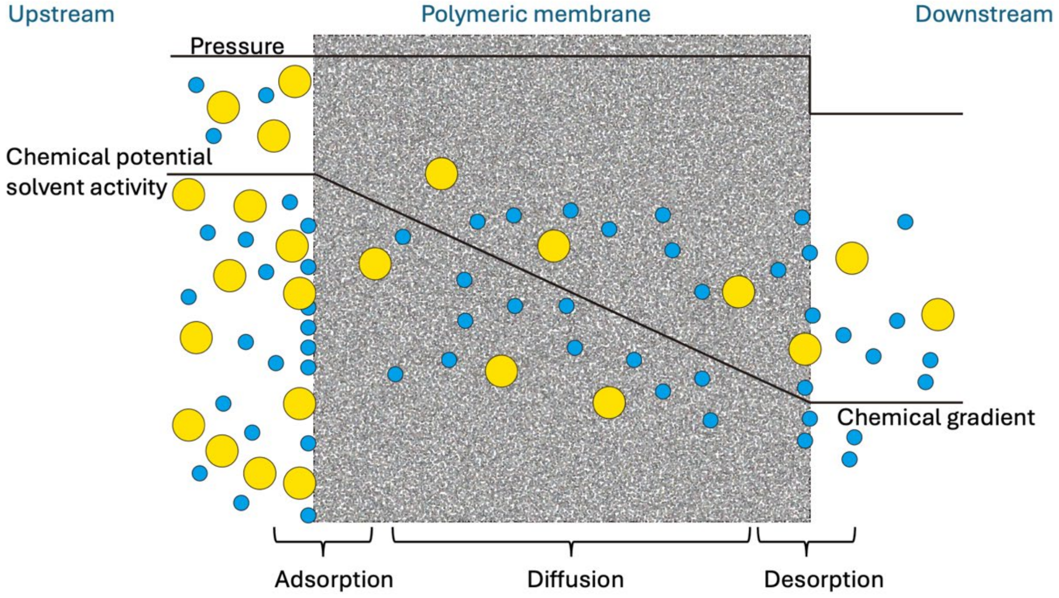

Fig. 2-2. Schematic illustration of the solution-diffusion mechanism for mixed gas transport through a polymeric membrane.

To better understand gas molecule diffusion in polymeric membranes, several models have been proposed to describe gas transport behaviour at the molecular level [39-44]. In rubbery polymers, gas transport is frequently explained using free volume theories, which relate gas diffusivity and concentration to the average intermolecular spacing within polymer chains.

These models typically correlate the mutual diffusion coefficients in gas-polymer systems with the free volume of the system [39-41]. Ganesh et al. [42] investigated the gas permeability of polyethylene terephthalate (PET) to support the free- volume diffusion model in glassy polymers. Building on this theory, Lee [45] developed an empirical correlation to assume the gas permeability from the polymer structure. Additionally, the dual-sorption model was introduced to explain gas transport by differentiating between the mobile and immobile states of gas molecules within the membrane matrix [43, 44]. This model effectively describes the variation of gas solubility, diffusion, and permeability coefficients with operating pressure. However, it assumes that plasticisation or significant swelling of the membrane does not occur, limiting its applicability in certain systems.

Furthermore, a molecular-scale diffusion mechanism was proposed to define the relationship between the membrane free volume and gas transport properties [46]. These models consistently assume that the free volume in the membrane bulk serves as the primary diffusion pathway for gas molecules [41, 42, 47]. Building on earlier studies, Pace and Datyner [46] proposed a model linking polymer microstructure to gas diffusion behaviour. As illustrated in Fig. 2-3, they suggested that the non-crystalline regions of a polymer exhibit a semi-crystalline arrangement in which polymer chain bundles align parallel to one another over several nanometres, forming tubule-like structures. These parallel tubules serve as channels for transporting penetrant gas molecules. The diffusion process involves transitions between adjacent tubules facilitated by the thermal motion of localised polymer chain segments. These motions generate transient openings large enough for gas molecules to pass through. Once a molecule has entered a new tubule, the transient channel closes, completing the transport step. According to this model, membrane selectivity is governed by the dynamics of these transient channels. Highly flexible polymer matrices with more frequent or larger openings result in higher diffusion coefficients and lower activation energies. In contrast, more rigid structures restrict motion and allow smaller gas species to permeate more readily than larger ones.

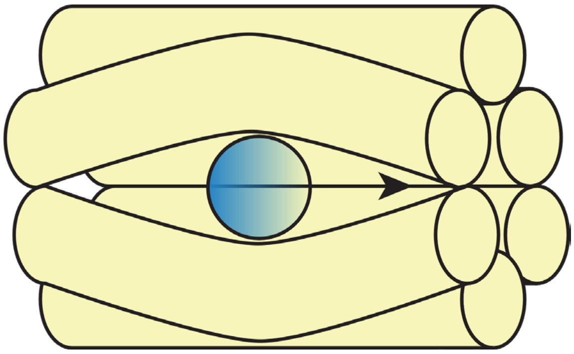

Fig. 2-3. Schematic illustration of small gas molecule transport through polymer chains.

Facilitated transport membranes (FTMs)

Facilitated transport membranes (FTMs) are a subclass of dense membranes used for gas separation, particularly for carbon dioxide or other reactive gases (Fig 2-1b) [48, 49]. Incorporating reactive carriers into the membrane matrix enables reversible chemical bonding with the target gas, thereby enhancing its permeability, which had been comprehensively reviewed by Rea et al. [50]. These membranes enhance diffusion efficiency within their bulk matrix, leading to higher permeability than conventional dense membranes. FTMs operate by coupling physical diffusion with reversible chemical reactions that facilitate the passage of reactive gases through the membrane [51]. During the separation process, gas molecules permeate the membrane via the solution-diffusion mechanism, while additives embedded within the bulk membrane promote the selective transport of reactive gases through chemical interactions. Typical additives include amine groups (primary, secondary, and tertiary), which assist in CO_2 transport. These reactions typically involve water molecules, and the general reaction mechanisms are outline in Equation (2-6) [52, 53]:

$$2RNH_2 + CO_2 \leftrightarrow RNHCOO^- + RNH_3{}^+ \tag{2}$$

$$RNH_2 + H_2O + CO_2 \leftrightarrow HCO_3{}^- + RNH_3{}^+ \tag{3}$$

$$2R_2NH + CO_2 \leftrightarrow R_2NCOO^- + R_2NH_2{}^+ \tag{4}$$

$$R_2NH + H_2O + CO_2 \leftrightarrow HCO_3{}^- + R_2NH_2{}^+ \tag{5}$$

$$R_3N + H_2O + CO_2 \leftrightarrow HCO_3{}^- + R_3NH_2{}^+ \tag{6}$$

These reactions enhance gas permeability and enable effective separation even under extreme conditions, such as high relative humidity. Transport membranes are typically categorised into two groups based on the type of carrier material. The first group employs mobile carriers, including supported liquid membranes (SLMs) and immobilised liquid membranes (ILMs), which consist of porous membrane structures impregnated with CO_2-philic ionic liquids. These liquids chemically interact with CO_2, thereby improving both the flux and selectivity. Hanioka et al. [54] demonstrated that N-aminopropyl-3-methylimidazolium bis(trifluoromethylsulfonyl)imide ([C_3NH_2mim][Tf_2N]) supported on porous polytetrafluoroethylene (PTFE) membranes achieved CO_2 permeability exceeding 1300 Barrers with a CO_2/CH_4 selectivity of 50 under a 1:9 CO_2/CH_4 feed. This membrane maintained stable performance at 1 atm for over 270 days. In another study, Fu et al. [55] developed enzymatic liquid membranes using anodisc alumina supports for CO_2/N_2 separation. A 0.05 mM carbonic anhydrase (CA) aqueous solution was applied via capillary action to create an ultrathin liquid membrane. This configuration enabled a CO_2 permeance of 2600 GPU and a CO_2/N_2 selectivity of approximately 790.

The second category uses fixed carriers to facilitate selective gas transport. Polymer such as Polyethylenimine (PEIm) and polyvinylamine (PVAm), which contain high densities of amine groups, chemically adsorb CO_2 within the membrane matrix. Sandru et al. [56] blended PVAm with polysulfone (PSF) to fabricate fixed-site-carrier membranes for CO_2 capture. These membranes achieved a CO_2 permeance of approximately 0.28 m^3 STP m^{-2} s^{-1} bar^{-1} and CO_2/N_2 selectivity of 197 under humidified conditions at a feed pressure of 2 bar, indicating the effectiveness of PVAm in promoting CO_2 transport. Tong and Ho [49] synthesised sterically hindered PVAm membranes for CO_2/N_2 separation, achieving a CO_2 permeability of approximately 6800 Barrers and a CO_2/N_2 selectivity of 350 at 102 °C. The steric hindrance enhanced CO_2 adsorption by up to twofold, thereby improving the permeance of the gas. These results underscore the importance of amine-based modifications in the fabrication of FTMs and their potential to enhance CO_2 permeability in membrane-based gas separation strategies.

Gas separation membrane processes have driven the extensive development of polymeric membranes. As shown in Table. 2-1, various commercial membranes have been implemented for applications such as biogas upgrading, natural gas purification, and air filtration. These membranes are typically fabricated as hollow fibres, which require high mechanical integrity to withstand medium-pressure separation environments (16-24 barg). They are housed in modules designed to maximise effective surface area, allowing for high throughput and gas purity of up to 99%. The scalability of these systems is facilitated by adjusting the module lengths to meet the demands of different permeate flow rates [57, 58]. Despite these advantages, polymeric membranes are generally unsuitable for high-temperature gas separation, such as those in flue gas treatment processes, where operating temperatures range from 150 °C to 1200 °C [59]. Furthermore, high-pressure conditions can induce plasticisation, which negatively affects membrane selectivity and long-term operational stability [60].

Table 2-1. Commercial polymeric membranes used in various gas separation processes.

Company	Model	Membrane materials	Application field	Separation performance	Ref.
Air Products	PRISM®	Polysulfone	Air filtration (O_2/N_2)	99.9% purity of CH_4	[61]
Air Liquid	MEDAL®	Polyimides	Air filtration (O_2/N_2)	99.9% purity of N_2; 31Nm^3/hr	[57]
Generon	NPU 750	Tetrabromopolycarbonate	Air filtration (O_2/N_2)	99% purity of N_2; 422 Nm^3/hr (350 psig)	[58]
MTR	VeporSep®	Silicon rubber	Syngas(H_2/CO) separation	85-95% H_2 purity	[62]

UBE	CO-C07F	Polyimide	Customised condition	99% purity of N_2; (16 barg)	[63]

2.1.2. Gas Separation Trade-off (Robeson upper bound)

Extensive research has been conducted on the use of polymeric membranes for gas separation, with the primary focus on evaluating their permeability and selectivity for various gas pairs. Numerous review articles have examined the relationship between membrane structure and gas separation performance. To synthesise high-performance membranes, the most critical parameters include membrane flux, thickness, permeance, and selectivity. Among these, permeability and selectivity are considered the key determinants of membrane applicability. Permeability influences the gas separation rate, whereas selectivity affects the permeate gas purity.

Gas permeance is defined as the ratio of the gas transmission rate to the partial pressure difference across the membrane, as specified by ASTM D1434-23 [64]. Although the SI unit for gas permeance is mol m^{-2} s^{-1} Pa^{-1}, the gas permeance unit (GPU) is more commonly used in membrane science literature. The unit conversion is expressed in Equation (7):

$$1\,GPU = 3.35 \times 10^{-10}\,mol\,m^{-2}\,s^{-1}\,Pa^{-1} = 1 \times 10^{-6}\,cm^3(STP)cm^{-2}s^{-1}cmHg^{-1} \qquad (7)$$

Since gas permeance depends on membrane thickness, this effect can be eliminated by multiplying by the membrane thickness to obtain gas permeability, which is commonly reported in Barrer. The conversion is shown in Equation (8):

$$1\,Barrer = 3.35 \times 10^{-16}\,mol\,m\,m^{-2}\,s^{-1}\,Pa^{-1} = 1 \times 10^{-10}\,cm^3(STP)cm\,cm^{-2}s^{-1}cmHg^{-1} \quad (8)$$

A substantial body of data has been compiled on polymeric membranes, establishing a fundamental trade-off between permeability and selectivity. This trade-off was first formalised by Robeson in 1991 [65], who introduced an upper bound relationship for various gas pairs. In

2008, Robeson revisited the upper bound [66], defining a benchmark state-of-the-art performance in polymeric membrane-based gas separation. Recent studies have proposed revised upper bounds that incorporate novel polymers with enhanced free volume, significantly improving gas separation performance [67, 68]. These upper bounds can be described by the empirical power-law relationship in Equation (9) as follows:

$$P_a = k\alpha_{ab}^{n} \tag{9}$$

where P_a is the permeability of gas A, α_{ab} is the selectivity for the gas pair from gas a and b, k is an empirical constant, and n is the empirical slope.

As shown in Fig. 2-4, the application of novel polymers has raised the upper bounds for CO_2/CH_4 and O_2/N_2. The inset table summarises the corresponding k and n fit parameters for each reference year. The original 1991 upper bound analysis was based on homogeneous membranes fabricated using similar film preparation techniques and standardised testing methods to ensure data consistency [65]. Subsequent investigations using advanced polymers, including polyimide, polybenzimidazole (PBI), poly(vinyl alcohol) (PVA), and polymers of intrinsic microporosity (PIM), have led to significantly improved upper bounds [67, 68]. These materials, characterised by high free volume, enable increased gas permeability while maintaining adequate selectivity, thereby enhancing the feasibility of these membranes for industrial applications.

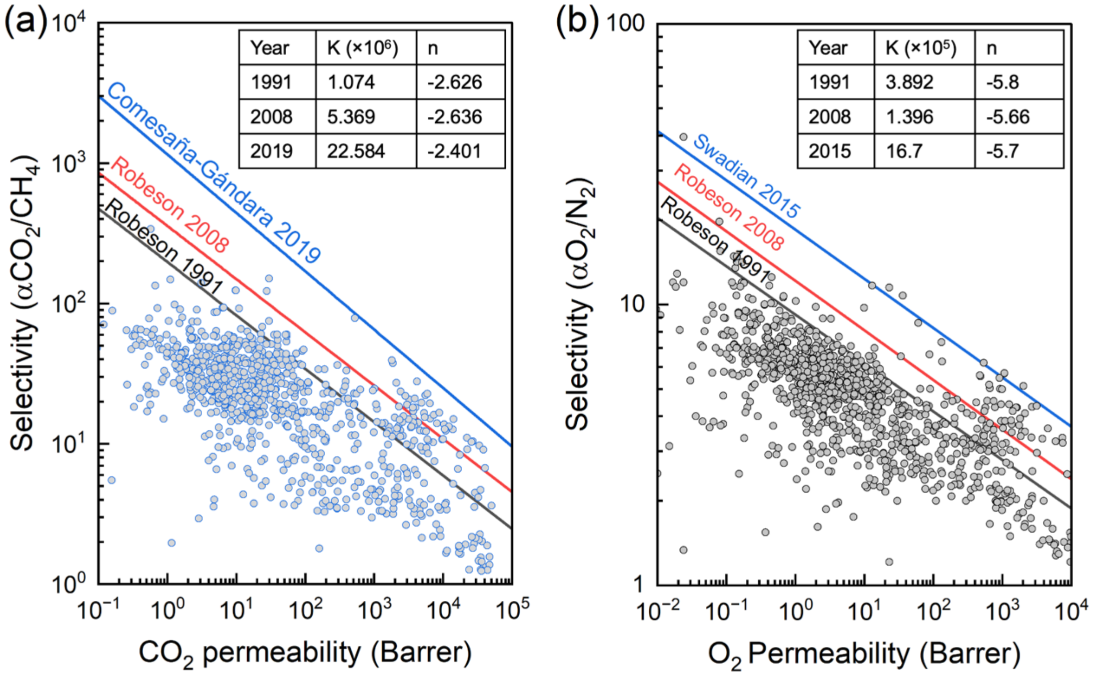

Fig. 2-4. Robeson upper bounds for (a) CO_2/CH_4 and (b) O_2/N_2 gas pairs, based on data obtained from the Membrane Society of Australasia database [66, 67, 69, 70]. The upper bounds illustrate the trade-off between permeability and selectivity, providing a benchmark for evaluating membrane performance.

The Robeson upper bound analysis is primarily based on empirical observations derived from experimental data. Notably, a theoretical model developed by Freeman [71] demonstrated strong agreement with these empirical findings. This model enabled accurate predictions of both the upper-bound slope and intercept. According to the activation energy theory, the predicted slope of the upper bound can be expressed as follows:

$$ln\ \alpha_{A/B} = -\lambda_{A/B}\ lnD_A + \left\{\ln\left(\frac{S_A}{S_B}\right) - \lambda_{A/B}(b - f\left(\frac{1-a}{RT}\right)\right\} \tag{10}$$

This equation highlights that gas selectivity is primarily governed by the diffusion coefficients of different polymers, while the influence of solubility coefficients remains relatively minor. In this expression, $\lambda_{A/B}$ represents the difference in the kinetic diameters of the gas molecules ($\lambda_{A/B} = d_b - d_a$), and b is a polymer-specific constant that varies depending on whether the material is rubbery or glassy.

Additionally, the graphical representation of empirical gas permeability data further illustrates the dominant role of diffusion over solubility in determining gas separation performance [71, 72]. The results indicate that the permeability of both gas A (fast permeating) and gas B (slow permeating) tends to increase concurrently when the permeability of either gas increases [72]. This trend can be attributed to the relationship between the gas diffusion coefficients and the free volume within the polymer matrix. The solubility ratio between gas pairs is generally assumed to fall within a narrow range across different polymers [65]. A linear relationship between the permeability of gas A and gas B can be described by Equation (11) as follows:

$$P_A = k_c \, P_B^n \tag{11}$$

To estimate the free volume characteristics of a polymer membrane, a logarithmic plot of Equation (11) can be used to determine the slope n, representing the strength of the correlation. As shown in Table 2-2, the kinetic diameters of common gases measured by Breck et al. [73] using zeolite adsorption methods closely align with the correlation diameters from Robeson [72]. This alignment suggests a strong analogy between gas diffusion through membranes and gas adsorption in zeolites, providing further validation for the proposed theoretical framework.

Table 2-2. Kinetic diameters of common small gases as reported by Breck and the corresponding correlation diameters from Robeson.

Gas type	Breck kinetic diameters, Å [73]	Correlation diameter, Å [72]
He	2.6	2.64
H_2	2.89	2.87
CO_2	3.3	3.32
O_2	3.46	3.34
N_2	3.64	3.56
CH_4	3.8	3.81

2.1.3. Porous Membranes

Gas transport through the bulk of porous membranes occurs via Knudsen diffusion and Poiseuille flow (Fig. 2-1(c) and (d)). The relative contributions of these mechanisms depend on the ratio between the membrane pore radius (r) and the gas molecule mean free path (λ) [74], which is defined by Equation (12):

$$\lambda = \frac{3\mu}{2P}\frac{\sqrt{\pi RT}}{2M} \tag{12}$$

where μ is the gas viscosity, M is the molecular weight, P is the pressure, R is the universal gas constant, and T is the temperature.

When the pore radius (r) is much greater than the mean free path ($r/\lambda >> 1$), typically in the macroporous to mesoporous range, gases flow through the membrane without significant separation, following the Poiseuille flow mechanism (also known as viscous or convective flow) [74]. Conversely, when ($r/\lambda < 1$), typically near the transition between mesoporous and microporous regions, Knudsen diffusion becomes the dominant gas transport mechanism. In this case, the mean free path exceeds the pore radius, resulting in frequent collisions between gas molecules and pore walls. Upon collision, gas molecules are momentarily absorbed on the wall surface before being reflected in random directions. Since intermolecular collisions are relatively infrequent, each gas species moves independently. Separation occurs due to differences in molecular velocities, as described by Equation (13):

$$F_{Knudsen} = \frac{8\mathrm{r}(P_f - P_p)}{3L\sqrt{2\pi MRT}} \tag{13}$$

where $F_{Knudsen}$ is the Knudsen gas flow rate, P_f and P_p are the partial pressures on the feed and permeate sides, respectively, L is the pore length, and M is the molecular weight of the gas.

Knudsen separation (Fig. 2-1(d)) typically occurs when the membrane pore diameter is smaller than 25 nm. The ideal Knudsen separation factor (Table 2-3) between two gas species can be calculated using their molecular weights, as shown in Equation (14):

$$\alpha_{1,2\ Knudsen} = \frac{\sqrt{M_2}}{\sqrt{M_1}} \tag{14}$$

where M_1 and M_2 are the molecular weights of gases 1 and 2, respectively.

However, in practical applications, the experimentally observed separation factor is often lower than the theoretical value due to additional transport phenomena such as concentration polarisation, back diffusion, and surface flow, all of which influence the effective viscosity and transport behaviour of gas molecules through the membrane [75, 76].

Table 2-3. The ideal Knudsen flow separation factor (Gas A/B) for selected gas mixture [74].

Gas A Gas B	He	H_2	CO_2	O_2	N_2	CH_4
He	1	0.71	3.32	2.83	2.65	2.00
H_2	1.41	1	4.68	3.99	3.73	2.82
CO_2	0.30	0.21	1	0.85	0.80	0.60
O_2	0.35	0.25	1.17	1	0.94	0.71
N_2	0.38	0.27	1.25	1.07	1	0.76
CH_4	0.50	0.35	1.66	1.41	1.32	1

Gas separation performance in porous membranes can be enhanced by the capillary condensation mechanism (Fig. 2-1e). This phenomenon occurs when the pores are sufficiently small—though not as small as those used in molecular sieving—and the permeating gas effectively wets the pore surface. Under these conditions, the adsorbed gas molecules form multiple molecular layers that eventually fill the pore completely [77]. Consequently, the membrane selectivity can surpass the theoretical Knudsen selectivity limit [78]. To further improve the influence of capillary condensation on gas separation, it is essential to study the confinement effects arising from interactions between gas molecules and the pore walls [79].

Another contributing mechanism is surface diffusion (Fig. 2-1f), which can complement capillary condensation to enhance membrane performance. Strong adsorption between gas molecules and the pore surface promotes longer surface migration (i.e., “jump distances”) along the pore wall, thereby increasing gas permeation flux [75, 80, 81].

When the pore radius is much smaller than the mean free path ($r<<\lambda$) and comparable to the kinetic diameter of the gas molecules (Table 2-2), gas separation in porous membranes is primarily governed by the molecular sieving mechanism (Fig.2-1g). This mechanism relies on membrane pores having diameters close to those of gas molecules. Molecules larger than the pore diameter are excluded, while smaller molecules can diffuse through the membrane bulk, enabling effective separation. However, fabricating membranes with highly uniform and precisely controlled pore sizes remains a significant challenge. Moreover, achieving a trade-off between pore size and overall porosity is necessary. Therefore, designing molecular sieving membranes that simultaneously offer both high gas permeability and high selectivity remains a key challenge in membrane engineering.

2.2. Carbon Molecular Sieve Membranes (CMSM)

Carbon molecular sieves (CMS) are promising membrane materials capable of significantly enhancing gas separation performance. These materials are produced via the pyrolysis of heat-resistant polymers or cellulose-based compounds at temperatures ranging from 500 °C to 900 °C under inert or vacuum conditions [12, 28, 82]. Importantly, these temperatures are below the threshold required for graphitisation (typically > 1500 °C), indicating that CMS comprises amorphous carbon structures with micropores suitable for separations based on molecular size exclusion.

The concept of CMS was first introduced by Jenkins and Kawamura in 1976 [83], who described it as an “extensive and stable network of graphitic ribbons” formed through the pyrolysis of polymer backbones. Subsequently, research demonstrated that CMS is composed of an amorphous, porous, and rigid carbon matrix interspersed with randomly distributed graphitic domains [84, 85]. To explain gas transport in CMS materials, Steel and Koros [84, 85] proposed an ideal structural model comprising slit-shaped pores that enable extended diffusive gas jumps. This model incorporates three essential dimensions: the molecule size, the jump length, and a negligible window thickness. Building on this framework, Koros later developed a more comprehensive CMS theory [86]. As illustrated in Fig. 2-5, when the polymer precursor is heated above its melting temperature (T_m), localised stress induces backbone cleavage, producing shorter, rigid chains that undergo aromatisation and linearisation. These rigid chains, driven by entropic forces, form "plate-like" structures reminiscent of rigid liquid crystalline polymers, which ultimately define the CMS pore architecture. The pyrolysis soak temperature determines the formation of individual “cells,” which are then organised during the final heating ramp. In the soaking stage, neighbouring cells coalesce into a larger network that shares common "walls" composed of ultramicroporous structures (<7 Å) . Lively et al. [87] later expanded on Koros’ structural model by investigating CMS formation from carbonised PIM-1 under a 4% H_2 atmosphere. Their findings suggested a configuration of thin aromatic carbon nanoribbons, aligned with micropores approximately 8 Å in size. These nanoribbons, three phenyl rings wide, potentially adopt a serpentine morphology, with stacked strands extending into interconnected graphene-like networks. The in-plane self-avoidance of these curved nanoribbons results in the formation of ultramicropores around 4 Å in diameter. This hypothesis implies that curved, snake-like graphenic nanoribbons and dispersed “orphan” strands form the fundamental structural components of CMS membranes [87].

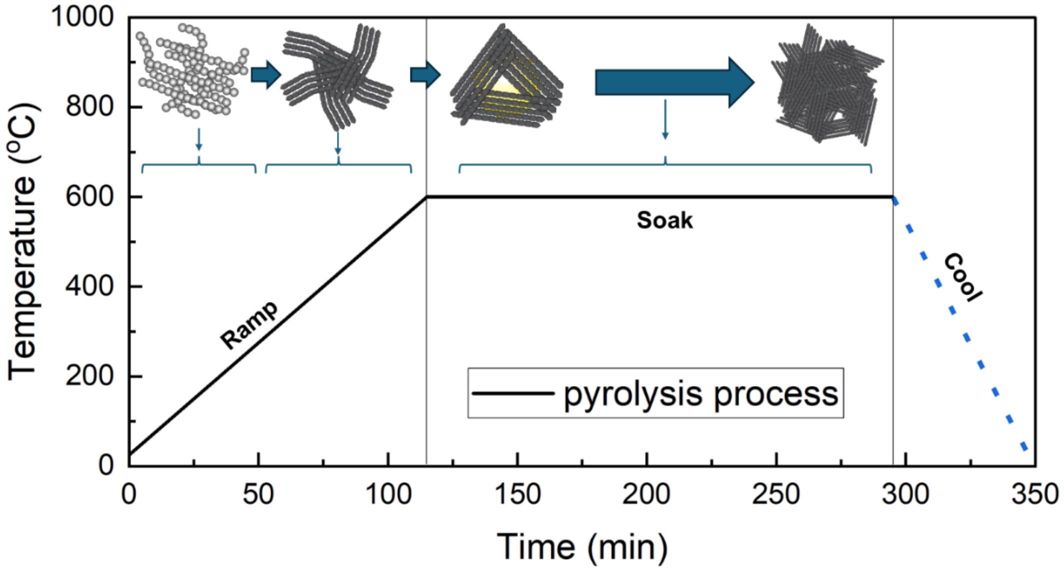

Fig. 2-5. Schematic illustration of the conversion of a polymeric precursor into CMS material, adapted from references [84, 85, 87].

2.2.1. Precursor Materials

In recent years, Genduso et al. [12] provided a comprehensive review of various polymer precursors used in the preparation of CMSM. They classified these precursors into low-temperature and high-temperature pyrolysis categories, using a decomposition onset temperature ($T_{d,s}$) threshold of 400 °C. Examples of low-temperature pyrolysis precursors included polyacrylonitrile (PAN) [88], cellulose-based materials [89, 90], poly(vinylidene chloride) (PVDC) [91, 92], polyfurfuryl alcohol (PFA) and phenolic resins (PR) [93-97]. High temperature pyrolysis precursors commonly involve polymers derived from monomers such as 3,3',4,4'-benzophenone tetracarboxylic dianhydride (BTDA), 4,4'-(hexafluoroisopropylidene) diphthalic anhydride (6FDA) and various nitrophthalic anhydrides. These monomers can be co-polymerised to synthesise novel precursors for CMSM fabrication. The following subsections are organised and reviewed low-temperature and high- temperature pyrolysis precursors.

2.2.1.1. Low-temperature Pyrolysis Precursors ($T_{d,s}$ < 400 °C)

Low-temperature pyrolysis precursors are defined by their thermal decomposition onset below 400 °C. Polyacrylonitrile (PAN) has been widely used in carbon fibre production, accounting for approximately 90% of global carbon fibre sales. It is a highly promising precursor for high-performance carbon materials [98]. PAN-based carbon membranes were first explored in the early 1990s by Schindler and Maier [99], and by Yoneyama and Nishihiro [100], who developed porous carbon membranes. Although composite CMS membranes have since been fabricated to enhance PAN membrane performance, only a few studies have reported their gas separation performance [101-103]. David and Ismail [88] reported that PAN-derived CMS hollow fibre membranes achieved an O_2 permeance of ~10 GPU and an O_2/N_2 permselectivity of 3.7.

Poly(vinylidene chloride) (PVDC), used commercially in products like Saran® due to its low oxygen permeability, is another notable precursor. Pyrolysis of PVDC at 500 °C under nitrogen results in carbon with pore sizes comparable to zeolite 5A [104]. During pyrolysis, linear PVDC undergoes cyclisation via the Diels-Alder mechanism, forming fused rings [105]. This process causes film shrinkage and increases surface roughness. To preserve membrane integrity and mechanical strength, PVDC membranes often require support structures [92, 106]. Reported O_2 permeance and O_2/N_2 selectivity are 1.4 GPU and 14, respectively [92]. Interestingly, Rao and Sircar [91] found that PVDC exhibits reverse selectivity for C_4H_{10}/H_2, with a separation factor of 94.4.

PFA, a low-cost, thermosetting resin with high carbon yield, begins decomposition at 200 °C [107]. It remains in a liquid state at room temperature and is widely used in epoxy resins and adhesives. Upon carbonisation, it serves as a suitable precursor for spray-coated CMS membrane [108-110]. PFA-derived CMS membranes have achieved O_2/N_2 selectivity as high as 30, with O_2 permeability around 8 Barrer [111].

Phenolic resins are another class of thermosetting adhesives used across various industries for their rigidity, dimensional stability, and creep resistance, especially in wood panel production [112]. Their aromatic structure enables the formation of amorphous carbon during pyrolysis, starting as low as 200 °C; however, the carbon yield drops rapidly above 400 °C [113]. CMS membranes derived from phenolic resins have demonstrated O_2 permeance of approximately 30 GPU and O_2/N_2 permselectivity of 12 [114]. Despite their low cost, these materials have seen limited use in CMS research due to competition from polymers with higher fractional free volumes [11]. A few studies have reported O_2 permeability up to 105 Barrer with O_2/N_2 permselectivity of 7.1 [115, 116].

Cellulose-based materials, being abundant, cost-effective, and sustainable, have been widely investigated as CMS membrane precursors [28, 117]. Recently, cellulose microcrystalline (MCC) and nanocrystalline (NCC) derivatives have shown promising gas separation performance [118-121]. These materials are also employed as performance-enhancing additives in polymer composites. For instance, Sazali et al. [121] reported that membranes containing 7 wt.% NCC achieved CO_2/N_2 permselectivity of ~66 and CO_2 permeance of 213 GPU.

In recent years, low-temperature pyrolysis precursors have received relatively less attention in the field of CMS membrane research. This decline is largely due to their limited gas separation performance compared to high-temperature pyrolysis-based alternatives, which dominate recent advances in CMS membrane development.

2.2.1.2. High-temperature Pyrolysis Precursors ($T_{d,s}$ > 400 °C)

High-temperature pyrolysis precursors ($T_{d,s}$) typically exhibit excellent thermal and mechanical stability, allowing their polymer backbones to withstand elevated thermal treatment. Their rigidity helps prevent degradation during carbonisation. Aromatic polyimides and their derivatives are widely used in CMS membrane fabrication due to their high glass transition temperature (T_g), melting temperature (T_m), and decomposition temperature (T_d) [12]. In 1992, Hatori et al. [122] investigated gas transport in CMS membranes derived from Kapton (PMDA-ODA) polyimide precursors pyrolysed at 800 °C, reporting a CO_2/N_2 permselectivity of 50 at room temperature. Subsequently, Jones and Koros (1994) developed CMS hollow-fibre membranes from polyimide precursors [25]. High-temperature pyrolysis precursors can be generally categorised into two major groups based on their backbone composition: (1) BTDA-based (3,3',4,4'-benzophenone tetracarboxylic dianhydride) polymers and (2) 6FDA-based (4,4'-(hexafluoroisopropylidene)diphthalic anhydride) polymers. Many precursors in these groups also include nitrophthalic anhydride units to enhance thermal stability. During pyrolysis, less stable C-N bonds decompose, producing short aromatic strands that transform into five-membered pyrrolic rings. These rings, resembling rod-like liquid crystal structures, exhibit improved packing behaviour compared to the original polymer matrix [123, 124].

As illustrated in Fig. 2-6(a), BTDA has been copolymerised with various diamines such as p,p'-oxydianiline (ODA), 5(6)-amino-1-(4′-aminophenyl-1,3-trimethylindane) (DAPI), 4,4'-isocyanatocyclohexylmethane (MDI), and toluene diisocyanate (TDI) to enhance CMS performance [125-129]. For instance, Lee et al. [125, 126] showed that BTDA-ODA CMS membranes achieved O_2 permeability of 200 Barrer and O_2/N_2 permselectivity of 13. They further investigated structural modifications by introducing alkyl substituents to increase the fractional free volume (FFV), although only minor changes were observed, likely due to side-group stripping during pyrolysis [130]. The commercially available Matrimid 5218, composed of BTDA and DAPI units, has been widely studied [84, 131-136]. Reported O_2 permeability ranges from 200 to 300 Barrer, with O_2/N_2 selectivity between 3 and 9 under varying pyrolysis conditions. Salleh et al. [119-121, 128, 129, 133, 134] evaluated BTDA-TDI/MDI (P84)-based CMS membranes and found lower O_2 permeability (15-30 GPU) compared to other BTDA systems, with O_2/N_2 permselectivity of approximately 9.3.

As shown in Fig. 2-6(b), 6FDA-derived polymers have also been widely applied in the fabrication of CMS membranes. Zhuang et al. [127] demonstrated that 6FDA precursors generally yield higher permeability than their BTDA counterparts, primarily due to their higher FFV. Koros et al. [137] corroborated these findings and noted that 6FDA can release CHF_3 gas during pyrolysis, creating larger pore volumes and further increasing FFV. In a modified system using 6FDA with diethyltoluenediamine (DETDA) and 3,5-diaminobenzoic acid (DABA) in a 3:2 molar ratio, the O_2 permeability exceeded 4000 Barrer, with an O_2/N_2 selectivity of 4.9. However, this membrane exhibited pronounced ageing behaviour under vacuum storage conditions.

Other backbones, such as polyetherimide (PEI), polyamide/imide (PA), and PBI, are also suitable for CMS fabrication due to their commercial availability and scalability. However, they typically require additional modifications, such as incorporating additives, supporting substrates, or optimising fabrication techniques, to match the separation performance of BTDA or 6FDA membranes. Tseng et al. [138-142] investigated PEI-based CMS membranes via different strategies, including tubular coatings, hollow-fibre spinning, and dopant addition. The highest-performing PEI-based CMS membrane. achieved CO_2 permeability of approximately 1000 Barrer with a CO_2/CH_4 selectivity of 27.6 [143]. PBI membranes have also shown promise. Chung et al. [144] found that non-carbonised PBI exhibited H_2/CO_2 selectivity ranging from 5 to 32, with H_2 permeability between 3.2 and 990 Barrer. After carbonisation, Omidval et al. [145] reported H_2/CO_2 selectivity of approximately 53 and H_2 permeability of

36 Barrer. During pyrolysis, PBI membranes may shrink to form hourglass-shaped pores, enhancing both permeability and permselectivity. Hosseini and Chung [146] reported a four-order-magnitude increase in H_2 permeability when PBI was carbonised at 800 °C. Additionally, cross-linking with Matrimid (75/25 wt.%) yielded H_2/CO_2 selectivity of 34, with a reduced H_2 permeability of 63.2 Barrer.

The selection of polymer precursor plays a crucial role in determining CMS membrane performance. Among high-temperature pyrolysis materials, 6FDA-derived polymers consistently demonstrate the highest gas permeabilities due to their high porosity and FFV. However, this performance gain often comes at the cost of reduced selectivity and increased susceptibility to ageing. Moreover, 6FDA-based polymers are less readily available in large quantities, which may limit their large-scale deployment in CMS membrane production.

(a)

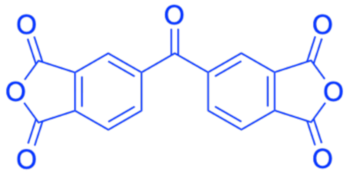

3,3',4,4'-Benzophenone tetracarboxylic dianhydride (BTDA)

(b)

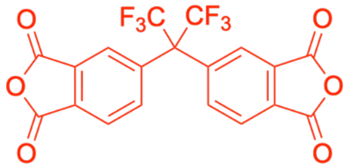

4,4′-(Hexafluoroisopropylidene)diphthalic anhydride (6FDA)

(c)

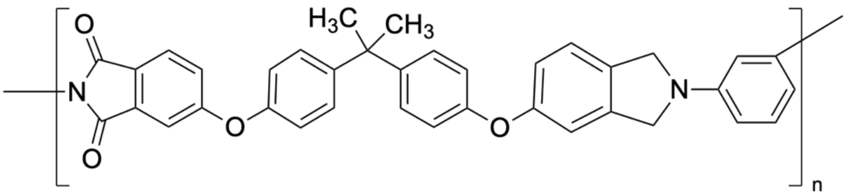

Polyetherimide (PEI)

Fig. 2-6. Chemical structures of carbonised polymer precursors: (a) BTDA, (b) 6FDA, and (c) PEI.

2.2.2. Preparation Conditions

2.2.2.1. Effect of Pyrolysis Temperature

Pyrolysis temperature is a critical parameter in the synthesis of high-quality CMSMs because it governs both the formation of the CMS structure and the rearrangement of polymer chains. It is one of the most commonly controlled conditions in CMSM research. There is a consensus that higher pyrolysis temperatures tend to reduce both pore size and porosity due to increased graphitisation of the polymer chains. Genduso et al. [12] conducted a comprehensive review of CMSMs developed over recent decades, using semi-log plots to illustrate the influence of pyrolysis temperature on CMSM performance. Their findings showed that CMSM permeability decreases with increasing pyrolysis temperature, whereas permselectivity tends to increase, though significant variability was observed. These trends reflect the classic permeability-selectivity trade-off observed in polymeric membrane materials. As shown in Fig. 2-8, PEI-based CMSMs were investigated at various pyrolysis temperatures without the use of additives to assess the impact on gas permeability [141, 147-153]. The results demonstrated that both CO_2 and CH_4 permeability were low at high (>700 °C) and low (<550 °C) pyrolysis temperatures, respectively. However, the overall gas permeability of PEI membranes did not follow a clear trend with temperature, likely due to differences in pyrolysis conditions, such as atmosphere and heating rate, which can lead to varying CMS structures. However, the CO_2/CH_4 permselectivity consistently increased with higher pyrolysis temperatures, suggesting that the formation of denser CMS structures with enhanced selectivity is promoted by elevated temperatures.

In a related study, Hazazi et al. [154] examined the impact of pyrolysis temperatures ranging from 550 °C to 1000 °C on spirobifluorene-based dianhydride with 3,3′-dimethylnaphthidine (SBFDA-DMN) derived CMSMs. The BET surface areas of the SBFDA-DMN membranes varied non-linearly with temperature: decreasing from 621 $m^2 g^{-1}$ (pristine) to 545 $m^2 g^{-1}$ at 550 °C, increasing to 615 $m^2 g^{-1}$ at 600 °C, subsequently dropping to ~518 $m^2 g^{-1}$ at 1000 °C. These variations have significant effects on pore volume and ultramicropore formation. As a result, the gas permeability decreased with increasing pyrolysis temperatures, attributable to the development of a more tightly packed structure. Similar findings have been reported for CMSMs derived from other polymer precursors, including cellulose [90], Matrimid [85], and 6FDA-DAM [155]. Although pyrolysis temperature is universally recognised as a key factor in CMSM fabrication, the optimal temperature varies depending on the specific polymer precursor. Therefore, no single pyrolysis temperature can be universally applied to all CMSM materials.

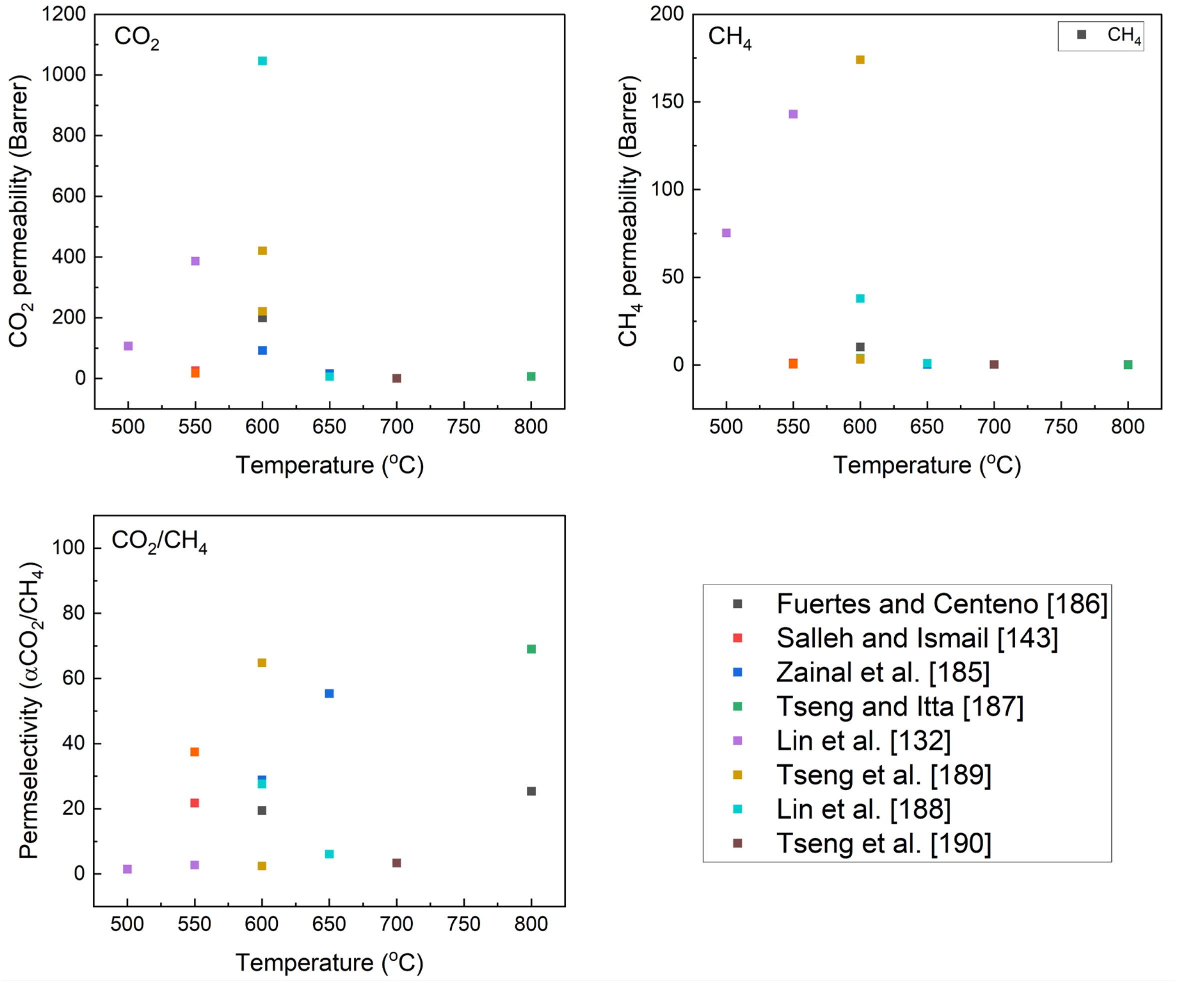

Fig. 2-7. Permeability and permselectivity of PEI-derived CMS membranes at various pyrolysis temperature based on literature data. (a) CO_2 permeability, (b) CH_4 permeability and (c) CO_2/CH_4 permselectivity, Data compiled from references [143, 148, 150, 153, 156-160].

2.2.2.2. Heating Rate Effect

The heating rate during pyrolysis plays a crucial role in determining the quality of CMSMs by controlling the transfer of thermal energy from the surrounding atmosphere to the membrane [95, 120, 161, 162]. In general, slower heating rates facilitate the formation of smaller pores and more ordered carbon structures. In contrast, rapid heating often induces structural defects, such as cracks, pinholes, and blisters, which compromise membrane selectivity [11].

Centeno et al. [95] studied CMSMs derived from phenolic resin at heating rates ranging from 0.5 °C min^{-1} to 10 °C min^{-1}. Higher heating rates accelerated the release of volatile organic compounds, producing membranes with permeability enhancements of approximately three orders of magnitude. However, this increase in permeability came at the expense of selectivity. Similarly, Salleh and Ismail [156] investigated PEI-based CMSMs and reported that heating rates of 3 – 5 °C min^{-1} yielded optimal CO_2/CH_4 selectivity. Their findings indicated that excessive heating rates lead to physical shrinkage and pore irregularities, which increase gas permeance but reduce selectivity.

In a separate study, Su and Lua [163] performed thermogravimetric analysis (TGA) on Kapton polyimide membranes and found that higher heating rates broadened the decomposition temperature range by approximately 150 °C. This phenomenon likely results in rapid carbonisation of the bulk polymer, contributing to the development of a dense CMS structure. As summarised in Table 2-4, comparisons of heating rate effects across various CMSM studies consistently demonstrate that higher heating rates tend to damage membrane structures, thereby enhancing permeability while reducing selectivity. The exception is the phenolic resin membranes reported by Centeno et al. [95], which exhibited unusually high permeability. Notably, Ismail's group [156, 164] recommended a heating rate of 3 °C min^{-1} as optimal for PEI-based CMSMs. However, in broader reviews, they acknowledged that a universal heating rate of 0.5 – 1 °C min^{-1} may be more appropriate for CMSM synthesis across diverse polymer precursors [11, 165].

Table 2-4. Effect of heating rate on CMS membrane preparation and CO_2 separation performance.

Precursor materials	Method	Ramp rate (°C min^{-1})	Permeability (Barrer)			Selectivity (α)		Ref
			CO_2	N_2	CH_4	CO_2/N_2	CO_2/CH_4	
Phenolic resin	Composite on ceramic	1	2200		1466		~1.5	[95]
		10	~22		0.08		27	
PI/NCC	Composite on ceramic	1	174^{a}	3.1^{a}	-	57	-	[119]
		3	214^{a}	3.2^{a}	-	66	-	
		7	182^{a}	3.1^{a}	-	58	-	
PEI	Composite on ceramic	1	211	5.6	3.3	38	64	[164]
		3	34	1.1	0.7	32	51	
		7	909	309	420	2.9	2.2	
PEI	Hollow fibre	1	~3^{a}		0.13		~23	[156]
		5	~1.5^{a}		0.02		~63	
		9	~7^{a}		0.35		~20	
Kapton® polyimide	Self-standing	1.33	0.5	0.004	-	122	-	[166]
		4.5	2.5	0.03	-	87.7	-	
		13.3	3.54	0.04	-	82.7	-	

[a] The data are expressed in gas permeance units (GPU).

2.2.2.3. Purge Flow Atmosphere Effect

The atmosphere during the pyrolysis process plays a critical role in tuning the pore size and porosity of CMSMs. These membranes can be synthesised under vacuum or in inert gas environments (He, N_2, Ar, or CO_2). As shown in Fig. 2-8, different pyrolysis atmospheres influence the structure and performance of CMSMs. Vacuum conditions promote the formation of denser carbon structures with reduced d-spacing, leading to lower gas permeability but higher selectivity [11]. Hosseini et al. [167] reported a 40% improvement in the selectivity for O_2/N_2, CO_2/CH_4, and CO_2/N_2 as the vacuum pressure decreased from 10^{-3} to 10^{-7} Torr, accompanied by a corresponding drop in gas permeability. This effect was attributed to slower heat transfer and increased weight loss and shrinkage at higher vacuum levels, which limited effective pore formation. Geoszler and Koros [168] found that vacuum pyrolysis follows a unimolecular degradation mechanism, whereas inert gas flow enhances heat and mass transfer, accelerating carbonisation. This leads to a higher free volume, thereby improving permeability but reducing selectivity. While they observed minimal differences among inert gases, an increased gas flow rate facilitated by-product removal. At 550 °C, a higher helium flow reduced weight loss to 2% and increased O_2 permeability by three orders of magnitude. However, increasing the flow rate had little impact at higher pyrolysis temperatures.

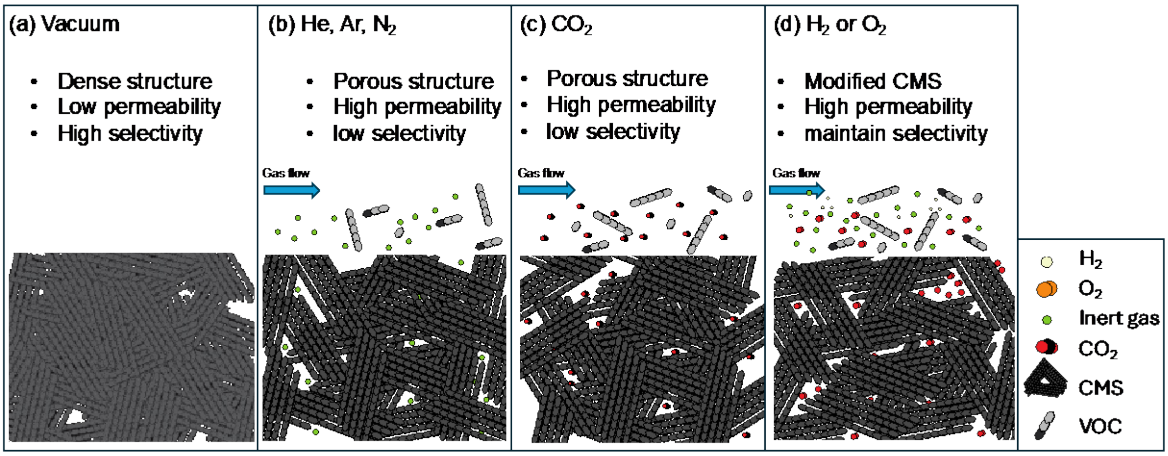

Fig. 2-8. Schematic representation of CMS membrane pyrolysis under different atmospheric conditions: (a) vacuum environment, (b) inert gases (He, Ar, or N_2), (c) carbon dioxide atmosphere, and (d) reactive gases (H_2 or O_2).

Inert gases also influence the properties of CMSM by facilitating the collision cascades of volatile organic compounds emitted during pyrolysis [82, 163, 168, 169]. Vu et al. [169] demonstrated that regulating helium flow at 200 mL min^{-1} increased membrane porosity but reduced $\alpha CO_2/CH_4$ by 65% compared to membranes prepared under vacuum. Argon, which induces more intense collision cascades than helium, tends to produce more porous CMSM surfaces, enhancing permeability while maintaining or slightly reducing selectivity [170, 171]. Sazali et al. [134] reported that Matrimid-based CMS membranes under an argon atmosphere exhibited 60% higher permeance than those treated under nitrogen. Centeno et al. [95] observed that pyrolysis under nitrogen increased the CO_2 permeability of PVDC-derived CMSMs by 3–

5 times compared to vacuum conditions, with minimal impact on selectivity. Additionally, a CO_2 atmosphere can act as a mild oxidising environment during pyrolysis at 800 °C, promoting the formation of a porous CMS surface [172]. However, in most cases, CO_2 primarily serves as a sweep gas to facilitate the removal of volatile compounds from the CMS structure [168, 173].

The introduction of reactive gases, such as O_2 or H_2, can further alter membrane structures by modifying the carbon matrix at the molecular level [174, 175]. For instance, the presence of 3 ppm O_2 during the pyrolysis of 6FDA/BPDA polyimide membrane promoted the formation of C=O functional groups, reducing pore size and enhancing selectivity [137]. Ma et al. [176] showed that pyrolysing PIM-1 membranes in an H_2 (4 vol.% in Ar) atmosphere effectively inhibited polymer aromatisation, enhancing permeability by 14-fold while maintaining selectivity through the formation of 5–7 Å pores. In summary, the pyrolysis atmosphere critically affects the CMSM structure and performance. While inert gases facilitate pore formation and enhance permeability, vacuum environments favour the development of denser structures with higher selectivity. Although used in small concentrations, reactive gases offer further potential for tuning pore structures and optimising CMSMs for targeted gas-separation applications.

2.2.3. CMS Membrane Structure

The CMS membrane structure can be classified into two categories: self-supported membranes (e.g., flat sheets, hollow fibres, or capillary tubes) and supported membranes (typically fabricated as disks or tubular structures) [26, 170, 177]. Although both types of CMS membranes have been widely explored, self-supported CMS membranes face significant challenges in large-scale production due to their inherent brittleness, which limits mechanical flexibility and complicates handling and processing operations [178, 179]. Supported CMS membranes offer a more viable option for industrial applications because they address the mechanical fragility of self-supported counterparts and align well with existing fabrication techniques used in composite membrane production [180]. However, a key limitation of supported CMS membranes is the formation of defects in the selective polymeric layer during the coating process. This issue requires the development of reliable fabrication methodologies that ensure uniform, defect-free polymer coatings before pyrolysis. Such advancements are crucial for the consistent production of high-performance carbon membranes. Moreover, standardised evaluation criteria are needed to assess coating methods, especially given the wide variation in the physical and chemical properties of polymer precursors and porous substrates. The following section presents advanced modification strategies designed to enhance the structural integrity and performance of supported CMS membranes while addressing the aforementioned fabrication challenges.

2.3. Advanced Strategy Modification

2.3.1. Composite CMSMs (Gutter Layers)

Thin-film composite membranes are typically characterised by an ultrathin, dense selective layer, generally less than 0.2 mm in thickness, deposited onto a microporous support layer [181]. Zhang and Lin [14] provide a comprehensive review on gutter layer for gas separation organic/organic or organic/inorganic composite membrane. Traditionally, the support layer provides only mechanical stability because its highly porous and non-selective nature contributes minimally to mass transfer resistance [7]. The thickness of the selective layer is a critical factor in the separation performance, as reducing the thickness lowers the mass transfer resistance and enhances the permeation of the target gas molecules. Recent developments in composite membrane fabrication have enabled the production of ultrathin selective layers (< 1 μm), further improving the permeance [7, 8, 10]. However, these ultrathin layers are susceptible to structural defects and infiltration into the pores of the support, which can significantly degrade separation performance. To address these issues, an intermediate "gutter layer" is often introduced between the support and the selective layer. This intermediate layer acts as a barrier to prevent polymer infiltration and facilitates the formation of a defect-free, continuous selective layer [14, 15]. Despite their importance, limited information is publicly available regarding the composition and performance of effective gutter layers, as such formulations are typically proprietary and protected by manufacturers [182, 183].

In principle, an effective gutter layer should exhibit low selectivity and high gas permeance, thereby supporting the selective layer without compromising the overall membrane performance [14]. Commonly used gutter materials include polydimethylsiloxane (PDMS), polytetrafluoroethylene (PTFR or Teflon), and poly(trimethylsilyl-propyne) (PTMSP), which exhibit CO_2 permeabilities in the range of 2,200 to 47,000 Barrer and CO_2/N_2 permselectivities between 4.1 and 9.5. In addition to polymers, porous materials, such as metal-organic frameworks (MOFs), have been incorporated into gutter layer designs to enhance interfacial compatibility and improve overall performance. For example, Xie et al. [184] employed amino-functionalised MOFs (NH_2-MIL-53) grown on anodisc substrates as a platform for coating polyethylene glycol dimethacrylate (PEGDMA) via a continuous polymer assembly method. This technique yielded an ultrathin selective layer (~ 30 nm) while preserving high porosity in the gutter layer. The resulting membrane demonstrated a CO_2 permeance of 90 Barrer and a CO_2/N_2 permselectivity of approximately 34.

To further address the interfacial challenges of coating selective layers onto inorganic substrates, Tseng et al. [30, 139, 158] introduced titanium dioxide (TiO_2) as a gutter layer to enhance interfacial adhesion between the PEI selective layer and porous alumina substrates. The strong affinity between TiO_2 and Al_2O_3 facilitated better interfacial bonding, resulting in defect-free coatings. However, this approach has a tradeoff: the potential reduction in substrate porosity due to the accumulation of TiO_2 within surface valleys, which partially blocks the pores. Despite this, the resulting membranes achieved a CO_2 permeability of approximately 72.9 Barrer and a CO_2/N_2 selectivity of 38.1. Substrate polishing is an often overlooked yet crucial step in composite membrane fabrication prior to the application of gutter and selective layers. Polishing cleans the substrate surface and reduces roughness. Wey et al. [142] evaluated the effects of sandpaper with particle sizes of 8 and 14 μm on porous alumina disks before TiO_2 coating. Their results showed that surface roughness increased from 74.9 to 99.1 nm as the sandpaper particle size increased, suggesting that higher substrate roughness enhances mechanical interlocking with the selective layer and improves the coating conditions. Similar findings have been reported in subsequent studies [139, 185].

These investigations confirm that the surface roughness of the substrate directly influences the morphology and performance of the selective layer. However, a comprehensive and systematic evaluation of polishing parameters for porous substrates is still lacking. This represents a clear research gap in optimising the selective layer-substate interface for enhanced membrane performance.

2.3.2. Mixed-Matrix Membranes (MMMs)

Beyond composite membrane strategies, the incorporation of functional or intrinsically porous materials directly into the polymer matrix, commonly referred to as the mixed-matrix membrane (MMM) approach, has proven effective in enhancing gas permeance. These embedded materials, often referred to as “fillers,” contribute additional porosity and functionality to the membrane structure. Moore and Koros [186] conducted a seminal study on MMMs by incorporating zeolite 4A into Ultem, to elucidate the interaction between fillers and polymer matrices. As illustrated in Fig. 2-9, their study categorises four typical morphologies from different filler distributions within the polymer matrix. Case I represents the ideal MMM configuration, where the fillers are uniformly dispersed throughout the polymer, confirming the intrinsic porosity of the fillers with the inherent selectivity of the polymer matrix. Case II is characterised by the formation of a polymer “halo” surrounding the filler particles, resulting from shrinkage stress during solvent evaporation and polymer chain rigidification. Case III involved interfacial voids between the filler and polymer, forming a “sieve-in-a-cage” structure. Although this morphology can increase gas permeability, it typically compromises selectivity. Case IV depicts the partial blockage of the filler surface pores by rigidified polymer chains, resulting in a significant reduction in gas permeability while maintaining relatively unchanged selectivity. These cases emphasise the critical role of controlling filler dispersion and interfacial compatibility during membrane fabrication. Poorly integrated fillers can introduce non-selective pathways or reduce the active surface area, thereby undermining membrane performance. Therefore, careful optimisation of filler loading, distribution, and polymer-filler interaction is essential. Structural characterisation and gas permeation analyses remain vital tools for validating MMM quality and determining optimal synthesis conditions.

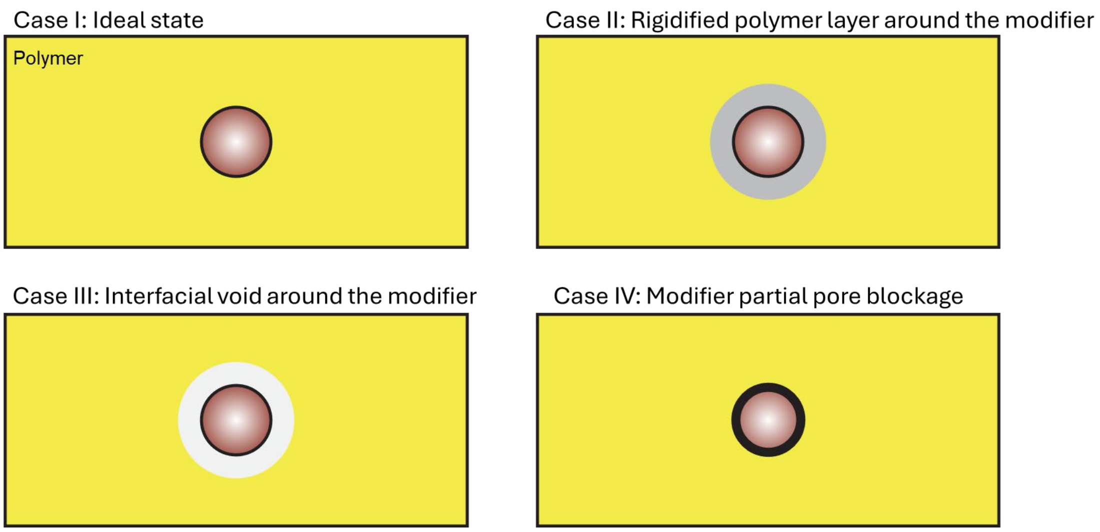

Fig. 2-9. Schematic illustration of the polymer-filler interface in MMM, highlighting interfacial interactions between the polymer matrix and filler particles [187, 188].

Furthermore, incorporating additives into polymeric membrane precursors can induce the formation of novel pore networks due to differences in heat capacity and decomposition temperatures between the additive and the polymer. These thermal disparities often result in the generation of distinct pore structures or voids within the membrane matrix, thereby altering gas separation performance. This process may be regarded as a form of co-pyrolysis, where two materials with varying thermal characteristics simultaneously undergo decomposition, potentially leading to significant structural and functional changes in the resulting membrane. Additives are generally categorised based on their thermal stability into two main groups: thermally labile materials (often used as templates) and thermally stable materials (commonly referred to as fillers). Thermally labile additives decompose completely at the target pyrolysis temperature, whereas thermally stable additives retain their structure and composition throughout the co-pyrolysis process. This classification provides a useful framework for identifying research gaps and selecting appropriate additives for tailored CMS membranes design and performance enhancement.

Templates

Thermally labile materials, which decompose during the co-pyrolysis process, serve as templates by leaving voids within the CMS membrane matrix. These voids increase free volume and porosity, thereby enhancing membrane performance. Common templates used in CMS membrane modification include polyvinylpyrrolidone (PVP) and polyethylene glycol (PEG), both of which decompose below 450 °C, facilitating the creation of additional free volumes and an enlarged surface area within the membrane structure [189, 190]. Kim et al. [126] reported that the co-pyrolysis of BTDA-ODA with PVP yielded CMS membranes with higher gas permeability and slightly reduced selectivity than unmodified membranes. Similar trends were observed when poly(p-phenylene oxide) (PPO) [191, 192] or PEI [149, 156] was used as a dopant in CMS membranes. PEG, in particular, is a well-known thermally labile additive that enhances microporosity [193-195]. Chua et al. [196, 197] examined cross-linked polyimide incorporating thermally labile monomers and demonstrated improved microporosity and enhanced CO_2 plasticisation resistance. Additionally, functional side chains, such as β-cyclodextrin (β-CD) or glucose, grafted onto the polymer backbone, can contribute to pore formation and increased interchain spacing upon pyrolysis, thereby improving gas permeability. Modifying polymer precursors through the incorporation of functional groups offers another viable route to tailor the microporous structure and membrane performance.

Zeolites and MWCNTs

Zeolites are commonly used as additives in the synthesis of mixed-matrix CMS membranes due to their well-defined molecular channels and rigid cavities, which enhance the porous network of the resulting membranes [198-200]. Their high thermal stability allows them to endure the carbonisation process and contribute to improved gas permeability. However, zeolite particles are prone to sedimentation and agglomeration within the membrane matrix at high doping concentrations, often resulting in diminished gas separation performance [201, 202]. Li et al. [203] investigated the incorporation of H-zeolite 5A in Matrimid polyimide-based membranes, followed by co-pyrolysis at 550 °C. At a maximum loading of 30 wt.%, the CO_2 permeability increased significantly from 29 Barrer to 2450 Barrer, whereas the CO_2/CH_4 selectivity decreased from 49.2 to 19.3. Notably, the persistence of "sieve-in-a-cage" structures in the CMS membrane, contributed to the reduced separation performance, indicating that H-zeolite 5A may not be an ideal additive for CMS membrane fabrication.

Carbon nanotubes (CNTs), particularly multi-walled carbon nanotubes (MWCNTs), have also attracted attention owing to their large inner diameters and unique structural characteristics that increases gas transport. Rao et al. [204] doped MWCNTs into PEI membranes to evaluate their effect on membrane porosity. The CO_2 permeability increased by more than two orders of magnitude relative to undoped PEI CMS membranes, and the CO_2/N_2 selectivity improved from 17.5 to 48.8. Despite these enhancements, the incorporation of CNTs can induce aggregation-related defects that complicate membrane fabrication. Similar challenges are encountered in zeolite-doped mixed-matrix CMS membranes, where weak interfacial interactions between fillers and the carbon matrix may hinder the formation of a continuous, defect-free structure, thereby limiting the overall effectiveness of the modification.

Metal organic frameworks (MOFs)

Metal-organic frameworks (MOFs) are porous, crystalline molecular sieves composed of metal-ion clusters coordinated with organic linkers [205, 206]. The pore size of MOFs can be adjusted by modifying the length of the organic linkers. Compared to other porous materials, MOFs offer several advantages, including high surface area with retained porosity, structural flexibility, tuneable pore dimensions, and customisable surface functionalities [207]. Healy et al. [208] reviewed the thermal stability of several commonly used MOFs, identifying their T_d and residue products information essential for assessing their viability as dopants in polymeric membranes for CMS MMM fabrication. However, most MOFs decompose at relatively low temperatures (150-575°C) [209-212], rendering them unsuitable for use in CMS membranes typically produced at higher temperatures (>600 °C) Wang et al. [213] incorporated 5 wt.% Fe_3O_4@ZIF-8 into polyimide-based CMS membranes and observed the formation of surface pores approximately 200 nm in diameter. This suggests that the continuous carbon structure may be compromised during pyrolysis, leading to structural defects in the membrane matrix. These findings underscore the need for further investigation into the relationship between the pore structure of MOFs and their thermal stability before their application in CMS membranes. At this stage, MOFs may not be suitable as modifiers for CMS MMMs unless they can yield a continuous carbon framework during membrane fabrication.

Covalent organic frameworks (COFs)

Covalent organic frameworks (COFs) are a novel class of crystalline porous materials composed entirely of organic linkers that offer structural similarities to MOFs but with enhanced polymer compatibility due to their purely organic composition [214]. Unlike MOFs, which often suffer from inorganic-organic interface mismatches, the organic nature of COFs may reduce the interfacial defects when incorporated as fillers in MMMs. Biswal et al. [215] demonstrated this compatibility by successfully incorporating two triformylphloroglucinol (Tp)-based COFs (TpPa-1 and TpBD) into PBI-Bul, achieving COF loadings of up to 50%. Moreover, H_2 permeability increased with COF pore size, whereas CO_2 permeability remained stable at approximately 15 Barrer. Such high filler loadings are typically difficult to achieve with MOFs. Zou et al. [216] reported that doping 1 wt. % honeycomb-structured TpPa-1 COF nanosheets into Polyether-block-amide (PEBA) membranes improved CO_2/N_2 selectivity, with CO_2 permeability and permselectivity increasing by 67% and 12.5%, respectively, compared to pristine PEBA. However, COFs exhibit limited thermal stability during pyrolysis. Evans et al. [217] revealed that COF crystallinity diminished at approximately 300 °C, as shown by variable-temperature X-ray diffraction (T_{XRD}), despite no significant thermal decomposition observed via TGA. This suggests that the intrinsic porous structure collapses, leading to the formation of amorphous carbon chains. The main decomposition stage occurs around 600 °C, during which COFs degrade into volatile organic compounds and CO_2. Therefore, COFs may not be a suitable additive for CMS membrane fabrication due to their insufficient thermal stability under pyrolysis conditions.

Biomimetic materials (BMMs)

Nature-inspired designs have increasingly influenced membrane technology, offering innovative strategies to enhance separation performance by mimicking the advantageous structures and functions of biological systems. For instance, the superhydrophobic surfaces of lotus leaves [218] and butterfly wings [219] have been successfully replicated to improve oil/water separation [220]. These bioinspired or biomimetic approaches have proven effective in enhancing material properties such as surface wettability, structural integrity, and overall separation performance.

In gas separation membranes, the CO_2 affinity and microporous characteristics observed in biological systems present attractive targets for improving membrane efficiency [221]. For example, Widakdo et al. [222] developed a biomimetic, electric-field-tunable membrane inspired by the stimuli-responsive behaviour of skin cell membranes. This membrane, composed of [BMIM][BF4] ionic liquid-coated graphene blended with a PVDF matrix, exhibited a CO_2 permeability of 81.9 Barrer and a CO_2/N_2 permselectivity of 61.13 without an electric field. Upon applying a 3V direct current, the CO_2 permeability and selectivity increased by 141% and 121%, respectively. These findings highlight the potential of bioinspired, stimulus-responsive systems in generating dynamic, tunable gas transport pathways. Nacre, another example from nature, is composed of aragonite crystals (300 μm) arranged between β-chitin layers (20 μm), forming a “bricks-and-mortar” structure with high toughness and resilience [223, 224]. Mimicking this architecture can enhance inter-layer spacing in nanosheet composite membranes. Dai et al. [225] explored a 1D-2D intercalated structure to support ionic liquid membranes, avoiding internal voids and defects in g-C_3N_4 nanosheet membranes, and achieving a CO_2 permeance of 954 GPU with a CO_2/N_2 selectivity of 55.5.

Carbonic anhydrase (CA), an enzyme present in animal red blood cells, plays a crucial role in CO_2 transport via a hydration mechanism. The most common CA structure features a central Zn^{2+} ion coordinated by three histidine residues and a water molecule, forming its active site [226, 227]. Fu et al. [228] immobilised bovine CA within oriented anodisc pore channels (~8nm diameter), forming water channels that facilitated CO_2 separation, achieving 2600 GPU in CO_2 permeance and a CO_2/N_2 selectivity of 788. However, practical deployment is limited by enzyme instability and water evaporation under operational conditions.

To address these limitations, synthetic biomimetic materials that replicate CA functionality while maintaining stability under harsh conditions are needed. Zheng et al. [48] developed CFA-1, a MOF based on zinc acetate dihydrate that mimics CA activity. When 3 wt.% of CFA-1 was incorporated into a Pebax membrane, CO_2 permeability and CO_2/N_2 selectivity increased by factors of 9.2 and 2.8, respectively, compared with the neat Pebax membrane (94.4 Barrer, 31.6 selectivity). However, loading above 5 wt.% resulted in interfacial defects. Similarly, Zhang et al. [229] reported a cobalt-based biomimetic material using Co^{2+} chelated with 2,6-bis(2-benzimidazolyl)pyridine (BBP), achieving a CO_2 permeance of approximately 900 Barrer and a CO_2/N_2 selectivity of 94.2 upon blending with Pebax. Despite promising results, the integration of BMMs into CMS membranes remains underexplored, primarily due to limited studies on their thermal stability. This represents a key research gap that warrants systematic investigation to validate the potential of CMS membranes in enhancing performance.

In summary, incorporating templates or additives into CMS precursors during co-pyrolysis can create membranes with larger or more tailored pores, enhancing their performance compared to undoped CMSMs. However, evaluating the thermal stability and structural integrity of additives before doping is essential to avoid adverse effects. Additive modifications enable the transfer of desirable intrinsic properties into the CMS matrix. Compared to molecular or polymer precursor modifications, additive strategies may offer a more cost-effective route, especially if small quantities yield significant performance gains, presenting an efficient and economical pathway to optimise CMS membrane fabrication.

2.4. Literature Comparison on PEI Membranes for Gas Separation

This section presents a comparative analysis of PEI-based membranes for gas separation applications. As shown in Table 2-5, four representative membrane modules (flat sheet, composite disk, composite tubular and hollow fibre) were compared in terms of fabrication complexity, performance limitations, surface area/volume ratio (SA/V), cost, and typical application fields [230]. The flat sheet and composite disk membrane are commonly adopted in laboratory-scale studies due to their low material cost, straightforward fabrication, and ease of characterisation [231]. However, their relatively low SA/V ratio, particularly in spiral-wound formats, can limit permeation flux, necessitating multiple modules to achieve industrially relevant productivity. In contrast, the composite tubular module provides a moderate SA/V ratio and improved mechanical robustness, making it suitable for pilot-scale studies and harsh operating environments, though it typically involves higher hardware costs and more complex assembly. The hollow fibre configuration offers the highest packing density and SA/V ratio, enabling compact module designs with superior flux [232]. However, it requires sophisticated fabrication techniques and more prone to aging and skin-layer defects [179, 233]. Overall, each module type exhibits distinct trade-offs between scalability, cost efficiency, and operational durability. Among them, the composite tubular module represents a promising transitional configuration between laboratory and pilot-scale investigations of carbon molecular sieve (CMS) membranes, offering an optimal balance between structural robustness and process applicability under severe operating environments while mitigating drawbacks such as brittleness and fracture during operation.

As summarised in Table 2-6, most studies reported the use of NMP as the casting solvent to fabricate both flat-sheet and hollow-fibre configurations. Polymeric PEI membranes generally exhibit low CO_2 permeability, ranging from 1.32 to 1.55 Barrer, with CO_2/N_2 selectivity ranging from 22.1 to 27.4. These values reflect a moderate separation performance typical of conventional polymeric membranes, which can be significantly enhanced by incorporating fillers or porous additives. Previous studies have demonstrated that introducing various porous fillers can improve CO_2 permeability by approximately 3-10 times, reaching values between 4.13 and 11.1 Barrer. Concurrently, a slight increase in CO_2/N_2 permselectivity was observed, ranging from 25.3 to 42.1. These findings suggest that the integration of fillers into the PEI matrix can effectively enhance both gas permeability and selectivity, provided that the doping concentration is optimised. Although PEI has been employed in composite membranes in conjunction with inorganic or organic porous substrates, only a few studies have reported the gas separation performance of such composite membranes. This indicates a significant research gap in the development of composite membranes designed to enhance gas separation performance through the use of PEI-coated structures.Moreover, PEI is widely used as a precursor material for CMSMs due to its high carbon yield and favourable thermal stability. The CO_2 permeability in PEI-derived CMSMs increases substantially compared to that of polymeric PEI membranes, ranging from 72.9 to 15,060 Barrer, depending on the pyrolysis conditions and the types of dopants used. Despite these promising improvements, achieving robust interfacial compatibility between PEI-derived membranes and porous substrates (e.g., alumina) remains a major challenge. Addressing this limitation is crucial for enhancing the scalability and industrial viability of PEI-based CMS membranes.

Table 2-5. Comparative summary of common membrane module configurations.

Membrane type	Synthesis & fabrication	Separation performance limits	Surface area/ volume ratio (SA/V)	Cost	Typical use
Flat sheet (as spiral-wound)	Simple casting, easy to vary thickness	Edge leakage/pinholes if sealing is imperfect, support–skin adhesion	**Low–moderate** (10^2-10^3 m^2 m^{-3})	Lowest R&D cost per sample	Materials discovery, parametric studies, early process-relevant screening
Composite disk	Composite on a flat support, minimal material	limited to lab cell conditions	**Very low** (not a deployable metric)	Lowest test cost; limited insight into scale-up economics	High-throughput materials screening, mechanism studies
Composite tubular	Moderate complexity fabrication	Lower packing density, interfacial defects	**Moderate** (10^2-10^3 m^2 m^{-3})	Larger footprint and higher hardware cost per m^2 than HF	Harsh-service pilots and deployment; good bridge from lab to plant
Hollow fibre	Highest complexity fabrication	Aging and skin defects	**Highest** (10^4-$10^{4.5}$ m^2 m^{-3})	Lowest **system cost per m²** at scale due to compact, high-packing modules	Pilot and deployment when packing density cost dominate

Table 2-6. Literature comparison of PEI-based membranes: polymeric, MMM, composite, and CMS membranes.

Membrane type	Membrane code	Solvent	Membrane types	Permeability (Barrer)						Permselectivity (α)				Ref.
				He	H_2	CO_2	O_2	N_2	CH_4	H_2/CH_4	CO_2/N_2	CO_2/CH_4	O_2/N_2	
Polymeric membrane	Ultem® 1000	-^{b}	Flat sheet	6.9	-	1.32	0.34	0.05	0.04	-	26.4	30	6.8	[234]
	Ultem® 1000	Chloroform	Flat sheet	8.8	-	1.48	0.38	0.054	0.04	-	27.4	37	7.3	[18]
	Ultem® 1000	-^{b}	Flat sheet	9.4	-	1.33	0.41	0.051	0.036	-	26.1	36.9	8.0	[235]
	Ultem® 1000	dichloromethane	Flat sheet	-	-	1.45	0.38	0.054	0.037	-	26.9	38.8	7.1	[236]
	Ultem® 1000	NMP	Flat sheet	6.8^{a}	-	-	-	-	0.283^{a}	-	-	-	-	[237]
	Ultem® 1000	γ-butyrolactone (GBL)	Flat sheet	-	1.1 ^{a}	-	-	-	0.3 ^{a}	3.6	-	-	-	[238]
	Ultem® 1000	-^{b}	Flat sheet	-	-	1.55	0.5	0.07		-	22.1		7.1	[239]
	Ultem® 1010	NMP	Flat sheet	-	-	-	0.36	0.049		-	0.0		7.5	[240]
	Ultem® 1000	NMP	Hollow fibre	-	19.6^{a}	-	-	0.214^{a}	-	-	-	-	-	[241]
	Extem® 1015	NMP	Hollow fibre	-	-	-	8.68^{a}	1.37 ^{a}	-	-	-	-	6.3	[242]
MMM	ZIF-8 (30 wt.%)	Methylene chloride	Flat sheet	-	-	11.1	-	0.357	0.274	-	31.1	40.5	-	[243]
	Silica	NMP	Flat sheet	-	-	1.63	0.45	-	-	-	-	-	-	[244]
	$Cu_3(BTC)_2$/	DMAc	Flat sheet	-	-	4.13	0.84	0.148	0.121	-	27.9	33.9	6.9	[245]
	20wt.% PIM-1	Chloroform	Flat sheet	22.6	-	6.58	1.6	0.26	0.19	-	25.3	34.6	6.1	[18]
	Zeolite	NMP	Flat sheet	69^{a}	-	11.3^{a}	3.26^{a}	0.423^{a}	0.285^{a}	-	26.7	39.6	7.7	[246]
	TiO_2	NMP	Flat sheet	-	-	17 ^{a}	-	0.5^{a}	0.41^{a}	-	34	41.1		[247]
	CMS (35 vol.%)	dichloromethane	Flat sheet	-	-	4.48	1.09	0.136	0.083	-	32.9	53.7	8.0	[236]
	Zeolite	NMP	Hollow fibre	48^{a}	-	6.23^{a}	5.4^{a}	0.207^{a}	0.142^{a}	-	30.1	43.9	8.2	[246]
	MIL-53	NMP	Flat sheet	-	-	17.8^{a}	-	0.423^{a}	-	-	42.1	-	-	[248]
	ZIF-8 (13 wt.%)	Chloroform	Hollow fibre	-	-	26	-	0.72	-	-	36.1	-	-	[249]
Polymeric Inorganic Composite membrane	SAPO-34/ Ultem	NMP/DSI	Tubular Alumina	-	-	1.19^{a}	-	-	0.019^{a}	-	-	60	-	[250]
	Ultem® 1000	NMP	Tubular Alumina	-	10.4	5	-	0.033	-	315.2	151.5	-	-	[251]
	Ultem® 1000	NMP	AKP30 disk	-	0.2	0.1	-	>0.0001	>0.0001	2200	~1000	~1000	-	[252]

Membrane type	Membrane code	Solvent	Membrane types	Permeability (Barrer)						Permselectivity (α)				Ref.
				He	H_2	CO_2	O_2	N_2	CH_4	H_2/CH_4	CO_2/N_2	CO_2/CH_4	O_2/N_2	
CMSMs[c]	PPO/Ultem® 1000	NMP	Composite alumina disk	-	255	200	-	13.9	10.3	24.8	14.4	19.3	-	[150]
	PPO/Ultem® 1000	NMP	Composite alumina disk	-	452	92.4	28.5	4.6	3.2	141.3	20.1	28.9	6.2	[153]
	TiO_2/Ultem® 1000	NMP	Composite alumina disk	-	-	221.6	-	-	3.4	-	-	65.2	-	[158]
	SBA-15/Ultem® 1000	NMP	Composite alumina disk	-	298	106.8	66.7	48.9	75.3	4.0	2.2	1.4	1.4	[152]
	Ultem® 1000	NMP	Composite alumina disk	-	600	72.9	17.0	1.91	0.83	723	38.2	87.8	8.9	[30]
	Ultem® 1000	NMP	Composite alumina disk	-	-	1463	724	30	-	-	48.8	-	24.1	[204]
	H-PEI (BAHPPF-6FDA type HPEI)	NMP	Hollow fibre	-	9291	15060	-	562	529	17.6	26.8	28.5	-	[253]
	Ultem® 1000	NMP	Hollow fibre	-	1138	-	-	10.6	3.87	294	-	-	-	[151]
	PVP/ Ultem® 1000	NMP	Hollow fibre	-	-	1.2[a]	-	0.028[a]	0.022[a]	-	42.9	54.5	-	[254]
	Ultem® 1000	NMP	Hollow fibre	-	1065	233	258	294	283	-	0.8	0.8	0.88	[255]
	Ultem® 1000	NMP	Composite tubular	-	89.5	74	31	10.2	14	-	7.3	5.3	3.04	[138]
	Ultem® 1000	NMP	Composite tubular	-	55.9	-	6.5	0.47	-	-	-	-	13.8	[139]

Barrer = 1×10^{-10} cm^3(STP) cm cm^{-2} s^{-1} $cmHg^{-1}$, GPU = 1×10^{-6} cm^3(STP) cm^{-2} s^{-1} $cmHg^{-1}$ = 3.35×10^{-10} mol m^{-2} s^{-1} Pa^{-1}

[a] Permeance results are expressed in gas permeance units (GPU).

[b] The membrane was synthesis by directly compression molding.

[c] The carbon molecular sieve membrane (CMSM) was prepared at a pyrolysis temperature between 550-650 °C to minimise variation from different thermal conditions.

2.5. Research Challenges and Objectives

A comprehensive review of gas separation membranes, particularly CMSMs and their advanced modifications, has revealed a critical research gap. This gap centres on the interfacial preparation between the polymeric selective layer and the inorganic substrate before pyrolysis. Specifically, there is a lack of systematic studies addressing the fabrication of gutter-layer free composite membranes capable of achieving high separation performance in tubular configurations. This underexplored area remains a compelling challenge in membrane engineering.

Moreover, while prior research has extensively examined the effects of pyrolysis conditions on various polymeric precursors, thus offering valuable guidance for CMSM development, limited attention has been directed towards the use of biomimetic materials in CMS membrane design, particularly regarding their structural evolution during pyrolysis. To address this gap, this thesis proposes four strategic approaches aimed at enhancing the performance of PEI-based CMS membranes for next-generation gas separation technologies.

Modification on alumina substrates as a gutter layer replacement in composite membranes

The interface between polymer membranes and porous inorganic substrates often exhibits poor compatibility, resulting in defects or voids. Although previous studies have proposed physical modifications, such as polishing, to eliminate interfacial defects, no systematic investigation has been conducted to evaluate the effectiveness of such surface treatments. This work aims to address this issue by systematically modifying the alumina substrate to enhance interfacial adhesion and eliminate the need for a gutter layer.

Vacuum-assisted dip-coating for the fabrication of polymeric composite membranes

The dip-coating process is a well-established method for depositing thin films onto substrates. In this study, a vacuum-assisted dip-coating process was developed to systematically investigate the effects of vacuum pressure and other key parameters on the coating quality of PEI membranes. This method is designed to achieve defect-free selective layers and evaluate the influence of various process parameters on membrane morphology and performance.

Synthesis of biomimetic materials inspired by carbonic anhydrase (CA)

To further enhance gas separation performance, biomimetic materials inspired by the enzyme carbonic anhydrase were synthesised. Based on the method proposed by Zhang et al. [229], cobalt-based BBP (CoBBP) was synthesised and incorporated into PEI membranes to explore its role in facilitating CO_2 transport. In addition, various metal ions were substituted into the BPP framework to assess their influence on the transport properties of CO_2 and other gases.

4. Fabrication and evaluation of the BMM-modified CMS membranes

PEI membranes doped with BMM were carbonised under high-vacuum conditions to produce BMM-modified CMS membranes. This novel approach investigates the structural transformation of BMMs during pyrolysis and evaluates their impact on gas permeability and selectivity. The results are expected to provide new insights into the design of high-performance CMSMs incorporating bioinspired additives.

Chapter 3 Methodology

3.1. Materials

Alpha alumina (α-Al_2O_3) tubes were purchased from Ceramic Oxide Fabricators (Victoria, Australia) with an outer diameter of 10 ± 0.1 mm and an inner diameter of 6.3 ± 0.1 mm. The tubes were cut to the desired length for subsequent membrane fabrication and testing. Sandpapers with varying grit sizes were acquired from STARCKE (Germany) in 1500, 3000, 5000, and 7000 grit and from Micro-Mesh (3M, USA) in 12000 grit. All sandpapers were used without pretreatment. Polyetherimide (PEI, Ultem 1000; 592.6 g mol^{-1} repeating unit) and N-methyl-2-pyrrolidone (NMP) were purchased from Sigma-Aldrich (USA) and used as the polymeric membrane precursor and solvent, respectively. For the synthesis of metal-based BBP complexes, the following precursors were used (all from Sigma-Aldrich, USA): 2,6-bis(2-benzimidazolyl)pyridine (BBP), iron (III) chloride ($FeCl_2$), cobalt(II) perchlorate hexahydrate ($Co(ClO_4)_2 \cdot 6H_2O$), nickel (II) chloride ($NiCl_2$), copper (II) chloride ($CuCl_2$), and zinc (II) chloride ($ZnCl_2$). Methanol, diethyl ether (Et_2O), and isopropyl alcohol (IPA) were used as solvents and cleaning agents. All reagents and solvents were used without further purification. Prior to water permeation tests, the alumina substrates were cleaned with deionised water and ethanol. Helium (He), hydrogen (H_2), carbon dioxide (CO_2), argon (Ar), oxygen (O_2), nitrogen (N_2), and methane (CH_4) were supplied by BOC (Australia) with a minimum purity of 99.5%. All gases except O_2 were further purified using a gas purification filter (Agilent, USA) to achieve a final purity of 99.9995% before use.

3.2. Composite Membrane Preparation

Four key processes were employed in this study to fabricate high-performance CMS composite membranes: (1) The effect of polishing on alumina substrates was systematically investigated to create a smooth, defect-free surface capable of supporting PEI-based polymeric membranes without the need for a gutter; (2) Coating conditions were optimised to enable uniform and defect-free deposition of PEI membranes; (3) Biomimetic materials (BMM) coordinated with various metal ions (Fe^{2+}, Co^{2+}, Ni^{2+}, Cu^{2+}, Zn^{2+}) were synthesised and assessed for their gas-facilitated transport properties. Optimal BMM doping concentrations in PEI membranes were identified to enhance the gas separation performance in mixed matrix membranes (MMMs); and (4) Post-treatment carbonisation of both pure PEI and BMM-doped PEI membranes was performed to produce CMS membranes. The potential of these membranes in high-performance gas separation applications was evaluated.

3.2.1. Polishing of Alumina Substrates

A custom-built polishing machine was developed to investigate the surface modification of alumina tubes. The as-received (unpolished) alumina tubes, referred to as virgin substrates, were pre-sintered at 600 °C by the manufacturer (Ceramic Oxide Fabricators, Melbourne, Australia) to form a dense tubular ceramic structure. As illustrated in Fig. 3-1, the polishing schematic shows: (a) a pulling motor (stepper motor, NEMA 17) and (b) a rotation motor, which enables topological polishing of the outer surface of the tube. Before polishing, the outer surface of each tube was cleaned with compressed air for 30 s to remove loose debris. The polishing sandpapers were pre-washed with deionised water, dried in an oven overnight, and used without further treatment. The details of the membrane investigations and parameters are presented in Table 4-2, and the control substrates was chosen as alumina substrates without polishing but sintering at 1200 °C.

As shown in Fig. 3-1(c), the alumina tube was mounted horizontally and connected to the rotation motor using silicone tubing to ensure alignment with the motor shaft. A homemade polishing machine was used to investigate the polishing effect on the alumina tubes. This configuration allowed controlled, uniform polishing of the outer surface. Details of the polishing parameters are provided in Chapter 4.

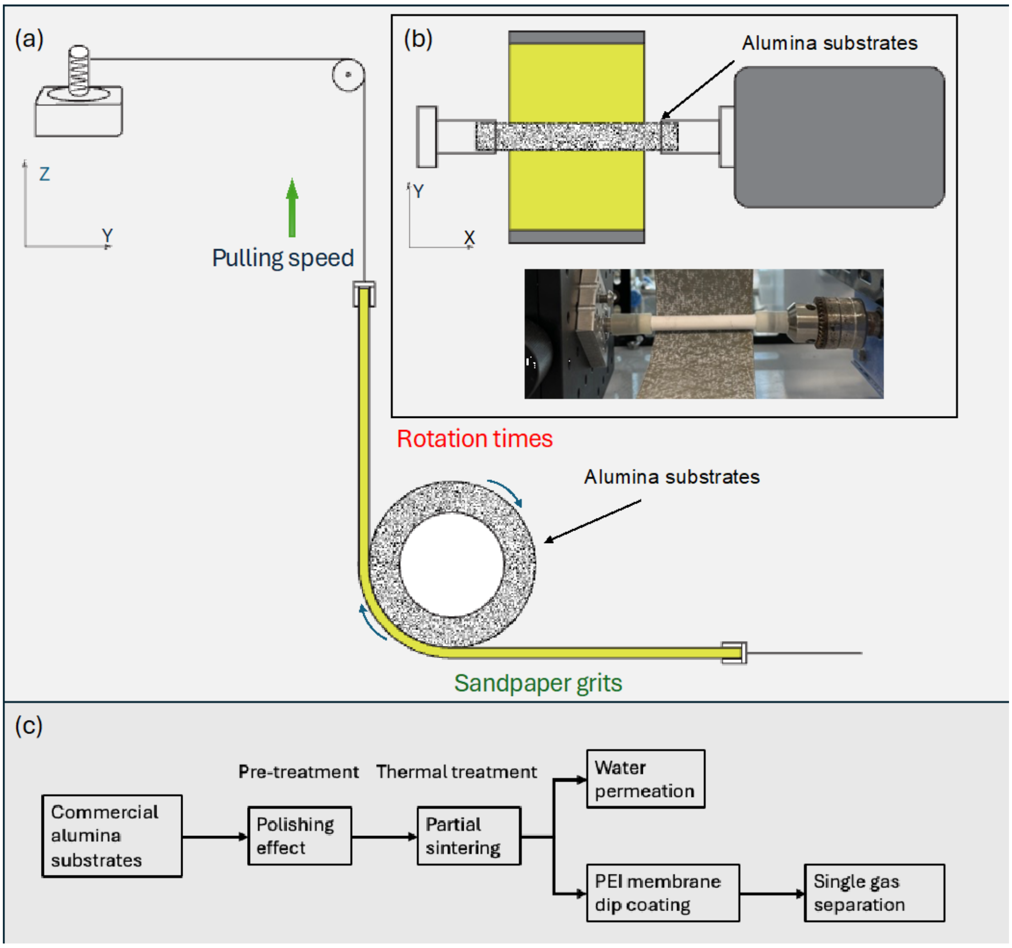

Fig. 3-1. Schematic of the custom-built pulling-polishing machine: (a) Y-Z axis view showing the pulling motor configuration, (b) X-Y axis view showing the rotation motor setup, and (c) the flow chart of the experimental procedure used in this study.

3.2.2. PEI Tubular Membrane Coating Process

A PEI solution with a concentration of 12 wt.% in NMP solvent was prepared for membrane fabrication. The solution was heated to 75 °C and stirred at 400 rpm to ensure complete dissolution and homogeneity. After cooling to room temperature, the solution was degassed for two hours using an ultrasonicator to remove trapped air. The degassed PEI solution was then used for membrane coating via a vacuum-assisted dip-coating process, as illustrated in Fig. 3-2. During the coating procedure, the dipping speed was controlled at 1600 μm s^{-1}, and the withdrawal speed was set to 300 μm s^{-1}. The alumina substrate was immersed in the PEI solution for 60 s, during which vacuum pressures of 0, -0.34, -0.5, -0.68 and -1.0 bar were applied to study the impact of vacuum intensity on coating quality. After the vacuum was gradually released to atmospheric pressure, the substrate was withdrawn from the solution. The coated substrate was then dried in an oven at 110 °C. This dip-coating and drying cycle was repeated twice to form a three-layer composite membrane, ensuring uniformity and structural integrity. Detailed investigations on the effects of vacuum pressure and coating parameters are discussed in Chapter 5.

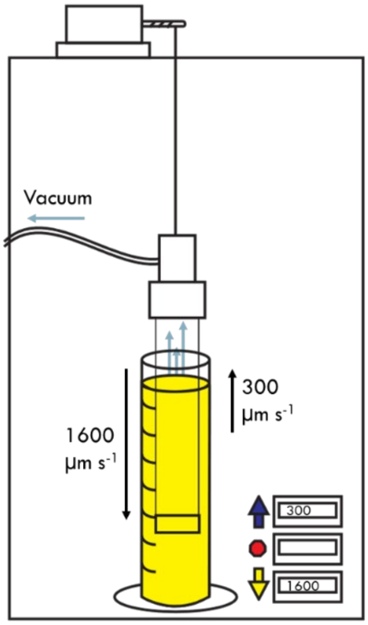

Fig. 3-2. Schematic of the vacuum-assisted dip-coating method. The dipping speed and withdraw speed of the alumina substrates was set with 1600 μm s^{-1} and 300 μm s^{-1}, respectively.

3.2.3. Biomimetic Materials Synthesis

A schematic flow chart of the BMM synthesis process is presented in Fig. 3-3(a). To prepare metal-based BBP (MtBBP), 10 mmol L^{-1} of metal salt and BBP precursor were individually dissolved in 10 mL of methanol and subjected to ultrasonication for 30 min at room temperature to yield equimolar solutions. Subsequently, these solutions were combined in a three-neck flask and heated at 60 °C for 4 h under reflux conditions to synthesise the MtBBP complex. The resulting mixture was centrifuged at 10,000 rpm for 30 min to collect the solid product. The concentrated powder was dried under vacuum at 60 °C overnight to remove residual methanol. To further purify the product, 5 mL of Et_2O and 5 mL of isopropyl alcohol were added. The solution was thoroughly mixed and centrifuged again under the same conditions. After the supernatant was decanted, the solid was dried again at 60 °C overnight under vacuum. This purification cycle was repeated twice to ensure the complete removal of impurities. The resulting material was designated as metal-ion-coordinated BBP, which was named according to the metal used. For instance, FeBBP denotes the product synthesised from $FeCl_2$ and BBP. As shown in Fig. 3-3(b), the chemical transformation from BBP to MtBBP illustrates the proposed structural configuration of the final coordination complex. The control membranes were designated as pure PEI polymeric membranes with the best condition from the Chapter 5 and 1 wt.% of BBP doped membranes to evaluate the performance differences between metal-doped BBP membranes and pure PEI membranes. The detailed coding of each synthesised complex is provided in Chapter 6.

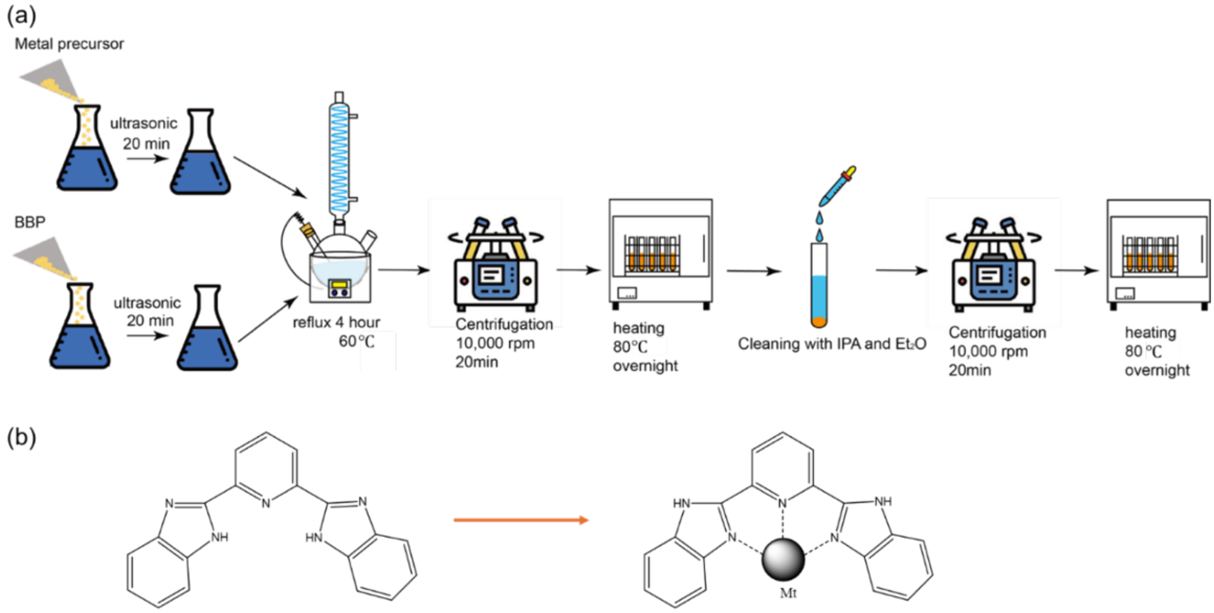

Fig. 3-3. The schematic of BMM synthesis. (a) the flow chart for the BMM synthesis and (b) the chemical structure of BBP convert to MtBBP.

3.2.4. BMM/PEI Membrane Preparation

Biomimetic materials (BMMs) were incorporated into the PEI coating solution to form a homogeneous membrane precursor. All BMMs exhibited good solubility in NMP, enabling uniform dispersion within the polymer solution. To investigate the effect of BMM concentration, 0-10 wt. % of CoBBP was added to the PEI solution to prepare a series of membrane precursor solutions for coating. For the analysis of metal ion effects, a fixed concentration of 1 wt.% BMM (relative to PEI) was blended with a solution containing 12 wt.% PEI and 88 wt.% NMP. The resulting solutions were stirred at 400 rpm and 75 °C for 24 h, followed by ultrasonication for 2 h to eliminate microbubbles before use in the vacuum-assisted dip-coating process.

3.2.5. Carbonised Membrane Synthesis

A PEI thin film was fabricated using a 12 wt.% PEI solution in NMP, serving as the control membrane. For the CoB-doped CMS membranes, 0.5–10 wt.% CoB (relative to the PEI weight) was added to the PEI/NMP solution. The resulting mixture was stirred at 75 °C for 24 h to ensure homogeneity. Before coating, all PEI-based solutions were ultrasonicated for 2 h to remove entrapped microbubbles. The thin films were deposited on alumina substrates using a vacuum-assisted dip-coating process, followed by drying in an oven at 110 °C for 3 h, in accordance with previously reported procedures. This coating and drying cycle was repeated three times to achieve a uniform and well-adhered membrane layer.

Before initiating pyrolysis, the system background leak rate was confirmed to be 1.5×10^{-5} mbar s^{-1} using the vacuum hold method. Under these conditions, the coated PEI and CoB_PEI samples were loaded into a tubular furnace and evacuated for 2 hours to achieve a vacuum pressure below 1 mbar. The temperature was then ramped from room temperature to 200 °C at 5 °C min^{-1} and held for 60 min to remove residual moisture and NMP. The temperature was then increased to 600 °C at a rate of 1 °C min^{-1} and maintained for 180 min before allowing the system to cool naturally to room temperature. The resulting membranes are designated as XCoB_CM, where X refers to the CoB doping concentration (0.5, 1, 2.5, 5, and 10 wt.%). The undoped carbon membrane was labelled PEI_CM and used as a control.

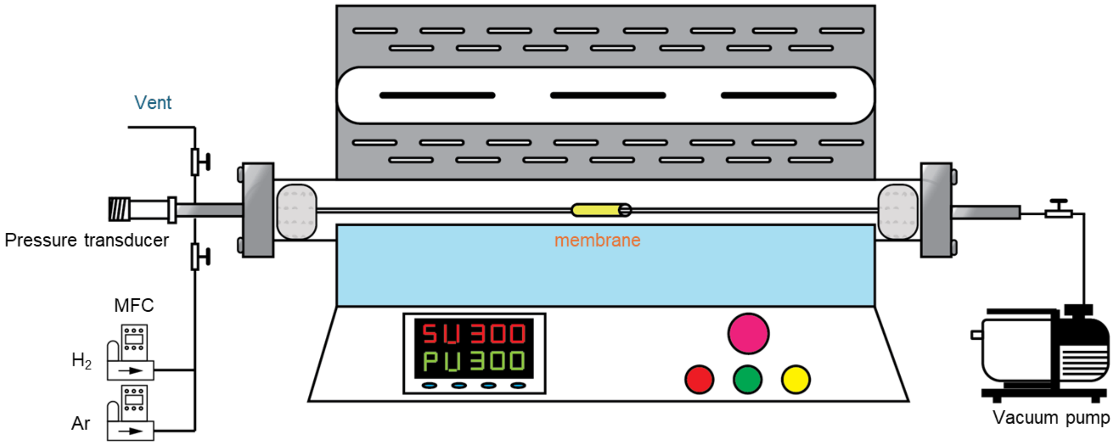

Fig. 3-4. Schematic diagram of the carbonisation process for PEI membranes.

3.3. Samples Characterisation

This section presents the characterisation of the samples, particularly the PEI pellets and metal-based BBP powders to evaluate their morphological, physical, and chemical properties.

3.3.1. Morphology Analysis (SEM)

The surface morphologies of the samples were examined using scanning electron microscopy (SEM, Phenom X1). Powdered samples were directly mounted onto carbon adhesive tape and coated with a 6-nm gold layer via sputter coating to enhance electrical conductivity. SEM imaging was performed under high-vacuum conditions at an accelerating voltage of 10 kV. A magnification of 10,000× was used to capture detailed surface features, and images were acquired at three randomly selected locations per sample to ensure representative data. Elemental mapping was performed using energy-dispersive X-ray spectroscopy (EDS) to assess the spatial distribution of elements within the samples. For EDS mapping, the resolution was set to 256 pixels, with a scan rate of 64 pixels per minute, optimising both image clarity and signal intensity. Each mapping scan was conducted over 300,000 points to ensure high-quality elemental distribution data.

3.3.2. Physical Properties of Membranes

3.3.2.1. X-ray Diffraction (XRD)

Powdered samples, including BMM and carbonised materials, were analysed using a powder X-ray diffraction (PXRD) instrument (Rigaku Smartlab SE, Rigaku, Japan). Each sample was loaded into a 0.5-mm-deep sample well with a 10-mm diameter, ensuring adequate surface exposure to X-rays. The PXRD system employed a Cu-Ka X-ray source (K_{a1} = 1.5406 Å, K_{a2} = 1.5444 Å), operating at 40 kV and 40 mA. A 10 mm incident slit and ½ divergence slit were used to control the X-ray beam during the measurement. Scans were performed at a rate of 5 ° min^{-1}, covering the 2θ range of 5° to 70°. To improve sample uniformity and signal consistency, the sample holder was rotated at 60 rpm throughout the measurement.

3.3.2.2. Thermogravimetric Analysis (TGA)

The thermal stability of the samples under inert conditions was evaluated using thermogravimetric analysis (TGA, TA Discovery SDT 650, TA Instruments, USA). This analysis was conducted to assess the degradation behaviour of BMM materials based on weight loss as a function of temperature. Approximately 5 mg of the powdered sample was placed in an alumina crucible, and the temperature was increased from 40 °C to 800 °C at a heating rate of 10 °C min^{-1}. A nitrogen flow rate of 20 mL min^{-1} was maintained to ensure pyrolysis under inert conditions and to accurately measure the residual mass.

3.3.2.3. Differential Scanning Calorimetry (DSC)

The endothermic and exothermic transitions of the BBP and CoB powders were analysed using a differential scanning calorimeter (DSC250, TA Instruments, Australia). The powdered samples were sealed in aluminium crucibles. In the first heating cycle, the temperature was increased from -40 °C to 300 °C at a rate of 10 °C min^{-1}. The samples were then rapidly cooled to -40 °C and reheated under identical conditions in a second heating cycle.

3.3.2.4. Physisorption (BET)

The pore size and pore size distribution of carbonised materials and carbon membranes were evaluated using a physisorption analyser (iQ-XR, Anton Paar, Austria). Each sample was placed in a quartz tube and degassed overnight at 300 °C to remove adsorbed gases. Subsequently, CO_2 adsorption analysis was performed at 0 °C. The resulting full isotherm was analysed using the density functional theory (DFT) model to determine the theoretical pore size and pore size distribution.

3.3.3. Chemical Properties of Membranes

3.3.3.1. Raman Spectroscopy

The Raman spectra of pyrolysed CoB (CoB_C) and pyrolysed PEI (PEI_C) powders were acquired using a Renishaw InVia Reflex Raman Microscope (Renishaw plc., Wotton-under-

Edge, UK). The instrument was equipped with a cooled charge-coupled device (CCD), holographic notch filters, and a 1200 l mm^{-1} near-infrared grating. Before measurement, calibration was performed using a silicon standard (520.5 ± 0.1 cm^{-1}). Raman excitation was achieved using a helium-neon (HeNe) laser operating at 633 nm (<1mW). Spectra were collected using a 20x/0.40 NA objective lens over a spectral range of 600-2500 cm^{-1}. Each spectrum was acquired with an accumulation of 100 scans, 5 s of exposure time, and 1% laser power. All measurements were performed in triplicate at different positions on each sample to ensure reproducibility.

3.3.3.2. ATR-FTIR Analysis

The functional group vibrations of the samples were analysed using Attenuated Total Reflectance Fourier Transform Infrared Spectroscopy (ATR-FTIR, Nicolet 6700, Thermo Fisher Scientific, USA). An infrared beam was directed through a diamond crystal and reflected off the sample surface, with the resulting absorbance peaks recorded by the instrument. Before testing, all samples were thoroughly dried and cleaned to eliminate moisture interference. Background spectra were collected before each measurement and averaged over 16 scans. A sufficient quantity of membrane material with adequate surface coverage was then placed on the diamond crystal to ensure full contact and minimise atmospheric interference. Subsequently, each sample was scanned 32 times to obtain averaged spectra. The scanning range was set from 650 cm^{-1} to 4000 cm^{-1} with a resolution of 4 cm^{-1}. All measurements were conducted in triplicate to ensure reproducibility and reduce misinterpretation of specific absorption peaks.

3.3.3.3. X-ray Photoelectron Spectroscopy (XPS)

The surface chemical composition of all samples was analysed using X-ray photoelectron spectroscopy (XPS). To minimise vacuum stabilisation time, samples with an effective surface area of 0.5 cm^2 were mounted on the sample holder using copper tape, which is applicable to both BMM and carbonised BMM samples. The holder was transferred to the XPS chamber, where a vacuum of 2 × 10^{-7} mTorr was achieved. XPS spectra were acquired using X-ray irradiation at 300 nm. A full survey scan was conducted over the binding energy range of 190-1400 eV, with 50 scans performed to enhance the signal-to-noise ratio (S/N). Subsequently, high-resolution spectra were collected for core-level regions, including C_{1s}, N_{1s}, and O_{1s}, to identify specific bonding environments and evaluate BMM chemical structures. Additionally, individual high-resolution spectra were obtained for each metal to assess its oxidation state, with each scan averaged over 20 repetitions.

3.3.3.4. Nuclear Magnetic Resonance (NMR)

The chemical bonding characteristics of the synthesised materials were analysed via nuclear magnetic resonance (NMR) spectroscopy. A sample quantity of 1-3 mg was dissolved in 5 mL of deuterated dimethyl sulfoxide (DMSO-d6) without further purification. All metal-based BBP compounds exhibited complete solubility in DMSO, with no visible undissolved solids. The prepared samples were sealed in NMR tubes and analysed using a 400 MHz NMR spectrometer. The resulting ^{1}H spectra were used to investigate chemical shifts and confirm structural modifications within the BBP framework, providing insight into the success of the synthesis.

3.3.3.5. Simultaneous Thermal Analysis Coupled with FTIR (STA-FTIR)

The gas-phase byproducts released during polymer pyrolysis were characterised using a STA-FTIR system (STA 449 F1 Jupiter®, Netzsch, USA). Approximately 5 mg of PEI, BBP, or CoB sample was placed in an 85 μL crucible. The thermal decomposition process was monitored from 40 °C to 800 °C. Thermogravimetric (TGA) and differential scanning calorimetry (DSC) signals were recorded using the STA module, while the evolved gases were carried by argon at 20 mL min^{-1} into the FTIR chamber for real-time gas analysis. FTIR spectra were recorded at 15 s intervals to capture the thermal degradation profile.

3.4. Membrane Characterisation

The membranes were characterised using various analytical techniques to evaluate their performance. Analysis focused on membrane morphology, as well as physical and chemical properties. The operational conditions and sample preparation methods for each instrument are detailed below.

3.4.1. Membrane Morphology Analysis

3.4.1.1. Scanning Electron Microscopy (SEM)

The surface and cross-sectional morphologies of the membrane samples were examined using a scanning electron microscope (Phenom X1). The membranes were covered with Kimwipes and fractured to obtain alumina pieces of appropriate size. The SEM measurement procedure followed the same protocol described in section 3.3.1.

3.4.1.2. Surface Roughness

The surface roughness of the alumina substrates was measured using a profilometer (DektakXT Bruker, USA). Each sample was secured in place using Blu-Tack to ensure level alignment with the measurement platform. A standard probe with a vertical resolution of 0.1 nm was used to scan a 1-mm path over a duration of 60 s. Surface roughness measurements were performed at three different positions on each sample to ensure reproducibility and accurate standard deviation calculations.

3.4.1.3. Transmission Electron Microscopy (TEM)

The microstructure of the membranes deposited on Al_2O_3 substrates was examined via transmission electron microscopy (TEM). Specimens were prepared using a focused ion beam (FIB) system (Thermo Fisher Scios). Characterisation was carried out using a Cs-corrected Hitachi HF5000 microscope operating at 200 kV, equipped with dual X-Max silicon drift detectors (SDD, Oxford Instruments). For scanning transmission electron microscopy-energy dispersive spectroscopy (STEM-EDS), signal acquisition exceeded 1,000,000 counts to ensure high data accuracy. Collected data were analysed using Digital Micrograph (Gatan Inc.) and Aztec software (Oxford Instruments).

3.4.2. Physical Properties of Membranes

3.4.2.1. Porosity Analysis

The porosity of the alumina substrates was determined using the gravimetric method [256] with a high-precision balance (Shimadzu AP225W, Japan, accuracy ± 0.01 mg). Initially, the dry weights (W_d) of all alumina substrates were measured in triplicate. Subsequently, the samples were immersed in 15 mL of kerosene for 72 h, allowing the liquid to fully penetrate the pores. After immersion, the surfaces were wiped with kimwipes to remove excess kerosene, and the wet weights (W_w) were recorded. The porosity (ε) was calculated using Equation 13:

$$\varepsilon = \frac{(W_w - W_d)/\rho_k}{(W_w - W_d)/\rho_k + W_d/\rho_a} \times 100\% \tag{13}$$

where ε is the porosity (%), W_w and W_d are the wet and dry weights of the substrates (mg), respectively. ρ_a is the density of alumina (3.9 g cm^{-3}), and ρ_k is the density of kerosene (0.8 g cm^{-3}). All measurements were conducted on at least three different substrate samples to ensure statistical accuracy.

3.4.2.2. Weight Loss Analysis

The efficiency of membrane polishing and sintering was evaluated using a gravimetric method. Cleaned alumina tubes and sandpapers were pre-weighted to determine the initial mass of the pre-treated alumina tube (W_0). After the polishing process, the mass of the alumina tubes was remeasured (W_P) using an electronic balance with an accuracy of ± 0.01 mg. The weight loss percentage was calculated using Equation (14):

$$Weight\ loss\ (\%) = \frac{(W_P - W_0)}{W_0} \times 100\ \% \tag{14}$$

3.4.2.3. X-ray Diffraction (XRD)

As shown in Fig. 3-5, The crystalline structure of the PEI membranes was characterised using a PANalytical X'Pert Pro X-ray diffractometer (Malvern Panalytical, USA) with a copper X-ray tube operated at 45kV and 40mA, a parallel mirror for the incident optic (optimised for thin film work) and a PixCel photon counting detector with a 7.5 mm wide window. As shown in Fig. 3-5, a custom-designed 3D-printed holder was used to mount the PEI membrane coated alumina tubes during measurement. This has been optimised during a previous project (ref to Reza's thesis) but briefly: the holder was optimised by adjusting both the incident horizontal slit (to optimise diffracted intensity while maintaining peak positional and shape integrity) and sample height. Using the first diffraction peak of alumina at 25.4° it was determined that decreasing the incident horizonal slit made almost no difference to peak position or shape but did reduce intensity, while maintaining the correct height of the sample was more important. The analysis was performed at a scan rate of 2° min-1 over a 2θ range of 5° to 50°, using Cu-Kα radiation (λ = 1.5406 Å) with a 10mm incident slit and a 1.0 mm detector slit. All diffraction patterns were normalised to the alumina peak at 25.4° to prevent overqualification of any peak shifts.

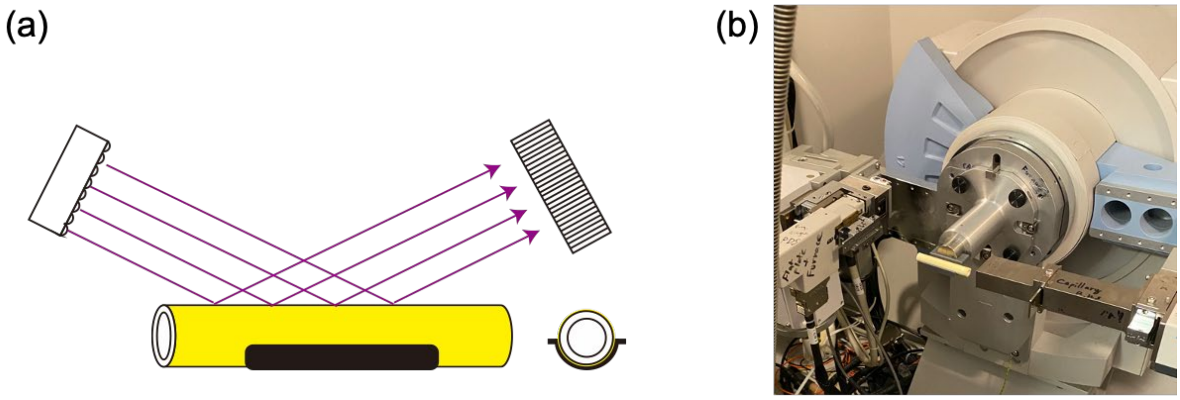

Fig. 3-5. 3-D printed membrane holder for XRD analysis: (a) Schematic diagram of the membrane holder to placement; and (b) photograph of the holder used in the XRD analysis.

3.4.2.4. Thermogravimetric Analysis (TGA)

For TGA analysis, PEI tubular membranes were carefully scraped from the alumina substrates, and approximately 5 mg of the collected sample was placed in an alumina crucible. The thermal analysis was conducted using the same heating program and instrumental conditions outlined in section 3.3.2.2

3.4.2.5. Differential Scanning Calorimetry (DSC)

PEI membrane samples were prepared by scraping small fragments from the alumina substrates and placing them into aluminium crucibles. The DSC analysis was performed according to the procedure described in Section 3.3.2.3.

3.4.2.6. CO_2 Physisorption (BET)

The pore size distribution of the CMS membrane was analysed via CO_2 physisorption. CMS membrane powders were obtained by scraping the carbonised layer from the alumina substrates. The measurements were performed following the same procedure detailed in section 3.3.2.4.

3.4.2.7. Positron Annihilation Lifetime Spectroscopy (PALS)

Positron annihilation lifetime spectroscopy (PALS) was employed to investigate the free volume characteristics within the PEI layer, as the positron lifetime is correlated with the average pore size in the sample matrix [257]. Bulk PEI and PEI thin films were analysed to determine potential changes in the packing structure. The PEI films were carefully separated from the alumina support, bundled into 1mm-think stacks, and positioned on either side of a mylar-encased $^{22}NaCl$ positron source (3.4 MBq, source correction 1.625 ns, 3.0 %). Measurements were conducted under nitrogen using ORTEC EG&G spectrometers. Each spectrum was acquired with an integrated count of 1×10^6, and at least five spectra were collected and averaged per sample. Data analysis was performed using LT-v9 software [258].

The spectra were typically resolved into three components: (1) τ_1 is attributed to para-positronium (p-Ps) annihilation, fixed at 0.125 ns; (2) τ_2, represents the free annihilation of positrons with electrons in the sample; and (3) τ_3 corresponds to ortho-positronium (o-Ps) annihilation, involving positrons bound to electrons with parallel spins.

In the case of PEI polymers, the o-Ps component (τ_3) could not be resolved due to quenching or inhibition effects. Therefore, only the τ_2 component was used to estimate the average pore radius (r) based on a modified Tau-Eldrup model [257], as shown in Equation (14):

$$\tau_2 = 0.260 \times \left(1 - \frac{r}{r+3.823} + \frac{1}{2\pi} sin\left[\frac{2\pi r}{r+3.823}\right]\right)^{-1} \tag{14}$$

Due to the use of a two-component fit, the intensity I_2 could not be directly correlated with pore number; therefore, only the average pore size was evaluated. Results indicated a substantial reduction in the average pore diameter for the thin PEI films compared to bulk PEI, corresponding to enhanced gas separation selectivity.

3.4.3. Chemical Properties of Membranes

3.4.3.1. Raman Spectroscopy

Cracked CMS membrane fragments with relatively flat surfaces were selected for analysis. The measurements were conducted following the procedure detailed in Section 3.3.3.1.

3.4.3.2. ATR-FTIR

All membrane samples were dried and cleaned prior to measurement to minimise moisture interference. FTIR spectra were acquired as outlined in Section 3.3.3.2, with each sample tested in triplicate to ensure reproducibility.

3.4.3.3. XPS

Small pieces of the CMS membrane were mounted onto copper tape to determine the chemical composition of the surface. The procedure followed the methodology described in Section 3.3.3.3.

3.4.3.4. STA-FTIR

Approximately 5 mg of PEI membrane was scraped from the alumina substrate to assess the residual NMP content. The STA-FTIR analysis was conducted in accordance with the protocol described in Section 3.3.3.4.

3.5. Membrane Permeation

In this study, the water permeation of alumina substrates was assessed using a dead-end filtration process, while the polymeric tubular membranes were evaluated through both pure gas permeation and mixed gas separation tests to determine their overall membrane performance.

3.5.1. Water Permeation

The water permeation characteristics of the alumina substrates were investigated using a pressurised dead-end filtration setup. A custom-designed tubular filtration system was constructed for this purpose. As illustrated in Fig. 3-6, the feed tank was filled with 2 L of deionised water for testing. One end of each alumina tube was sealed with a silicone block, and the other end was connected to the permeate side within a sealed filtration chamber. The permeate volume was recorded using a digital balance (A&D, EK-410, Japan). To ensure membrane compaction, an initial pressurisation step at 2 bar was conducted for 30 min. The operating pressure was then reduced to 1.5 bar for a 60-min filtration experiment. The pressure-normalised water flux was calculated using Equation (15):

$$Normalised\ water\ flux\ (J_w) = \frac{Q}{A \times \Delta t \times \Delta P} \qquad (15)$$

Where Q is the permeate volume (L), A is the effective membrane area (m^2), Δt is the filtration time (h), and ΔP is the transmembrane pressure (bar).

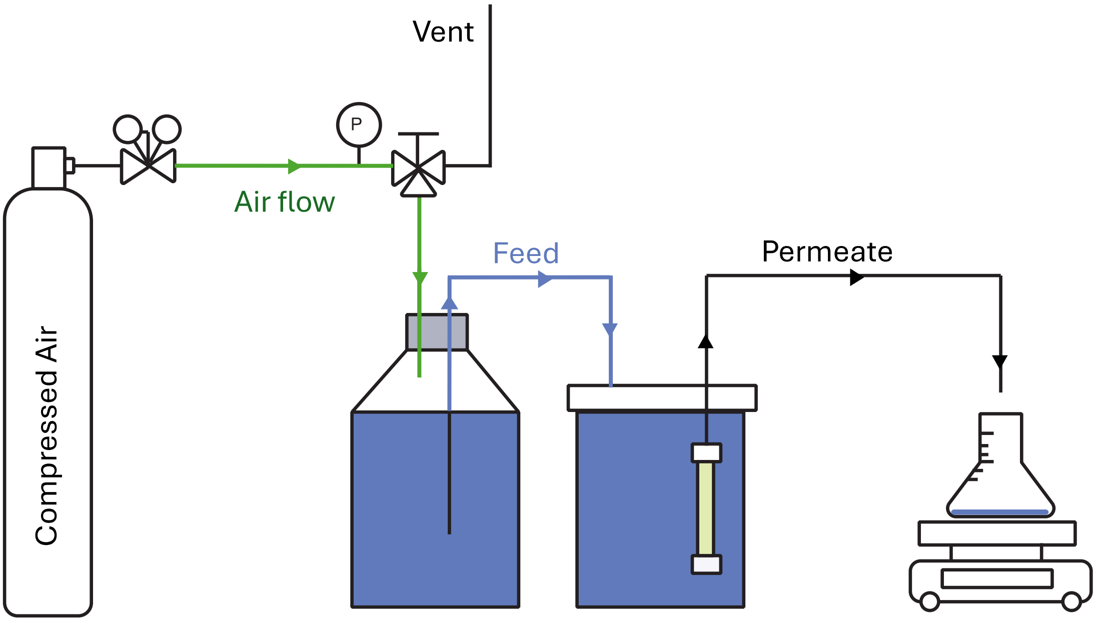

Fig. 3-6. Schematic of the self-assembled dead-end filtration system.

3.5.2. Pure Gas Permeation System

The gas permeation performance of the PEI membranes was evaluated using a constant-volume/variable-pressure method. A custom-built single-gas permeation setup was employed to test small-kinetic-diameter gas molecules. As illustrated in Fig. 3-7 (a), a system with a small reservoir (~30 cm^3) was used for low-permeance membranes. The permeate pressure was monitored using an MKS 626D pressure transducer (0 to 10 Torr range, 0.001% resolution). Under this configuration, the system exhibited a leak rate of less than 3.4×10^{-6} Torr s^{-1} during overnight leak testing. For high-permeance membranes, a second system incorporating a larger reservoir (~500 cm^3) was used, as shown in Fig. 3-7(b). In this setup, pressure changes were measured using a Swagelok S-series transducer (0-4 bar range, 0.0025% resolution). This system is suitable for measuring membrane permeance in the range of 0.2 to ~3000 GPU, with a baseline leak rate of approximately 0.036 mbar s^{-1}. Each membrane was sealed within a stainless-steel membrane module using Swagelok fittings and evacuated overnight to achieve a base pressure of 1×10^{-3} Torr. Following evacuation, all valves (V-a to V-d) were closed, and the system was held under vacuum for one hour to verify leak integrity. To begin a test, valves V-a and V-b were opened, introducing 2 bar of a specific test gas into the feed chamber. Once the system stabilised, permeate-side pressure data were recorded over time, and gas permeance (P) was calculated using Equation (16):

$$Gas\ permeance\ (P) = \frac{V}{\Delta P\times A\times R\times T}\left(\frac{dp_{test}}{dt} - \frac{dp_{leak}}{dt}\right) \qquad (16)$$

Where V is the permeate volume (m^3), A is the effective membrane area (m^2), R is the universal gas constant (8.31 m^3 Pa mol^{-1} K^{-1}), and the T is the operating temperature (K). $\frac{dp}{dt}$ represents the time-dependent rate of pressure increase, p_{test} and p_{leak} represent the pressure data obtained during the membrane permeation test and the baseline leak rate of the system, respectively.

After one hour of testing or upon reaching the maximum transducer pressure reading, V-d was opened to release the feed gas. V-d was then closed, and V-c was opened to re-evacuate both feed and permeate chambers back to 1×10^{-3} Torr before introducing the next test gas. The ideal selectivity (α) between two gases was determined using Equation (17):

$$Permselectivity\ (\alpha) = \frac{P_A}{\mathrm{P}_B} \qquad (17)$$

Where P_A and P_B represent the permeances of gases A and B, respectively.

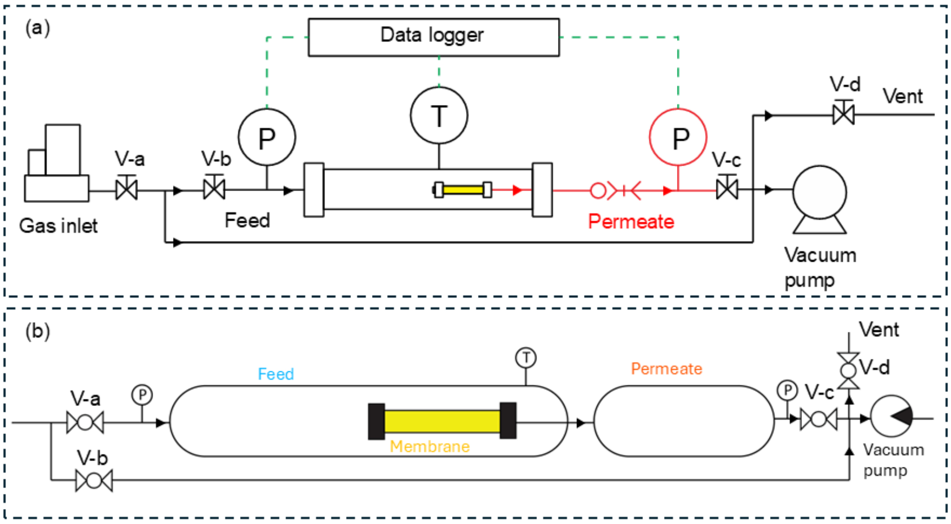

Fig. 3-7. Schematic of the pure gas permeation test setup: (a) low-permeance membrane module; and (b) high-permeance membrane module.

The diffusion coefficient of the PEI membranes coated under different conditions was calculated to evaluate the effect of the fabrication parameters on gas diffusion behaviour. The diffusion coefficient (D_e) was determined using Equation (18):

$$Diffusion\ coefficient\ (D_e) = \frac{L^2}{6\theta} \tag{18}$$

Where D_e is the diffusion coefficient (cm^2 s^{-1}), L is the membrane thickness (cm), and θ is the time lag, which is determined from the time-lag method based on the linear portion of the time-dependent permeation curve. This analysis was performed using linear fitting, yielding a high correlation coefficient ($R^2 = 0.999$), which confirms the reliability of the fitting method.

The solubility coefficient (S) of the membrane was then calculated using the classic permeation relationship given in Equation (19):

$$P = DS \tag{19}$$

Where P is the gas permeance, D is the diffusion coefficient, and S is the solubility coefficient.

3.5.3. Mixed Gas Permeation System

A custom-built mixed gas separation system was developed to evaluate membrane separation performance under binary gas and humid conditions. As illustrated in Fig. 3-8(a), the membrane was sealed within a temperature-controlled chamber. A binary gas mixture was introduced at a flow rate of 100 mL min^{-1} using two mass flow controllers with adjustable feed compositions. A back-pressure regulator maintained the system pressure of 3 bar (absolute). An argon sweep gas (20 mL min^{-1}) was used on the permeate side to carry the penetrant gases to a mass flow metre, after which the gas composition was analysed by gas chromatography (GC). Gas permeance and selectivity were calculated using Equations (20) and (21), respectively:

$$Gas\ permeance\ (P_i) = \frac{Q_i}{\Delta P \times A} \qquad (20)$$

Where Q_i is the flow rate (mol/s) of permeate gas i, ΔP is the partial pressure difference of gas i across the membrane (Pa), and A is the effective membrane area (m^2).

$$Selectivity\ (\alpha) = \frac{P_i}{\mathrm{P}_j} \qquad (21)$$

Selectivity between gas i and gas j was determined from the permeance values obtained via GC analysis.

The setup for experiments under 100% humidity is shown in Fig. 3-8(b). A 2-L gas-washing tank was placed on the feed side and equipped with a temperature controller to generate saturated water vapour. A 100 mL min^{-1} gas mixture of CO_2/CH_4 (10/90 vol.%) was passed through the tank, evaporating water into the gas stream upstream of the membrane. To ensure sustained humidity, 200 mL of reverse osmosis (RO) water was added to the tank, and the temperature was maintained at 80 °C to achieve near-saturation. Under these conditions, a relative humidity of 100% was theoretically achieved prior to complete water consumption. On the downstream side, a water chiller set at -5 °C was installed to condense and capture excess moisture, thereby preventing water vapour containment of the GC system. This humidity test simulated challenging conditions such as biogas upgrading or humid gas separations, where the moisture content is significant.

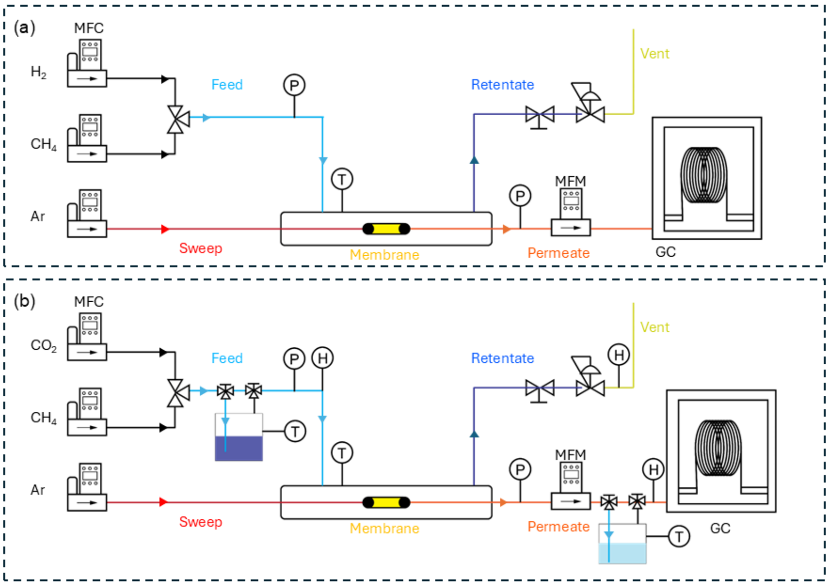

Fig. 3-8. Schematic of the binary gas permeation system setup: (a) binary gas separation system with model feed gas composition; (b) binary gas separation system under 100% relative humidity conditions.

3.6. Statistical Analysis

All data are presented as the average of three independent measurements or samples (n = 3). A two-sample t-test was performed to assess the statistical significance of differences between groups. Error bars represent either one standard deviation from the mean or p-value, as specified in the respective figure captions. Data are presented as mean ± SD. Statistical significance was determined by t-test (* $p < 0.05$; ** $p < 0.001$). By definition, the p-value represents the probability of obtaining the observed results under the assumption that the null hypothesis is true. A lower p-value indicates a higher level of statistical significance. In this study, a p-value of 0.05 (*) or lower was considered statistically significant [259].

Chapter 4 Effect of Polishing on Substrate Surface Properties

In this chapter, we published this work in the *Separation and Purification Technology*, 2025. **375**: p. 133753. The detailed investigation is presented below.

4.1. Abstract

Nanocomposite membranes have been research focus of numerous gas separation applications. Understanding the interfacial properties between inorganic and organic materials is crucial for enhancing membrane performance. In particular, the design of interface topology, pore texture, and chemistry on membrane support surfaces can have a profound effect on both gas permeance and selectivity. Therefore, careful control of interfacial surface properties between the membrane active layer and the underlying support is challenge. In this study, a newly-customised, automatic, tubular polishing system was designed and implemented to control the surface properties of tubular alumina substrates for gas separation membrane processing. The effects of sandpaper grits, sandpaper pulling speed and tube rotation speed, as well as calcination temperature on surface finishing were thoroughly examined and evaluated for water flux and gas separation performance of nanocomposite membranes. After polishing process, the surface roughness of alumina substrates significantly increased from 238 nm to 568 nm. The best polished alumina tubes were treated with a 7000 grits sandpaper, 2.3 s polishing time, 1600 rpm rotation, and a partial sintering temperature of 1200 °C achieved a comparable surface pore diameter of 0.2 μm, 43.4% porosity, and an average pure water flux of 28.2 ± 1.4 LMH bar^{-1}. This combination of alumina substrate pre-conditioning offered the ideal interfacial surface properties for dip-coating of polyetherimide membranes, which produced a competitively high CO_2/N_2 permselectivity of 21.9 ± 1.0 and CO_2/CH_4 of 21.1 ± 1.4 for CO_2 separation membrane development.

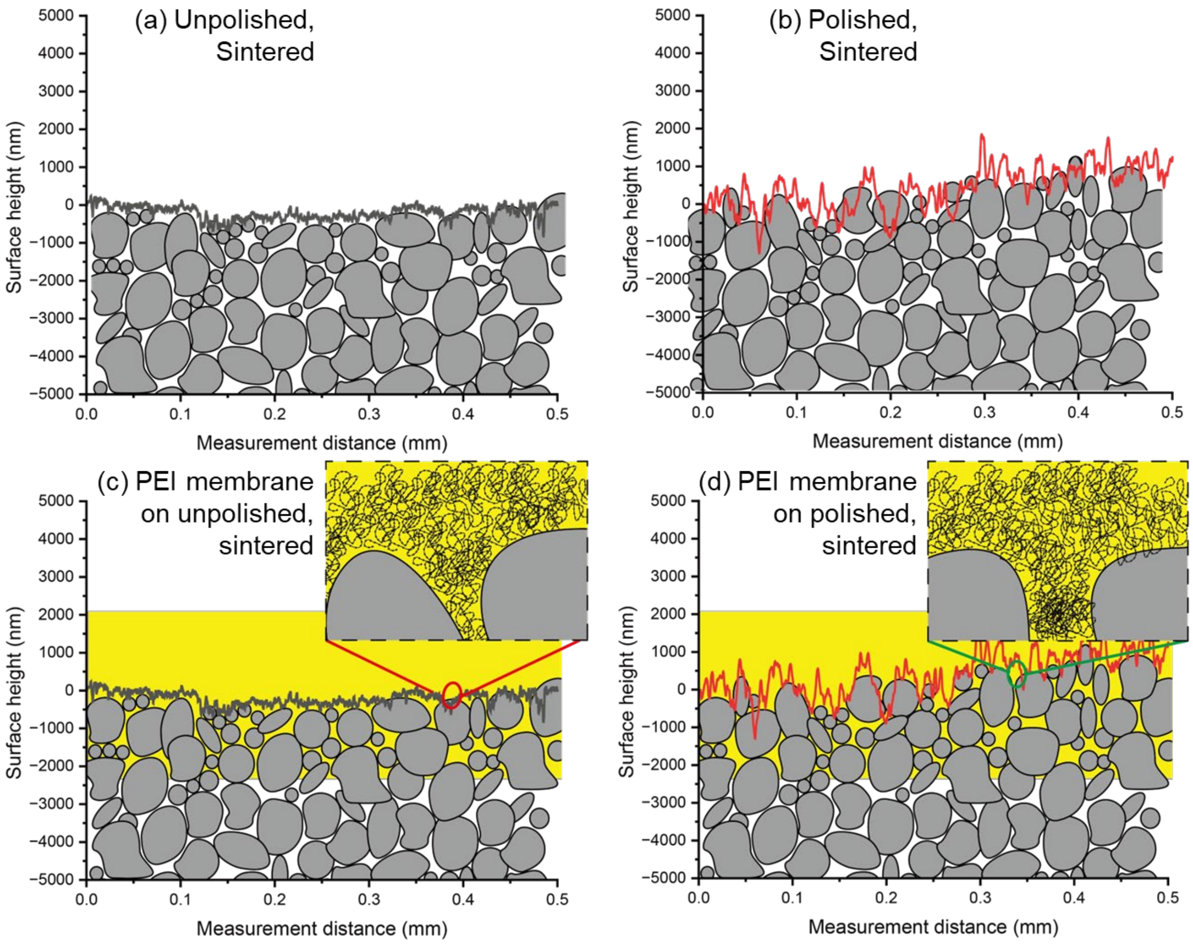

4.2. Introduction

Alumina (Al_2O_3) powder is a very versatile ceramic material that has diverse applications in many engineering relevant industries. Due to its outstanding structure, porosity, physicochemical and mechanical properties, alumina ceramic membranes and filters, for example, impart enhanced fouling resistance, high permeability, recoverability, chemical stability, and long lifetime compared to conventional polymeric membranes [260, 261]. In 1984, Leenaars et al. [262] described the use of Boehmite sol-gel technique for manufacturing ultra-porous, crack-free alumina ceramic membranes for water purification has led to an increased research attention. Due to its unique hydrogen bonding and compatibility with a wide range of materials, alumina powders or sol-gel-derived alumina are typically engineered as the porous substrate or intermediate supporting layer [263] for the separation or semiconductor devices

[264]. Since then, alumina ceramic membranes and alumina substrates have been investigated for microfiltration (MF) [265], ultrafiltration (UF) [266], nanofiltration (NF) [267], and reverse osmosis (RO) membranes [268].

Polymeric composite membranes with inorganic substrates as supports offers several advantages for the high-performance, gas separation membranes [8]. This approach uses minimal materials and precursors for creating thin-film selective layers and allows customization of each layer during membrane manufacturing, rendering it suitable for industrial coating applications [9, 10]. Furthermore, inorganic substrates confer high thermal stability, exceptional chemical resistance, and excellent mechanical strength making inorganic substrates the ideal candidates for supporting layers. They also present opportunities for inorganic substrate recycling and reuse, upcycling and renewable applications [269]. Therefore, it is imperative to investigate substrate surface quality and modification strategy to understand how substrate surface properties control the thin-film membrane properties thereby enhancing membrane coating performance [270, 271].

The two of most common crystalline structures of alumina nanomaterials are alpha (α-) and gamma (γ-), of which the membrane or substrate formed by the former has pore sizes ranging from 30 – 300 nm and the latter has average pore sizes ranging from 2 – 50 nm [272]. Other less common crystalline structures of alumina, such as θ-Al_2O_3 [273], η-Al_2O_3 [274], or χ-Al_2O_3 [275] are formed at lower calcination temperature which are not ideal for ceramic membrane applications. These intermediate crystal phases are converted into an α-Al_2O_3 crystalline structure under a high-temperature sintering process (1500 – 2500 °C), which is a standard procedure for fabricating ceramic alumina tubes or membranes [270, 271].

As an alumina substrate tube for membrane deposition, careful engineering of the substrate surface and interfacial properties are critical to ensuring coating compatibility, and ultimately, achieving the desirable membrane performance and separation efficiency [261, 276]. In addition, alumina sol-gel techniques are further employed to control the interfacial properties between the substrate layer and the selective layer for nanocomposite membrane synthesis. As such, investigating substrate modification methodology becomes imperative [277, 278].

From a manufacturing scale-up standpoint, physical modification, such as sandblasting, polishing, and passivation, may be practical to prepare alumina substrates tailored for membrane separation applications. Sandblasting can effectively enhance substrate roughness by controlling sand particle size and the technique is known to reinforce the physical and interfacial strength of the composite ceramic materials [279, 280]. However, its suitability for modifying porous alumina substrates is questionable due to potential pore blockage and the subsequent time-consuming, post-treatment required after sandblasting. The passivation modification can fill the rough surface by inducing a thin layer of atoms on the membrane surface. The coating layer aims to change the roughness to improve the negative fixed charge density or chemical resistance of the membrane [281, 282]. However, passivation modification is only used for the formation of metal oxides in products. It is difficult to modify inorganic alumina because it is a common passivation agent for modifying metal oxides [283].

The polishing process commonly employs commercial sandpapers with uniform particles distributed across the paper surface to eliminate protrusions on substrates. The grit size of sandpaper plays an important role in determining the smoothness of the final surface quality. Li et al. [139] investigated alumina substrates and TiO_2 coated alumina substrates (O.D with 12 mm and 5 cm length) were polished with 1000 grits of sandpaper and a 0.05 μm particles size polishing liquid for 5 min for each polishing process. Both samples demonstrated a decrease in roughness of approximately 72% and 83%, respectively, after the polishing processes. Moreover, polyetherimide (PEI) based carbon molecular sieving membranes were deposited on both polished alumina substrates and TiO_2 coated alumina substrates, and the permselectivity of O_2/N_2 for TiO_2 coated alumina substrates was enhanced 10 folds compared with that of non-TiO_2 coated alumina substrates. This suggests that sandpaper polishing removes the surface protrusions of the alumina substrates, and doping TiO_2 can fill the pits on the alumina substrates to considerably reduce the surface roughness for supporting the carbon molecular sieving membrane on the TiO_2 coated alumina substrates. Ryi. et al. [284, 285] investigated polished treatment of Palladium-based (Pd) membrane surface using Al_2O_3 particles mixture with a size of 0.9 μm and a concentration of 0.1 g L^{-1} Al_2O_3 sludge to eliminate the pinhole on the Pd membrane. The polishing parameter was studied using an applied pressure of 15 g cm^{-2} with 60 s polishing time. The permselectivity of polished Pd membrane can improve 3 orders of magnitude of H_2/He permselectivity compared to the non-polished Pd membranes. This indicates that polishing improves membrane performance by modifying the interface and reducing pinholes on the Pd surface. To the best of our knowledge, there is no research investigation focusing on tubular polishing effect as a pretreatment step for alumina substrate tubes to be used for membrane dip-coating deposition. It is essential to understand the relationship between the surface properties imparted by the polishing process and the polishing parameters in forming the desired substrate layer and the subsequent selective layer for nanocomposite membranes.

Polyetherimide (PEI) is a high-performance polymer that has been widely applied in electrical insulation and medical devices [18]. Moreover, it exhibits excellent thermal stability, good chemical resistance, high processability, and relatively low material costs, making it a candidate material for composite membrane fabrication [18, 237]. For gas separation applications, the PEI membranes and PEI-derived carbon membranes underscored excellent separation efficiency for hydrogen purification, CO_2 capture, gas sweetening, oxygen purification, and helium separation from petroleum reservoirs. In particular, CO_2 separation performance demonstrated high CO_2 permeability in the range of 1 to 142 Barrer with a modest permselectivities of 25 (CO_2/N_2), 30 (CO_2/CH_4), 3.5 (CO_2/C_2H_6), and 3.58 (CO_2/C_3H_8) [234, 286-288]. From this body of work, one major challenge that PEI membranes experience is well-coated on inorganic porous substrates and reinforcing the coating performance to reduce the amount of PEI consumable [139].

In this study, we designed the first proof-of-concept, polished alumina tubes as membrane substrates for PEI composite membranes prepared via dip-coating process. To ensure reproducible, high quality alumina substrates, a range of polishing parameters, such as the tube rotation speed, sandpaper pulling speed and the sandpaper grit size are systemically investigated for creating well-tailored, alumina substrate surfaces. Prior to dip-coating of PEI thin-films, the effects of partial-sintering temperature on surface roughness, pore size, porosity, and water permeability of the alumina substrates were also examined, which is followed by dip-coating the alumina substrates with polyetherimide (Ultem® 1000) dope to form dense, gas selective membranes for CO_2 separation applications.

4.3. Methodology

4.3.1. The Membrane Parameters

The details for the polishing modification and the membrane coating were demonstrated at section 3.2.1 and 3.4. The sandpaper holder was equipped on a pulling motor, and the sandpaper pulling step was fully automated. For the polishing step, pulling speed (PS) from 1.4 to 9.1 cm s^{-1}, tube rotation speed (RS) from 650 to 1600 rpm, and sandpaper grits (SG) from 1500 to 12000 grits size were investigated. Subsequently, the alumina tubes were placed in the muffle furnace for the pre-sintering step with a controlling temperature profile (ramping rate 5 °C) using the pre-sintering temperature (ST) 800-1200 °C. The details substrate code is shown in Table 4-1.

Table 4-1. Alumina substrate sample matrix prepared by different pretreatment parameters and polishing conditions. The polishing condition was using the tube rotational speed at 1600 rpm and the sandpaper pulling speed with 9.1 m s^{-1}.

Substrate code	Sandpaper grit size	Partial sintering temperature (℃)
A800	7000	800
A1000		1000
A1200		1200
SG1500	1500	1200
SG3000	3000	
SG5000	5000	
SG7000	**7000**	
SG12000	12000	

Table 4-2. Alumina substrate sample matrix prepared by polishing parameters, the alumina substrates was polished with 7000 grits and sintered at 1200 ℃. **Bolded sample code represents identical alumina substrate.**

Substrate code	Rotation speed (rpm)	Pulling speed/Polishing time (s)[a]	Number of rotation (rev)[b]
R650	650	9.1/2.3	25
R850	850		33
R1100	1100		42
R1600 [c]	**1600**		**61**
P9.1[c]	1600	**9.1/2.3**	**61**
P4.9		4.9/4.3	131
P2.8		2.8/7.5	200
P1.4		1.4/15	400

[a] The polishing time is calculated: the sandpaper length/ pulling speed.

[b] The number of rotation is calculated by Rotation speed / (Pulling speed × Sandpaper length).

[c] Alumina substrate synthesised under same condition.

The flow chart of this experimental chapter was placed in Fig. 4-1. Initially, a series of investigation on the alumina substrates were investigated to identify the surface modification performance on the alumina substates. Furthermore, the water permeation and the surface characteristic were applied to investigate the membrane performance. Therefore, the rotational speed and the sandpaper pulling speed were coated with PEI polymeric membrane to determine the membrane performance. Then investigate the polymeric membrane separation performance on the alumina substrates.

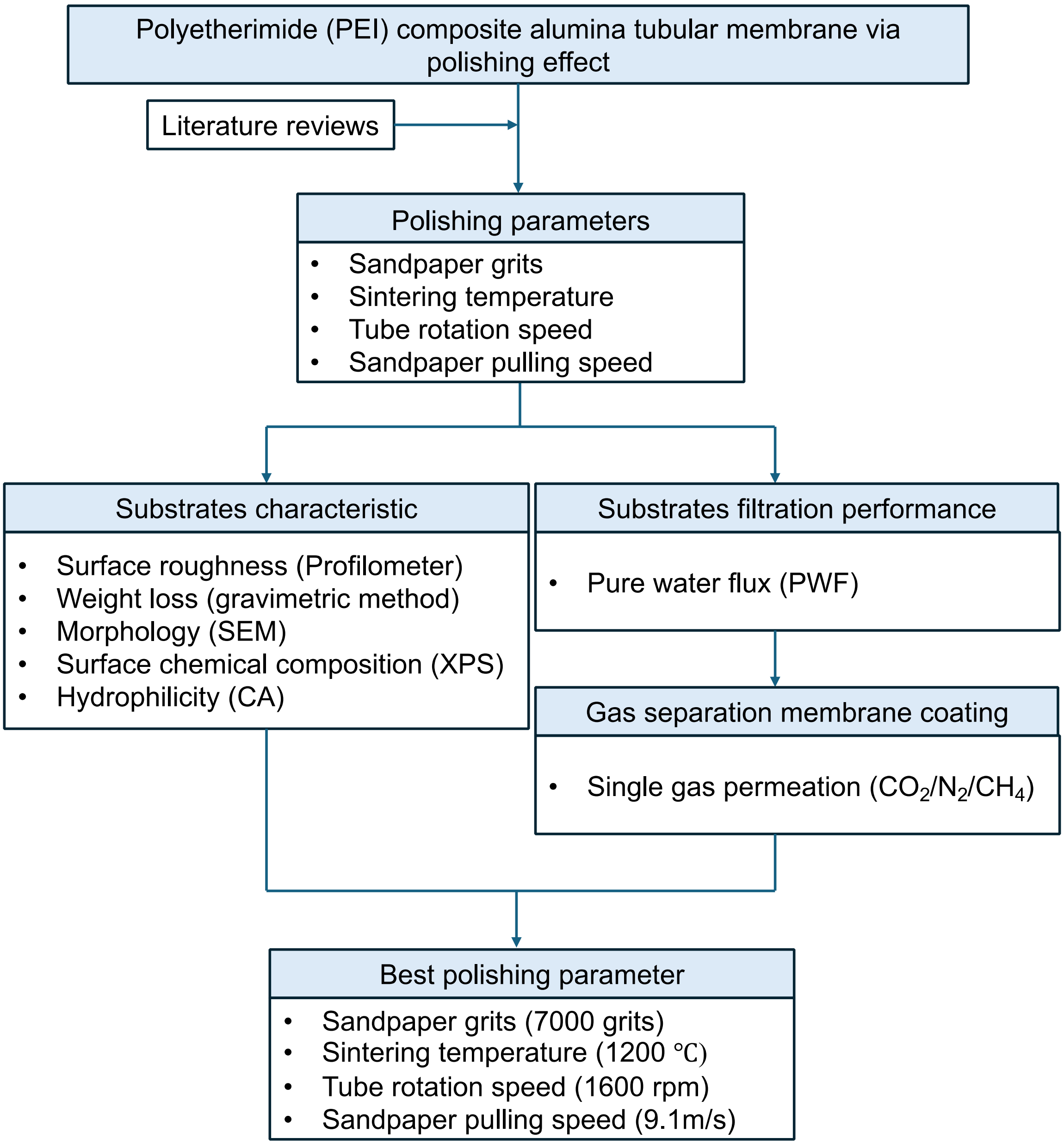

Fig. 4-1. The flow chart for polishing experimental on the alumina substrates.

4.4. Result and Discussion

4.4.1. The Sintering Temperature (ST) Effect After Polishing Processes

After the polishing step, alumina tubes were subjected to a partial-sintering process using 800 °C, 1000 °C, and 1200 °C to stabilise the alumina tube. The Fig. 4-2 characterised the physical ability of the alumina substrates sintering at various temperature. As shown in Fig. 4-2(a), the normalised pure water flux (PWF) of pristine alumina substrate was 35.8 ± 2.0 LMH bar^{-1} and it slightly increased to 39.9 ± 0.9 LMH bar^{-1} at 1000 °C with a p value < 0.05, and then it decreased to 28.3 ± 2.3 LMH bar^{-1} at 1200 °C. As shown in Fig. 4-2(b), the outer diameter of the alumina substrates diminished as the pre-sintering temperature increased, and this reduction (6.2%) is statistically significant ($p \approx 0.05$), suggesting that the alumina particles aggregated and densified at outer surfaces with increasing temperatures. In contrast, inner lumen diameters of the alumina substrates showed negligible variation with temperature changed. This dimensional change of the pretreated alumina substrates indicates that the densification process is strongly temperature-dependent and the deformation predominantly occurred asymmetrically on the outside of the tubes, despite the thermal property remains uniform throughout the bulk material [289, 290].

These findings align with the porosity evaluation measured using the gravimetric method. As shown in Fig. 4-2(c), the pristine alumina substrate has a porosity of 47.8 ± 0.2%, which remained relatively unchanged at 800 °C and 1000 °C. When temperature was increased to 1200 °C, the porosity decreased significantly to 43.3 ± 0.3%. This reduction in porosity can be attributed to alumina particle agglomeration and reduced pore tortuosity, which effectively reduced the overall porosity of the substrates [291]. Coupling with cross-sectional morphology, the SEM images reveal the alumina particle sizes are indifferent between the pristine alumina and those of A800 and A1000 (Fig. 4-2d1-d3). Upon further increasing the temperature, A1200 (Fig. 4-2d4) shows a large degree of alumina particle packing and particle coalescing on the surface of the particles, due to the partial onset of sintering and densification effects leading to surface pore closure [292]. This trend is consistent with the water flux results and the tube size dimensionality, indicating that slight thermal densification of alumina substrate on the particle surface resulted in a decrease in contact surface area and solute transport. The relationship was also previously demonstrated by Ray et al. and Rocha et al. for porous alumina membranes via ultrafiltration process [276, 293]. A higher sintering temperature increased the alumina grain size and reduced the permeation channel for the dense alumina substrates, and a lower water permeation was observed in our testing.

Alumina tubes were further subjected to a range of polishing conditions as a pretreatment step followed by partial sintering at 1200 ℃. The sandpaper grit size, pulling speed of sandpaper and rotational speed were verified to evaluate the impact of the tube polishing on surface texture and morphology, factors that are critical for subsequent coating of materials at the interface.

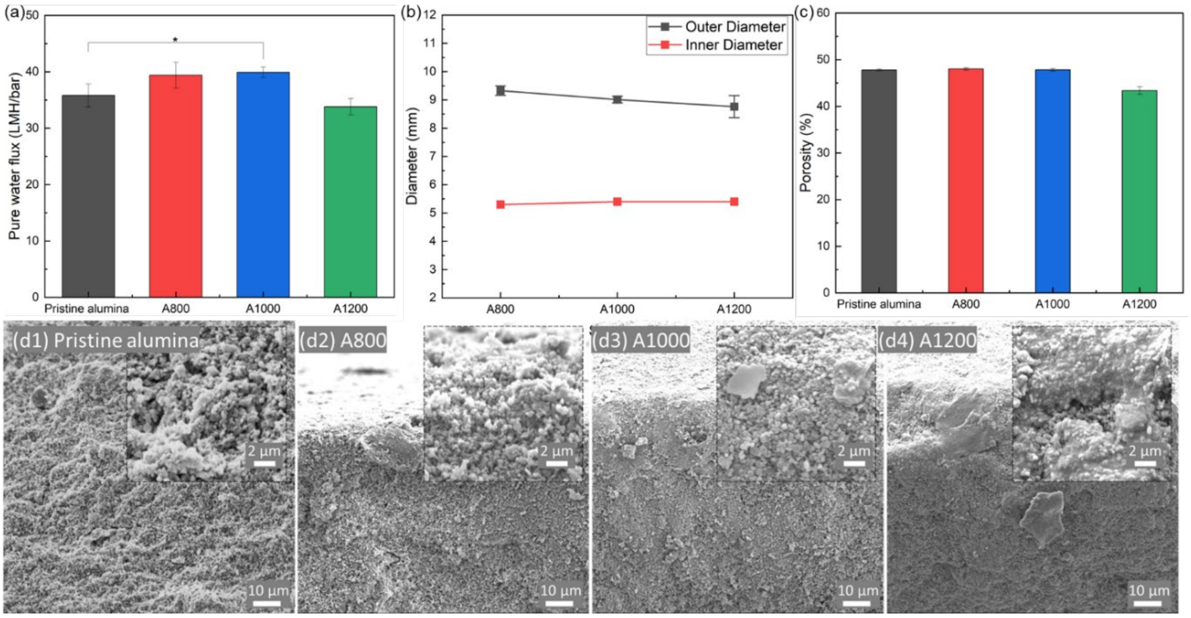

Fig. 4-2. Comparison of pristine alumina tube with sintered tubes at various temperatures. (a) the average pure water flux, (b) the outer and inner diameters, (c) porosity and (d) the cross-section images of the sintering temperature effect for the alumina tubes with the magnification

2000x and the inset figure is 10000x. Data represent the mean for three substrate samples ± 1 SD of the mean with p value (*) ≈ 0.05.

4.4.2. Sandpaper Grits (SG) Effect

A various sandpaper grits polishing on the alumina substrates before the sintering at 1200 °C determined that sandpaper grit affects the alumina substrate. Using the weight loss and the water permeability can determine the substrates performance to evaluate the sandpaper grit effect. The higher the sandpaper codes, the finer the particles sizes, resulting in a more refined surface finishing. As shown in Fig. 4-3(a), the weight loss percent of polished alumina tubes decreases from 1.15 ± 0.19 % (SG1500) to 0.3 ± 0.04 % (SG7000) and then 0.4 ± 0.03 % (SG 12000). The results showed that finer grit size (smaller particle size) led to a lower degree of surface abrasion and a lower amount of alumina particles removed via polishing. After heat treatment, the polished/sintered alumina tubes (1200 °C) show that the weight losses between the SG samples were indifferent with an average weight loss percent of 0.2%, which indicates that weight loss by thermal densification of the alumina tubes is universal.

Fig. 4-3(b) shows the pure water flux (PWF) of polished/sintered alumina substrates as a function of sandpaper grits size. With increasing grit size, the PWF trended gradually from 36.4 ± 2 LMH bar^{-1} for SG1500 to 32.9 ± 0.8 LMH bar^{-1} for SG5000 and SG7000 reaching to a lowest value of 30.6 ± 1.4 LMH bar^{-1} for SG12000. Using surface profilometry to examine the surface macro topology, the root mean square surface roughness of the alumina tubes was measured between 500 to 800 nm without a consistent trend (Fig. S4-1) between polished tubes. Lower grit sandpapers (1500 and 3000 grit) possess larger particles on the surface of sandpaper, which create higher friction and abrasion on the alumina particles on the substrate surface leading to higher surface roughness [294]. The larger hills and valleys formed on the alumina substrates were observed by SEM and profilometry are evidence of the polished surface caused by the sandpaper [294, 295]. When the higher grit sandpapers were applied, the alumina substrate surface resulted in a lower surface roughness than the substrates polished by lower sandpaper grit size. Polishing with finer sandpapers (7000- and 12000-grits) produced a higher measured surface roughness than polishing with 5000-grits, which yielded the minimum surface roughness. It is because the finer sandpaper grits create more micro-scratch onto the alumina substrates that enhance the surface roughness. Moreover, it is observed that the polished tubes are significantly rougher than the unpolished tubes (250 nm) indicating that the polishing regime effectively removed a significantly amount of alumina microparticles.

Table S4-1 presents the porosity of the sandpaper polished alumina substrates. As the sandpaper grit increased from 1500 to 12000, the porosity of the alumina substrates marginally increased from 42.5 ± 0.2 % to 43.9 ± 0.9 %. However, this trend did not result in an increased water flux. Because the surface structure mainly consisted of smaller alumina particles after polishing, most of the larger alumina particles are removed causing the surface porosity to be altered. Therefore, a lower grit sandpaper demonstrated greater efficacy in removing alumina particles and enlarging the surface pore size and surface porosity, resulting in enhanced water permeation. It is worth noting that upon the removal of small alumina particles on the surface after polishing, the surface pores on the alumina substrate become more exposed. The trends demonstrate that sandpaper polishing with selective grit size can offer a simple and controlled process to tailored water fluxes through porous ceramic tubes. As seen in Fig. 4-3(a), weight loss of alumina tube reached 0.33 ± 0.04 % with a greater reproducibility when 7000 sandpaper grit was used with approximately 33.4 ± 1.2 LMH bar^{-1}. Therefore, this condition was further explored for other polishing parameters.

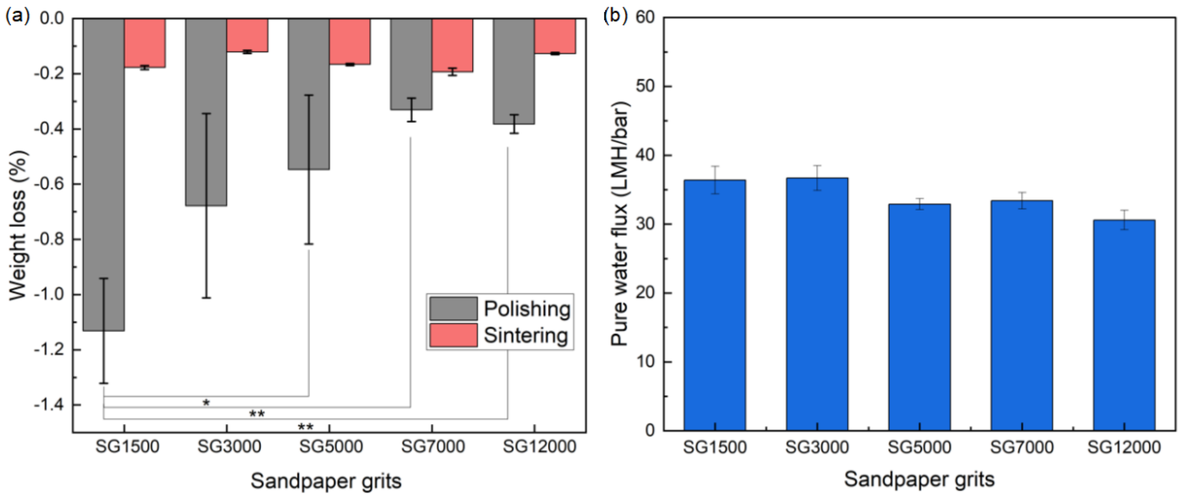

Fig. 4-3. Pre-polished and post-heated alumina tubes (A1200) polished by different sandpaper grit size showing (a) the weight loss and (b) the average pure water flux of final alumina tubes. Data represent the mean for three substrate samples ± 1 SD of the mean with p value (*) ≈ 0.05 and (**) ≈ 0.001.

4.4.3. Polishing Rotation and Pulling Speeds

The parameters of rotational speed (R) and pulling speed (P) were employed to investigate the polishing effect of alumina substrates by choosing the 7000 sandpaper grit. After polishing, all alumina supports were subjected to a 1200 °C partial sintering condition. As shown in Fig. 4-4(a), the weight loss percent of the alumina substrates as a function of alumina tube rotation speed (R650 – R1600) lies in the range between 0.26% ± 0.02% and 0.33% ± 0.02% before and after sintering, indicating that the tube rotation speed did not greatly affect the substrate overall weight. However, higher rotational speed translates to a greater number of revolutions, hence it is expected that it would lead to a significantly greater weight loss, which is not as observed. The p value ≤ 0.05 for R1100 and R1600 compared to R650 demonstrates that the results are statistically different after the polishing but the weight loss after sintering between the groups are not significant. The main reason for such a case could be that the sandpaper grit may be overladen with alumina particles during polishing resulting in a gradual loss of cutting efficiency as numbers of tube revolution increased. Hence, no further alumina particles could be removed once the grit is completely covered by a layer of alumina particles.

When increasing the pulling speed of the sandpaper, as shown in Fig. 4-4(b), the weight loss of alumina substrates significantly increases with decreasing pulling speed reaching the highest weight loss percent of 1.38% ± 0.04% (P1.4). Due to the slower sandpaper pulling speed, the contact time and the contact area between the sandpaper and alumina tube are increased allowing a longer exposure time of substrate surface in every rotation to more grit area in a controlled fashion. The statistically differences between all four tubes were $p \leq 0.001$ compared to the control, demonstrating longer polishing time removes significantly more alumina particles on the substrate surface.

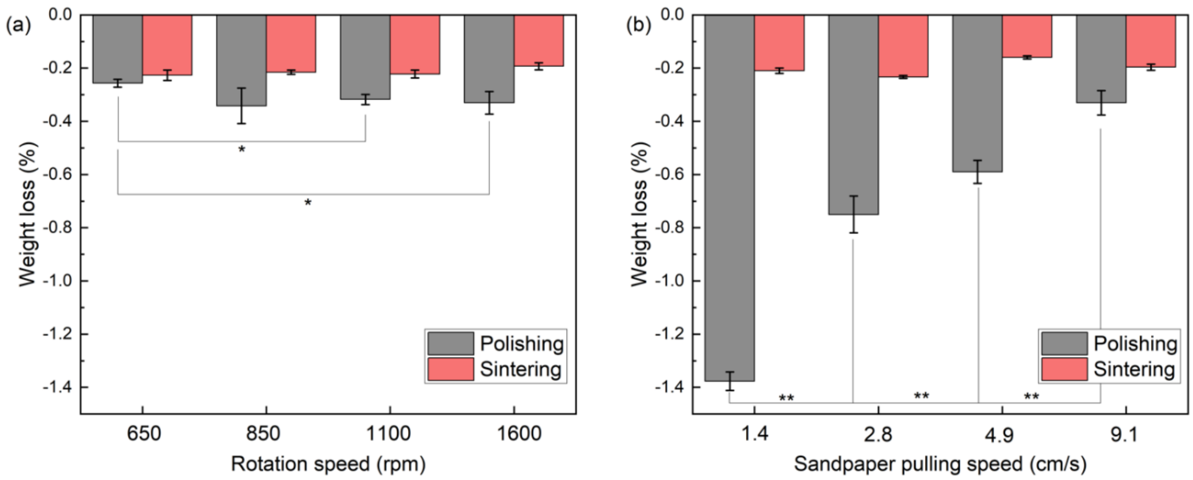

Fig. 4-4. The weight loss percent of alumina substrates as a function of (a) tube rotation speed and (b) the sandpaper pulling speed. Data represent the mean for three substrate samples ± 1 SD of the mean with p value (*) ≈ 0.05 and (**) ≈ 0.001.

4.4.4. The Physical Characteristics of Polishing Alumina Substrates

SEM technique was used to examine the surfaces and cross-sections of all post-sintered alumina substrates with and without polishing. As shown in Fig. S4-4, the substrate surfaces and cross-sectional images of alumina tubes showed indifferent morphology at micrometer scale irrespective of polishing treatments.

However, as shown by the root mean-square surface roughness (R_q) results in Fig. 4-5, the polished alumina tubes showed 200-300% R_q increase comparing to the unpolished tubes (R_q = 247 ± 68 nm). By increasing the tube rotation speed (Fig. 4-5(a)), the R_q of R650 tube was approximately 743 ± 20 nm, which significantly decreased to 568 ± 10 nm for the R1600 tube. There were also noticeable differences in the pulling speed series. When the polishing speed was reduced from 9.1 cm/s to 2.8 cm/s, the surface roughness of the alumina substrates decreased from 568 ± 10 nm to 448 ± 33 nm due to the increased contact time and area. However, at a speed of 1.4 cm/s, the surface roughness increased slightly to 663 ± 65 nm. The alumina substrates displayed a smooth surface at a rotation speed and pulling speed of R850 and P2.8, respectively. However, extended the polishing processes may cause the surface to break upon contact with sandpaper due to the instability and lack of integration of the surface alumina particles, resulting in surface features resembling hills and valleys. This further increases the surface roughness and the surface height distance analysis results are supplied in Fig. S4-2 for reference.

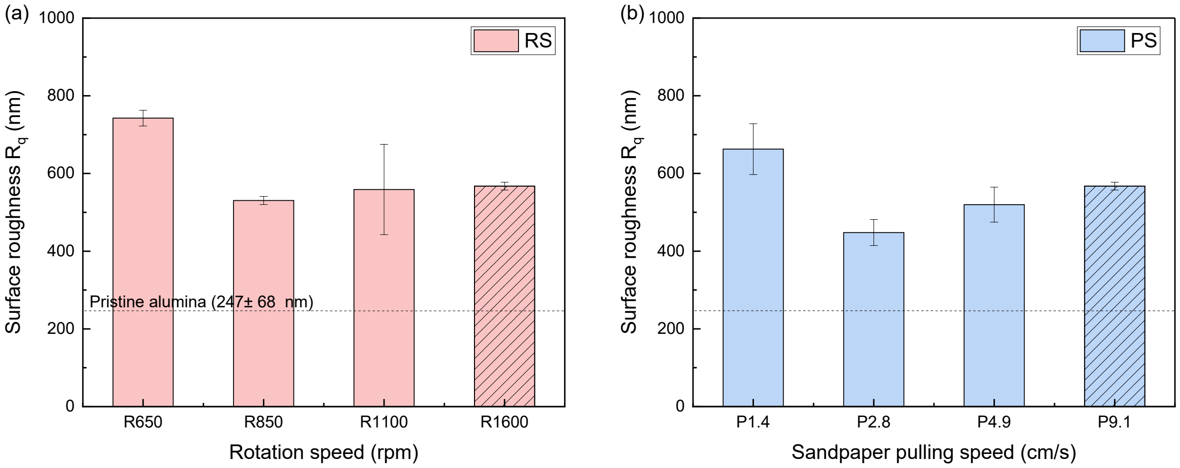

Fig. 4-5. Surface roughness from profilometer measurement as a function of (a) rotation speed and (b) sandpaper pulling speed. The dashed line is the roughness measured for the unpolished alumina substrates.

The hydrophilicity of the alumina substrates was evaluated and determined in Fig. S4-3. Due to the porous and hydrophilic of these substrates, contact angle measurements need to be obtained within extremely brief timeframes (less than one second). The contact angle of all alumina substrates ranged between 8° and 13°, indicating that these alumina substrates are super-hydrophilic and are unaffected by surface polishing.

Table 4-2 illustrates the Feret diameters as derived from SEM surface images, reflecting the impact of polishing on the alumina substrates. The equivalent circle diameter decreased from 0.42 µm (R650) to 0.33 µm (R1100) as R increased, followed by a slight rise to 0.37 µm (R1600). Notably, the P groups demonstrated a similar trend: as sandpaper pulling speeds increased, so did the equivalent circle diameter, consistent with the observed weight loss.

XPS analysis of all alumina substrates revealed the Al_{2p} and O_{1s} peaks of the alumina substrates. As shown in Fig. S4-5-S4-8, all the various polishing parameters demonstrated a significant peak at 74.6 eV, which is attributed to the alumina oxide peak of Al_2O_3. The O_{1s} spectra is shown in Fig. S4-6, XPS spectra showing O_{1s} peaks of alumina substrates from polished R groups. The peaks were deconvoluted into two peaks, one at 532.6 eV representing Al-O bond in Al_2O_3 and the other one at 531 eV representing OH groups on the surface. The XPS result shows that the surface chemical bonding remains the same as the original alumina substrates, and only alter the surface morphology and topology.

Table 4-3. The porosity and equivalent circle diameter of R and P- groups of alumina substrates.

Code	Porosity (%)	Equivalent circle diameter (μm)
Unpolished	42.8 ± 0.6	0.35 ± 0.12
R650	43.0 ± 0.4	0.42 ± 0.15
R850	42.4 ± 0.4	0.38 ± 0.11
R1100	43.5 ± 0.8	0.33 ± 0.08
R1600	**43.4 ± 0.8**	**0.37** ± 0.13
P1.4	43.5 ± 0.4	0.32 ± 0.07
P2.8	42.0 ± 0.5	0.38 ± 0.12
P4.9	43.2 ± 0.4	0.36 ± 0.10
P9.1	**43.4 ± 0.8**	**0.37** ± 0.13

4.4.5. Water Permeation of Polished Alumina Substrates

Fig. 4-6(a) shows that the water permeation of the alumina tubes exhibited minor variations across different tube rotation speeds during testing. Unpolished alumina substrates displayed water permeation of approximately 35.2 ± 0.8 LMH bar^{-1} over a one-hour test period. When the rotation speed increased, the average pure water flux decreased to 26.6 ± 0.8 LMH bar^{-1} (R1100) and slightly increased to 28.2 ± 1.4 LMH bar^{-1} (R1600). A two-sample hypothesis T-test indicated notable variation between unpolished and polished substrates, revealing that tube rotation speeds exceeding 850 rpm could influence the pure water flux ($P \leq 0.001$). The 99.5%

confidence interval for the highest speed suggests a considerable distinction between unpolished and polished substrates. However, lower significant differences were found between the unpolished and 650 rpm samples ($P \leq 0.05$), possibly because of insufficient polishing cycles on the alumina substrates, which slightly affected the filtration performance. In the pulling speed sample group, the pulling speed regulated the polishing time on the alumina substrates, yielding insignificant outcomes compared to P 9.1. As shown in Fig. 4-6(b), P7.5 exhibited the highest average pure water flux (31.2 ± 0.2 LMH bar^{-1}) amongst the pulling speed groups. However, two-sample t-test assessments revealed no statistically significant differences between P7.5 and other pulling speed parameters. This indicates that reducing the pulling speed does not further affect the pure water flux of the alumina substrates.

Based on the characterisation results, the hydrophilicity and porosity of the alumina substrates demonstrated similar performance in various polishing parameters, and the equivalent circle diameter and surface roughness might be the main factors influencing the average pure water flux difference on the alumina substrates. According to Hagen-Poiseuille equation, the water flux is proportional four folds of membrane pore size [296]. The lower equivalent circle diameter reduced the water flux significantly. As shown in Table. 4-2, the water flux decreased with the equivalent circle diameter, and a lower pore size demonstrated a lower water flux on the alumina substrates. However, the unpolished alumina substrates exhibited the lowest pore size compared with the polished alumina substrates, and the surface roughness might be the other contributing factor affecting the water flux. Increased surface roughness of the membrane barrier may reduce the mass transfer rate, as the height of surface layer exceeds that of the fluid turbulence layer, thereby affecting the Reynolds number and liquid viscosity in tangential flow regime [297, 298]. Alumina substrates may create empty voids during water permeation, leading to stagnant zones where water transport is limited [299, 300]. Consequently, a similar effect was observed in the membranes with higher surface roughness, where the surface roughness of R650 was over 3 folds greater than that of unpolished alumina substrates. The surface roughness of alumina substrates decreased the water flux due to the lower mass transfer rate than the unpolished alumina substrates, even the pore size of R650 is larger than that of unpolished substrates. Therefore, surface modification with appropriate polishing conditions may improve water permeation and flux stability by reducing substrate surface roughness.

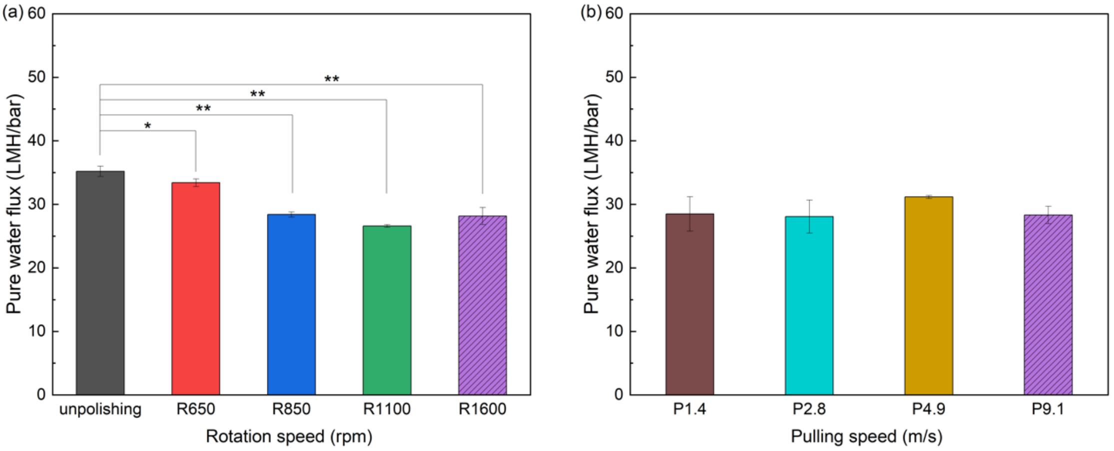

Fig. 4-6. The average pure water flux of the (a) rotation speed and (b) pulling speed. Data represent the mean for three substrate samples ± 1 SD of the mean with p value (*) ≈ 0.05 and (**) ≈ 0.001.

4.4.6. Gas Permeance and Permselectivities

The polished alumina substrates were coated with polyetherimide (PEI) to determine if these substrates can be used for thin film coating of polymeric materials and also analyse the effect of polishing parameters on the gas separation performance of the PEI membranes using CO_2, N_2 and CH_4. Fig. 4-7 shows the CO_2, N_2 and CH_4 single gas permeance (Fig. 4-7a) and CO_2/N_2 and CO_2/CH_4 permselectivities (Fig. 4-7b) as a function of R and P, as well as rotational cycles (derived from R and P). From the R group, the CO_2 permeance remained between 10^{-10} and 10^{-11} mol m^{-2} s^{-1} Pa^{-1} for all the membranes yet N_2 and CH_4 gas permeances produced a stark step change between R650 and R850 – R1600 range, which indicates a critical juncture of 33 rotational cycles. In contrast, the PS group series with a fixed 1600 rpm, all gas permeances remain quite similar. For example, R1600/P9.1 membrane, the CO_2, N_2 and CH_4 single gas permeances are $3.6 \times 10^{-11} \pm 1.3 \times 10^{-12}$ mol m^{-2} s^{-1} Pa^{-1} (0.11 ± 0.01 GPU), $1.6 \times 10^{-12} \pm 1.8 \times 10^{-13}$ mol m^{-2} s^{-1} Pa^{-1} (0.004 ± 0.001 GPU) and $1.7 \times 10^{-12} \pm 1.7 \times 10^{-13}$ mol m^{-2} s^{-1} Pa^{-1} ($0.004 \pm 4 \times 10^{-4}$ GPU), respectively. From these results, the permselectivity (Fig. 4-7b) displayed reasonable separation in the range between 14.0 ± 3.7 (P1.4) and 21.9 ± 1.0 (P9.1) on average for both CO_2/N_2 and CO_2/CH_4, which are twenty-fold greater than those of the unpolished or virgin substrate. In comparison, the permeation results are on par to those of the other PEI bulk membranes reported in the literature, Barbari et al. [286]and Takahashi et al [234] showed that the PEI bulk membranes produced CO_2 permeance of 1.7×10^{-11} mol m^{-2} s^{-1} Pa^{-1} with CO_2/N_2 and CO_2/CH_4 permselectivities of 25 – 26.4 and 30 – 37.4, respectively, which are comparable to the gas permeation performance (Fig. 4-7). Khan et al. [301] provided similar CO_2 permeance at 1.29 GPU with permselectivity of CO_2/CH_4 at 23.3. This suggests that the PEI composite membranes with a working selective layer were successfully coated on and supported by the polished alumina substrate tubes in this study. These clarify that the polishing process on alumina substrates can successfully coating the non-defect PEI. The trends clearly demonstrate that PS derived substrates are of similar surface quality for thin film polymeric membrane coating that offered consistent gas permeation performance, whereas R parameter offered a more decisive factor above R850 to gain a smooth surface finish. Therefore, physical modification by surface polishing is an easy and effective technique to control substrate quality and surface property for potential water and gas separation applications.

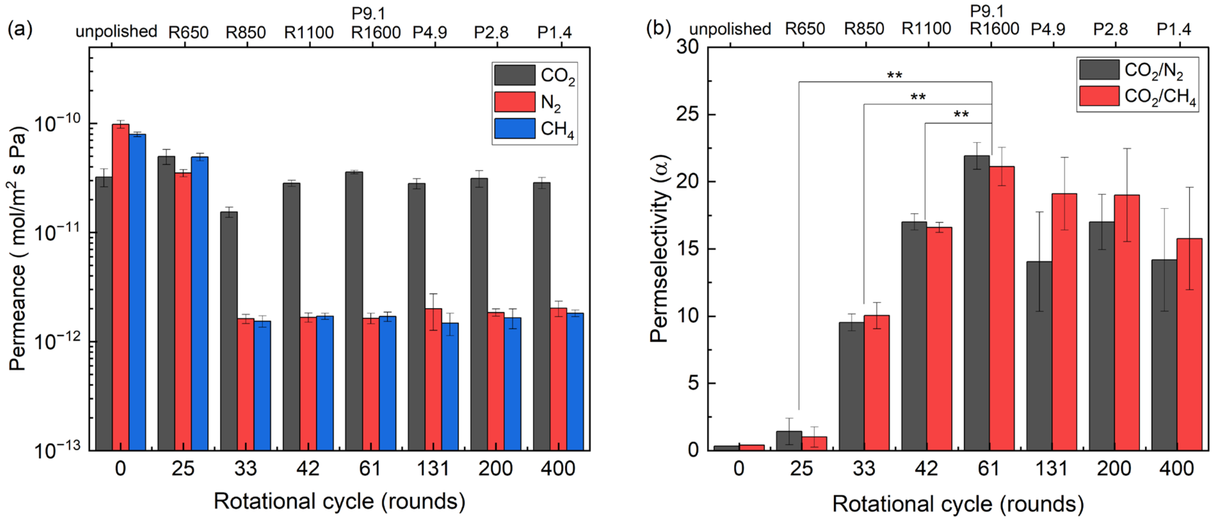

Fig. 4-7. The single gas permeance and the permselectivity of the polishing parameter of the alumina substrates coating with PEI membranes. (a) the gas permeance with CO_2, N_2 and CH_4 and (b) the permselectivity of the CO_2/N_2 and CO_2/CH_4. Data represent the mean for three substrate samples ± 1 SD of the mean with p value (**) ≈ 0.001.

4.4.7. Interfacial Compatibility Between PEI and Alumina Substrates

To illustrate the polishing effect of alumina tubes on the dip-coating performance, a detail discussion on the vacuum-assisted, dip-coating process is shown in Fig. 4-8. In this study, deposition of PEI layer onto tubular alumina substrates was enabled by vacuum suctioning in the tube lumen to provide a driving force. By inducing a vacuum pressure, infiltration of the dope solution is expected to occur into the substrate during the immersion in the polymer dope solution, ensuring the adherence for polymeric solution on the alumina substrates [16]. The substrate immersion step was performed momentarily for 60 s followed by the slow release of the vacuum pressure, allowing both sides of the substrate tube to reach equilibrium at atmospheric pressure.

During the withdrawal phase, the polymeric solution was mainly influenced by capillary force and the viscous drag. However, since the dope solution solvent is NMP, which has a boiling point at 202 °C and is not expected to evaporate during this step, the capillary force induced by solvent drying becomes negligible. Consequently, viscous drag and gravity predominantly govern the solution drainage, particularly any loosely-adhered polymer solution on the substrate surface drains back into the polymer bulk solution [16].

Moreover, surface roughness also played an important role in controlling the dip-coating performance of the polymer. As shown in Fig. 4-8, the schematic of the unpolished and polished alumina substrates depicts the microscopic surface roughness influence on viscous drainage during the withdrawal step. With an increased surface roughness, it is envisaged that a greater frictional force is experienced by the PEI solution on the alumina substrate surface due to increased wettability, which can counteract the viscous drag force to some degree during substrate withdrawal [185]. As a result, the PEI solution adheres more effectively to the substrate, yielding a more uniform and well-coated membrane surface. On the other hand, unpolished substrate or shorter polish duration produced lower substrate surface roughness leading to a lower wettability and a larger viscous drainage.

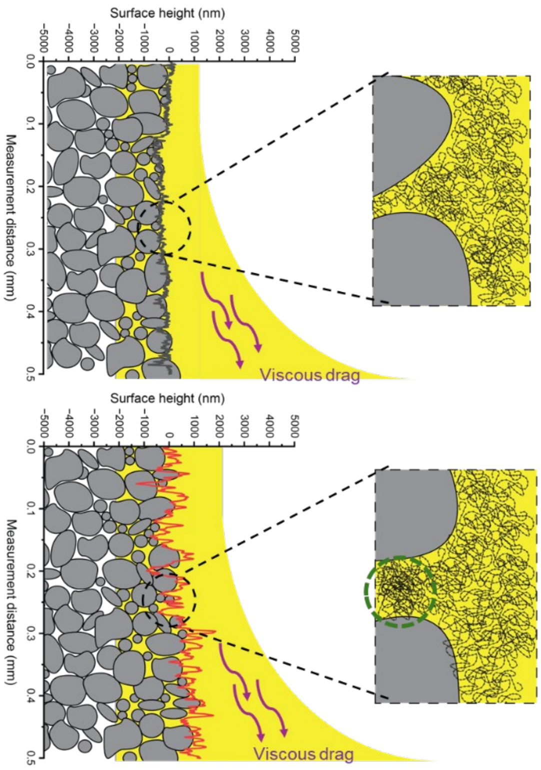

Fig. 4-8. The schematic of polishing effect on surface roughness during film deposition between unpolished and polished membranes.

4.5. Conclusion

In this chapter, we designed a tubular polishing rig and systematically investigated polishing parameters for tubular alumina substrates to control the surface quality and improve thin film coating capability for gas separation membranes. Higher sandpaper grits may provide more consistent polishing performance and increased water flow. Increasing the tube rotation speed can result in a smoother surface and a reduction in the diameter of surface pores, it also affects the water flux and the water stability. The pure water flux permeation testing demonstrated high stability in an hour of water flux testing in pulling speed groups. It shows that the rotational cycle between 61- 200 rounds can provide a stable and equal surface pore structure for water permeation. When casting the PEI thin film on the polished alumina substrates, the membrane demonstrated excellent permselectivity between CO_2, N_2 and CH_4 due to the formation of a continuous, PEI selective layer. The well-formed PEI membrane improved the gas permselectivity by twenty-fold compared to the bulk polymeric membranes. In conclusion, the polishing process provided a suitable substrate pre-treatment step for ensuring substrate quality and consistency for manufacturing thin film membranes with a variety of gas separation applications.

4.6. Supporting Information

Table S4-1. The porosity of the alumina tubes polished and thermally processed by different sandpaper grits size.

Membrane code	Porosity (%)
Unpolishing	47.8 ± 0.2
SG1500	42.5 ± 0.2
SG3000	42.7 ± 0.4
SG5000	43.0 ± 0.7
SG7000	43.4 ± 0.8
SG12000	43.9 ± 0.9

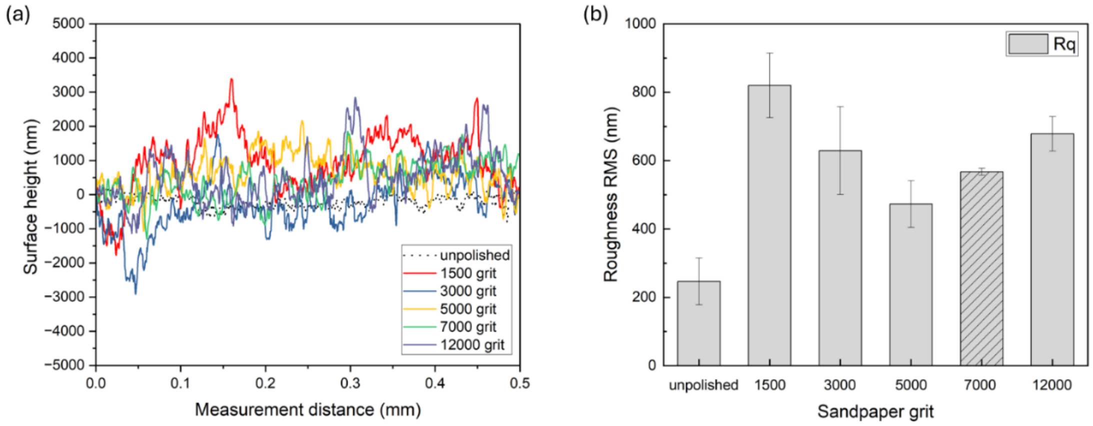

Fig. S4-1. The surface roughness of the alumina tubes prepared by different sandpaper grits from the profilometer analysis showing (a) surface height data and (b) the root mean square (RMS) of the surface roughness.

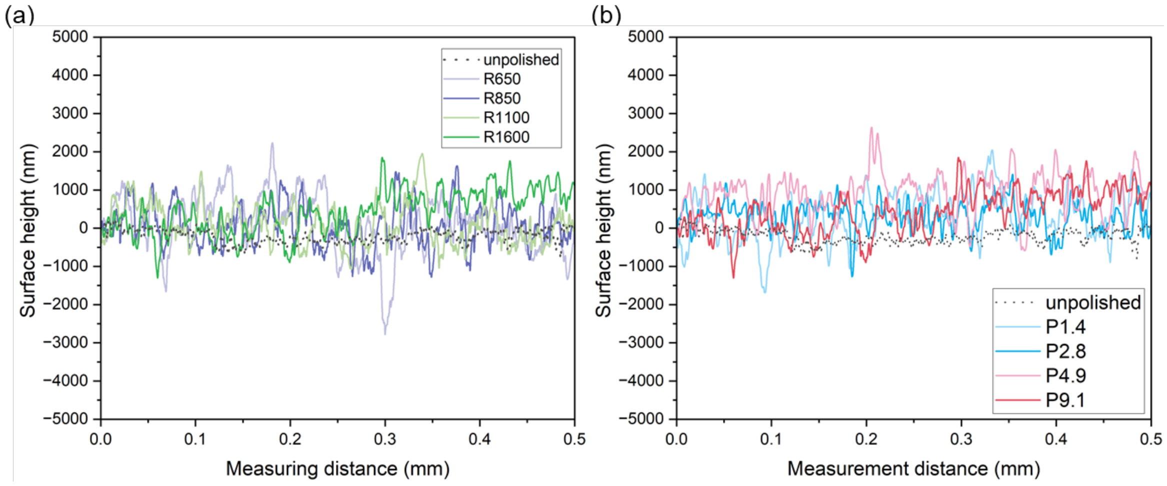

Fig. S4-2. The raw data from the profilometer (a) tube rotation speed and (b) the sandpaper pulling speed.

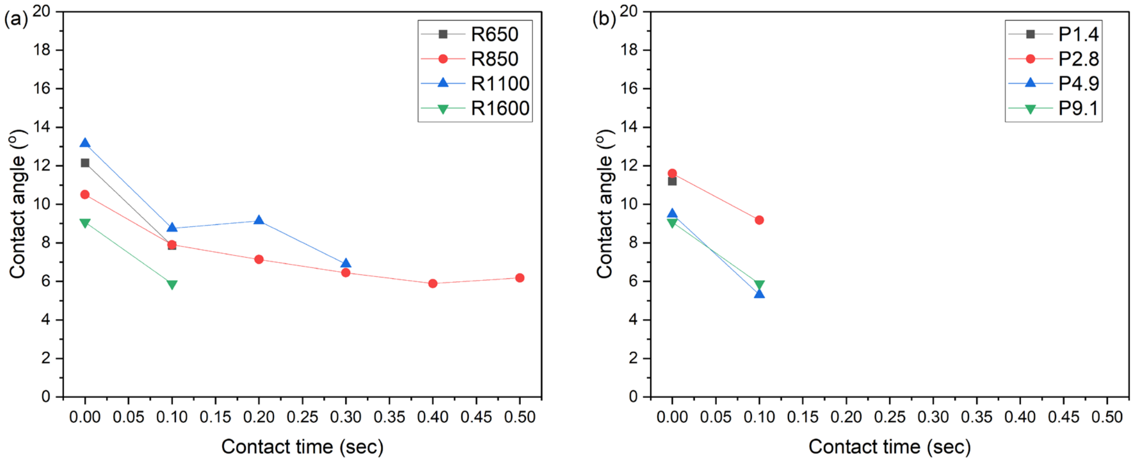

Fig. S4-3. The dynamic contact angle measurement of (a) tube rotation speed and (b) sandpaper pulling speed.

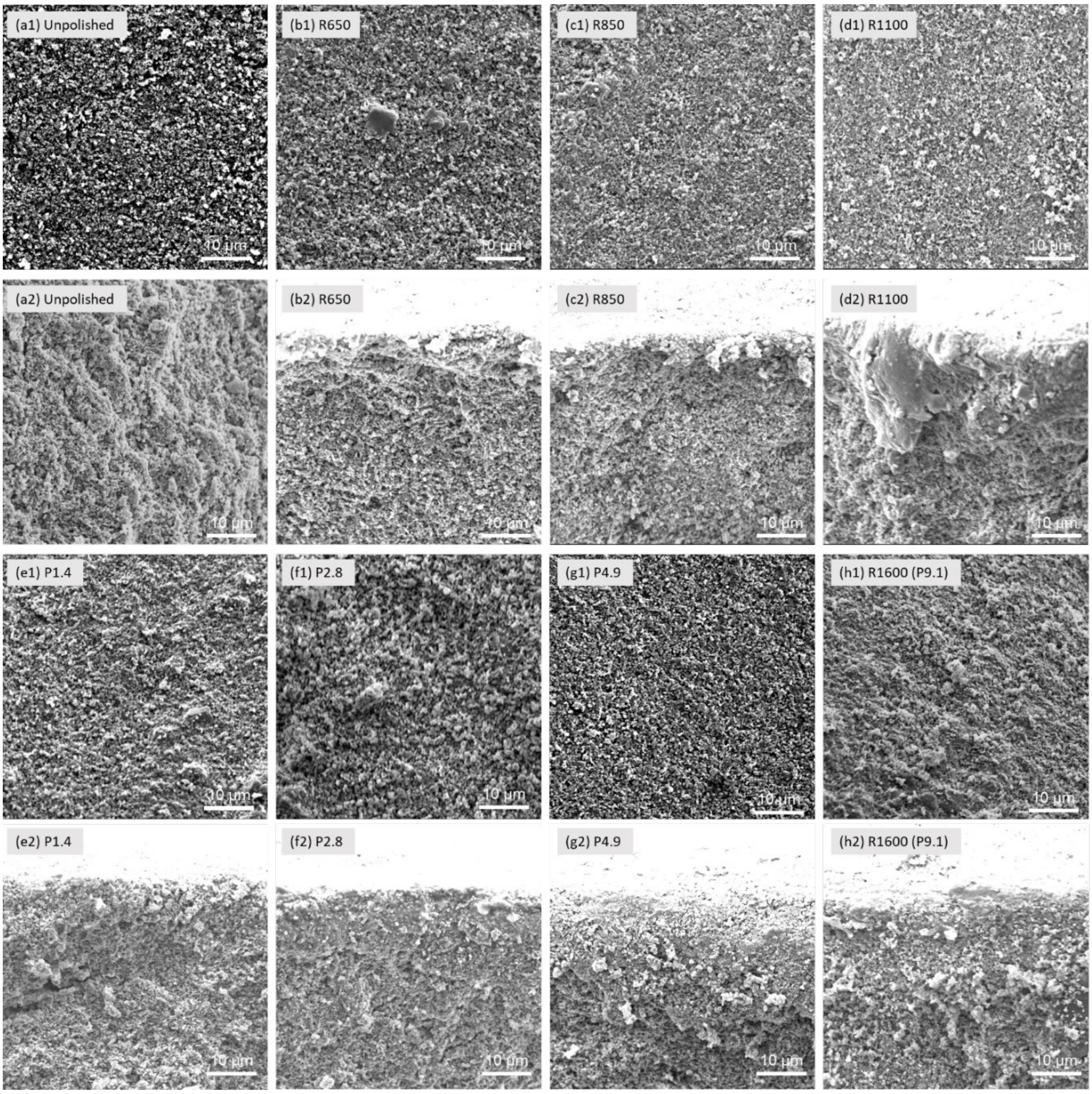

Fig. S4-4. The surface (1) and cross-section (2) morphology of the alumina substrates. (a) unpolished alumina substrates and (b-d) the rotation speed groups and (e-h) the pulling speed groups.

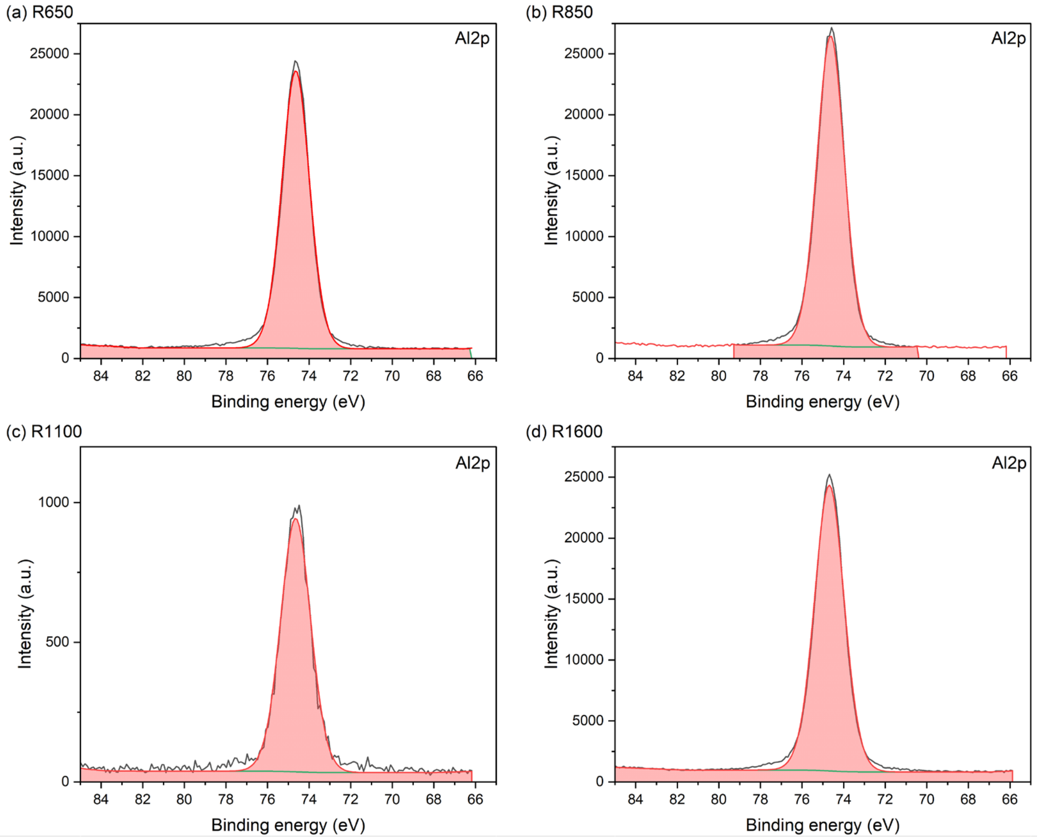

Fig. S4-5. The Al_{2p} XPS spectra of the alumina substrates polished with RS groups.

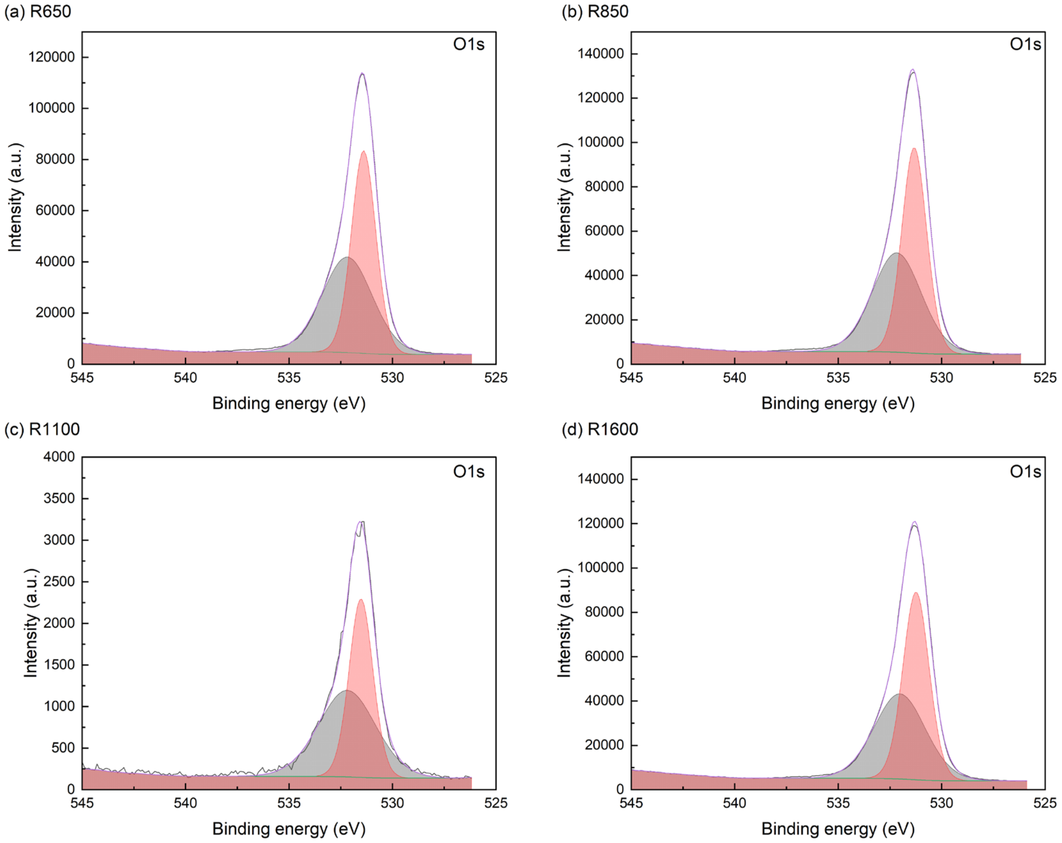

Fig. S4-6. The O_{1s} XPS spectra of the alumina substrates polished RS groups.

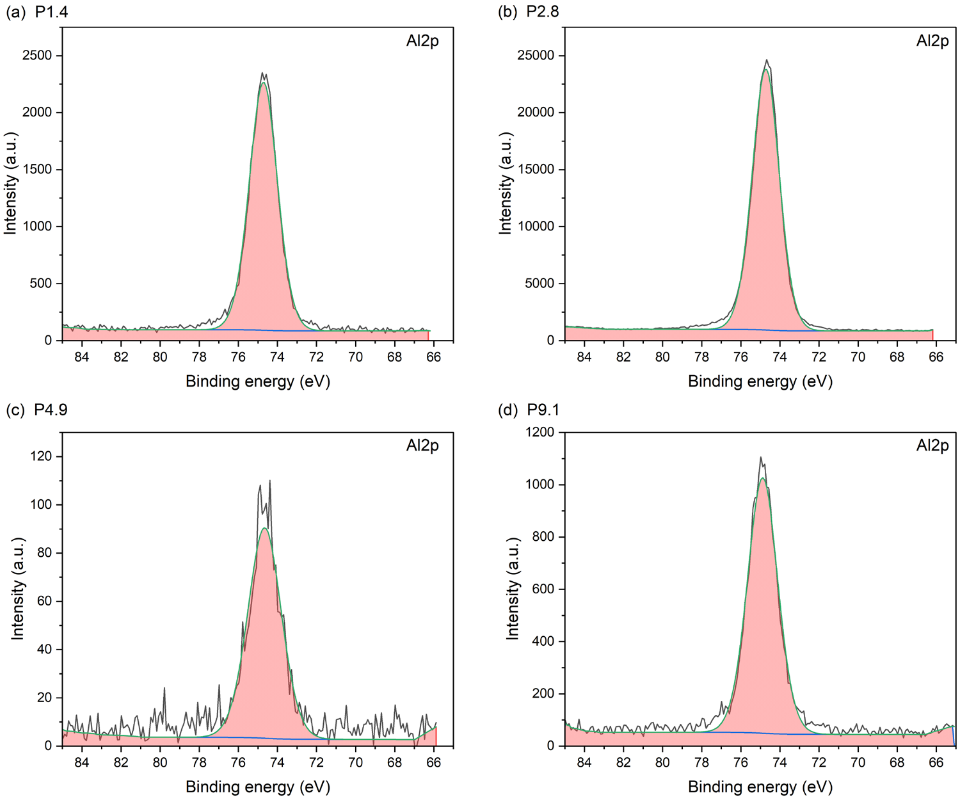

Fig. S4-7. The Al_{2p} XPS spectra of the alumina substrates polished with different pulling speed.

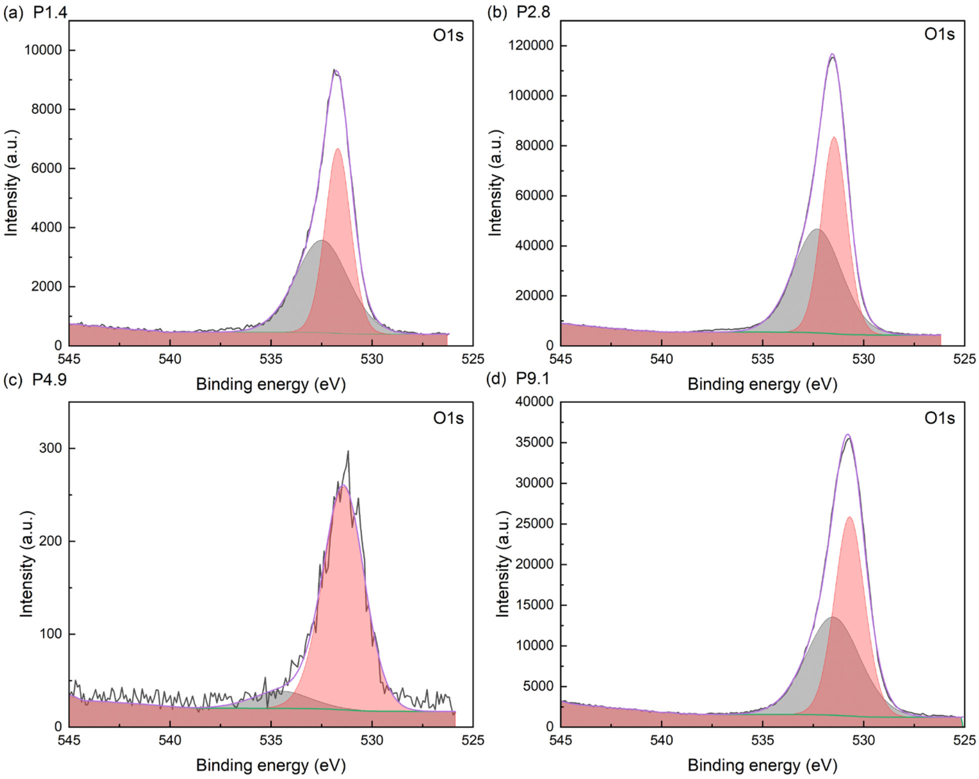

Fig. S4-8. The O_{1s} XPS spectra of the alumina substrates polished with different pulling speed.

Chapter 5 The Influence of Dip-coating and Drying Process on PEI Composite Membranes

In this chapter, the development of PEI-based composite membranes on alumina substrates was systematically investigated to optimise polymeric membrane coating performance (Section 5.1). A vacuum-assisted dip-coating method was employed to fabricate defect-free PEI membranes on porous alumina supports. Key parameters including PEI concentration, number of coating layers, and vacuum-assisted conditions were carefully examined to understand their influence on the polymer chain arrangement and membrane uniformity. Additionally, the impact of solvent retention, particularly the effect of residual N-methyl-2-pyrrolidone (NMP), was evaluated to ensure its effective removal during various drying temperature (Section 5.2). This allowed for the identification of optimal coating conditions that minimize solvent interference and promote stable membrane structures. Under this investigation, the defect-free PEI membrane can be coated on the alumina substrates to fill up the research gaps for forming the defect-free PEI composite membranes.

5.1. Parametric Investigation on the Vacuum-assisted Dip-coating Process

Section 5.1 is submitted to Separation and Purification Technology journal (under review).

5.1.1. Abstract

Composite membranes between polymeric membranes and inorganic substrates have been widely investigated for gas separation applications. Soft polymeric coatings on hard substrates are favourable due to the high mechanical strength imparted by the hard substrates and the high separation capacity conferred by the thin polymeric selective layer. To achieve these desirable properties whilst ensuring that the membrane manufacturing process is scalable and reproducible, this study systematically investigated the design of a vacuum-assisted, dip-coating process for gutter-free, tubular membranes as a function of vacuum pressure and drying temperature to produce a thin film polyetherimide (PEI) selective layer on an alumina substrate for gas molecular-sieving applications. Well-defined PEI alumina membranes were discovered for specific sets of synthesis conditions pertaining to a low vacuum (> -1 bar) dip-coating and drying (110 °C) film consolidation. The composite PEI membrane demonstrated interlayer confinement effect within the selective layer upon second deposition further improving the CO_2/N_2 permselectivity from 1 to 21.9 ± 0.9 and CO_2/CH_4 permselectivity from 1 to 20.5 ± 1.4 with a pore aperture of 4.6 ± 0.1 Å allowing He, H_2, and CO_2 passage. The findings of this study demonstrated important correlations between the vacuum-assisted dip-coating, drying parameter and gas separation performance in controlling the membrane sieving property for He, H_2, and CO_2 in N_2 and CH_4 permeations.

5.1.2. Introduction

Polymeric membrane technology is a mature, commercial separation technology that is cheap to operate, can be easily modularized and scale-up to offer predictable gas separation properties. However, polymeric membranes cannot achieve the high gas purity and high flux requirement due to material limitations such as physical aging, chemical degradation and plasticization [65, 66, 70]. This phenomenon is a well-known performance trade-off between permeability and selectivity, as depicted empirically by the Robeson upper bound in 1991, 2008, and 2019 [65, 66, 70]. Recently high performance polymers, such as polymers of intrinsic microporosity [302, 303], perfluoropolymers [304, 305], thermally-rearranged polymer [21, 23], and polyimides [306, 307] have redefined the trade-off boundary due to their unique chemical structures and material properties.

Amongst the polyimides, polyetherimide (PEI) is widely known for its commercial membrane under registered trademark of Matrimid®, Torlon® and Ultem®. PEI has a rigid bulky $C(CH_3)_2$ group with a stiff central structure interlocked by the flexible “-O-” linkage for the diamine and dianhydrides groups [159, 241], and the membranes have excellent gas separation performance and good plasticization resistance [18, 19, 243], as well as good thermal stability and high mechanical strength [308-311]. Similarly, PEI have also been proven to be beneficial for constructing molecular sieve membranes [140, 312]. For example, Ultem® derived membranes showed good CO_2/N_2 and CO_2/CH_4 permselectivities, which lie in the range of 20 – 80 with modest CO_2 permeability of 10 Barrer [18, 249, 288, 313], albeit the performance is still constrained by long-term stability. More recently, Ultem® based PEI membranes blended with highly permselective materials, such as zeolite or MOF, have shown to overcome low gas selectivity and plasticization effect [243, 246, 249]. Dai et al. [249] demonstrated mixed matrix membranes by doping ZIF-8 into PEI hollow fibre membranes improved CO_2 permeance by 60 % and CO_2/N_2 permselectivity by 25 % at 25 °C. Nematolahi et al. [314] reported that doping 3 wt.% of nickel modified zeolite into PEI membrane also enhanced CO_2 permeability by 45 % and the CO_2/N_2 permselectivity increased from 25 to 34. These studies have postulated that the presence of these inorganic fillers restricts the polymer chain rotation via chain confinement effect to confer the gas permselectivity improvement. Although separation performance can be enhanced through inorganic modifiers, research efforts on the gas purity and true selectivity of the product gases also need to be coupled to meet the specific industrial separation requirements.

Generally, composite membranes composed of polymer thin films and mesoporous/macroporous inorganic substrates possess polymer thin film thickness in the range between 0.1 to 1 μm to reduce mass transfer resistance [8, 10, 315]. They are typically 1 to 3 magnitudes thinner than free-standing polymeric membranes (50 – 150 μm). Without a gutter layer, the polymeric layers deposition onto porous inorganic substrates requires good material compatibility, defect-free polymer thin films and polymer infiltration into the voids of inorganic substrates [10, 234]. To ensure these requirements are met, a comprehensive parametric study on coating deposition strategy is crucial.

Tubular and hollow fibre configurations are highly desirable due to the greater surface area to volume ratio. The methodologies for composite membrane fabrication in tubular configuration include brush coating [316, 317], spray coating [318, 319], continuous coating [320, 321], and dip coating [32, 121, 133, 141]. These coating methods have been widely investigated for industrial applications in composite membranes. However, the methodology of thin-film composite membrane coating process for gas separation applications has not been sufficiently developed for tubular configurations, especially demonstrating high processing fidelity.

Dip-coating process is regarded as one of the high-throughput, cost-effective coating techniques for modifying tubular substrates and composite tubular membranes because of its simple setup and controllable operation. However, repeated coating steps to ensure crack-free, homogeneous membrane layer are essential albeit the process often leads to increased membrane thickness and mass transfer resistance. Ismail et al. [32, 121, 133] investigated a series of PEI polymer coatings on ceramic tubular substrates using BTDA-FDI/MDI (P-84) as the polymer source. The CO_2 permeance and CO_2/CH_4 selectivity of 1.13 GPU and 1.66, respectively. Their gas separation performance was significantly lower than that of other P-84 bulk membranes (14.4 Barrers and 33.4 $\alpha CO_2/CH_4$) [322]. Sedigh et al. [159] examined tubular membranes with PEI-based inner-layer coated alumina, which exhibited a He/N_2 permselectivity ranging from 20 to 25 after the membranes undergone carbonisation post-treatment. However, in all these bench-scale research works, the dip-coating methodology was not standardised, and membrane reproducibility was difficult to be established due to inexplicable multifactorial effects. Therefore, a comprehensive investigation into the PEI conditions for fabricating a defect-free composite membrane without a gutter layer is beneficial for gas separation membrane applications.

In this study, we investigated a series of PEI membranes supported on alumina ceramic tubes as a function of PEI dope concentration, vacuum pressure during dip coating process, and coating layers to understand the correlations between the fabrication conditions, membrane morphology, thermophysical properties, size exclusion capacity, and gas separation performance in order to engineer composite membranes with a high degree of membrane reproducibility.

5.1.3. Experimental

The PEI composite membrane fabrication procedure is described in section 3.2.2. Additionally, flow charts of the experimental setup are provided in in Fig. 5-1. A vacuum-assist dip-coating process was incorporated for PEI deposition synthesis procedure. Furthermore, the detail of experimental setup was listed in section 3.3.3. The membrane codes and fabrication parameter conditions are listed in Table 5-1.

Table 5-1. The parameters of membrane preparation in this study. Bolded text represents identical membrane sample.

Membrane code	PEI concentration (wt.%)	Coating layer	Vacuum Pressure (gauge, bar)	Drying temperature (°C)
8PEI(3)/-1.0	8	**3**	**-1.0**	**110**
10PEI(3)/-1.0	10			
12PEI(3)/-1.0	**12**			
15PEI(3)/-1.0	15			
12PEI(1)/-1.0	**12**	1	**-1.0**	**110**
12PEI(2)/-1.0		2		
12PEI(3)/-1.0		**3**		

12PEI(3)/0	**12**	**3**	0	**110**
12PEI(3)/-0.34			-0.34	
12PEI(3)/-0.5			-0.50	
12PEI(3)/-0.68			-0.68	
12PEI(3)/-1.0			**-1.0**	

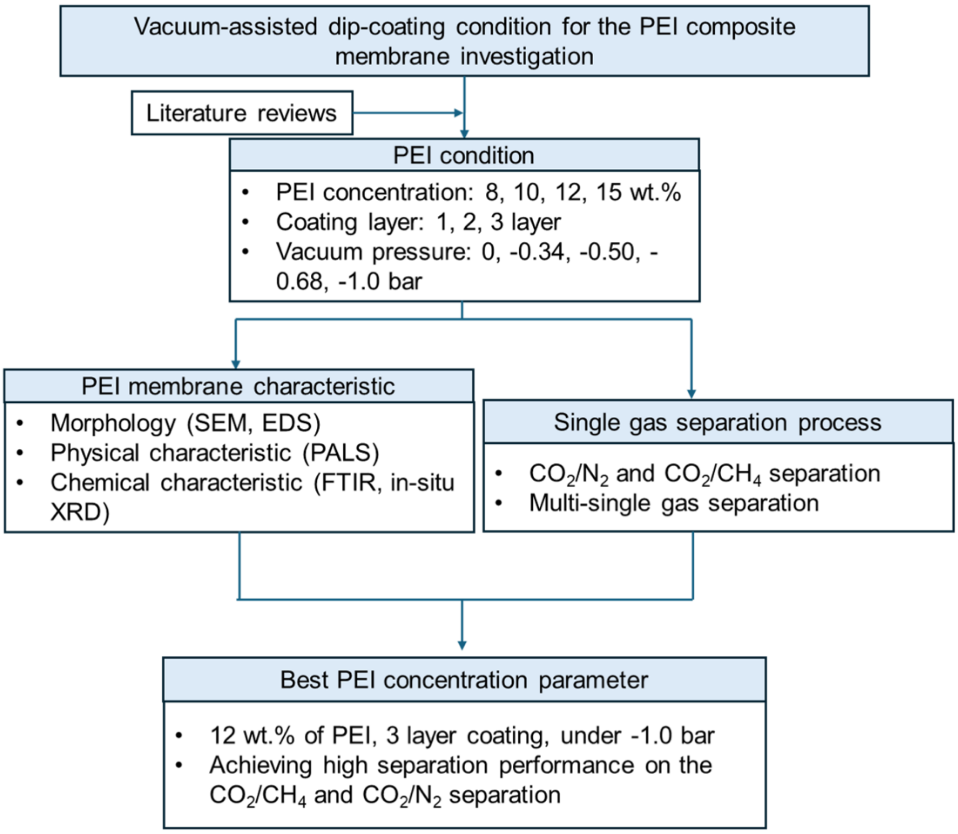

Fig. 5-1. Flow chart of the vacuum-assisted dip-coating method for the PEI composite membrane synthesis.

5.1.4. Results

5.1.4.1. Membrane Material Characterisation

5.1.4.1.1 Membrane Morphology

The membrane cross-section morphology was determined via SEM. Fig. 5-2(a) shows a clear PEI layer could be seen on top of the tubular alumina substrate, which was used to estimate the coating thickness (Table 5-2).

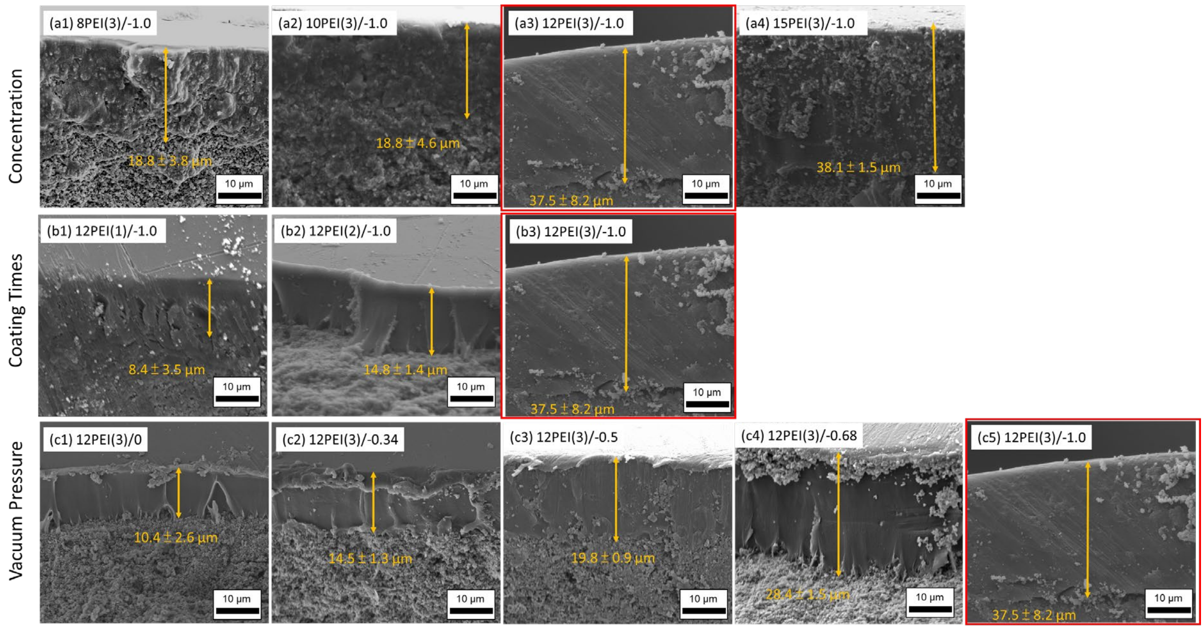

Fig. 5-2. The cross-section morphology of the PEI membrane samples for (a) the PEI concentration effect, (b) the 12 PEI layer effect, and (c) the vacuum pressure effect. The red box images are the same from 12PEI(3)/-1.0 sample. All membranes were filmed with 5000x magnification with 10 μm scale bar.

Table 5-2. The membrane thickness of all PEI membranes. Bolded membrane code represents identical membrane result.

Groups	Membrane code	Membrane thickness (μm)
Concentration effect	8PEI(3)/-1.0	18.8 ± 3.8
	10PEI(3)/-1.0	18.8 ± 4.6
	12PEI(3)/-1.0	**37.5 ± 8.2**
	15PEI(3)/-1.0	38.1 ± 1.5
Coating effect	12PEI(1)/-1.0	8.4 ± 3.5
	12PEI(2)/-1.0	14.8 ± 1.4
	12PEI(3)/-1.0	**37.5 ± 8.2**
Vacuum pressure effect	12PEI(3)/0	10.4 ± 2.6
	12PEI(3)/-0.34	14.5 ± 1.3

12PEI(3)/-0.5	19.8 ± 1.3
12PEI(3)/-0.68	28.4 ± 1.5
12PEI(3)/-1.0	**37.5 ± 8.2**

For the concentration membrane series (Fig. 5-2(a1) to 2(a4)), the three times coated PEI layer thickness increases from 18.8 μm to 38.1 μm for 8 to 15 wt.%. Interestingly, the membrane thickness is indifferent for the 8 and 10 wt.%, which is likely due to the solution being too dilute hence the degree of phase separation is non-uniform. Conversely, a significantly increase in PEI layer thickness is observed from 18.8 μm to 37.5 μm when the PEI concentration increases from 10 to 12 wt.%, and stabilised at 38 μm, even at the higher PEI concentration of 15 wt.%.

Generally, the higher dope concentration leads to increased viscosity resulting in thicker, denser film, which can enhance gas selectivity but reduce permeability. In addition, as viscosity is a function of polymer-polymer interaction and entanglement, the extent of the polymer coverage on the substrate and in the substrate pores become greater leading to layer compaction and thus decreases mass transfer. To overcome polymer layer densification, the coupling effect of the capillary forces of the substrate assisted by vacuum suctioning during dip-coating provides a rapid onset of polymer infiltration and deeper liquid entrainment, the extent of which is more significant at lower polymer dope concentration. Therefore, the propensity of the 8 and 10 wt.% to form a continuous, dense film on the substrate surface is lower, and would not be desirable for gas separation membranes even with three coating cycles. On close examination of Fig. 5-2(a1) to 2(a4), all membranes do not show any polymer delamination, which is evidenced by a good interfacial contact between the PEI layers themselves and with the alumina substrate surface. In fact, it has been previously suggested that the presence of hydroxyl groups on alumina and the dianhydride groups of polyetherimide can undergo covalent bonding and hydrogen bonding during the drying process [323]. As a result, it is expected that the PEI layer has good attachment and compatibility with the alumina substrates.

Furthermore, 1, 2, and 3 membrane layer series of 12 wt.% PEI membranes were prepared. As shown in Fig. 5-2(b1) to 2(b3) and the corresponding EDS images (Fig. S7-1(a) to (c)), the membrane thickness significantly increased from 8.4 µm to 37.5 µm from 1 layer to 3 layers. Interestingly, the increment of membrane thickness from 2nd to 3rd coating (22.7 µm) is much higher than from 1st to 2nd coating (6.4 µm). During the withdrawal process, surface topology and porosity play very important role in determining the amount of drag force (withdrawal speed) and capillary force (vacuum assisted). It is expected that after the first PEI layer is formed continuously and the surface becomes smoother (Fig. 5-2b1), the degree of capillary force induced by the alumina substrate is minimized such that the 2nd and 3rd layers were able to form slowly over the first PEI layer with greater material compatibility, leading to a thicker film.

The effect of vacuum pressure during dip-coating on the 12 wt.% PEI layer thickness was also studied. As shown in Fig. 5-2(c1) to 2(c5), when the vacuum pressure increased from no vacuum (12PEI(3)/0) to -0.5 and -1.0, the PEI layer thickness increases considerably from 10.4 to 19.8 µm and 37.5 µm, respectively. That means the higher negative pressure induced by vacuum force can result in increasing membrane thickness during the dip-coating process. This provides an additional driving force to ensure polymer infiltration and polymer compaction/interpenetration are simultaneously achieved to form a continuous, crack-free, dense PEI film with the assurance of good interfacial attachment. However, as eluded earlier, how such PEI layer morphology and thickness translates to membrane separation properties will be crucial to determine its separation efficiency.

5.1.4.1.2 Chemical Structure Analysis

The XRD and ATR-FTIR analysis of the PEI composite membrane was used to detect the crystalline structure and the specific functional groups in the PEI film. As shown in Fig. 5-3(a), a non-destructive high resolution-XRD was utilized to investigate the crystalline structure of the PEI membranes on alumina tube. The exhibited peaks of the alumina tube at 2θ angles are 25.4°, 35.0°, 37.6° and 43.2°, which correspond to the (012), (104), (110), (113) of the rhombohedral α-alumina structure, respectively [324, 325].

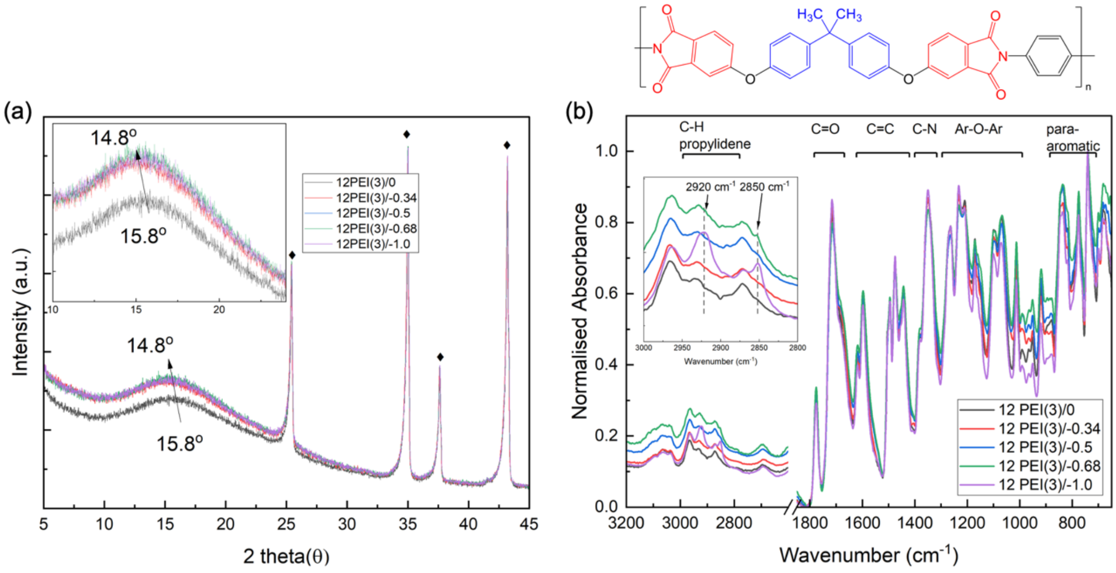

Fig. 5-3. The characteristic of (a) XRD and (b) ATR-FTIR result for the vacuum membrane series. The PEI chemical structure is colour highlighted with the red region being phthalimide and the blue region being propylidene.

The ATR-FTIR analysis was employed to identify the chemical functional groups and the various vibrational stretching groups present in the vacuum membrane sample series. Due to the detection depth (5 μm) of the ATR-FTIR technique, the results only pertain to the chemical characteristics on the membrane surface. To compare the spectra of the different membrane samples, FTIR spectrum was normalized using the 710 cm^{-1} peak, which was seen to be the most stable, highest peak in all the spectra, as per previously described normalization methodology of FTIR spectrum for PEI [326, 327].

As shown in Fig. 5-3(b), peaks at 2970, 2930 and 2870 cm^{-1} are attributed to the C-H stretching vibrations of propylidene groups in the PEI polymer backbone [326, 327]. Notably, two new shoulder peaks emerged at 2920 and 2870 cm^{-1} which intensify with increasing vacuum pressure. These two new peaks are also attributed to the C-H stretching of propylidene groups pertaining to the same functional groups at 2920 and 2850 cm^{-1} but are characterised by minimal interactions with the other functional groups in the PEI. It is postulated that with increasing inter-polymer chain distance, more degrees of freedom in the molecular vibrations of the propylidene groups are permitted, thus manifesting these two new C-H stretching vibrations observed at 2920 and 2850 cm^{-1}. The results are also in good accord with the peak shift towards lower diffraction angles for the amorphous PEI observed in the XRD.

5.1.4.1.3 PALS Analyse

PALS can be used to show the polymer network pore structure of the polyimide membranes due to the strong electron affinity exhibited by the imide moieties, such that there is a pronounced inhibition of the positronium, leading to a reduction intensity of the τ_3 component [22, 328]. Therefore, the two-component fitting analysis provides valuable insight into the free volume within the polymer layer to distinguish between 12PEI(3)/0 and 12PEI(3)/-1.0 [257]. For the PALS analysis to be meaningful, careful sample preparation involving micro-sectioning of the membranes from the top surface to form thin films that are packed into 1 mm thick bundle is required.

As shown in Table 5-3, the positron lifetime of the second component and the calculated pore diameter offers insights into the potential pore size differences between 12PEI(3)/0 and the 12PEI(3)/-1.0 membrane as well as the repeat. Following the vacuum-assisted dip-coating process, a significant reduction in membrane pore size is observed, diminishing from 5.51 ± 0.05 Å to 4.64 ± 0.1 Å. This outcome underscores the substantial impact of polymer chain confinement between the PEI and alumina substrates. Furthermore, the consistency of the data is verified by examining a separate 12PEI/-1.0 sample, which proved the pore size of 12PEI(3)/-1.0 is approximately 4.64 ± 0.1 Å. The reduced pore diameter serves to hinder the permeation of gas molecules through the membrane, facilitating efficient channels for gas separation.

Table 5-3. The pore diameter of 12PEI/0 and 12PEI/-1.0 membranes with 2-component fitting.

Membrane code	τ_2 (ns)	± 1 SD	Diameter (nm)	± 1 SD
12PEI(3)/0	0.395	0.002	0.551	0.005
12PEI(3)/-1.0	0.359	0.003	0.473	0.010
12PEI(3)/-1.0 _Repeat	0.351	0.003	0.455	0.010

5.1.4.2. Pure Gas Permeation Performance

Single CO_2, N_2, and CH_4 gas permeation tests of the PEI composite membranes prepared by using different PEI dope concentration, deposition layer, and vacuum pressure (Table 1) were carried out to determine the membrane gas permeance and permselectivity, as well as to demonstrate their fabrication reproducibility with triplicate membrane samples. The gas permeance results and the diffusion coefficients of all membranes were presented in Fig. 5-4.

As shown in Fig. 5-4(a1), the concentration series of PEI membranes demonstrated that gas permeances decreased with increasing PEI dope concentration. Membranes made using 8 wt.% of PEI dope concentration achieved a gas permeance on average of $5.14 \times 10^{-9} \pm 1.5 \times 10^{-9}$ mol m^{-2} s^{-1} pa^{-1} for both CO_2 and N_2, which did not form a continuous layer and thus was non-selective. As PEI dope concentration increases to 12 wt.%, the gas permeance of 12PEI(3)/-1.0 membranes decreased by two and three magnitude orders to $3.59 \times 10^{-11} \pm 1.3 \times 10^{-12}$ mol m^{-2} s^{-1} pa^{-1}for CO_2 and $1.64 \times 10^{-12} \pm 4.83 \times 10^{-13}$ and $1.70 \times 10^{-12} \pm 1.67 \times 10^{-13}$ mol m^{-2} s^{-1} pa^{-1} for both N_2 and CH_4, which yielded CO_2/N_2 of 21.9 ± 0.9 and CO_2/CH_4 of 20.5 ± 1.4. Upon further increasing the PEI solution concentration (15 wt.%), the CO_2 permeance reached $8.73 \times 10^{-12} \pm 1.4 \times 10^{-13}$ mol m^{-2} s^{-1} pa^{-1}, which is a 50% lower than that of the 12PEI(3)/-1.0 membrane. Similarly, the N_2 and CH_4 permeances are approximately 50% less than the same permeances of 12PEI(3)/-1.0 membrane. Not surprisingly, gas permeances decreases as polymer dope concentration increases due to the increase in membrane thickness and polymer packing density leading to an increase mass transfer resistance.

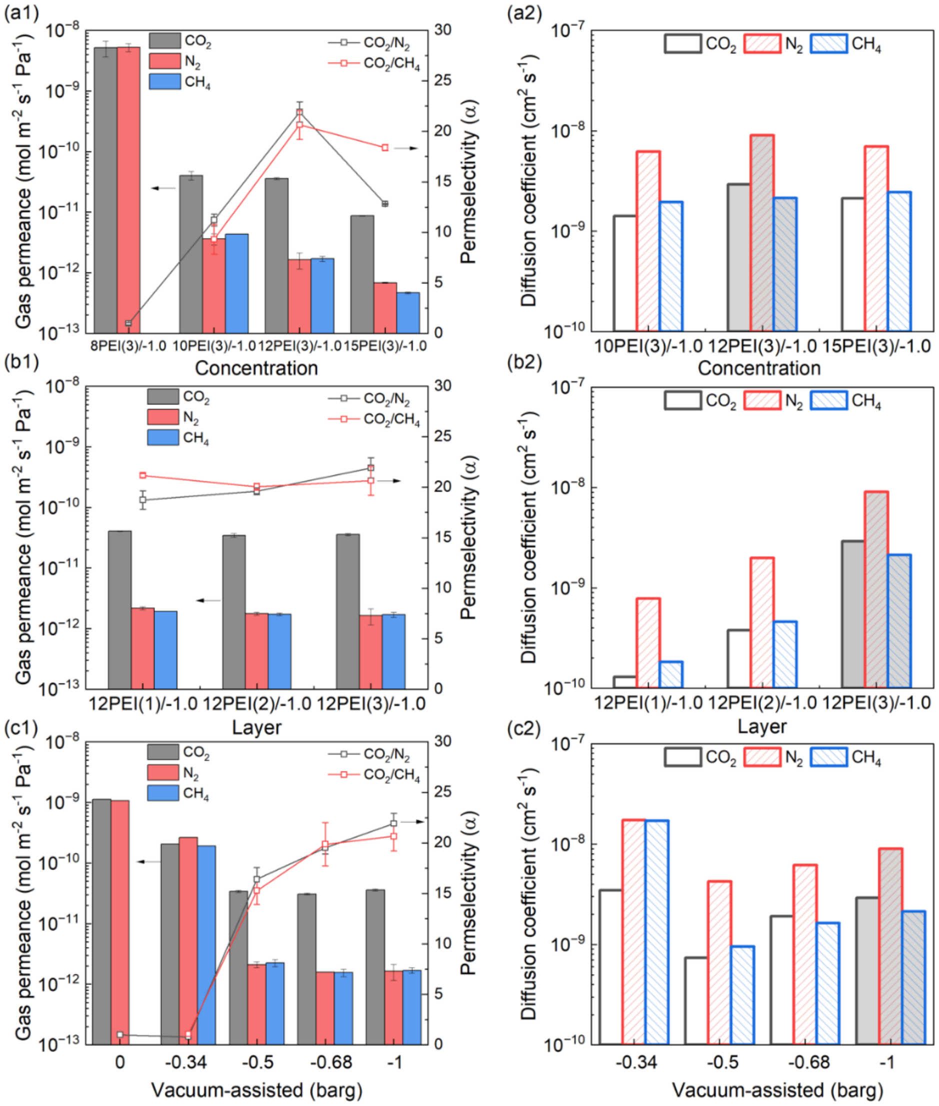

Fig. 5-4. The CO_2, N_2, and CH_4 single gas permeation result of the PEI membranes showing (a1-c1) gas permeance and gas permselectivity for α CO_2/N_2 and α CO_2/CH_4, and (a2-c2) diffusion coefficients of CO_2, N_2, and CH_4.

As shown in Fig. 5-4(b1), the number of dip-coating/drying cycle is an important parameter to investigate due to the need to achieve a continuous, defect-free, selective layer whilst it may significantly affect the gas permeance. For a single coat membrane, 12PEI(1)/-1.0, the CO_2 permeance was measured at $4.02 \times 10^{-11} \pm 3.7 \times 10^{-13}$ mol m^{-2} s^{-1} pa^{-1}. As the dipping cycle increases, 12PEI(2)/-1.0 produced a CO_2 permeance of $3.18 \times 10^{-11} \pm 2.4 \times 10^{-12}$ mol m^{-2} s^{-1} pa^{-1}, which is similar to that of the 12PEI(3)/-1.0. Moreover, the N_2 and CH_4 permeances exhibited similar values for all the three membranes averaging approximately 1.64×10^{-12} mol m^{-2} s^{-1} pa^{-1} and 1.7×10^{-12} mol m^{-2} s^{-1} pa^{-1}, respectively. Interestingly, the number of dip-coating/drying cycle investigation clearly showed all three membranes with 1, 2, and 3 coats formed a continuous, selective layer demonstrated very similar single CO_2, N_2 and CH_4 gas permeances, and similar CO_2/N_2 and CO_2/CH_4 permselectivities.

The gas permeance resulting from the vacuum-pressure effect during the dip-coating process was also measured. This demonstrated a clear cut-off between defective and non-defective membranes at -0.5 bar of vacuum pressure. By comparing the gas permeances between no vacuum (12PEI(3)/0) and -0.5 bar vacuum-assisted (12PEI(3)/-0.5) as shown in Fig. 5(c1), CO_2 permeance decreased 1 to 2 orders of magnitude, yet N_2 permeance decreased 2 to 3 orders of magnitude. From -0.5 bar onwards, the membranes show virtually no decrease in the CO_2 permeance but both N_2 and CH_4 permeances had further suffered a minor loss (10%). For example, N_2 permeance decreased from $2.1 \times 10^{-12} \pm 2.37 \times 10^{-13}$ mol m^{-2} s^{-1} pa^{-1} (12PEI(3)/-0.5) to $1.58 \times 10^{-12} \pm 2 \times 10^{-15}$ mol m^{-2} s^{-1} pa^{-1} (12PEI(3)/-0.68). An increase in vacuum pressure from 0 to -0.5 bar resulted in the elimination of large defects and voids, leading to the formation of a selective PEI membrane at -0.50 bar, characterised by permselectivities of 16.4 ± 1.1 (α CO_2/N_2) and 15.2 ± 1.3 (α CO_2/CH_4). Further increasing the vacuum pressure to -1 bar enhanced polymer packing density, thereby prevented the intermicrovoids formation and offered the highest permselectivities of 21.9 for CO_2/N_2 and 20.5 for CO_2/CH_4 for 12PEI(3)/-1.0 membranes.

The diffusion coefficient of the PEI membranes was calculated using the time-lag method to characterize the PEI membranes [329]. Both 8PEI(3)/-1.0 and 12PEI(3)/0 membrane results were excluded from the analysis because of the fast time lag component that cannot be accurately measured. From Fig. 5-4(a2), the 12PEI(3)/-1.0 obtained the highest CO_2 and N_2 diffusion coefficients compared to 10PEI(3)/-1.0 and 15PEI(3)/-1.0 membranes. For example, the diffusion coefficient of CO_2 for 12PEI(3)/-1.0 is 106 % and 38 % higher compared to 10PEI(3)/-1.0 and 15PEI(3)/-1.0, respectively. Similarly, the N_2 diffusion coefficient of 12PEI(3)/-1.0 is 45 % and 70 % higher than the that of 10PEI(3)/-1.0 and 15PEI(3)/1.0, respectively. As shown in Fig. 5-4(b2) for the membrane layer series, the layer effect demonstrated that the three layers coated membrane had the highest diffusion coefficient compared to 1-layer and 2-layer membranes due to its increased membrane thickness. Shishatskii et al. [330] determined that the diffusion coefficient decreases with reducing thickness of the glassy polymeric membranes (poly(vinyltrimethyl silane) (PVTMS) and poly(trimethylsilyl norbornene) (PTMSNB)).

As shown in Fig. 5-4(c2), the diffusion coefficient of CO_2, N_2, and CH_4 increases with increasing vacuum pressure from 12PEI(3)/-0.5 to 12PEI(3)/-1.0 membranes. The highest diffusion coefficient was found for the membrane prepared using -1 bar of vacuum pressure during dip-coating; 12PEI(3)/-1.0 besides the membrane prepared at -0.34 bar, which was found to have defects (non-permselective). For example, the CO_2 diffusion coefficient of 12PEI(3)/-1.0 was 53 % and 297 % higher than that of the 12PEI(3)/-0.68 and 12PEI(3)/-0.5, respectively. Interesting, all three membranes prepared using -0.5, -0.68, and -1.0 bar show N_2 diffusion coefficient higher than CO_2 and CH_4 diffusion coefficients, which is presumably due to its gas inertness and thus N_2 is expected to have the least interaction with the PEI material.

In contrast, CO_2 is a polar gas that can be adsorbed onto the PEI polymer chain, therefore has a lower diffusion coefficient [331]. Moreover, CH_4 gas seem slowest to diffuse through the membrane bulk compared to CO_2 and N_2 molecules due to its largest kinetic diameter of all three.

From these results, a normalised function was proposed to calculate the diffusion coefficient accounting for the membrane thickness [330]. As shown in Fig. S7-2, the gradient of the normalised diffusion coefficient and membrane thickness indicates a positive correlation with the membrane diffusivity for all three gases tested (CO_2, N_2, and CH_4). In general, the membrane permeability does not depend on the membrane thickness when the membrane thickness exceeds above 50 μm [332]. Firpo et al. determined that the CO_2 permeability increased with the PDMS membrane thickness with 1-30 μm [332]. Similar results had been reported for poly[1-(trimethylsilyl)-1-propyne and Kapton® polyimide membranes that thicker membranes offered a larger diffusivity due to the excess free volume [330, 332-334].

In order to assess for membrane size exclusion capacity, single gas permeation of 12PEI(3)/-1.0 membrane (in triplicate) was further investigated using a series of light gases with increasing kinetic diameter ranging from 2.6 Å (He) to 3.8 Å (CH_4). As shown in Fig. 5-5(a), the single gas permeance of the 12PEI(3)/-1.0 membrane demonstrated a good sieving performance between H_2 (2.89 Å) and N_2 (3.64 Å). The gas permeance decreases as the kinetic diameter of gases increases giving rise to the highest gas permeance measured at 2.6×10^{-10} mol m^{-2} s^{-1} pa^{-1} for He and the lowest gas permeance measured at approximately 1.6×10^{-12} mol m^{-2} s^{-1} pa^{-1} for N_2 and CH_4. These results are in good agreement with the pore aperture (4.64 ± 0.1 Å) found in the PALS, even though the pore aperture of the 12PEI/-1.0 membrane being larger than that of N_2 (3.64 Å) and CH_4 (3.8 Å). This effect can be explained by the influence of Lennard-Jones potential governing the interactions between the gas molecules and the membrane pore wall. For the non-adsorptive gases such as N_2 and CH_4, it is understood that the gas diffusion will be taking place through the pathway of minimum potential energy through the membrane pores. Hence, the gas molecules will maintain at an equilibrium distance from the pore wall to minimise its interactions if possible.

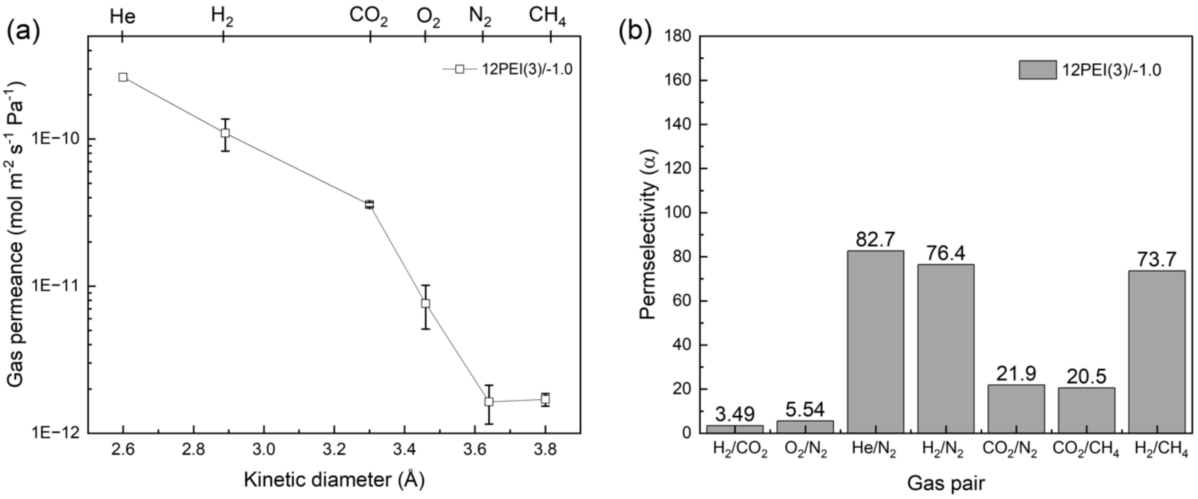

Fig. 5-5. (a) the pure gas permeance in different kinetic diameter gases (testing condition at 35 °C and 2 bar) and (b) the permselectivity of various gas pairs.

Fig. 5-5(b) shows high He/N_2, H_2/N_2, and H_2/CH_4 permselectivities of 82.7, 76.4 and 73.7, respectively, indicating good separation capacity for the lighter gases. Furthermore, the PEI selective layer offers a high affinity for CO_2 gas due to the strong interaction of CO_2 with the ether anhydride of the PEI backbones, which improved the membrane solubility, and thus enhanced the membrane permeance [331]. These results demonstrated that the 12PEI(3)/-1.0 membrane has the potential to be applied in various gas separation processes, especially for the He and H_2 purifications.

5.1.4.3. Literature Comparison

The gas separation properties of Ultem® have been extensively investigated on flat sheet and hollow fibre membranes. However, there have been limited investigations on composite membranes on inorganic substrates because of the low synthesis success rate and a lack of interfacial stability between the polymeric layer and the inorganic substrates. As shown in Table

5-4, compared with other polymeric materials coated on inorganic tubular substrates, our reproducible results well agree with the literature values.

Ogieglo et al. [335] showed that the PIM-6FDA-OH coated on the porous stainless-steel substrates exhibited different gas permeability and permselectivity results compared to bulk PIM-6FDA-OH membranes. The gas permeability of PIM-6FDA-OH decreased owing to collapsing microporosity and structural tightening, resulting in reduced permeability and increased permselectivity. Sazali et al. [121, 133] investigated two types of polyimides (P84 and Matrimid) coatings on the ceramic substrates. The gas permeability and permselectivity of the polyimide membranes were significantly lower than those of the bulk membranes. This suggests that the interface between organic and inorganic materials existed defects or large voids that reduce the membrane performance. Therefore, the intermediate layer coating was employed to reinforce the interface.

In the flat sheet membranes, PEI selective layer demonstrated 1.20-1.48 Barrer with 22-28 ($\alpha_{CO2/N2}$) and 30-37 ($\alpha_{CO2/CH4}$) [18, 234-236, 239, 245, 286]. The membranes followed the classical polymeric membrane trade-off for gas separation. Furthermore, PEI exhibited favourable properties for synthesising hollow fibre membranes for various applications. In our study, we managed to reduce the PEI membrane thickness to less than 40 µm by thrice coating PEI onto the alumina substrates. It can be observed from the PALS results that the 12PEI(3)/-1.0 membrane (D = 4.6 Å) exhibited a smaller pore size compared to the 12PEI(3)/0 membranes (D = 5.5 Å). These results illustrate that the vacuum-assisted dip-coating methodology can be used to tailor PEI membrane pore size, which have not yet been reported for the PEI materials.

Table 5-4. The comparison of flat sheet, hollow fibre and tubular PEI composite membranes for gas separation.

Membrane	Permeability (Barrer)			Permselectivity (α)		Membrane types	Ref.
	P_{CO2}	P_{N2}	P_{CH4}	$\alpha_{CO2/CH4}$	$\alpha_{CO2/N2}$		
PEI (Ultem®)	1.20	0.043	0.032	37.0	27.9	Flat sheet	[245]
PEI (Ultem®)	1.30	0.053	0.035	37.4	24.5	Flat sheet	[286]
PEI (Ultem®)	1.32	0.050	0.040	30.0	26.4	Flat sheet	[234]
PEI (Ultem®)	1.48	0.054	0.040	37.0	27.4	Flat sheet	[18]
PEI (Ultem®)	1.55	0.070	—	—	22.1	Flat sheet	[239]
PEI (Ultem®)	25.7[a]	16.6[a]	13.4[a]	1.91	1.54	Hollow fibre	[156]
PEI (Ultem®)	1.40	0.046	—	—	30.4	Hollow fibre	[249]
PIM-6FDA-OH	25.8[a]	0.90[a]	0.4[a]	64.5	28.7	Composite Tubular	[335]
PI (P84)	1.13[a]	0.70[a]	0.68[a]	1.66	1.61	Composite Tubular	[121]
PI (Matrimid)	6.50	1.00	—	—	6.45	Composite Tubular	[133]
12PEI(3)/-1.0	3.86	0.218	0.177	20.5	21.9	Composite Tubular	This work

[a] The gas data was provided as gas permeance unit (GPU).

5.1.5. Conclusion

A systematic study of vacuum-assist dip-coating processes was carried out to investigate the dip coating and vacuum pressure parameters for PEI composite tubular membranes. Based on the results of the dope concentration, layer, and vacuum-assisted deposition conditions, 12 wt.% PEI coated on the alumina tube can form dense membranes to separate a range of small gases with reasonable permselectivities. Under the best conditions, 12PEI(3)/-1.0 membrane demonstrated excellent pore aperture size of 4.64 ± 0.1 Å, suggesting that the pore size is finely tuned for light gas separation applications. Furthermore, no previous studies have demonstrated that composite PEI membrane can maintain the same permselectivity results as the bulk PEI membranes whilst achieving remarkable gas permeability. This study demonstrates the feasibility of a vacuum-assisted dip-coating process for synthesising a composite PEI tubular membrane for gas separation applications with promising scalability and reproducibility results, which may provide a new pathway for advanced membrane coating technology.

5.2. Residual NMP solvent effect in the PEI composite membranes

Section 5.2 is submitted to Journal of Membrane Science (under review).

5.2.1. Abstract

Controlled n-methyl pyrrolidone (NMP) solvent removal from polymeric membrane manufacturing after the coating process is a crucial step to prepare macroporous membranes via non-solvent induced phase separation, or to prepare dense membranes via solvent evaporation. However, this crucial step has largely been under-emphasized. In order to achieve a pinhole-free and highly stable dense membrane for gas separation applications, it is necessary to fully understand the correlations between the processing conditions and membrane performance as a function of adventitious NMP residue. This study investigated the effect of residual NMP solvent on the physicochemical properties of polyetherimide (PEI) membranes supported on tubular α-alumina substrates. By controlling the drying temperatures (80 to 250 °C), NMP residual concentration in the PEI membrane layer was successfully removed at 195 °C. This finding suggests that the membrane film consolidation temperature can be lower than both the NMP boiling point (202 °C) and the PEI glass-transition temperature (215 °C) to effectively remove the solvent from the membrane coated film. In the single gas permeation results, the membrane dried at 80 °C with a 12% of NMP residue demonstrated 350% and 460% enhancements of N_2 and CH_4 diffusion coefficients, respectively, yet gas permselectivity was 30-60% lower than those of the completely dried membrane at 195 °C. In contrast, the CO_2 diffusion coefficient results were comparable, which is likely due to the high NMP-CO_2 affinity from polar-polar interactions. Furthermore, the membrane dried at 195 °C achieved the highest H_2 permeance of $2.1 \times 10^{-10} \pm 2.2 \times 10^{-11}$ mol m^{-2} s^{-1} Pa^{-1}, yielding a H_2/CH_4 permselectivity of 243 ± 23 and a CO_2/CH_4 of 31.9 ± 3.1. By systematically studying the thermal-induced evaporation of NMP in the film drying process, it was found a strong correlation between the

concentration of NMP residue and gas separation properties to further improve PEI membrane separation performance.

5.2.2. Introduction

Gas separation membrane technology for gas sweetening and purification processes is a competitive technology in terms of cost, performance, footprint, and safety over the traditional pressure-swing solvent absorption and cryogenic absorption technologies [24, 336, 337]. Over the past few decades, the processing strategy of designing polymeric membrane microstructure to control the free volume and pore texture of the membranes for gas separation has become very sophisticated [235, 307, 338]. To prepare nonporous thin film of gas separation membranes (0.5 to 50 μm in thickness), a number of phase separation methods are typically considered, namely non-solvent-induced phase separation (NIPS) [339, 340], thermally-induced phase separation (TIPS) [233, 341], vapour-induced phase separation (VIPS) [342, 343], and solvent evaporation [344, 345]. In all these methods, solvents are utilised to improve the polymer processability to prepare a dope solution and allow solvent exchanges or evaporation to alter the membrane morphology [346]. Typically, NIPS, TIPS and VIPS processes take place in a non-solvent to induce the membrane phase separation to create a thin-selective layer with a microporous structure [347]. During the phase separation process, the solvent is removed via solvent exchange from the membrane bulk within short periods [348-350]. These phase-induced separation processes may also create a macroporous structure on the selective layer leading to Knudson flow regime, which is not ideal for gas separation applications [52, 351].

The solvent evaporation involves a specific thermal treatment regime typically with a predetermined temperature profile at a constant holding temperature that overcomes vapour pressure of the solvent (boiling point). This process facilitates solvent evaporation from the wet polymer aiming to completely remove the solvent [344, 345]. Solvent evaporation is commonly employed to prepare dense membranes for gas separation research applications.

However, numerous reports have found a small quantity of solvent may still remain entrapped within the polymer chain even long after the membrane has solidified via the solvent evaporation process, and thus induces membrane plasticization and physical aging [352-354]. For example, Fu et al. [353] demonstrated the dichloromethane residual in the polyimide membranes altered the membrane microstructure, mechanical strength and gas transport properties. The higher amount of dichloromethane maintained in the membrane bulk, the larger the free-volume holes which lead to a two-fold increase in the O_2 permeability from 1.99 Barrer (0.87 wt.% dichloromethane content) to 3.98 Barrer (3.7 wt.%). Macchione et al. [355] investigated the impact of residual perfluoropolyether (Galden HT 55) solvent in Hyflon® AD60X amorphous perfluoropolymer membranes prepared at room temperature and 200 °C drying temperature for gas CO_2/N_2 separation. The CO_2/N_2 permselectivity of perfluoropolymer membranes increased from 5.5 (room temperature) to 8.1 (200 °C) suggesting that the presence of residual solvent increased the diffusivity of nitrogen but no mechanism was illustrated. Another study showed that residual solvent may enhance the gas permselectivity. Joly et al. [354] investigated five commercial solvents, including *N*-methyl-2-pyrrolidone (NMP), *N*-*N*-dimethyl acetamide (DMAc), tetrahydrofurane (THF), 1,4-dioxane and dichloromethane (CH_2Cl_2), on the gas separation properties of 6FDA-mPDA polyimide membranes using CO_2/N_2 permselectivity as a performance measure. DMAc possessed the most significant impact on the membrane transport properties. The residual DMAc solvent was found between 4.5 and 0.95 wt.% in the membranes prepared via a shorter (90 min) and a longer (48 h) drying processes at 200 °C, respectively. For the membranes ladened with 4.5 wt.% DMAc compared to 0.95 wt.% DMAc, the CO_2 and N_2 gas permeabilities decreased by 25% and 70% while CO_2/N_2 permselectivity increased from 22.7 to 31.7, respectively. This indicated that DMAc removal increased the CO_2 and N_2 solubilities by approximately 27% and 200%, respectively. This was attributed by the imprint provided by DMAc, which affected polyimide membrane separation performance.

Overall, a literature analysis of the gas permeability for membranes concludes that solvent residue causes membrane plasticisation, which leads to a loss of separation performance. However, for dense thin membranes in tubular configuration obtained by solvent evaporation, the properties of selective layer as a function of residual solvent amount for tubular PEI membranes could have very different effect as opposed to the flat sheet films. In this study, we investigated a series of polyetherimide (PEI) membranes on tubular α-alumina ceramic substrate prepared by a custom-designed, vacuum-assisted, dip-coating technique, followed by solvent evaporation as a function of drying temperature (80 – 250 °C) to regulate the removal of NMP. The tubular PEI membranes were examined via in-line coupled TGA-FTIR, DSC, XRD, SEM-EDS, and single gas permeation to systematically correlate the physicochemical properties with the molecular sieving gas separation properties as a function of solvent residue.

5.2.3. Methodology

Following the previous section, the effect of residual solvent in the PEI composite membranes was investigated under the optimal conditions established in section 6.1. As shown in Fig. 5-6, the experimental procedure for this section is illustrated in the corresponding flow diagram.

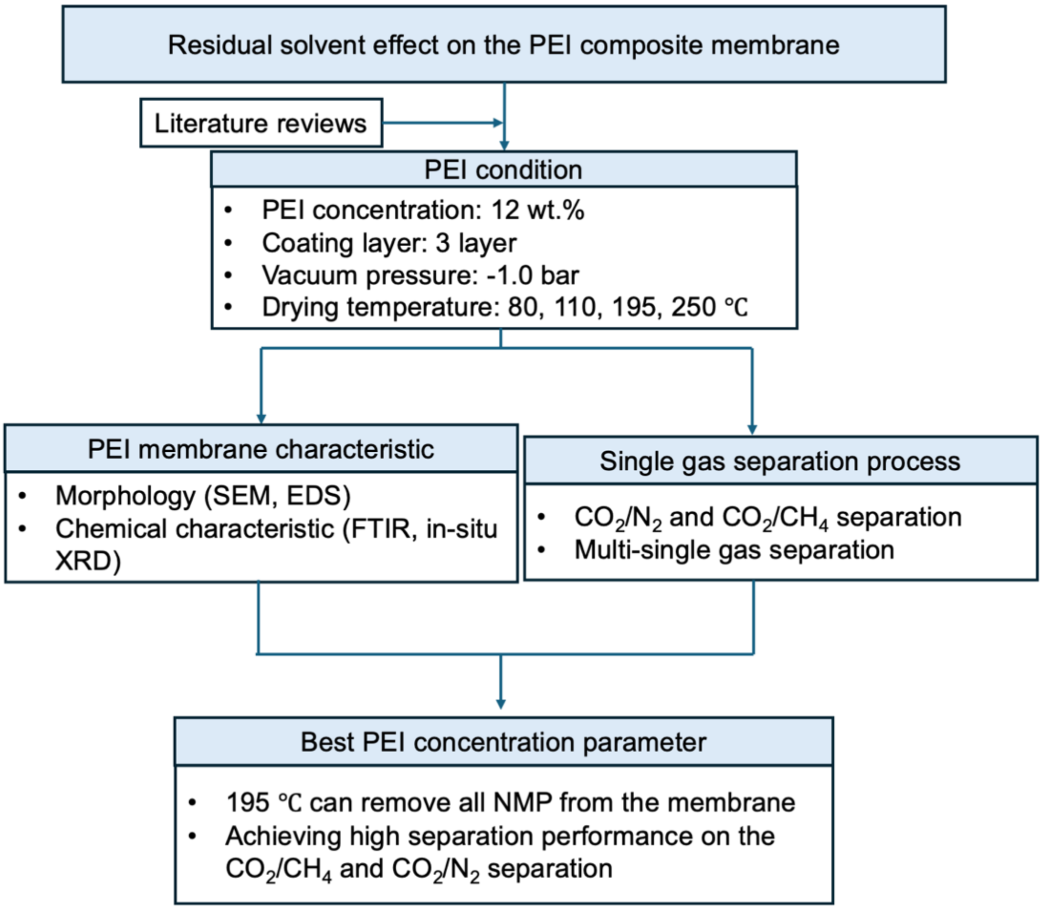

Fig. 5-6. The flow chart of the experimental setup for the residue NMP effect in PEI membranes.

5.2.4. Results

5.2.4.1. Membrane Material Characterisation

5.2.4.1.1 Residual solvent effect

The mass loss in the membranes and virgin PEI polymer was studied using thermogravimetric analysis to determine if drying temperature (80 – 250 ℃) could regulate the amount of NMP residue in the membranes. Fig. 5-7 presents the weight loss of membranes prepared under different drying temperatures, highlighting the variations in residual NMP composition as a function of drying conditions. As shown in Fig. 5-7(a), the mass loss of the membrane samples and the virgin PEI polymer produced two distinct thermal decomposition stages between 80 ℃ and 650 ℃ in N_2 atmosphere. The first stage consists of solvent evaporation at 120 – 250 ℃ followed by PEI thermal decomposition at 450 – 550 ℃ [354, 356-358]. As can be seen in the percentage weight loss, NMP residual amount is significantly greater in samples prepared at lower drying temperature such that 11.8 wt.% of NMP was found in the 80 °C sample (PEI_80), 5.1 wt.% in the 110 °C sample (PEI_110), and near 0% in the 195 °C (PEI_195) and 250 °C (PEI_250) samples. Notably, PEI_195 sample was able to achieve near 100% of NMP removal as the weight loss is indifferent to that of the PEI_250 sample and the virgin PEI_bulk. At around 650 °C, when air was introduced as the atmosphere, a third mass loss stage was observed to be attributed to oxidative thermal decomposition of the PEI material for the whole series.

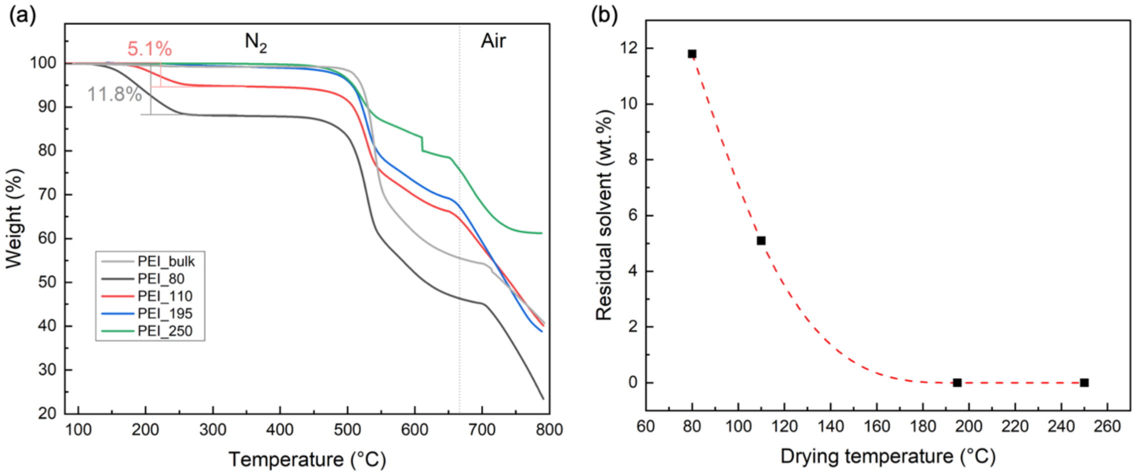

Fig. 5-7. TGA analysis of the PEI membrane samples and virgin PEI bulk showing (a) weight loss profile and (b) residual NMP solvent by differential sample weight between 80 °C and 300 °C as a function of drying temperature used to prepare the tubular PEI membranes.

Fig. 5-7(b) shows the percentage of mass loss between 80 °C and 300 °C attributed to the mass of the residual NMP solvent removed from the samples. Considering that the boiling point of NMP occurs at approximately 202 °C [354, 359], the result signifies that we can use a slightly lower temperature than the NMP's boiling point to reach a complete removal of the solvent to yield a dried membrane film on the tubular substrate as demonstrated by PEI_195. This phenomenon may be attributed to the thin-film geometry enabled by vacuum assisted dip-coating to produce a thin PEI layer that is conducive to fast vaporisation of the solvent during the drying process [360].

Further thermo-chemical analysis of the membrane samples was conducted using TGA-FTIR for in-line detection of the vaporised NMP organics and other volatile by-products emitted in the gas phase during thermal decomposition. As shown in Fig. 5-8, the FTIR spectra of the volatile compounds in the gas phase released from the membrane samples (PEI_110, PEI_195, and PEI_250) were tracked as a function of TGA temperature from 40 to 400 °C. Firstly, there are several characteristic stretching vibrations that appear to be relatively stable throughout the temperature range, namely 1600 cm^{-1}, 2300 cm^{-1}, and 3500 – 4000 cm^{-1}. These are attributed to the presence of adventitious water adsorption and CO_2 absorption within the membrane bulk [361]. Comparatively, the presence of the water peaks (1600 cm^{-1}, 3500 – 4000 cm^{-1}) is much reduced in the PEI_195 sample (Fig. 5-8b) whilst the relative CO_2 peak (2300 cm^{-1}) was larger in intensity, of which it diminished in the PEI_250 sample (Fig. 5-8c).

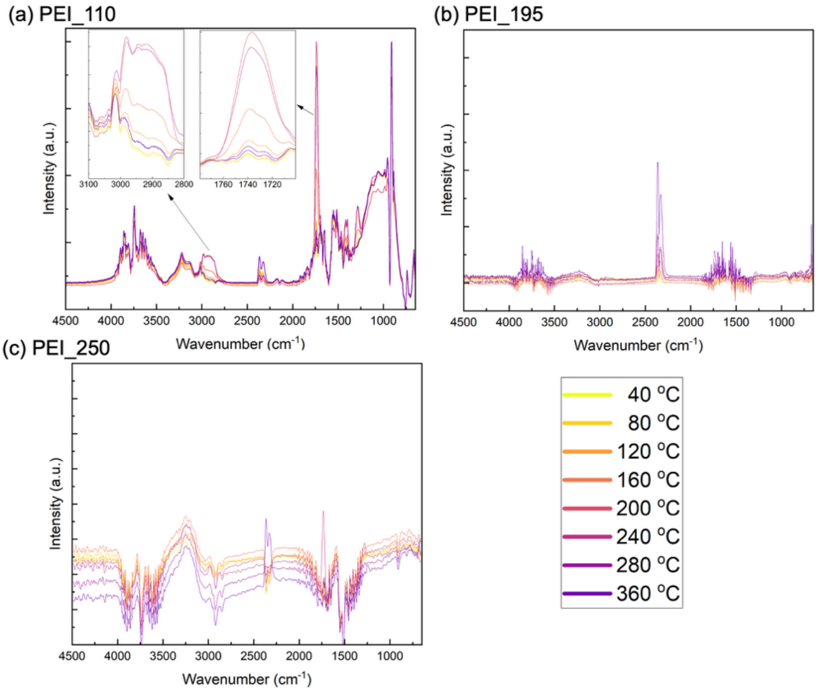

Fig. 5-8. The FTIR spectra of the volatile products evolved during the TGA-FTIR analysis of the (a) PEI_110, (b) PEI_195 and (c) PEI_250 membrane samples.

Fig. 5-8(a) shows the FTIR spectrum of the volatile products for the PEI_110 sample, for which it was found to have contained 5.1 wt.% of NMP solvent (Fig. 1(b)). Several significant peak changes occur during the thermal decomposition between 40 °C and 360 °C. Firstly, the peaks at 1740 cm^{-1}, 2915 cm^{-1}, and 2980 cm^{-1} attributed to respective stretching vibrations of the C=O, CH_2 and CH_3 groups of the NMP can clearly be seen to change in concert with increasing temperature [362, 363]. Specifically, as shown in the inset images of Fig. 5-8(a), a broad shoulder peak that lies in the 2900 – 3100 cm^{-1} region attributed to the asymmetric CH_2 and CH_3 stretching vibrations and the strong intense C=O peak centered at 1740 cm^{-1} belonging to the NMP structure distinctly increased from 120 °C reaching to a maximum intensity near 200 °C, after which is followed by a sharp disappearance at 280 °C. As evidenced from the TGA-FTIR results, the removal of NMP occurred within the temperature range between 120 °C and 280 °C over a short course of approximately 16 min governed by the ramping rate (10 °C min^{-1}).

As shown in Fig. 5-8(b) and 5-8(c), there are no characteristic peaks attributed to the NMP that could be detected in the PEI_195 and PEI_250 samples by the gas phase FTIR during the TGA analysis. This observation clearly demonstrates that the NMP solvent residue is completely removed and thus absent from the PEI membranes during the solvent evaporation process at 195 °C and 250 °C, which also corroborates the TGA findings (Fig. 5-7).

To further confirm the presence of NMP residue in the membranes, ATR-FTIR analysis was performed. For brevity, PEI_110 and PEI_195 were selected to represent the change of the membrane chemistry after SEPS. At outset, both spectra were normalised using the peak at 710 cm^{-1}, which was observed to be the most consistent and prominent across all spectra, and in accordance with previously established normalisation methods for PEI [326, 327]. As shown in Fig. 5-9, three specific peaks (2970, 2920, and 2870 cm^{-1}) are attributed to the C-H stretching of propylidene groups in the PEI bulk [326, 327]. The peaks observed at 1776 cm^{-1} and 1715 cm^{-1} are assigned to the asymmetric and symmetric stretching vibrations of the C=O bond, and the asymmetric and aromatic stretching vibrations of the C=C bond are observed at 1598 cm^{-1} and 1475 cm^{-1}, respectively [364]. C-N bonding is linked to the peaks detected at 1350 cm^{-1} and 740 cm^{-1} [364]. Additionally, the peaks at 1264 cm^{-1} and 1100 cm^{-1} are attributed to aryl (Ar) ether bonds [365]. These distinctive peaks are related to the PEI backbone structure.

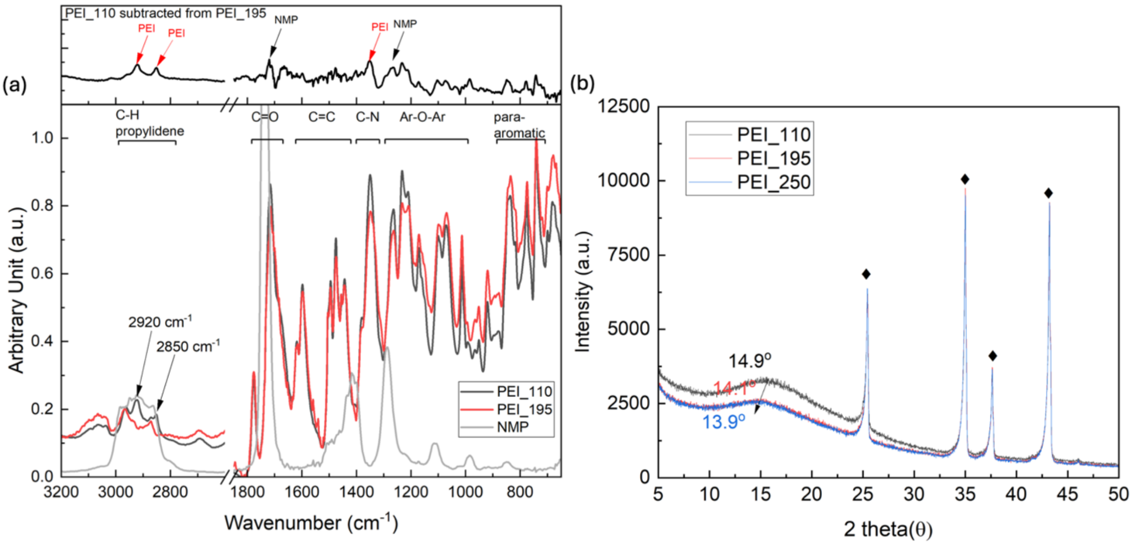

Fig. 5-9. The ATR-FTIR analysis for the PEI_110, PEI_195 and the subtraction between both membranes. The ATR-FTIR spectrum of the NMP was extracted from the database of the National Institute of Standards and Technology [366].

To distinguish the residual NMP from the PEI_110, a subtraction between PEI_110 and PEI_195 was applied to evaluate the peak differences. In the subtracted spectrum, two distinct positive peaks located at 1716 cm^{-1} and 1267 cm^{-1} are attributed to the stretching vibrations of C=O bonds and pyrrolidinone of the residual NMP in the PEI_110, respectively. Interestingly, additional peaks at 1350, 2920, and 2850 cm^{-1} are also observed in the difference spectrum.

The peak at 1350 cm^{-1} may be attributed to strongly with polar amide and imide groups of PEI through dipole-dipole interactions and weak hydrogen bonding interactions between PEI and NMP molecules, which could affect the polymer chain arrangement, as also reflected in the C–H stretching bands at 2920 cm^{-1} and 2850 cm^{-1}. We postulate that NMP residue in the PEI membrane can result in some degree of bond vibrational perturbations of associated functional groups in the polymer backbone. The conjecture is also observed in the XRD analyses (Fig. 5-9b), which show the broad peak centred at 14.1° 2θ characteristic of the amorphous structure of PEI membrane experienced a peak shift to 13.2° 2θ in the presence of the NMP residue.

The thermal transition of the PEI polymer was examined by DSC, which is expected to be very different in the presence of the NMP residue. As shown in Fig. 5-10(a), both the 1st and 2nd heating cycles show the T_g of the virgin PEI bulk is located at 211 °C (1st heating) and 217 °C (2nd heating), [131, 204]. In contrast, PEI_110 sample in Fig 4(b) shows two broad transitions at 142 °C and 195 °C in the 1st heating cycle, suggesting that there are two stages of thermal transitions during the release of NMP from the polymer matrix. It seems there is a relatively faster heat release at around 142 °C followed by a relatively longer and larger release around 195 °C reaching to a minimum of heat flow at 220 °C. These results are congruous with the NMP volatile product detected in the TGA-FTIR. Due to the presence of NMP, the T_g of the PEI_110 sample was not evidenced in the 1st heating cycle. In fact, T_g of the PEI_110 sample only appeared in the 2nd heating cycle at 216 °C free from the NMP residue. Interestingly, during the 1st cooling cycle, the T_g of PEI was observed at ~208 °C. Unsurprisingly, the DSC of PEI_250 sample (Fig. 5-10c) shows the T_g appear at 214 °C (1st heating) and 216 °C (2nd heating). These results again mirror the T_g transition observed in the 2nd heating cycles of the virgin PEI_bulk (Fig. 5-10a) and PEI_110 (Fig. 5-10b), indicating that there is no NMP residue in the PEI_bulk, PEI_110 after 1st heating/cooling, and PEI_195 sample. This finding provided crucial evidence that SEPS process using 195 °C is sufficient to remove all the NMP solvent residue off the PEI membrane film.

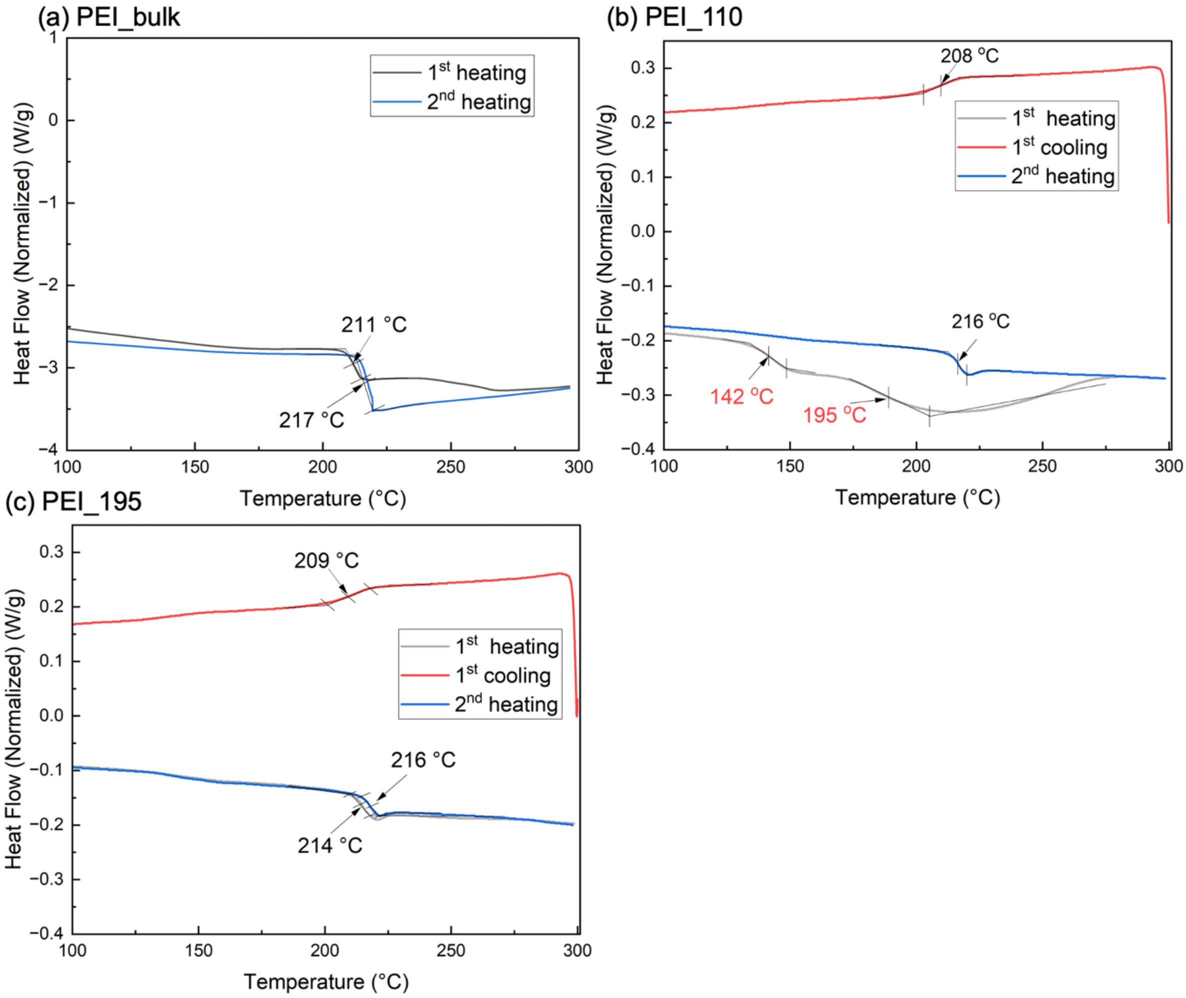

Fig. 5-10. The DSC analysis for the (a) PEI_bulk, (b) PEI_110, and (c) PEI_195 membranes.

5.2.4.1.2 Membrane morphology

Cross-sectional images of the PEI membranes were obtained by SEM and the elemental distribution was collected by EDS. All PEI membranes, apart from PEI_80, appear to possess a clear boundary between a top layer and a macroporous substrate. Fig. 5-11(a) shows PEI_80 cross-section has a significant amount of alumina in the PEI top layer. Following 80 °C solvent evaporation temperature, the membrane was expected to be still wet with NMP and thus not fully dried as TGA shows there was still 11.8 wt.% of NMP remained in the polymer matrix.

This semi-wet polymer is expected to relax and infiltrate into the macropores of the alumina substrate forming an inhomogeneous composite layer as portrayed by the heterogeneous distribution of the carbon and aluminium in the image. This composite layer is measured on average of 29.8 ± 1.4 μm. Also, it can be seen in Fig. 5(a), the composite layer of PEI_80 possessed a large number of voids unfilled by the PEI throughout the top section. This finding is consistent with previous studies that demonstrated that NMP residue significantly lowers membrane quality, causes macrovoid formation and increases overall free volume [353, 367].

In contrast, PEI_110, PEI_195, and PEI_250 membrane's cross sections illustrate a relatively dense, macrovoid-free, PEI top layer. For these membranes, EDS imaging shows that the top layer consistently comprises of the element carbon with a PEI top layer thickness ranging from 24.6 ± 3.2 (PEI_110), 19.0 ± 2.3 (PEI_195) to 17.3 ± 0.4 μm (PEI_250). As polymer concentration and packing density increase upon the removal of the NMP, the PEI top layer thickness decreases, which trended sensibly with the increasing SEPS temperature in this study.

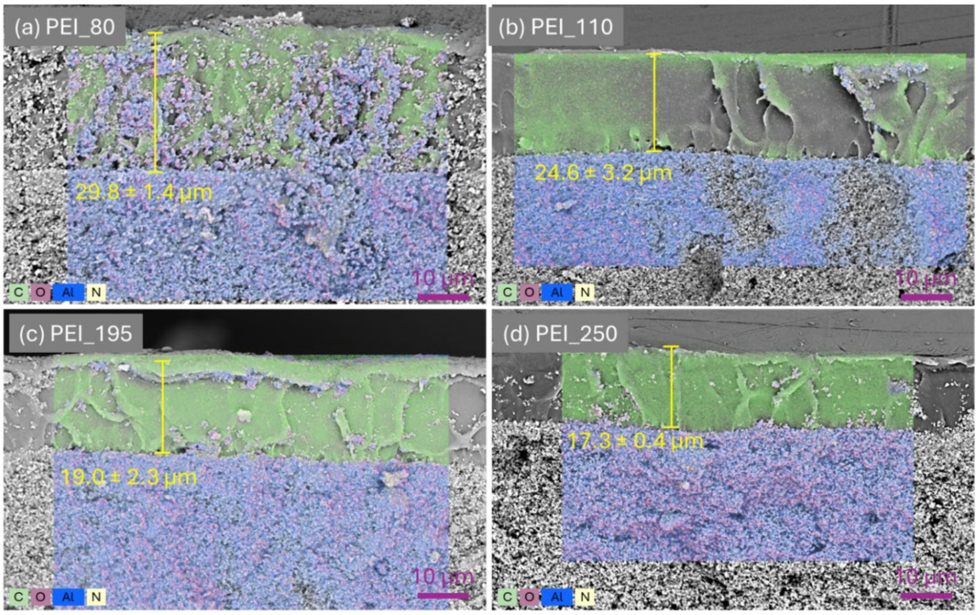

Fig. 5-11. The cross-sectional morphology with EDS mapping for the composite membrane, (a) PEI_80, (b) PEI_110, (c) PEI_195, and (d) PEI_250. All membranes were examined under

5000x magnification for EDS analysis. The colour of each atom detected was as follows: C (green), O (purple), Al (blue) and N (light yellow).

5.2.4.2. Residual NMP effect on the gas permeation behaviour

A number of small gases with kinetic diameters of < 3.8 Å were selected to probe the membrane sieving property and gas transport behaviour for the PEI membranes prepared by 80, 110, 195 and 250 °C solvent evaporation process. As shown in Fig. 5-12(a), the hydrogen gas permeance decreased as the residual NMP amount increased, with PEI_195 exhibiting the highest H_2 permeance of $2.1 \times 10^{-10} \pm 2.2 \times 10^{-11}$ mol m^{-2} s^{-1} Pa^{-1}, followed by PEI_250 ($1.6 \times 10^{-10} \pm 2.4 \times 10^{-12}$ mol m^{-2} s^{-1} Pa^{-1}). Similarly, the hydrogen permeances of the PEI_110 and PEI_80 membranes are approximately 49 % and 54 % lower than that of the PEI_195, indicating that the residual NMP negatively impacted on the hydrogen gas permeance. In contrast, both the PEI_110 and PEI_80 membranes with a residual amount of NMP demonstrated gas permeance enhancement for the larger sized gases such as CO_2, N_2 and CH_4. The CO_2, N_2, and CH_4 gas permeances of PEI_80 membrane were $3.3 \times 10^{-11} \pm 2.7 \times 10^{-12}$, $2.0 \times 10^{-12} \pm 6.0 \times 10^{-13}$, and $2.1 \times 10^{-12} \pm 1.6 \times 10^{-13}$ mol m^{-2} s^{-1} Pa^{-1}, respectively. The presence of 11.8 wt.% NMP in the PEI_80 membrane resulted in an increase of gas permeances of 30% CO_2, 46% N_2, and 181% CH_4 compared to the PEI_250. The gas permeance enhancement is mirrored by the PEI_110 (5.1 wt% NMP) membrane with enhancement values of 42% CO_2, 18% N_2, and 138% CH_4 compared to the PEI_250. However, both PEI_195 and PEI_250 (with negligible NMP) had very comparable gas permeance values without any significant differences for each gas type.

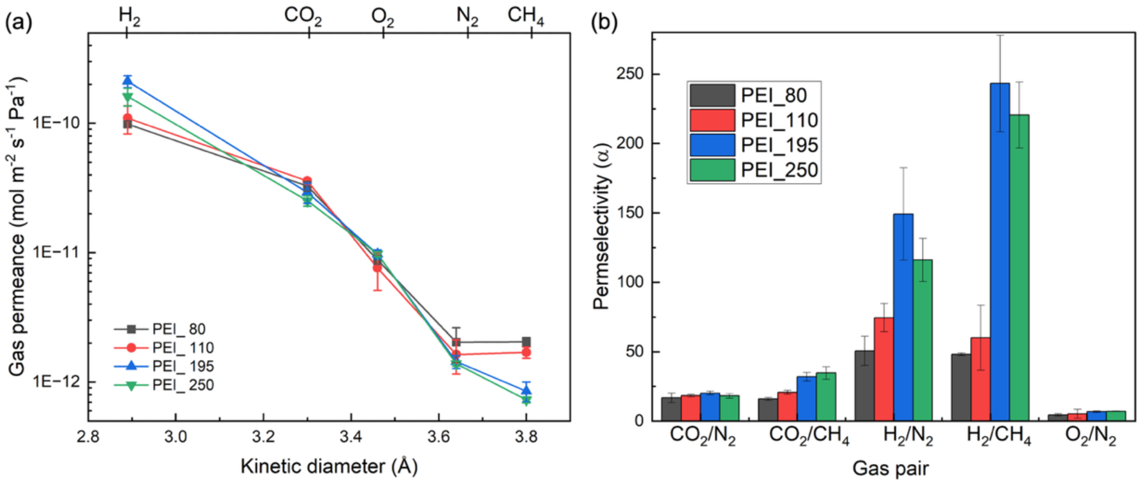

Fig. 5-12. Single gas permeation performance of PEI membrane prepared by 80, 110, 195, and 250 ℃ drying temperature. (a) The single gas permeance and (b) the permselectivities of selected gas pairs

Fig. 5-12(b) shows the permselectivity of CO_2/N_2, CO_2/CH_4, H_2/N_2, H_2/CH_4 and O_2/N_2 gas pairs. PEI_80 produced comparable CO_2/N_2 and CO_2/CH_4 of 16.7 ± 3.4 and 16.0 ± 1.1, respectively. As the drying temperature increased, the same gas pairs reached 20.2 ± 1.3 CO_2/N_2 and 31.9 ± 3.1 CO_2/CH_4 for PEI_195, and the same permselectivities are not so dissimilar for PEI_250. Moreover, PEI_195 membranes produced H_2/CH_4 permselectivity of 243 ± 34, which was approximately 5-fold larger than that of PEI_80 (48 ± 0.9), and approximately 4-fold larger than that of PEI_110 (60 ± 23). The O_2/N_2 permselectivity showed similar trend to other gas pairs. The maximum O_2/N_2 permselectivity was 7.0 ± 0.3 by PEI_250 was, which is 56% higher than that of PEI_80 (4.5 ± 0.9). All gas pair permselectivities increased with increasing drying temperature, indicating that the removal of NMP was highly desirable as the separation factors all improved between the small kinetic diameter gases (H_2, CO_2, and O_2) and the larger kinetic diameter gases (N_2 and CH_4). Furthermore, the diffusivity and solubility of all membranes were calculated and compared with the PEI references, it did not show a clear trend due to the methodology is different in various research team. That is hard to compare with a clear performance of the NMP effect in the diffusivities and solubilities of PEI membranes.

5.2.5. Conclusion

The present study investigated the effect of NMP residue on the physico-chemical properties, morphology and the gas transport behaviour of PEI supported membranes as a function of solvent evaporation phase separation temperature between 80 °C and 250 °C. Unequivocally, NMP molecules and PEI have strong hydrogen bonding with the C-N groups in the polymer backbones, affecting several characteristic stretching vibrations of the neighbouring groups and further increasing polymer free volume in the membrane. Furthermore, single gas permeation tests demonstrated that with an approximately 5% of NMP residue, the CO_2, N_2, and CH_4 permeances of PEI_110 membrane increased by 42%, 18%, and 138%, respectively, compared to the NMP-free membranes (PEI_195 and PEI_250). Consequently CO_2/CH_4 permselectivity was lowered by 41%. This effect is attributed to the steric hinderance of NMP reducing the adsorption on the polymer chain and further accentuating the trade-off between diffusivity and solubility for non-adsorbing gases (N_2, and CH_4). Moreover, the optimal drying temperature for the PEI supported membranes was determined to be 195 °C, which is 7 °C and 20 °C lower than the NMP's boiling point and PEI's glass transition temperature, respectively. Furthermore, it yielded approximately $2.1 \times 10^{-10} \pm 2.2 \times 10^{-11}$ mol m^{-2} s^{-1} Pa^{-1} and $2.9 \times 10^{-11} \pm 5.2 \times 10^{-12}$ mol m^{-2} s^{-1} Pa^{-1} for the H_2 and CO_2 permeances, respectively. The permselectivities of H_2/CH_4 and CO_2/CH_4 were 243 ± 34 and 31.9 ± 3.1, respectively. The findings of this study will further offer insight on the understanding of solvent effects as processing liquid for the manufacturing of high-performance polymeric membranes targeted for small gas separation processes.

5.3. Supporting information

SEM-EDS mapping of the membrane's cross-sectional morphology was examined to investigate polymer infiltration and PEI membrane thickness. **Fig. S3** shows the elemental mapping of the membrane layer series of 12PEI (12 wt.%) membranes. The mapping results of C (purple) and Al (turquoise) atoms are representative of the PEI polymer and alumina substrate distribution. This clearly demonstrates that the membranes formed a top layer on the alumina substrate without any obvious infiltration of PEI polymer into the substrates even with a single coat (12PEI(1)/-1.0). The SEM-EDS result was used to determine the average membrane thickness estimation by measuring the distance from the surface to the interface boundary.

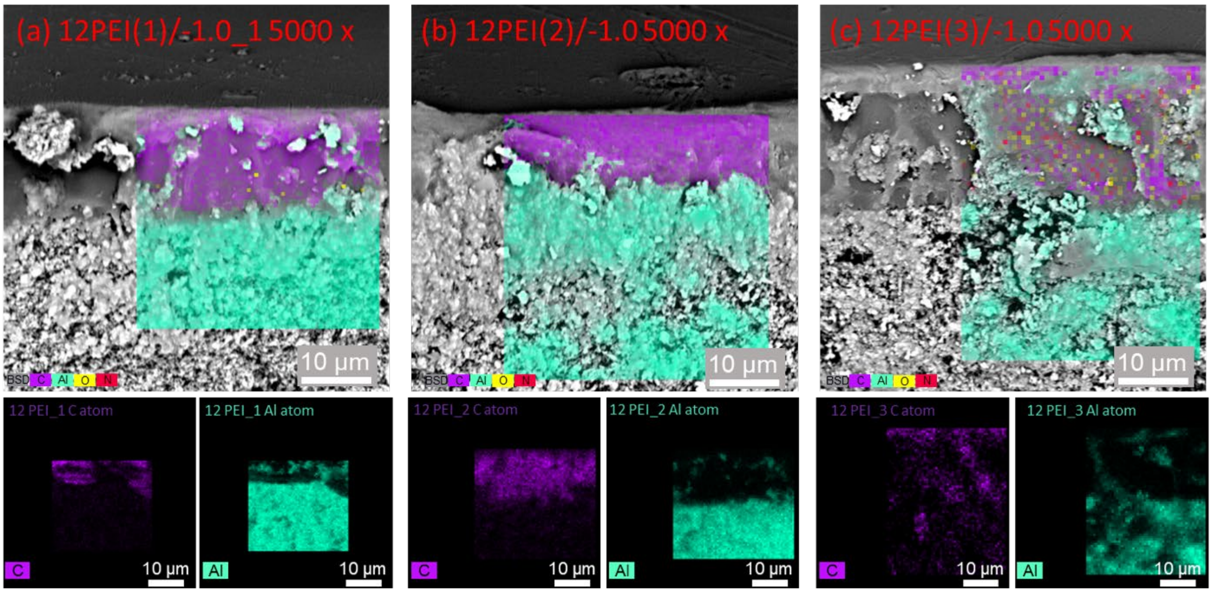

Fig. S5-1. The EDS mapping of cross-section morphology of 12 PEI membranes for the layer series. (a) 12PEI(1)/-1.0, (b) 12PEI(2)/-1.0 and (c) 12PEI(3)/-1.0.

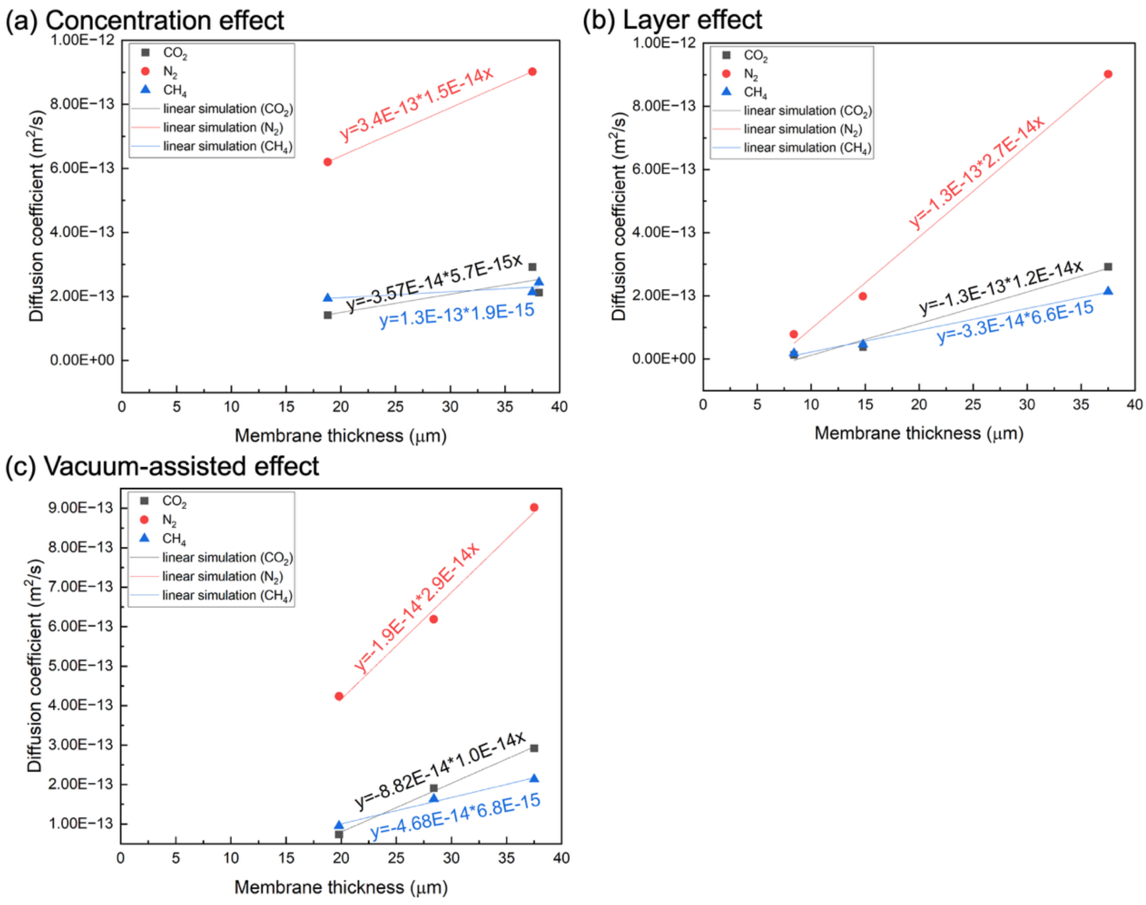

Fig. S5-2. The CO_2, N_2, and CH_4 diffusion coefficient with respective to the membrane thickness for (a) concentration effect, (b) layer effect and (c) vacuum-assisted effect.

Table S5-1. The data comparison of permeability, diffusivity and solubility of PEI membranes.

PEI membrane (Author)	Permeability (Barrer)			Permselectivity ($\alpha_{x/y}$)		Diffusivity (10^{-8} m^2 s^{-1})			Diffusivity selectivity ($\alpha_{x/y}$)		Solubility (10^{-2} cm^3(STP) cm^{-3} cmHg^{-1})			Solubility selectivity ($\alpha_{x/y}$)		Ref
	CO_2	N_2	CH_4	CO_2/N_2	CO_2/CH_4	CO_2	N_2	CH_4	CO_2/N_2	CO_2/CH_4	CO_2	N_2	CH_4	CO_2/N_2	CO_2/CH_4	
BarBari et al.(1988)											0.58	0.16	0.05	3.67	12.03	[368]
Barbari et al. (1988)						1.14	0.57	0.11	1.99	10.1						[369]
Barbari et al. (1989)	1.32		0.04		37.4	0.37		0.04		8.61	2.72		0.63		4.34	[313]
Larocca and pessan(2003)	1.27					0.10					12.9					[60]
Vu et al. (2003)	1.45	0.05	0.04	27.9	35.3	1.04		0.11		9.45	0.70		0.17		4.11	[236]
López-González et al. (2005)	1.55	0.07		22.1		0.14	0.19		0.74		7.32^{a}	0.40^{a}		18.3		[370]
											11.4^{b}	0.37^{b}		30.8		[370]
Takahashi and Paul (2006)	1.32	0.05	0.04		30.0											[234]
Hao et al (2014)	1.48	0.05	0.04	27.4	37.0											[18]
Chirkov et al. (2016)	4.29	0.1	0.13	43	33	0.39	0.37	0.09	1.05	4.33	1100	2.70	14	407	78.6	[371]
Ronova et al (2018)	2.29	0.1	0.03	22.9	79.0	0.39	0.37	0.09	1.05	4.33	5.87	0.27		21.7		[372]
Yanez et al. (2021)	2.1	0.03	0.05	70	42											[373]
Checchetto et al. (2022)	1.17	0.04				0.85	1		0.85		1.38	0.04		34.4		[374]
Yu et al. (2007)	3.65	0.14	0.21	27	17	0.80	1.41	0.30	0.57	4.3	450	9.7	70	46.3	6.42	[375]
Hu et al. (2003)	2.2					2.6					0.63	0.1		6.4		[47]
PEI_80	2.78	0.17	0.17	16.8	16.0	0.12	0.78	2.24	0.16	0.55	23.8	0.23	0.82	106	29.2	This work
PEI_110	2.56	0.12	0.12	18.4	20.8	0.12	0.39	0.09	0.32	1.36	21.1	0.37	1.36	57.9	15.6	
PEI_195	1.59	0.08	0.05	20.2	32.0	0.15	0.18	0.04	0.84	3.50	12.9	0.46	1.21	27.8	10.7	
PEI_250	1.24	0.07	0.04	18.2	34.7	0.09	0.17	0.04	0.56	2.34	17.8	0.60	1.60	28.8	11.7	

[a] This data was measured from sorption device.

[b] This data was calculated from S=P/D

Chapter 6 Biomimetic metal-BBP/PEI mixed matrix membranes

In this chapter, we describe biomimetic materials (BMM) that were synthesised to enhance the gas permeability of PEI membranes by emulating the CO_2 conversion mechanism of carbonic anhydrase (CA). The initial investigation involved doping PEI membranes with varying concentrations of cobalt-based BMM to form a mixed-matrix membrane, thereby enabling the assessment of influence of concentration on performance (Section 6.1). Additionally, the effects of different metal ions (Fe^{2+}, Ni^{2+}, Cu^{2+}, and Zn^{2+}) on the active sites of the BMMs were examined to evaluate the role of the metal bases (Section 6.2). This study aimed to identify the optimal metal ion concentration to effectively mimic CA activity during the gas separation process in PEI membranes.

6.1. Concentration effect of cobalt-based BMM modified PEI composite membrane

6.1.1. Abstract

Biomimetic materials display potential for facilitating the selective transport of specific gases through membrane structures, thereby enhancing overall membrane performance. In this study, a biomimetic material, Co-2,6-bis(2-benzimidazolyl) pyridine (CoBBP), with a structure resembling that of carbonic anhydrase was investigated to improve the H_2 and CO_2 permeability of polymeric membranes. ATR-FTIR and Raman spectroscopy confirmed the successful synthesis on CoBBP. Subsequently, 0.5–10 w/w% of CoBBP were incorporated into PEI membranes to evaluate their gas separation performance. Upon doping with 1 wt.% CoBBP, the H_2 permeability increased by approximately 20%, from 7.7 Barrer to 9.4 Barrer. In addition, the H_2/CH_4 permselectivity improved significantly from 62.9 to 102.2. These results indicate that even a small amount of CoBBP enhanced the diffusion of hydrogen molecules through the

membrane matrix. Furthermore, mixed-gas separation tests under 100% relative humidity revealed that CO_2 permeability doubled within the first 4 h of permeation testing. The CO_2/CH_4 selectivity remained stable for over 24 h. These findings suggest that the addition of CoBBP improves both the performance and efficiency of the polymeric membranes in humid environments by facilitating CO_2 transport through the dense polymer matrix.

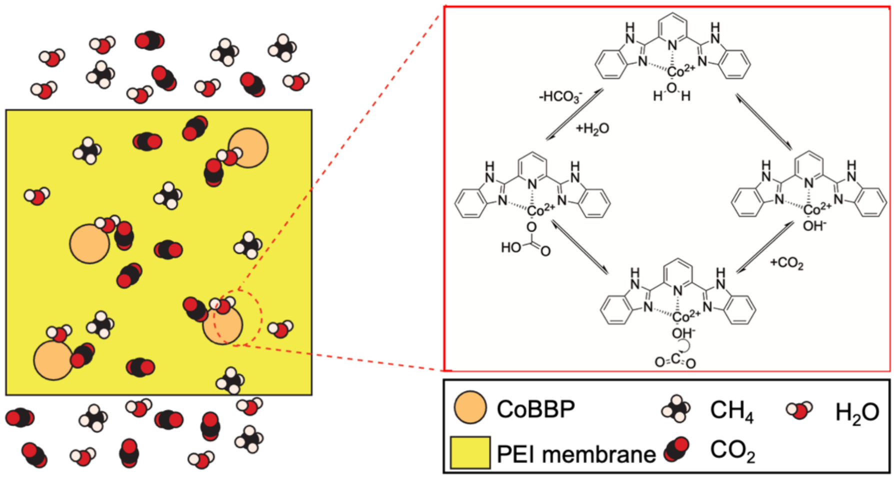

Fig. 6-1. Schematic illustrating the mechanism by which CoBBP membranes facilitate gas separation.

6.1.2. Introduction

Researchers have long been intrigued by biological systems because of their intricate complexity and remarkable efficiency in performing essential functions to sustain life [376]. Recently, increased understanding of molecular structures and their functional mechanisms has inspired the design of materials that mimic specific functional molecules. This biomimetic approach has gained popularity for enhancing gas separation efficiency by replicating the selective transport pathways observed in natural systems [377, 378]. Compared with directly using biological species in-line, replicating their functional structures with synthetic materials avoids limitations related to deactivation in harsh environments [379].

Carbonic anhydrase (CA) is an example of an enzyme that facilitates gaseous transport in biological systems. It is found in natural red blood cells, and facilitates CO_2 through bicarbonate metabolism via a hydration mechanism. Its structure typically comprises a central zinc ion coordinated by three histidine residues and a water molecule [226, 227]. The active site of CA can easily follow the mechanism of $CO_2+H_2O \leftrightharpoons H_2CO_3 \leftrightharpoons HCO_3^-+H^+$ in the pH range of 5-8 [380], as shown in Fig. 6-1. Furthermore, CO_2 conversion can reach a range from 104 to 106 reactions per second, indicating potential for CCS applications [227]. Fu et al. [228] confined bovine CA in oriented Anodisc pore channels (~ 8 nm ID) to create thin water channels for gas separation. CO_2 permeance reached 2600 GPU with CO_2/N_2 selectivity at 788, indicating that bovine CA can transport CO_2 through the membrane bulk with excellent selectivity. However, the operational conditions require careful consideration, as enzyme deactivation and liquid evaporation can damage the membrane. Therefore, a biomimetic material that mimics the CA enzyme must be synthesised to overcome the limitations associated with operation in hazardous environments. Zheng et al. [48] investigated CFA-1, a MOF-based mimic of CA, which enhanced CO_2 permeability and $\alpha CO_2/N_2$ by 9.2 and 2.8 times, respectively, when 3 wt.% was incorporated into Pebax. However, increased loading introduced interfacial defects. Zhang et al. [229] successfully synthesized a cobalt-chelated 2,6-bis(2-benzimidazolyl) pyridine (CoBBP), which structurally mimicked CA enzymes. When blended into a Pebax membrane, CoBBP significantly improved CO_2 permeability (675.5 Barrer) and CO_2/N_2 selectivity (62), attributed to water-facilitated CO_2 transport via hydration mechanisms; the proposed mechanism is shown in Fig. 6-1. However, biomimetic membrane studies to date have not been comprehensively evaluated for gas separation applications and the CO_2 transport mechanism is not well understood. Therefore, developing biomimetic materials compatible with common solvent systems is essential for practical implementation.

In this study, CoBBP (Section 6.1) along with FeBBP, CuBBP, NiBBP, and ZnBBP (Section 6.2) were selected to be incorporated into PEI membranes to examine the effects of biomimetic moieties and metal ion coordination on PEI mix matrix membranes owing to their potential for CO_2 capture and transport of small kinetic diameters target gases (H_2 and CO_2) using single-gas permeation tests and binary gas separation.

6.1.3. Methodology

The materials used in this chapter are listed in Chapter 3, 3.1 Materials. $Co(ClO_4)_2{\cdot}6H_2O$ was chelated with the BBP structure to form the cobalt-based BBP (CoBBP) for further modification. The details of the CoBBP synthesis are described in Section 3.2.3. After successful synthesis, various concentrations of CoBBP were doped into the PEI solution; then, the membrane synthesis process as illustrated in Section 3.2.4, was performed to produce various concentrations of CoBBP doped PEI membranes. The membrane code and corresponding composition are shown in Table 6-1.

Table 6-1. Parameters for CoBBP membrane fabrication.

Membrane code	PEI concentration (wt.%)	NMP concentration (wt.%)	Additive concentration (w/w (PEI).%)
PEI	12	88	-
BBP	12	88	1
0.5CoBBP	12	88	0.5
1CoBBP			1
2.5CoBBP			2.5
5CoBBP			5
10CoBBP			10

The experimental design in Section 6.1 focuses on using different concentrations of CoBBP to establish the effect of concentration on membrane performance and is illustrated in

Fig. 6-2. Characterisation of CoBBP was conducted to evaluate the chemical properties and structure. Additionally, the best CoBBP mixed matrix membrane with the highest permeability and permselectivity was further examined under 100% relative humidity conditions to assess the CO_2/CH_4 separation performance and compare the separation performance with that of PEI and BBP membranes.

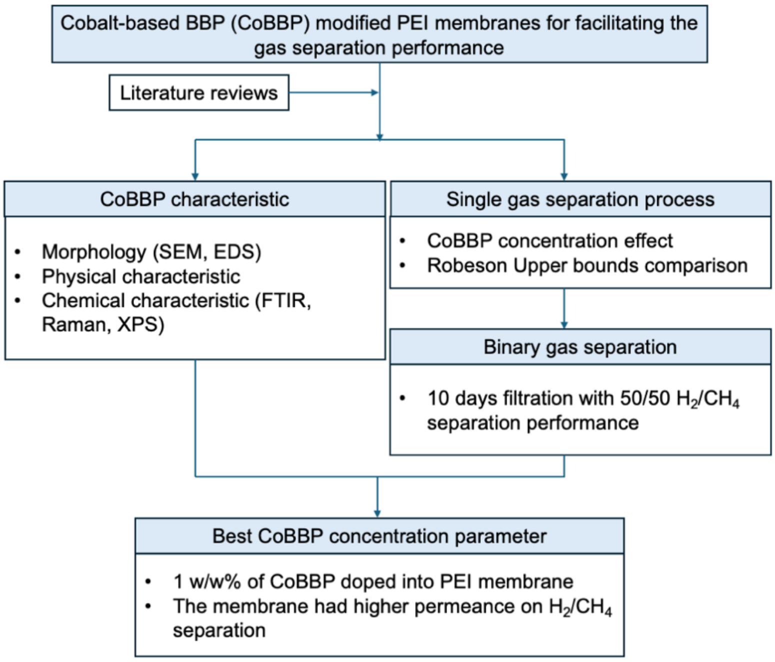

Fig. 6-2. Flow chart of CoBBP modified PEI polymeric membrane investigation with various concentrations.

6.1.4. Results and discussion

6.1.4.1. Characterization of CoBBP

A series of characteristics were used to evaluate the structural variation after chelating the Co ions in BBP. As shown in Fig. 6-3(a) and (b), the morphologies of BBP and CoBBP exhibit significant structural changes. BBP has disordered structural characteristics, whereas CoBBP has a 5-7 μm cubic structure, as indicated by SEM. This observation indicated the structural changes of CoBBP and considerable synthesis changes in its morphology. XPS analysis was used to investigate the surface bonding characteristics of BBP and CoBBP. As shown in Table

6-2, the Co/N atomic ratio was approximately 1:5, because one BBP chemical structure included five N atoms, suggesting that one Co atom might be chelated with one BBP structure (Fig. 6-3(c)). As shown in Fig. 6-3(d), the N_{1s} spectrum of BBP exhibits two characteristic peaks at 398.4 and 400 eV, corresponding to pyridinic and pyrrolic N, respectively. Upon coordination with Co ions, the N_{1s} peak area ratio of pyrrolic to pyridinic N is approximately 1.0, which increases to approximately 3.5 in CoBBP. This shift indicates a selective interaction between Co(II) ions and pyridinic N atoms, resulting in decreased signal intensity for the pyridinic component owing to coordination-driven electron density changes. Furthermore, the high resolution C_{1s} and Co_{2p} spectra was shown in Fig. S6-1, indicated that Co ions exist as divalent Co.

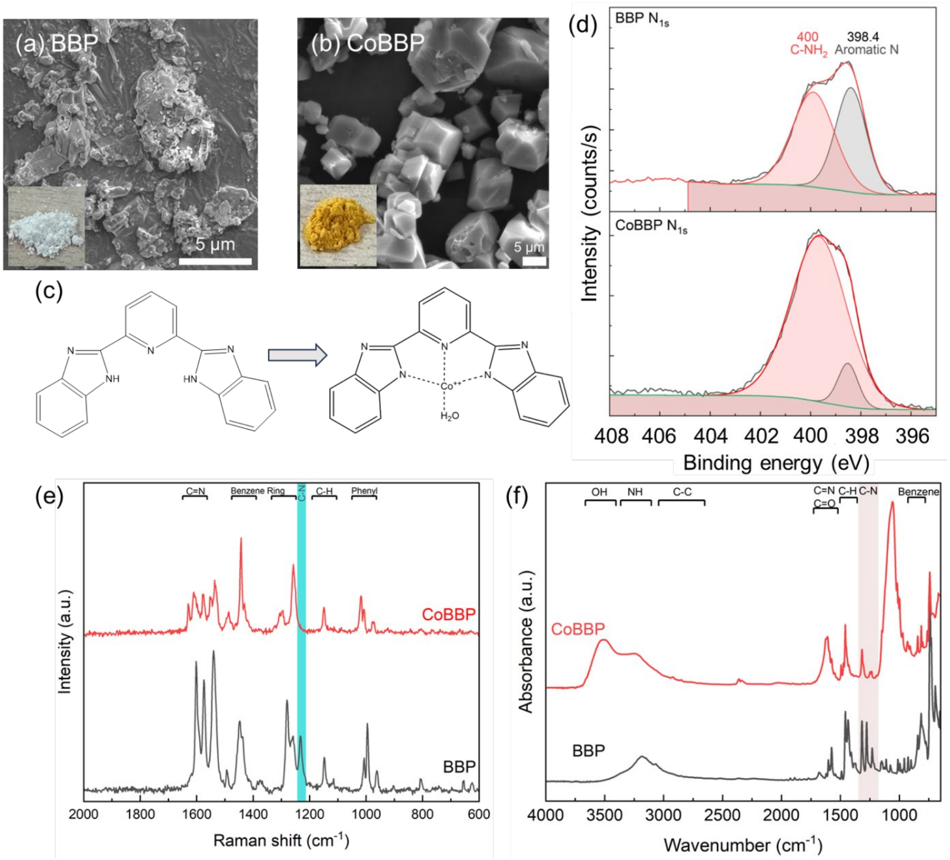

Fig. 6-3. Characteristics of BBP and CoBBP. SEM and digital images of (a) BBP and (b) CoBBP, filmed under 5000× magnification, (c) chemical structure, (d) N_{1s} spectra of XPS analysis, (e) Raman spectrum and (f) FTIR spectrum.

Table 6-2. Atomic results and normalised data for the BBP and CoBBP from XPS analysis.

Raw data	C (atom %)	N (atom %)	O (atom %)	Metal (atom %)
BBP	72.03	27.97		
CoBBP	69.83	9.35	18.86	1.97
Normalised data	**C**	**N**	**O**	**Co**
BBP	12.88	5		
CoBBP	37.34	5	10.09	1.05

Because BBP contains both pyrrolic and pyridinic N atoms within the benzimidazole framework, the specific chelation site of the Co(II) ion must be determined. As shown in Fig. 6-3(e), the Raman spectrum of BBP contains peak attributed to phenyl ring breathing at 1006 cm^{-1} and ring stretching vibrations at 1258 and 1415 cm^{-1}, along with a C–C aliphatic stretching vibration at 1148 cm^{-1}, representing the molecular backbone. The C–N and C=N stretching modes of the benzimidazole moiety appear at 1233 and 1574 cm^{-1}, respectively. In the CoBBP spectrum, the C–N stretching peak disappears while the C=N band remains, indicating that the pyridinic nitrogen probably participates in chelation, thereby reducing its vibrational activity.

FTIR spectroscopy further confirmed the structural modifications (Fig. 6-3(f)). The spectrum of BBP shows peaks at ~740 cm^{-1}, 825 cm^{-1}, 1275 cm^{-1}, and 1460 cm^{-1}, corresponding to δPh(C–H), νC=C, and νC–N vibrations, respectively [381, 382]. Additional bands at 1570 cm^{-1} (νC=N), 3050 cm^{-1} (νC=CH), and 3190 cm^{-1} (νN–H) are also present [383]. Upon Co coordination, several peaks in the FTIR spectrum of CoBBP shift marginally to lower frequencies, indicating complex formation. Notably, two new peaks appear in the CoBBP spectrum at ~1050 cm^{-1} and ~3500 cm^{-1}. The 1050 cm^{-1} peak is attributed to the metal–ligand (Co–N) bond [384], and the broad 3500 cm^{-1} band corresponds to O–H stretching from coordinated water molecules [385]. These results suggest that Co(II) coordinates with three pyridinic N atoms of BBP and one water molecule during complex formation, consistent with the proposed CoBBP structure. The NMR spectra of BBP and CoBBP are shown in Fig. S6-2

6.1.4.2. Membrane Characteristic

The composite membrane morphology was analysed using the SEM with EDS to evaluate the membrane thickness and the CoBBP distribution in the membrane. The cross-sectional SEM images of composite membranes are shown in Fig. S6-3.As show in Fig. 6-4(a-c), the elemental mapping demonstrates a clear organic/inorganic boundary on the interface, and there is no significant polymeric membrane infiltration into the porous alumina substrates. Notably, Co was detected in the 10CoBBP sample at approximately 0.22 wt.%, confirming the successful incorporation of CoBBP into the PEI matrix.

To further investigate the cobalt content, TGA analyses were performed from 40℃ to 800 ℃ under air to assess the residual weight. As shown in Fig. 6-4(d-f), the remaining weight increased from 0% to 26.5% as the CoBBP doping amount increased from 0 to 10 w/w%, indicating a proportional increase in the amounts of Co. Additionally, as the CoBBP content increased from 0 to 1 wt.%, the membrane thickness decreased from 30.5 ± 0.8 μm to 23.6 ± 1.2 μm, due to the higher packing density and densification in the membrane bulk. At 5 wt.% loading, the thickness slightly increased to 25.3 ± 2.1 μm, but no statistical difference with the 1CoBBP membrane was observed (Fig S6-3(c)). However, when the CoBBP content increased further to 10 wt.%, the thickness decreased again to 21.1 ± 0.8 μm, this decrease may be attributed to hindered polymer chain mobility and suppressed film growth at higher filler concentrations [386].

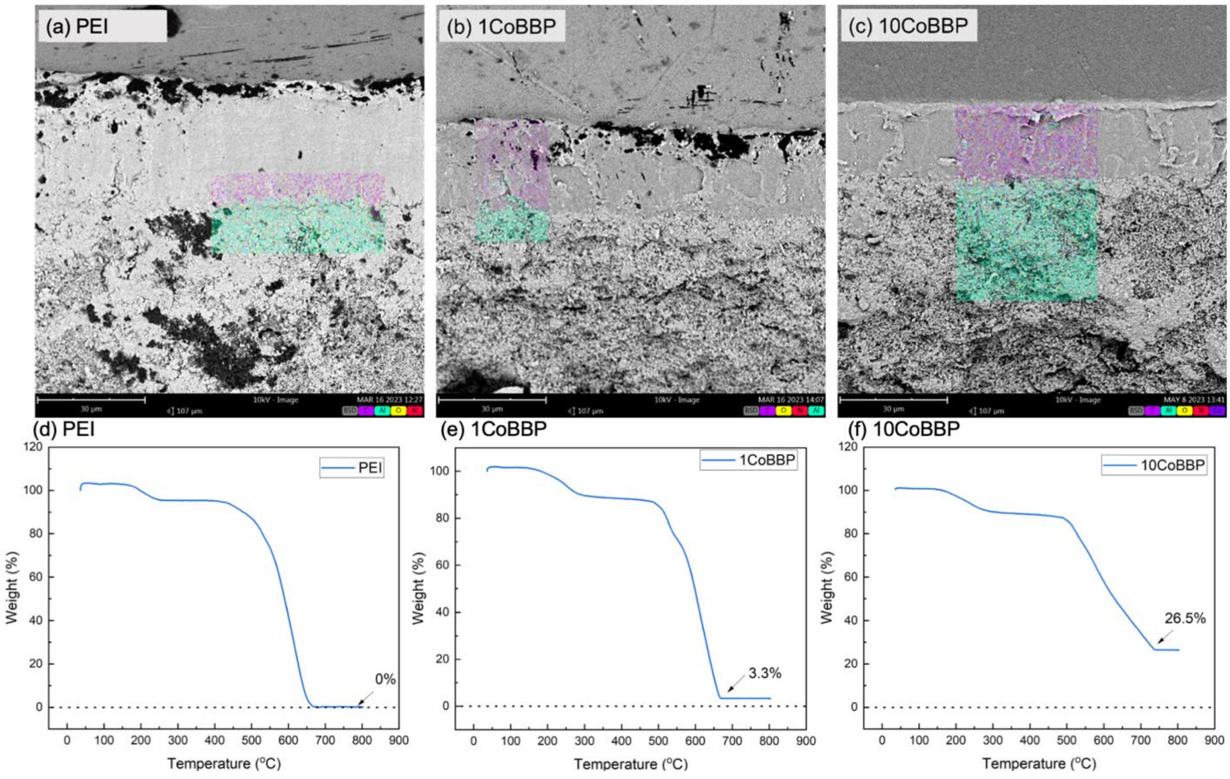

Fig. 6-4. EDS mapping of the cross-sectional images to identify elemental distribution. (a) PEI, (b) 1CoBBP, and (c) 10 CoBBP. The TGA analyse result under air condition for (d) PEI, (e) 1CoBBP and (f) 10CoBBP to investigation the remaining weight of CoBBP.

6.1.4.3. Single Gas Permeation Performance

The single gas permeation test for all membranes was performed using the customable single-gas permeation system at 35 °C and 3 absolute bars. As shown in Fig. 6-5, the gas permeance and the permselectivity of membranes can evaluate the additive performance for the PEI membrane in various gas separation performance. As shown in Fig. 6-5(a), the PEI membrane exhibited H_2, CO_2, and N_2 permeances of $1.25 \times 10^{-10} \pm 5 \times 10^{-12}$ mol m^{-2} s^{-1} Pa^{-1}, $3.59 \times 10^{-11} \pm 1.3 \times 10^{-12}$ mol m^{-2} s^{-1} Pa^{-1}, and $1.64 \times 10^{-12} \pm 5 \times 10^{-13}$ mol m^{-2} s^{-1} Pa^{-1}, respectively. Incorporating 1 wt. % BBP into the PEI membranes (BBP) led to a 25% and 68% decrease in H_2 and CO_2 permeance, respectively. N_2 permeance remained within the same range. This observation suggests that BBP may selectively adsorb smaller gas molecules such as H_2 and

CO_2, limiting their transport through the membrane. The 1CoBBP membrane had a 51% higher H_2 permeance and nearly double the CO_2 permeance ($3.68 \times 10^{-11} \pm 3.4 \times 10^{-12}$ mol m^{-2} s^{-1} Pa^{-1}) when compared with that of the BBP membranes.

The effect of CoBBP concentration on gas permeation was systematically evaluated. At lower loadings, CoBBP resulted in gas permeance values comparable to or slightly higher than those of the PEI membrane. The highest H_2 permeance was observed at 0.5CoBBP, reaching $(1.59 \pm 0.08) \times 10^{-11}$ mol m^{-2} s^{-1} Pa^{-1}, representing an approximate 27% increase relative to that of the PEI membranes. However, a progressive decline in permeance was observed with increasing CoBBP content. At 1CoBBP, hydrogen permeance decreased by approximately 13% compared with that of the 0.5CoBBP membrane and further decreased to $(1.10 \pm 0.04) \times 10^{-10}$ mol m^{-2} s^{-1} Pa^{-1} at 10CoBBP, corresponding to a 12% reduction compared with that of PEI membranes.

As shown in Fig. 6-5(b), the H_2/CH_4 permselectivity exhibited a notable enhancement upon the incorporation of CoBBP into the PEI membranes. Specifically, the $\alpha H_2/CH_4$ increased from 62.9 ± 2.5 (PEI) to 102.2 ± 5 (1CoBBP), indicating that even a small amount of CoBBP can enhance permselectivity. However, with further increases in CoBBP concentration, the gas permselectivity decreased to 72.7 ± 10 (5CoBBP), suggesting that higher concentrations of CoBBP may lead to reduced H_2 permeability and consequently lower permselectivity. Interestingly, for 10 CoBBP, the increase in $\alpha H_2/CH_4$ may be attributed to the higher gas permeability resulting from the steric hindrance of the CoBBP additive, which reduces the permeability of both H_2 and CH_4. The permselectivities for CO_2/CH_4 and CO_2/N_2 did not deviate significantly from those of the pure PEI membrane; however, compared to the BBP-doped PEI membrane, the permselectivity increased substantially by 59% and 80%, respectively. This suggests that the CO_2 adsorption mechanism inherent to the BBP structure may have been altered following the chelation of Co metal ions within the structure. Compared to pure BBP, the cobalt-based BBP demonstrated superior gas separation performance, as cobalt exhibited better gas permeance than the BBP monomer. A H_2 gas permeance of approximately 48% was observed when the same amount of BBP was incorporated into the PEI membranes. To chelate the metal within the BBP structure, gas molecules can be adsorbed and facilitated through the bulk membrane. However, gas permeance was reduced when the BBP chelate site was exposed to the membrane bulk.

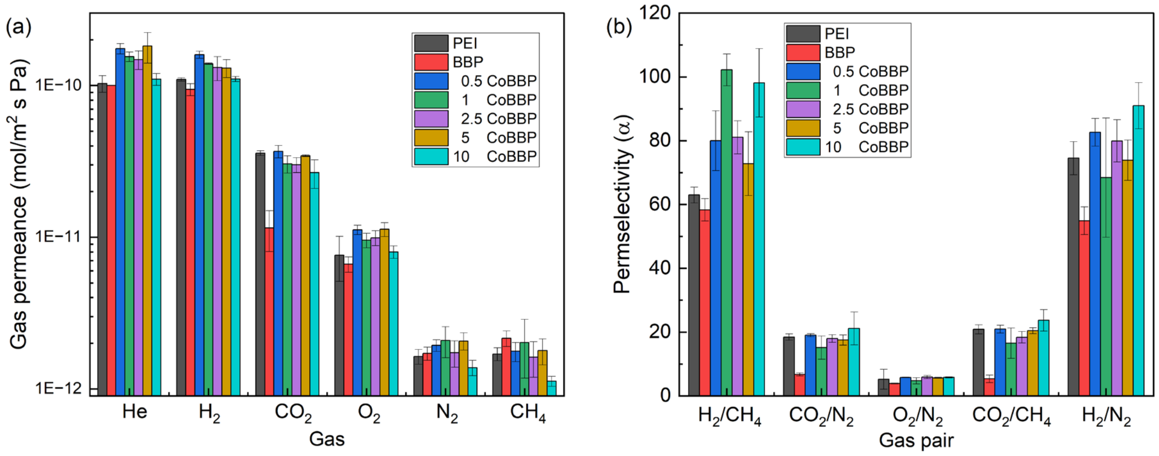

Fig. 6-5. (a) Single gas permeance of all membranes, where the error bars in the figure indicate the average permeance ± 1SD obtained from three variety membranes tests and (b) Permselectivity of all membranes for H_2/CH_4, CO_2/N_2, O_2/N_2, CO_2/CH_2, and H_2/N_2 separation.

As shown in Fig. 6-6, the ideal result of these membranes plotted on the Robeson upper bound of 2008 indicates that this membrane is similar to the pure PEI membrane and is still far from the 2008 upper bound [387]. However, CoBBP performs better than PEI membranes in terms of H_2 and O_2 permeabilities and H_2/N_2 and O_2/N_2 permselectivities. Furthermore, the results including the performance of He/N_2, H_2/N_2, and CO_2/N_2 selectivity may be attributed to the nature of the gas molecules, where He is a noble gas and a monatomic molecule, H_2 is a diatomic molecule consisting of two identical H atoms, and CO_2 is a triatomic molecule composed of two different atoms. The presence of intermolecular forces, such as hydrogen bonding or dipole-dipole interactions within the polyatomic molecules [388], could lead to interactions with membranes and potentially influence the gas permeance.

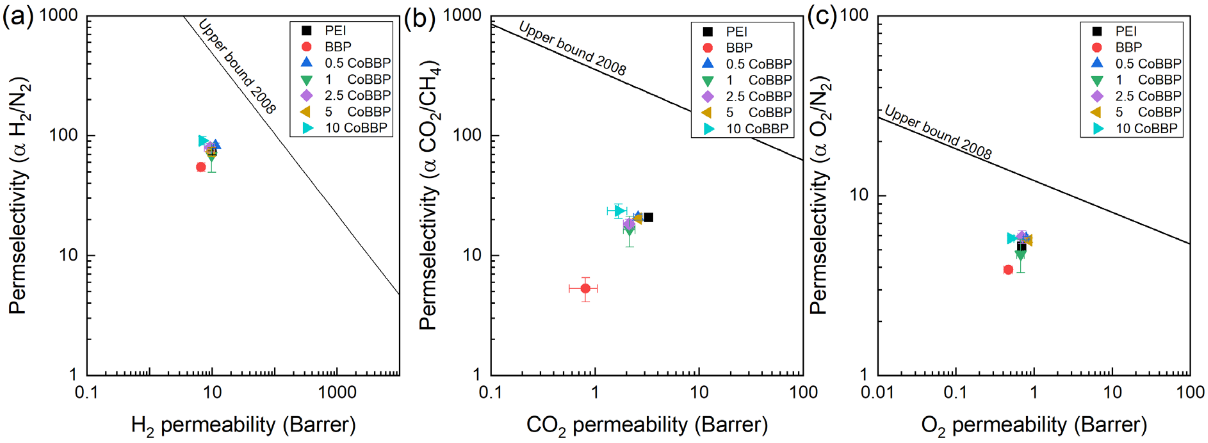

Fig. 6-6. Single gas permeability result in Robeson upper bound 2008. (a) H_2/N_2, (b) CO_2/CH_4, and (c) O_2/N_2.

Moreover, the relative permeability (P_{CoBBP}/P_{PEI}) in relation to the CoBBP content ($\boldsymbol{\phi}$) in the PEI membrane can be used to evaluate gas permeability efficiency [389, 390]. As shown in Fig. S6-4, the standard Maxwell equation was applied to simulate a range of reduced permeation polarisability values (β) from -0.5 to 1, to determine the CoBBP dopant ability. When a β value of -0.5 represents an impermeable additive, while a β value is 1 corresponds to a highly permeable additive. As shown in Fig. S6-4, the H_2 permeability of CoBBP membrane demonstrated similar trends with the simulation of the impermeable additive performance [391]. The higher concentration of CoBBP reduce the gas permeability in the membrane bulk. Interestingly, the CO_2 permeability deviated the impermeable trend compared to the trend of H_2, the higher gas dropped to the membrane demonstrated the membrane had a higher reduction, it may be due to the adsorption mechanism for the materials to alter the MMM for the CO_2 permeability.

6.1.4.4. Binary Gas Permeation Performance

A simulated binary gas mixture of H_2 and N_2 was used to investigate the gas permeation performance of pure PEI and the 1 wt.% CoBBP- doped membranes. The feed pressure was maintained at 3 absolute bars to investigate the H_2 separation performance. As shown in Fig. 6-7, the H_2/N_2 mixture were tested at various feed conditions, with each data point collected after a 2-hour testing period. The H_2 permeance of PEI and 1CoBBP was 2.7 and 2.0 $\times10^{-10}$ mol m^{-2} s^{-1} Pa^{-1}, respectively. This result indicates that the incorporation of CoBBP enhances the gas permeance across a range of feed conditions. Specifically, at high H_2 feed concentrations ($\geq$ 50%), the 1CoBBP membrane exhibited approximately 37% greater H_2 permeance than that of the PEI membrane. Furthermore, under low H_2 feed concentrations, the enhancement was more marked. These findings suggest that the CoBBP- doped membrane enables improved separation performance, particularly under low H_2 concentration conditions. However, the low N_2 permeance from both membranes is still sufficient for GC analysis (lower than the GC detection limitation). As shown in Fig. S6-5, no significant N_2 gas was detected after 18 hours of permeation testing.

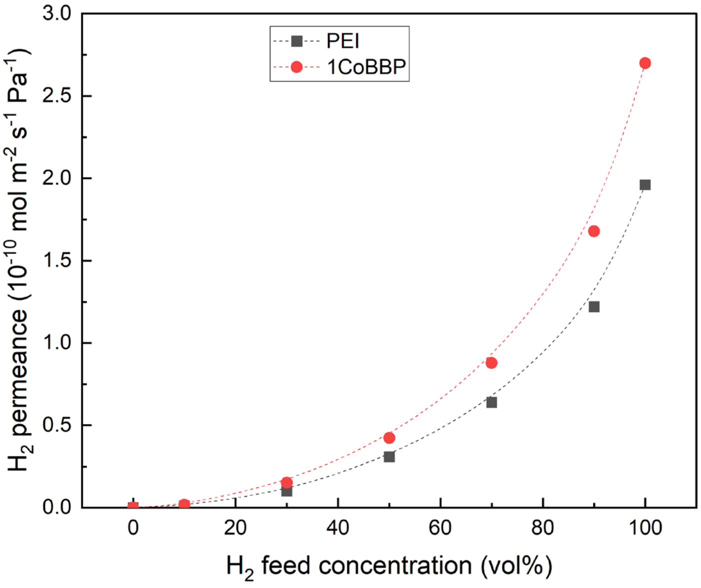

Fig. 6-7. The H_2 permeance from the varying H_2/N_2 mixed gas permeation of PEI and 1CoBBP membranes.

6.1.4.5. Binary Gas Permeation under 100% Relative Humidity

The effect of humidity on the gas separation performance of PEI, BBP, and 1CoBBP was investigated using a 50/50 CO_2/CH_4 gas mixture at 100% relative humidity at 4 bar, as shown in Fig. 6-8. For the PEI membrane, CO_2 permeance decreased by approximately 20% within the first 5 hours, indicating that moisture might have swelled the polymer chain and decreased the CO_2 permeability [307, 372]. However, the CH_4 permeability remained constant. This led to a slight reduction in CO_2/CH_4 selectivity from 20.5 to 18.5. After 24 h of permeation testing, the CO_2 and CH_4 permeances increased. As shown in Fig. 6-8, the PEI membrane operate over 20 hours, the CO_2 and CH_4 permeance increased to 1.24×10^{-11} mol m^{-2} s^{-1} Pa^{-1} and 6.7×10^{-13} mol m^{-2} s^{-1} Pa^{-1}, respectively, suggesting minimal impact of humidity on PEI membrane performance.

In contrast, the BBP membrane displayed a sharp and sustained decrease in both CO_2 and CH_4 permeance during the initial 2 hours, from 4.95×10^{-11} mol m^{-2} s^{-1} Pa^{-1}and 9.71×10^{-12} mol m^{-2} s^{-1} Pa^{-1} to 8.7×10^{-12} mol m^{-2} s^{-1} Pa^{-1} and 1.0 ×10^{-12} mol m^{-2} s^{-1} Pa^{-1}, respectively. This behaviour is attributed to potential interactions between water molecules and imide groups in the BBP structure, leading to reduced fractional free volume [392, 393]. Despite the reduced permeance of the membrane, the decrease in the membrane permeance further enhanced CO_2/CH_4 selectivity.

The 1CoBBP membrane exhibited a distinct result, during the first 3.5 hours, CO_2 and CH_4 permeance increased from 1.21 × 10^{-11} and 6.69 ×10^{-13} mol m^{-2} s^{-1} Pa^{-1} to 2.44 ×10^{-11} and 1.34 ×10^{-12} mol m^{-2} s^{-1} Pa^{-1}, respectively. This suggests a water-assisted transport mechanism, potentially facilitated by Co chelation sites, which enhance CO_2 diffusion through the membrane matrix [229]. While this led to a twofold increase in CO_2 permeance, a similar rise in CH_4 permeance limited improvements in selectivity. Furthermore, the pure CO_2 permeance with 100% relative humidity analyse on the 1CoBBP membrane also indicated that the membrane facilitated the CO_2 permeance performance. However, when the membrane was operated under pure CH_4 with 100% relative humidity CH_4 permeance was not observed, probably because the permeance might be lower than the limit of GC.

These findings are consistent with those obtained in previous studies by Correa et al. [331, 394], which indicate that the water molecules may adsorb onto the carbonyl groups in the PEI via hydrogen bonding, thereby reducing FFV and gas permeability. Baldanza et al. [395] indicated up to a 12.2% reduction in CO_2 permeability at 80% humidity in a 45 °C environment. In contrast, 1CoBBP demonstrated an enhanced CO_2 permeability under humid conditions, supporting a CO_2 gas facilitated by a water-mediated transport mechanism similar to that described by Zhang et al. [229].

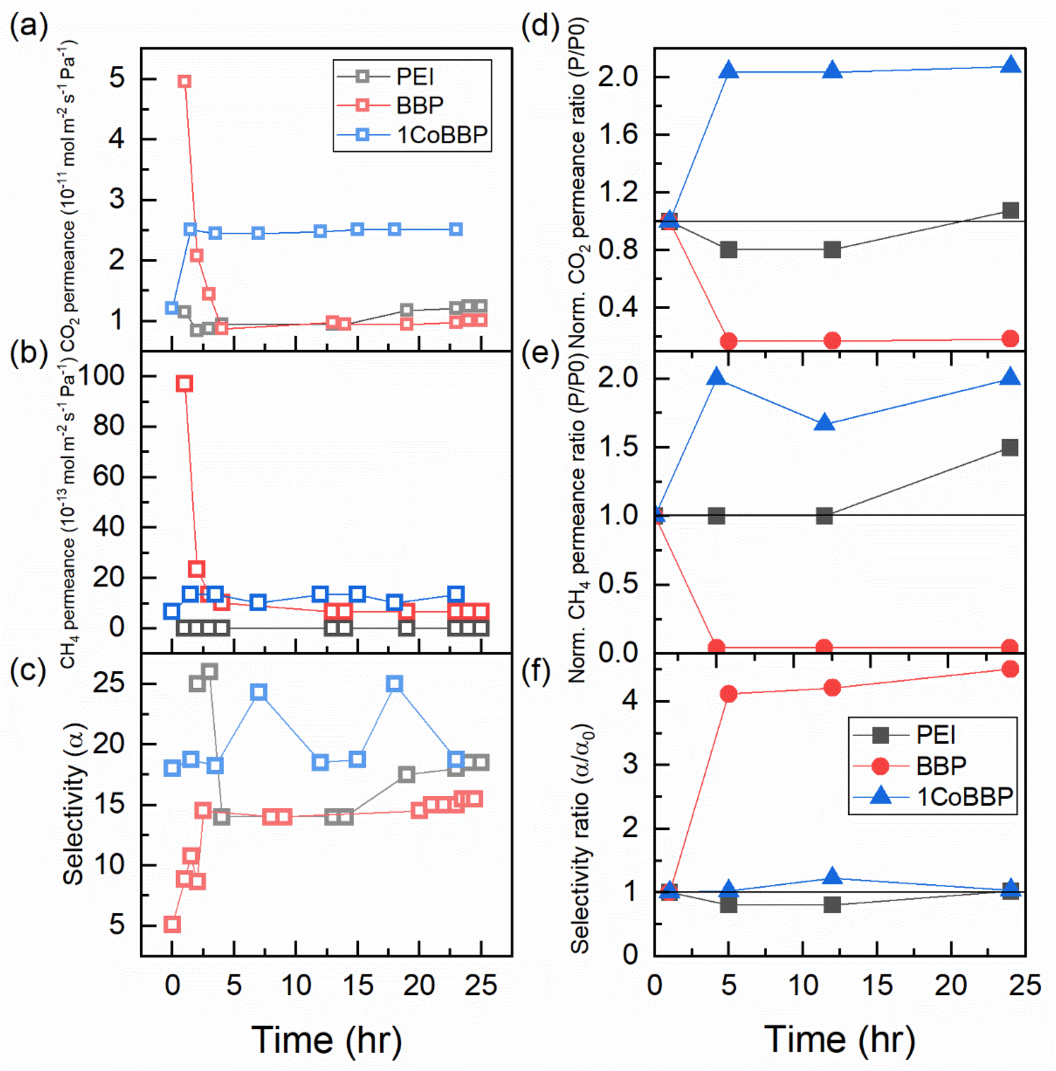

Fig. 6-8. Binary gas permeation test for the PEI, BBP and 1CoBBP membranes under 100% humidity at 80°C. (a) CO_2 permeance, (b) CH_4 permeance, (c) CO_2/CH_4 selectivity (d) normalised CO_2 permeance, (e) normalised CH_4 permeance, and (f) normalised CO_2 /CH_4 selectivity.

6.1.5. Conclusion

In summary, this study revealed that a novel modifier on the PEI membrane may be used for gas separation application in high humidity environments. The material characterization of CoBBP confirmed the coordination of Co with BBP and successful synthesis of CoBBP.

Membrane characterization indicated a defect-free surface, provided measurements of membrane thickness, and confirmed successful coating of the membrane on the alumina tube during the dip-coating process. Notably, various concentrations of MMMs exhibited increased H_2/CH_4 and H_2/N_2 permselectivity, although the higher CoBBP doped membrane demonstrated a decrease in the gas permeability because of the strong steric hindrance on the membrane bulk. The 1CoBBP membrane demonstrated the best trade-off between permeability and permselectivity; the H_2 permeability was over 25% and 48% higher than that of the pure PEI and BBP-modified PEI membranes, respectively. Moreover, in a 100% relative humidity environment, the 1CoBBP membrane demonstrated a two-fold increase in CO_2 permeability compared with the initial CO_2 permeability, indicating that the CoBBP modifier can enhance membrane permeability in high-moisture environments.

6.2. Metal Ions Effect of BMM Modified PEI Composite Membrane

6.2.1. Introduction

To explore the applications of CA biomimetic materials, the structure and active centres of biomimetic materials must be known to determine their CO_2 conversion performance. Kim et al. [227] investigated a series of non-native metal modified human carbonic anhydrase II and natural CA to elucidate how the coordination geometries affect conversion efficiency. The tetrahedral structure of natural CA ensures faster conversion that of the octahedral structure. Shortened H_2 and metal ion distances can benefit proton transfer and faster conversion. The change in the structure causes a hindrance effect that reduces the conversion efficiency. The result indicates that the metal ion efficiency as follows: Zn > Co > Ni > Cu. Kitajima et al. [396] performed more complex investigations on divalent metal ions from Mn to Zn. The CO_2 fixation abilities followed the order Zn> Cu> Ni> Mn> Fe; the hydration activities followed the order Zn>> Co> Ni> Cu≈ 0. This demonstrates that Zn may be the best choice for the conversion active site, as opposed to Cu. However, as Cu ions have a better fixation ability than that of other metal ions, they do not release CO_2 during conversion. This may prove advantageous for membrane separation owing to the higher fixation abilities, which indicates that the modifier could improve CO_2 adsorption for the membrane bulk. Therefore, investigating different metal ions as the active centre for biomimetic materials is necessary to determine the best modification for the membranes.

In the previous section, CoBBP demonstrated good performance for H_2 permeability in the PEI composite membranes and demonstrated a higher CO_2 permeability at high relative humidity environment; therefore, a suitable condition for doping into the PEI membranes might be 1 w/w.% for membrane modification. Therefore, a series of metal ions (Fe, Ni, Cu, and Zn) was selected to determine the metal active site effect on improving polymeric membrane gas separation performance.

6.2.2. Methodology

Various metal ions were separately doped with the BBP precursors using the process described in Section 3.3. As shown in Fig. 6-9, the colour changes of each material demonstrated successful chelation of the metal ions on the BBP structure. The colour change before and after synthesis is listed in Table 6-3. The results indicate that the transition state of the metal ions was changed during the synthesis.

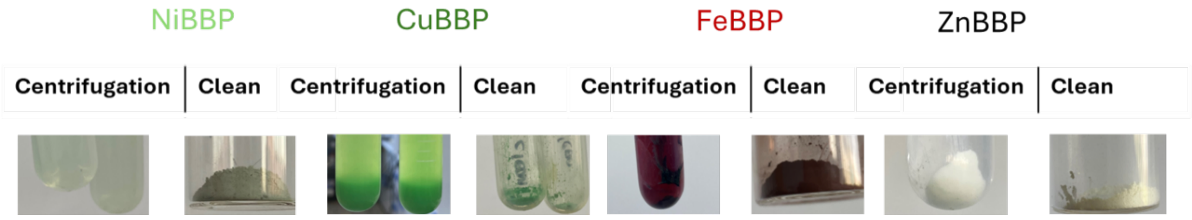

Fig. 6-9. The digital images of colour change of the metal base-BBP after syntehsis.

Table 6-3. The colour changes before and after synthesis

Sample code	Metal ions precursor	After synthesis
FeBBP	Yellow	Dark red
NiBBP	Yellow	Light green
CuBBP	Yellow	Green
ZnBBP	Transparent	White

The experimental setup for this section is shown in Fig. 6-10. Various MtBBP compounds were doped into the PEI composite membranes to investigate the effect of biomimetic material modification on gas permeance. Furthermore, the membranes were evaluated under 100% relative humidity (RH) using a CO_2/CH_4 mixed gas feed to assess their performance under humid conditions.

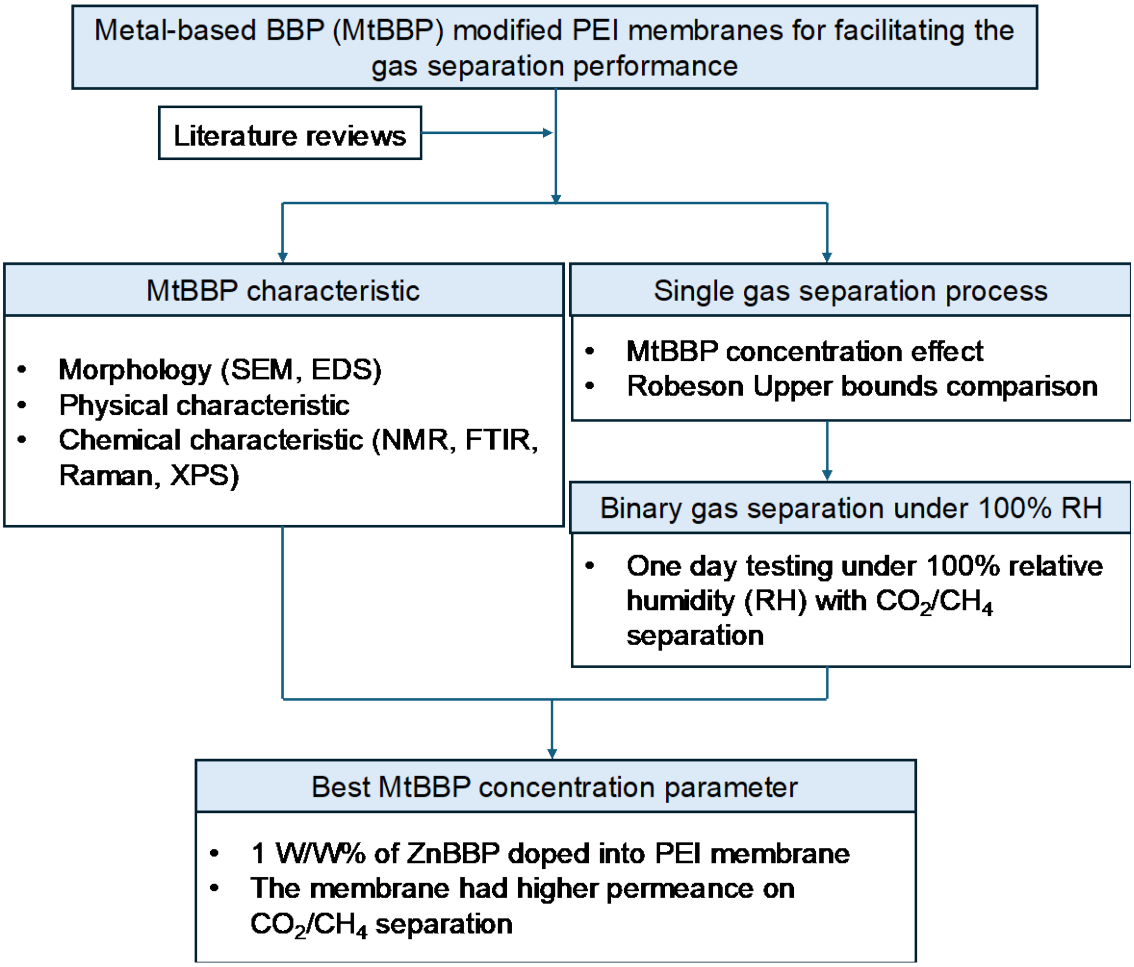

Fig. 6-10. Flow chart for the experimental setup of the MtBBP investigation.

6.2.3. Result and Discussion

6.2.3.1. MtBBP Characteristic

The chemical structure of pristine BBP and its metal-chelated derivatives were analysed by ATR-FTIR and Raman spectroscopy. As shown in Fig. 6-11(a), the ATR-FTIR spectrum of BBP revealed a broad N-H stretching band at 3200 cm^{-1}, indicative of the benzimidazole moiety. The region between 1500 and 1650 cm^{-1} corresponds to C=N stretching vibrations, characteristic of the pyridine ring [397]. The peaks at 1457 and 1436 cm^{-1} represent C-H stretching, and those at 1320, 1276, and 1226 cm^{-1} correspond to the C-N bonding stretching of the main peak structure of BBP [398]. Upon metal coordination, notable spectral changes were observed. The C=N stretching band at approximately 1600 cm^{-1} displayed a shift of 2–5

cm^{-1} across all metal complexes, although the peaks at 1575 and 1588 cm^{-1} remained relatively unchanged. A general decrease in intensity across the major peaks suggests altered polymer chain dynamics owing to metal binding. Shifts were noted upon C–N bonding; although the 1315 cm^{-1} peak remained unchanged, the 1276 cm^{-1} band exhibited a blue shift in ZnBBP and CuBBP, and a red shift in FeBBP and NiBBP. Significant changes in the N–H region, including multiple new peaks and shifts, suggest that metal chelation occurs predominantly through N–H coordination, whereas C=N bonding remains less affected. These observations support the role of the N–H group as the primary coordination site for metal complexation in BBP structures.

As shown in Fig. 6-11(b), the Raman spectra of all the metal-based BBP and BBP precursors displayed peak shifting owing to the BBP structure. The 1000 and 1250 cm^{-1} peaks are attributed to the phenyl and ring structure of benzimidazole and pyridine, respectively. The main structure of the BBP could be confirmed. After chelating with the metal ions, the C-N peak (1250 cm^{-1}) disappeared. New peaks formed at 1629 cm^{-1}, 1556 cm^{-1}, and 1310 cm^{-1}, indicating that the vibration of the aromatic stretching changed after the metal ions were chelated on the BBP structures. Similar peaks were observed upon chelation with different metal ions. The Raman spectra provided good evidence for identifying the metal ions that are chelated via C-N bonding from the BBP structure but not the C=N bond in the benzimidazole structure. The NMR spectra of all samples are shown in Fig. S6-6 and the morphology of all MtBBP is shown in Fig. S6-7.

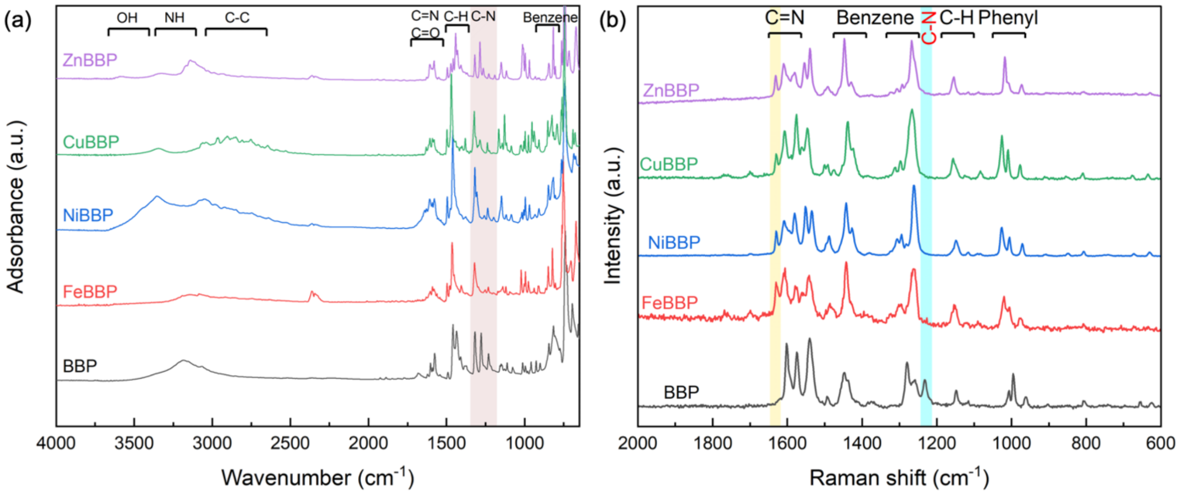

Fig. 6-11. The functional groups and bands stretching analyse for BBP and MtBBP (a) ATR-FTIR analyse and (b) Raman spectra.

The surface chemical compositions of MtBBP and BBP were analysed using XPS. As illustrated in Fig. 6-12(a), the C_{1s} spectrum of BBP revealed three principal peaks. The C-C bonds of BBP were identified by the presence of a peak at 284.8 eV, which is a standardised peak for all polymer structures [399]. Another peak was detected at 285.6 eV, corresponding to C-N bonding within the BBP structure [400]. The third peak in the C_{1s} spectrum, located at 289.5 eV, may be attributed to impurities and oxidative contaminants [401]. Following the synthesis of MtBBP, the peaks attributed to C-C and C-N persisted in the spectra of most MtBBP samples, with the exception of ZnBBP. A novel peak was observed in the MtBBP spectrum corresponding to the N-C=O peak at 288 eV, suggesting the potential capture of water molecules within the structure during the process [402]. As depicted in Fig. 6-12(b), the N_{1s} peaks provided further evidence for peak shifting and a new structural combination indicative of MtBBP formation. The spectrum of BBP exhibited two characteristic peaks attributed to its chemical structure, at 398.4 eV (pyridinic) and 399.8 eV (pyrrolic) [403]. A significant peak shift was observed following the synthesis of FeBBP, CuBBP, and ZnBBP, with the 399.8 eV peak shifting to 401.3 eV. This shift may be attributed to the arrangement of metal ions with a pyrrolic structure analogous to the sp^2 N bonding configuration, which potentially alters the electron transition energy during detection [400]. Notably, the N_{1s} spectrum of NiBBP is comparable with that of BBP, although the peak exhibited a -0.3 eV shift. These characteristics confirmed the successful modification of BBP with different metal ions, which may enhance the performance of the PEI membrane when integrated with these metal ions. Furthermore, the metal ions spectra were also demonstrated the valence state of the MtBBP. As shown in Fig. S6-8, NiBBP, CuBBP, and ZnBBP were demonstrated a clear Ni^{2+}, Cu^{2+}, and Zn^{2+} ions. However, FeBBP demonstrated a mixed state with Fe^{2+} and Fe^{3+} in the synthesis samples.

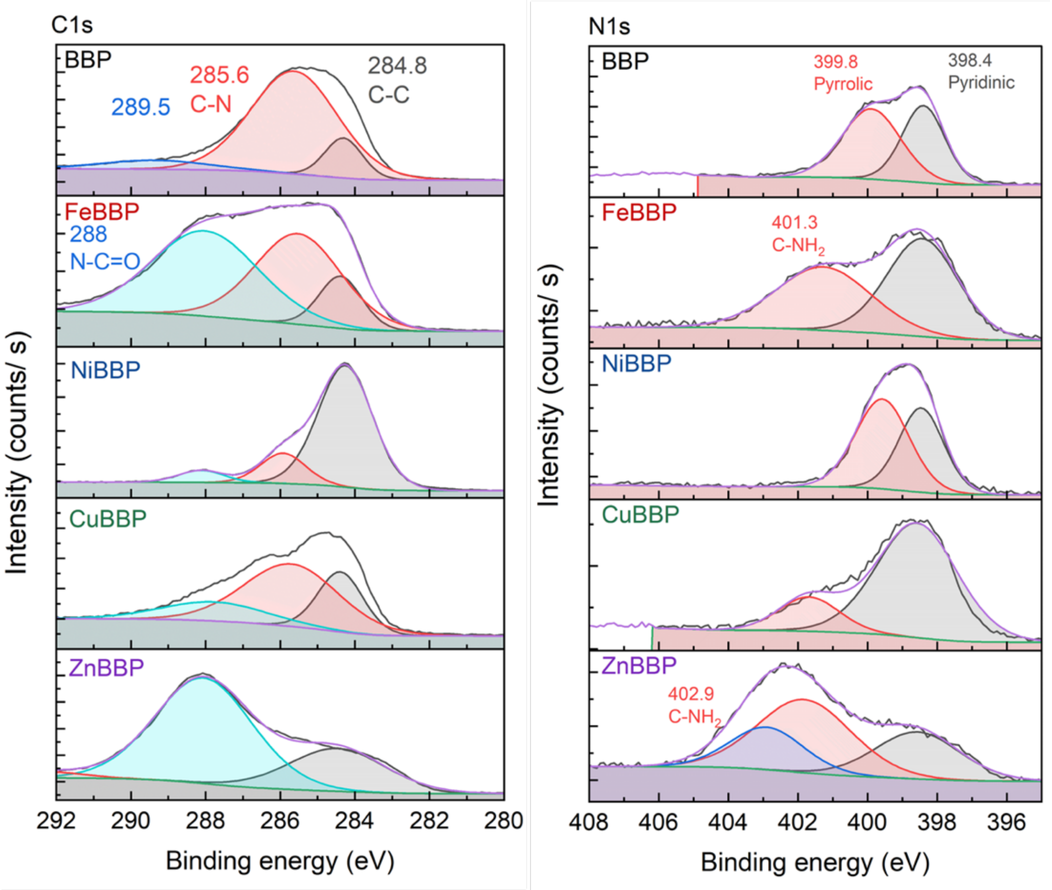

Fig. 6-12. Specific atom spectra of XPS analyses for MtBBP (a) C_{1s} and (b) N_{1s} spectra.

Table 6-4. Atomic ratio of MtBBP obtained using XPS analyse.

Membrane	C (atom.%)	N (atom.%)	O (atom.%)	Metal (atom.%)
FeBBP	72.91	10.18	13.02	2.16
NiBBP	73.46	10.21	12.20	1.90
CuBBP	72.79	7.31	16.04	1.27
ZnBBP	75.89	12.66	9.01	2.43

The physisorption of all MtBBP and BBP was examined using the BET method to measure the pore volume and specific surface area, thereby identifying pore structure and morphologies. As shown in Fig. S6-9, the N_2 isotherm of all MtBBP structures demonstrated a type-II istotherm structure (non-porous or macroporous structure) [404], indicating that BBP is characterised as a dense material with a non-porous structure, with a pore volume of only 0.037 cc g^{-1}. Following the chelation of metals onto the structure, as listed in Table 6-5, both NiBBP and ZnBBP exhibited a modest increase in pore volume and surface area, with an approximate 58% increase in both parameters. This suggests that Ni and Zn ions do not adequately augment the membrane pore structure to enhance free volume within the PEI membranes, potentially maintaining performance akin to that of BBP materials. Conversely, Fe and Cu ions demonstrated a substantial increase in pore volume and surface area post-chelation with BBP. The surface areas of FeBBP and CuBBP increased by approximately 94.8% and 328%, respectively, following synthesis, although adsorption diagrams indicated that they remained as dense materials lacking an interpore structure. This implies that Fe and Cu ions may facilitate the formation of a macroporous structure when compared with the BBP structure. Consequently, these materials may enhance the gas separation process, as a higher pore volume can improve free volume within the membrane bulk.

Table 6-5. Physisorption analyses for MtBBP under N_2 gas at 77 K.

Sample	Pore volume (cc/g)	Surface area (m^2/g)	DFT half pore width (Å)
BBP	0.037	21.5	13.8
FeBBP	0.075	41.9	16.2
NiBBP	0.053	33.9	12.1
CuBBP	0.153	92.1	13.8
ZnBBP	0.059	39.2	12.1

6.2.4. Membrane Characteristic

6.2.4.1. Pure Gas Permeance

A series of pure gases was used to determine the pure gas permeance of the membranes. All MtBBP modified membranes (MtB_M) demonstrated a similar sieving effect to that of the pure PEI membrane; notably, the smaller kinetic diameter gaseous molecules demonstrated different gas permeance performance. As shown in Fig. 6-13(a), FeB_M demonstrated a considerable increase in the permeance of all gases of approximately 2–4 fold compared with that of the BBP doped PEI membranes. The CO_2 permeance increased $(1.15 \pm 0.11) \times 10^{-10}$ from $(5.1 \pm 2.2) \times 10^{-11}$ mol m^{-2} s^{-1} Pa^{-1}. CuB_M exhibited a marked increase in gas permeance, with He, H_2, CO_2, and O_2 permeances increasing by approximately 72%, 83%, 300%, and 86%, respectively. For gases with larger kinetic diameters, N_2 and CH_4 permeance rose by 31% and 2%, respectively, relative to that of the BBP_M. The overall increase is attributed to the higher surface area of CuBBP particles, which probably introduces additional free volume into the PEI matrix, facilitating greater gas transport. The exceptional increase in CO_2 permeance of CuBBP may contribute to CO_2 fixation or enhanced solubility within the membrane bulk, further boosting permeation. Similarly, ZnB_M followed a comparable trend, with He, H_2, CO_2, and O_2 permeances increasing by approximately 11%, 68%, 225%, and 68%, respectively. In contrast, NiB_M displayed a performance closely resembling that of the BBP_M for most gases. However, CO_2 permeance improved by over 58%, while N_2 and CH_4 permeance decreased by 31% and 47%, respectively. This selective suppression of larger gas molecules suggests that NiBBP membrane may offer improved gas separation performance, particularly for CO_2/N_2 or CO_2/CH_4 separations.

As shown in Fig.6-13(b), the ideal membrane permselectivities for various gas pairs (H_2/CO_2, He/N_2, H_2/CH_4, CO_2/CH_4, and O_2/N_2) were evaluated. The H_2/CO_2 permselectivity of both the BBP_M and MtB_M remained consistent at approximately 8.2. Among the MtBBP variants, NiB_M exhibited the highest He/N_2 permselectivity, approximately double that of the pristine BBP membrane, followed by CuB_M, with a 56% improvement. By contrast, ZnB_M displayed a He/N_2 permselectivity similar to that of BBP_M, whereas FeB_M exhibited the lowest permselectivity owing to increased N_2 permeance. A similar trend was observed in H_2/N_2 permselectivity, suggesting that the MtBBP membranes maintain a consistent separation behaviour for light gases such as He and H_2. Notably, all MtBBP membranes demonstrated enhanced CO_2/CH_4 and O_2/N_2 permselectivities compared with that of BBP. The 1CuBBP membrane achieved the highest CO_2/CH_4 permselectivity of 21.3, approximately four times greater than that of the BBP membrane (5.3), primarily because of the increased CO_2 permeance while maintaining a similar CH permeance. Additionally, all O_2/N_2 permselectivities ranged from 5.5 to 5.8, except for that of 1FeBBP, which had a lower value of 3.3, indicating an overall improvement in the O_2/N_2 value compared to 3.9 of the BBP membrane.

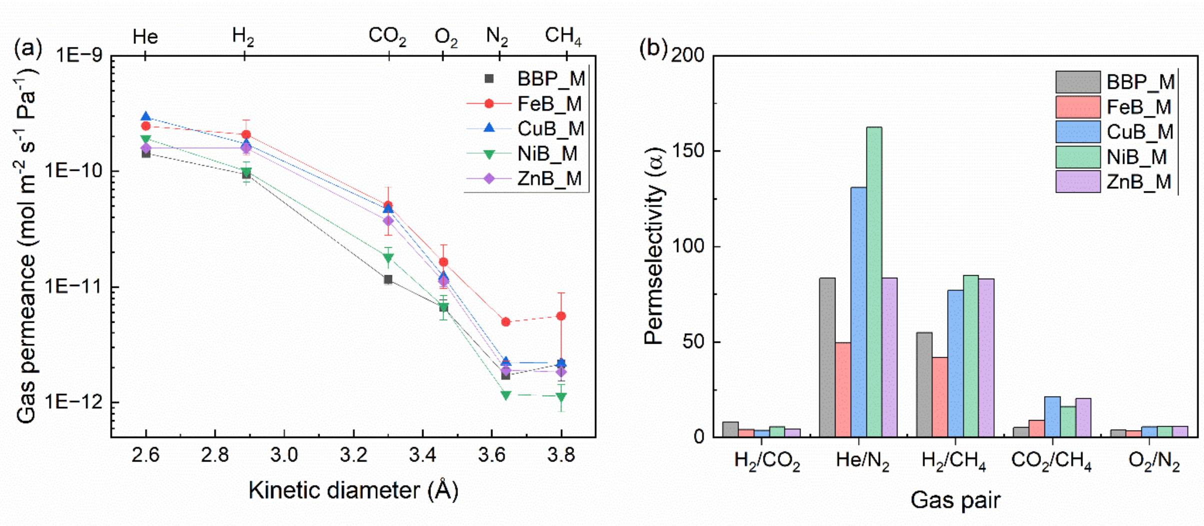

Fig. 6-13. Single gas permeance test of MtBBP/PEI membranes. (a) the gas permeance of a series of small kinetic diameters gases (<3.8 Å) and (b) permselectivities of various gas pairs.

6.2.4.2. Mixed Gas Permeance

H_2/N_2 and He/N_2 mixed gas separation

Based on the single gas separation performance, CuB_M and FeB_M membranes were chosen to examine the mixed gas separation under various feed conditions, ranging from 0–100 vol. % for H_2/N_2 and He/N_2. As illustrated in Fig. 6-14(a), both CuB_M and FeB_M exhibited superior gas permeance compared with that of the pristine PEI membrane under various feed conditions. However, N_2 permeance fell below the GC detection limit, and was not observed in the permeate gas product, suggesting the detection limit is below 10^{-12} mol m^{-2} s^{-1} Pa^{-1}. With a 100% H_2 concentration for the feed, the H_2 permeance of CuB_M and FeB_M membranes outperformed the pure PEI membrane (1.96×10^{-10} mol m^{-2} s^{-1} Pa^{-1}), displaying enhancements of over 74% and 100%, respectively, similar to that of the single gas measurement (Fig. 6-5). Moreover, when the feed H_2 concentration exceeded 50%, the H_2 permeance of FeB_M exceed 3.33×10^{-10} mol m^{-2} s^{-1} Pa^{-1}, which was 74 % higher than that of PEI membranes. Similarly, the H_2 permeance of CuB_M was 100% higher compared to PEI membranes. Conversely, FeB_M and CuB_M membranes demonstrated different gas permeance for the low feed H_2 composition (<50%). The H_2 permeance of CuB_M displayed a 270% enhancement compared to that of the pure PEI membranes, while H_2 permeance of FeB_M maintained the same enhancement ratio (50%). This indicates that the CuBBP additive can improve the H_2 permeance at low feed ratios (10–30 vol.%).

As shown in Fig. 6-14(b), the He/N_2 mixed gas separation was also conducted to evaluate the separation performance of membrane. Similar to the H_2/N_2 separation results, both FeB_M and CuB_M exhibited enhanced He permeance across various He/N_2 feed gas ratios. Notably, the FeB_M demonstrated a higher He permeance compared to CuB_M and PEI membrane. Notably, the PEB_M demonstrated the highest He permeance. At a 90/10 He/N_2 feed gas tatio, the He permeance of FeB_M reached 7.2×10^{-10} mol m^{-2} s^{-1} Pa^{-1}, representing a 177% increase compared to the pure PEI membrane. Furthermore, significant enhancement was observed at a 30/70 He/N_2 feed gas ratio, where FeB_M exhibited a more than two-fold increase compared with that of the pure PEI membrane. This improvement may be attributed to the larger effective surface area provided by the FeB_M, which provided a more fraction free volume within the PEI membrane matrix, thereby formatting more efficient gas transport pathways. Additionally, the broader pore size distribution offered by FeBBP can augment gas separation performance, further enhancing He permeance during He/N_2 separation testing. This could explained by the diffusion coefficient for He in the PEI membrane can exceed the diffusion coefficient for N_2 by over an order of magnitude, significantly enhancing He permeance [39].

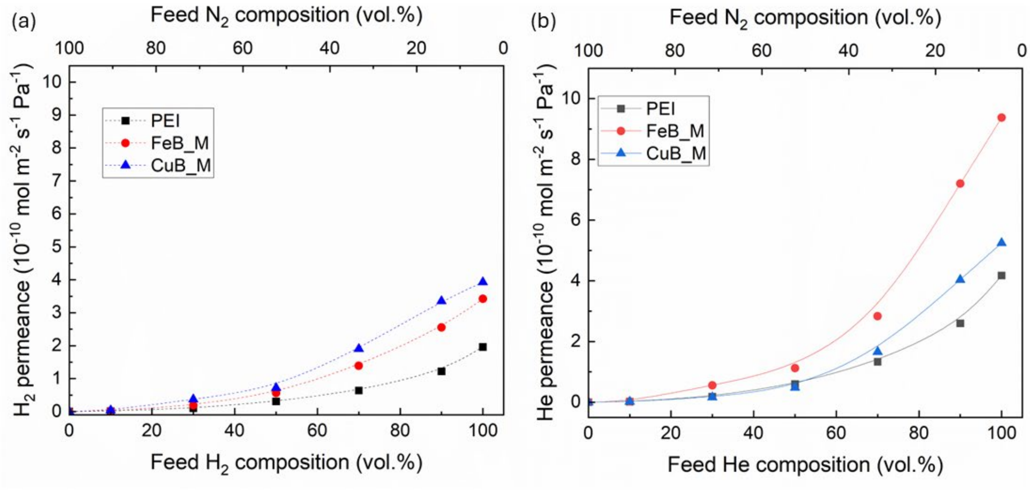

Fig. 6-14. Dried mixed gas separation under various feed concentrations at 35 °C at 2 bar. (a) H_2/N_2 and (b) He/N_2.

CO_2/CH_4 mixed gas separation

For CO_2/CH_4 mixed gas separation, BBP_M, FeB_M, CuB_M, and ZnB_M, were applied to evaluate to evaluate the membrane separation capacity under 50/50 feed gas ratio at 4 bar, across a temperature range of 35 to 80 °C. The CO_2/CH_4 selectivity of the MtBBP membranes was evaluated under mixed-gas conditions at 80 °C yielding a measurable CH_4 permeance. As shown in Table 6-6, the 1BBP membrane exhibited consistent permselectivity and mixed-gas selectivity results, maintaining a low separation performance with little variation across the operation temperatures ($\alpha_{CO2/CH4} \approx 5.1–5.9$). In contrast, the MtBBP membranes showed notable deviations between pure-gas permselectivity and actual selectivity under mixed-gas conditions at 80 °C. The 1CuBBP membrane displayed a slight decrease in CO_2/CH_4 selectivity compared to its permselectivity (16.6 vs. 21.3), possibly due to reduced CO_2 affinity or increased CH_4 permeation at higher temperatures. Remarkably, the 1FeBBP and 1ZnBBP membranes exhibited significantly enhanced selectivity at 80 °C, reaching values of 20.8 and 31.6, respectively, despite their CO_2 permeance decreasing with temperature. This unexpected increase in mixed-gas selectivity is likely driven by a combination of mechanisms: (1) metal-induced steric hindrance [405, 406], (2) preferential interaction between CO_2 and the Fe^{3+}/Zn^{2+} coordination sites, enhancing CO_2 transport relative to that of CH_4 [407-409], and (3) competitive sorption in the mixed-gas environment, where CO_2 dominates the available sorption sites, effectively block CH_4 adsorption and reducing its uptake [410, 411]. These results underscore the role of metal coordination chemistry in tuning the gas separation performance of MtBBP membranes under practical operating conditions. However, these assumptions on the gas separation mechanism for the MtBBP membranes would require a detailed investigation of the gas transport in future works.

Table 6-6. Selectivity $\alpha CO_2/CH_4$ of MtB_M at three operating temperatures under a CO_2/CH_4 feed with 50/50 vol.% at 4 bar.

Membrane	Single gas measurement	Mixed gas measurement			100%RH Mixed gas
	Permselectivity (α CO_2/CH_4)	Selectivity (α CO_2/CH_4)			
	35 °C	35 °C	50 °C	80 °C	80 °C
BBP_M	5.3	5.4	5.9	5.1	15.5
FeB_M	8.9	-	-	20.8	19.7
CuB_M	21.3	-	-	16.6	18.2
ZnB_M	20.3	-	-	31.6	19.5

As shown in Fig. 6-15(a), CO_2 permeance exhibited two distinct trends depending on the membrane type. For the BBP_M, CO_2 permeance increased significantly from 1.7×10^{-11} to 4.7×10^{-11} mol m^{-2} s^{-1} Pa^{-1} as the temperature rose from 35 °C to 80 °C. A comparable trend was observed for the CuB_M, where the permeance increased from 1.7×10^{-11} to 2.3×10^{-11} mol m^{-2} s^{-1} Pa^{-1}. In contrast, the FeB_M and ZnB_M membranes exhibited a decrease in CO_2

permeance with increasing temperatures. Specifically, the permeance of FeB_M decreased from 1.8 × 10^{-11} to 1.2 × 10^{-11} mol m^{-2} s^{-1} Pa^{-1} at 50 °C, followed by a slight recovery to 1.3 × 10^{-11} mol m^{-2} s^{-1} Pa^{-1} at 80 °C. Meanwhile, the ZnB_M membrane displayed a substantial decrease from 2.3 × 10^{-11} to 8.7 × 10^{-12} mol m^{-2} s^{-1} Pa^{-1} as the operating temperature increased from 35 °C to 80 °C.

These trends are further elucidated in the Arrhenius plots (Fig. 6-15b), which provide insight into the activation energies (E_a) for CO_2 permeation. The calculated E_a was 18.8, -5.38, 5.79 and -19.2 kJ/mol for BBP_M, FeB_M, CuB_M, and ZnB_M, respectively. According to the solution-diffusion mechanism, gas solubility typically decreases with increasing temperature, while diffusivity increases, resulting in enhanced gas permeance [412, 413]. This phenomenon was observed in the BBP_M and CuB_M membranes. However, FeB_M and ZnB_M exhibited opposite behaviour, with reduced CO_2 permeance at elevated temperatures, suggesting a significant loss of CO_2 adsorption capacity and suppressed diffusion within the MtBBP matrix under these conditions. However, CH_4 permeance measurements at low temperatures (< 80 °C) were not feasible for most membranes and was limited by GC detecting limitation.

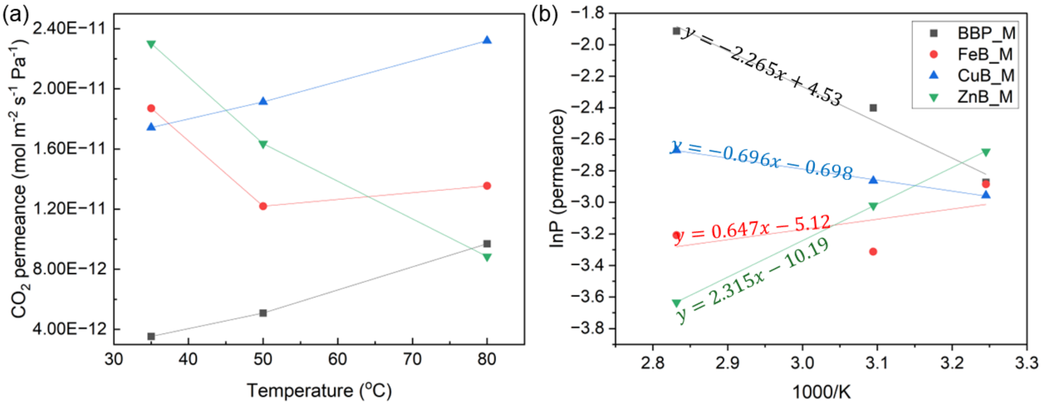

Fig. 6-15. CO_2/CH_4 (50/50) mixed gas separation for BBP_M, FeB_M, CuB_M and ZnB_M at 4 bar as a function of operational temperature. (a) The CO_2 permeance of the MtB_M and (b) Arrhenius and slope analyses plot of permeance.

6.2.4.3. Mixed Gas Permeation under 100% Relative Humidity (RH)

All five membranes PEI, BBP_M, FeB_M, CuB_M, and ZnB_M were evaluated under wet-gas conditions using a CO_2/CH_4 feed gas ratio of 50:50 vol.% at 100% RH, with a total feed pressure of 4 bar and an operating temperature of 80 °C. To ensure stable data acquisition, the membrane module was stabilized for one hour before initiating GC measurements. Each membrane underwent continuous testing over a 24-hour period. Humidified CO_2/CH_4 gas mixture was selected to examine the stability of the membrane pores and the MtBBP to further understand the humidity effect on CO_2/CH_4 gas transport.

As shown in Fig. 6-16(a–c), FeB_M and CuB_M exhibited the highest CO_2 permeance values by the end of the testing period, reaching 2.35×10^{-11} mol m^{-2} s^{-1} Pa^{-1} and 2.61×10^{-11} mol m^{-2} s^{-1} Pa^{-1}, respectively. These membranes also demonstrated the highest CH_4 permeance, with measurements of 1.2×10^{-12} mol m^{-2} s^{-1} Pa^{-1} for FeB_M and 1.6×10^{-12} mol m^{-2} s^{-1} Pa^{-1} for CuB_M, which were approximately twice as high as those observed for the PEI membranes. The ZnB_M membrane displayed a marginal increase in CO_2 permeance from 8.9×10^{-12} mol m^{-2} s^{-1} Pa^{-1} at 1 h to 1.3×10^{-11} mol m^{-2} s^{-1} Pa^{-1} at 25 h, while CH_4 permeance increased significantly from 2.8×10^{-13} mol m^{-2} s^{-1} Pa^{-1} to 7.2×10^{-13} mol m^{-2} s^{-1} Pa^{-1} over the same period.

To better understand membrane stability and permeance behaviour, the permeance data were normalised against initial gas permeance measured at 1 h (Fig. 6-16(d–f)). The normalized results revealed that the enhancement in CO_2 permeance followed the order: FeB_M > ZnB_M > CuB_M. Conversely, CH_4 permeance enhancement followed the trend: ZnB_M > FeB_M > CuB_M. These observations suggest that Fe and Zn coordination contributed more effectively to CO_2 transport under humid conditions compared with Cu. Interestingly, both FeB_M and ZnB_M exhibited positive E_a for CO_2 permeation in prior analyses, implying a sorption-driven transport mechanism. This behaviour aligns with the hypothesized role of water molecules in enhancing CO_2 permeation via mechanisms akin to the enzymatic action of carbonic anhydrase, facilitating reversible CO_2 hydration and diffusion through the membrane bulk (Section 6.1/Fig. 6-1). However, the substantial increase in CH_4 permeance under humid conditions remains less understood. The solubility of the CO_2 and CH_4 is approximately 5.8×10^{-4} mol L^{-1} and 9.29×10^{-6} mol L^{-1}at 80°C, respectively, which can be negligible during considering the interaction between the gas dissolve in the feed water tank [414, 415]. Furthermore, the CH_4 may competition sorption with the CO_2 and H_2O with the PEI membrane and the BMM materials, thereby increase the CH_4 permeance. Overall, while the BMM modified membranes may not markedly improve CO_2/CH_4 selectivity, they appear effective in facilitating CO_2 transport under humid conditions, especially in the presence of Fe and Zn coordination sites.

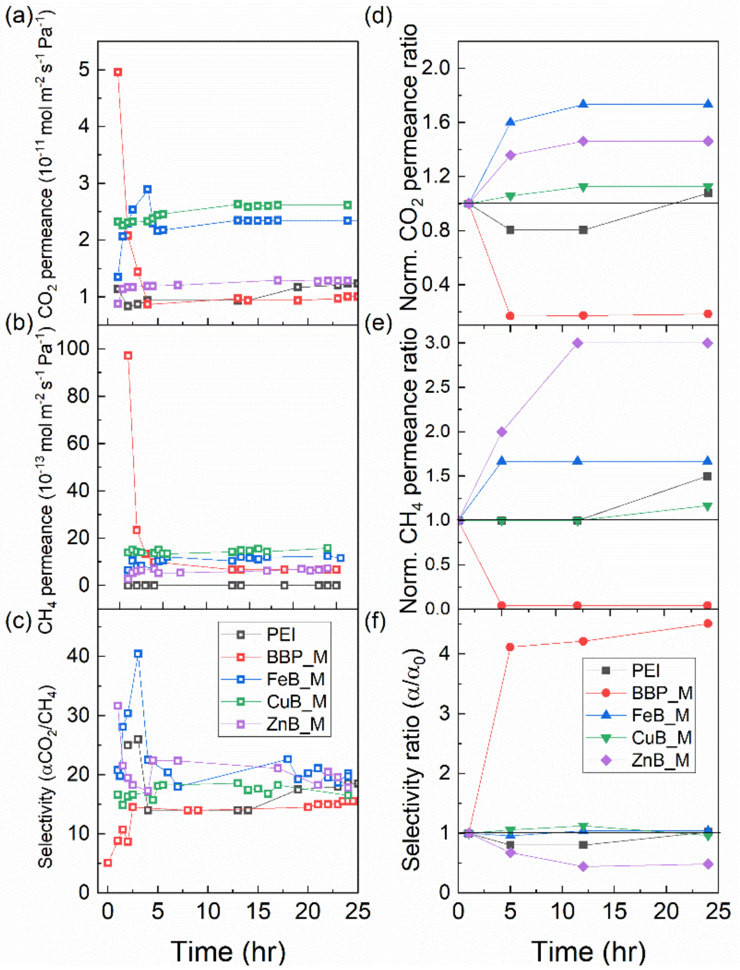

Fig. 6-16. Binary gas permeation test for the PEI, 1BBP, 1FeBBP, 1CuBBP and 1ZnBBP membranes under 100% humidity at 80 °C. (a) CO_2 permeance, (b) CH_4 permeance, (c)

CO_2/CH_4 selectivity (d) normalised CO_2 permeance, (e) normalised CH_4 permeance, and (f) normalised CO_2 /CH_4 selectivity.

6.2.5. Conclusion

A series of metal-based BBP (MtBBP) modifiers, FeBBP, NiBBP, CuBBP, and ZnBBP, and BBP precursors was synthesised and incorporated into PEI membranes to enhance CO_2/CH_4 separation. Raman analysis confirmed successful coordination via benzimidazole groups. Single-gas tests indicated that 1FeBBP achieved the highest CO_2 permeance (2–4 fold over that of BBP), while 1CuBBP also displayed enhanced performance with a permselectivity CO_2/CH_4 of 21.3. Arrhenius analysis under mixed gases revealed sorption-assisted transport in FeB_M and ZnB_M. Notably, under humid, high-temperature (80 °C, 100% RH) conditions, FeB_M and ZnB_M displayed significantly increased CO_2 permeance, probably owing to preferential CO_2 coordination and competitive sorption effects. These results suggest that FeBBP and ZnBBP can mimic carbonic anhydrase-like behaviour, promoting CO_2 transport under wet conditions. Among them, ZnBBP offers the best balance of selectivity and stability. However, further improvement of the PEI matrix required to enhance overall gas permeability for practical applications.

6.3. Supporting Information

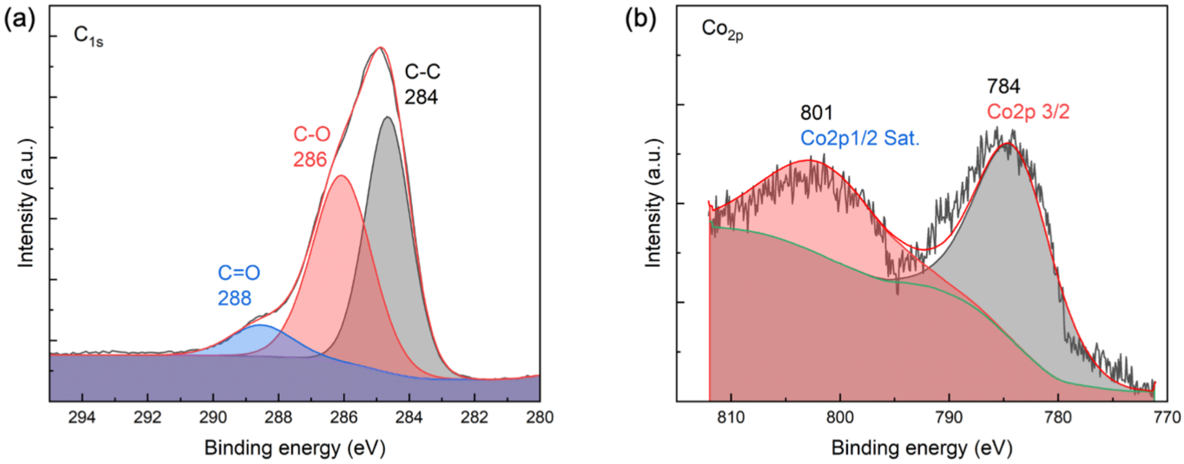

Fig. S6-1. High-resolution C_{1s} and Co_{2p} spectra of CoBBP.

The ^{1}H NMR spectrum of BBP (Fig. S6-2a) dissolved in DMSO-d_6 and analyse at 400 MHz, reveals chemical shifts at δ 13.03 (s, 3H), 8.36 (d, *J* = 7.8 Hz, 2H), 8.19 (dd, *J* = 8.3, 7.3 Hz, 1H), 7.80 – 7.75 (m, 6H), and 7.34 (s, 7H), consistent with the predicted structure from Chemdraw (inset chemical structure). After Co coordination, the CoBBP spectrum (Fig.S6-2b) shows new chemical shifts at δ 12.66 (s, 6H), 10.49 (s, 8H), 8.36 (d, *J* = 7.7 Hz, 1H), 7.80 – 7.73 (m, 2H), 7.33 (d, *J* = 6.4 Hz, 1H), and 3.75 (s, 4H). The disappearance of the 8.16 ppm signal, along with the emergence of a new peak at 10.49 ppm, suggests Co coordination with the pyridine moiety, affecting the local proton environment. Additionally, the 3.75 ppm signal indicates the presence of water molecules incorporated in the coordination complex. These observations collectively confirm the successful synthesis and coordination environment of the CoBBP complex.

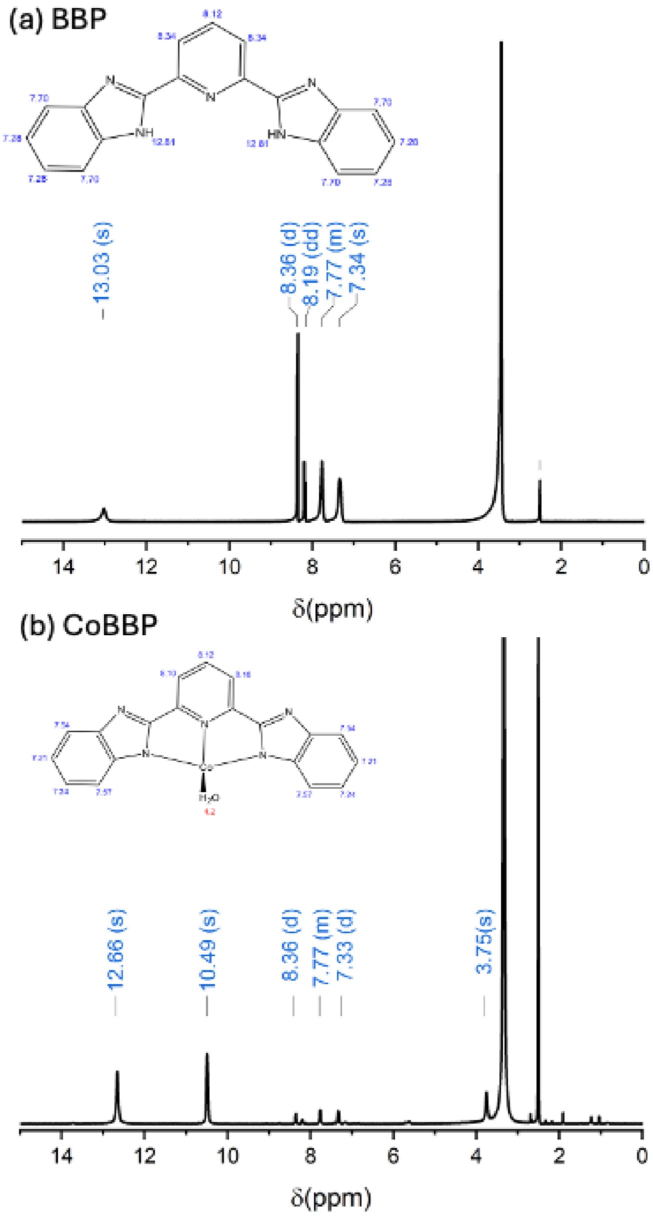

Fig. S6-2. ^{1}H NMR spectrum for (a) BBP and (b) CoBBP. The corresponding predicted NMR peaks are listed in the inset chemical structure.

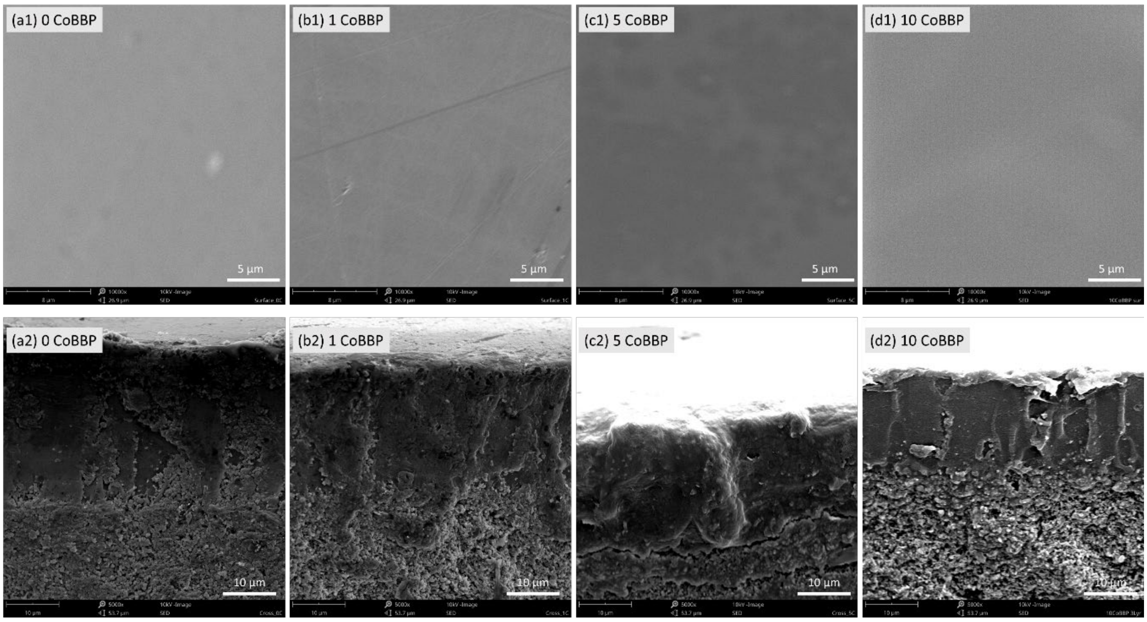

Fig. S6-3. SEM analyses of the thin-film composite membranes (a) PEI, (b) 1 CoBBP, (c) 5 CoBBP, and (d) 10 CoBBP. (1) surface morphology with magnification 10000x and (2) cross-sectional images with magnification 5000x.

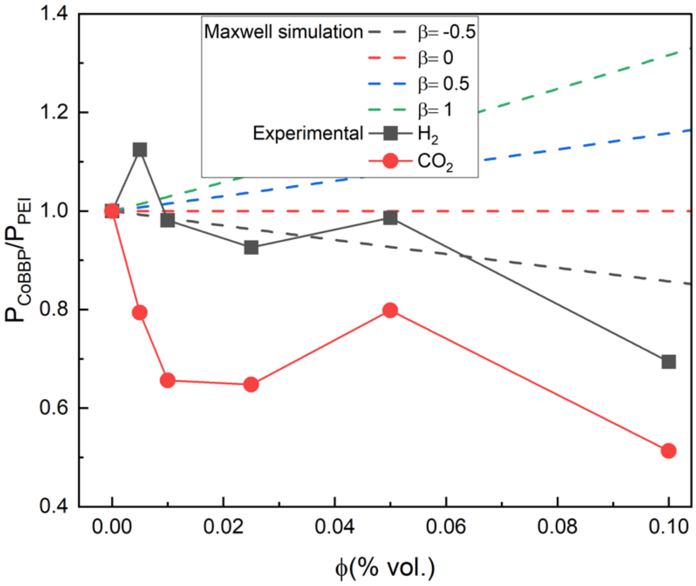

Fig. S6-4. The H_2 and CO_2 permeability of CoBBP doped into PEI membrane with Maxwell equation simulation.

The overnight separation of 50/50 vol.% of H_2/N_2 was analyzed for the 1CoBBP membrane to investigate the long-term permeation. The initial H_2 permeance of 1CoBBP was 4.9 $\times 10^{-11}$ mol m^{-2} s^{-1} Pa^{-1}, and decreased marginally to 4.4 $\times 10^{-11}$ mol m^{-2} s^{-1} Pa^{-1} after 8 hours of testing, followed by a permeance of 4.1 $\times 10^{-11}$ mol m^{-2} s^{-1} Pa^{-1} after 18 hours of testing, indicating that the competitive adsorption between H_2 and N_2 in the membrane reduces the membrane permeation performance of the 1CoBBP membranes. For the longer permeation testing, a lower H_2 permeance was obtained for the system.

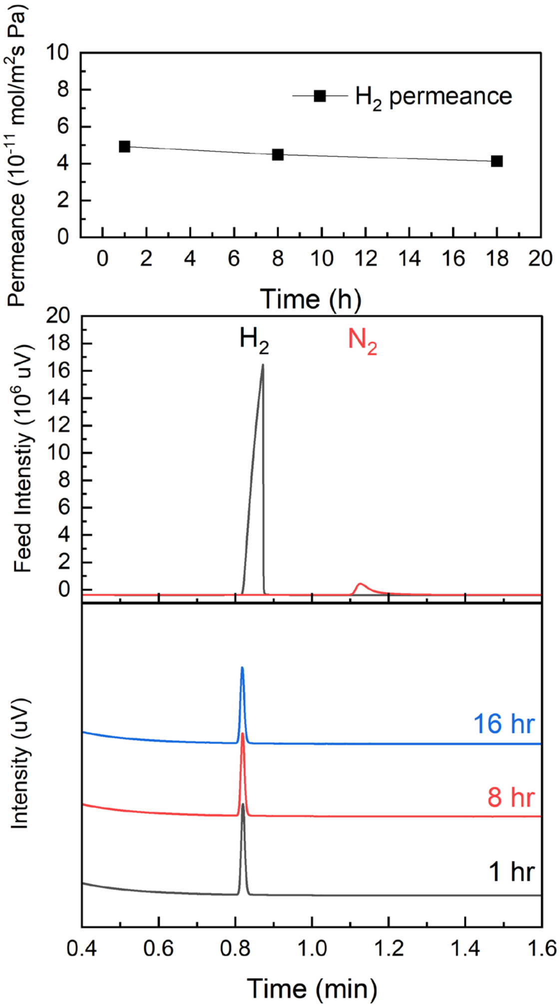

Fig. S6-5. Overnight H_2/N_2 50/50 vol.% feed permeation testing for the CoBBP membranes.

The ^{1}H NMR spectral details of each metal-based BBP are listed below. 2,6-*Bis*(2-benzimidazolyl)pyridine (BBP):δ 13.03 (s, 3H), 8.36 (d, J = 7.8 Hz, 2H), 8.19 (dd, J = 8.3, 7.3 Hz, 1H), 7.80–7.75 (m, 6H), 7.34 (s, 7H). Iron-2,6-*Bis*(2-benzimidazolyl)pyridine (FeBBP): δ 13.31 (s, 1H), 8.28 (s, 2H), 7.70 (s, 2H), 7.26 (s, 2H), 4.38 (s, 1H). Nickel-2,6-*Bis*(2-benzimidazolyl)pyridine (NiBBP): δ 15.70 (s, 1H), 15.63 (s, 2H), 8.34 (s, 6H), 7.44 (s, 3H), 6.99 (s, 6H), 6.13 (s, 3H), 1.22 (s, 1H), 1.03 (d, J = 6.0 Hz, 2H), 0.86–0.78 (m, 1H). Copper-2,6-*Bis*(2-benzimidazolyl)pyridine (CuBBP): δ 9.82 (s, 1H), 8.32 (d, 2H), 8.14 (d, 2H), 6.84 (m, 4H), 6.52 (s,1H), 1.03 (s, = 6.0 Hz, 1H). Zinc-2,6-*Bis*(2-benzimidazolyl)pyridine (ZnBBP): δ 13.20 (s, 1H), 8.40 (s, 1H), 7.77 (s, 2H), 7.36 (s, 2H).

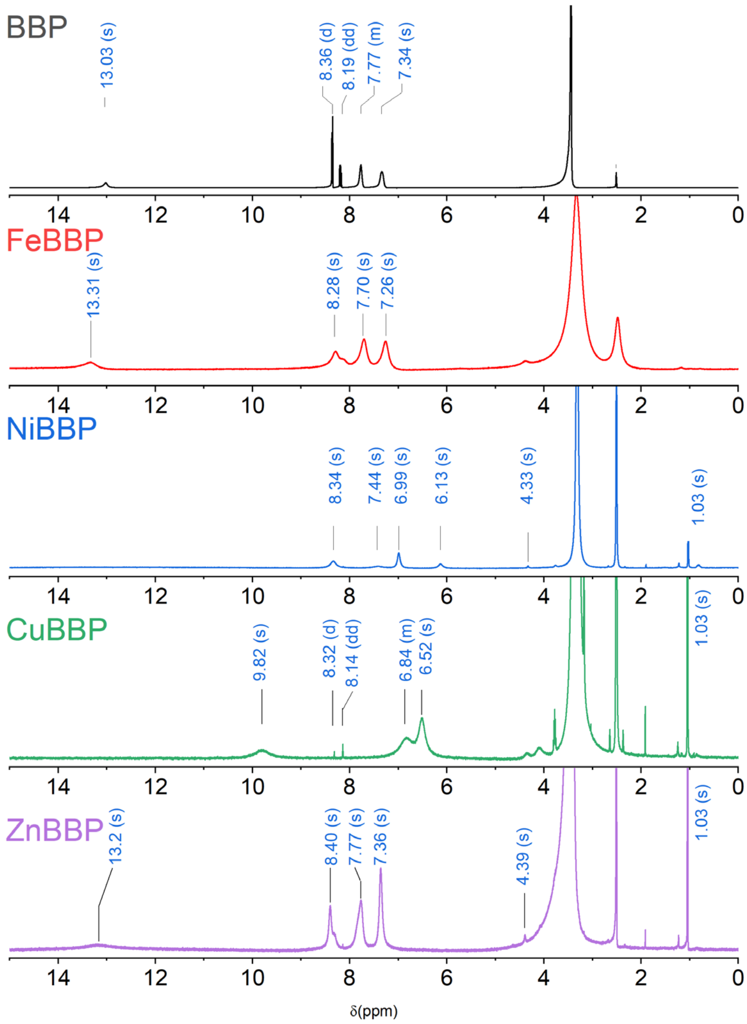

Fig. S6-6. ^{1}H NMR spectra of BBP and MtBBP after synthesis.

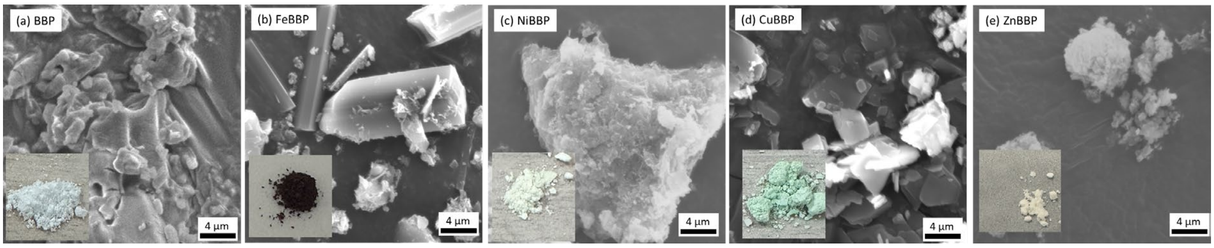

Fig. S6-7. SEM images of (a) BBP, (b) FeBBP, (c) NiBBP, (d) CuBBP and (e) ZnBBP, with the magnification 10000x.The inset images are the digital images of each sample.

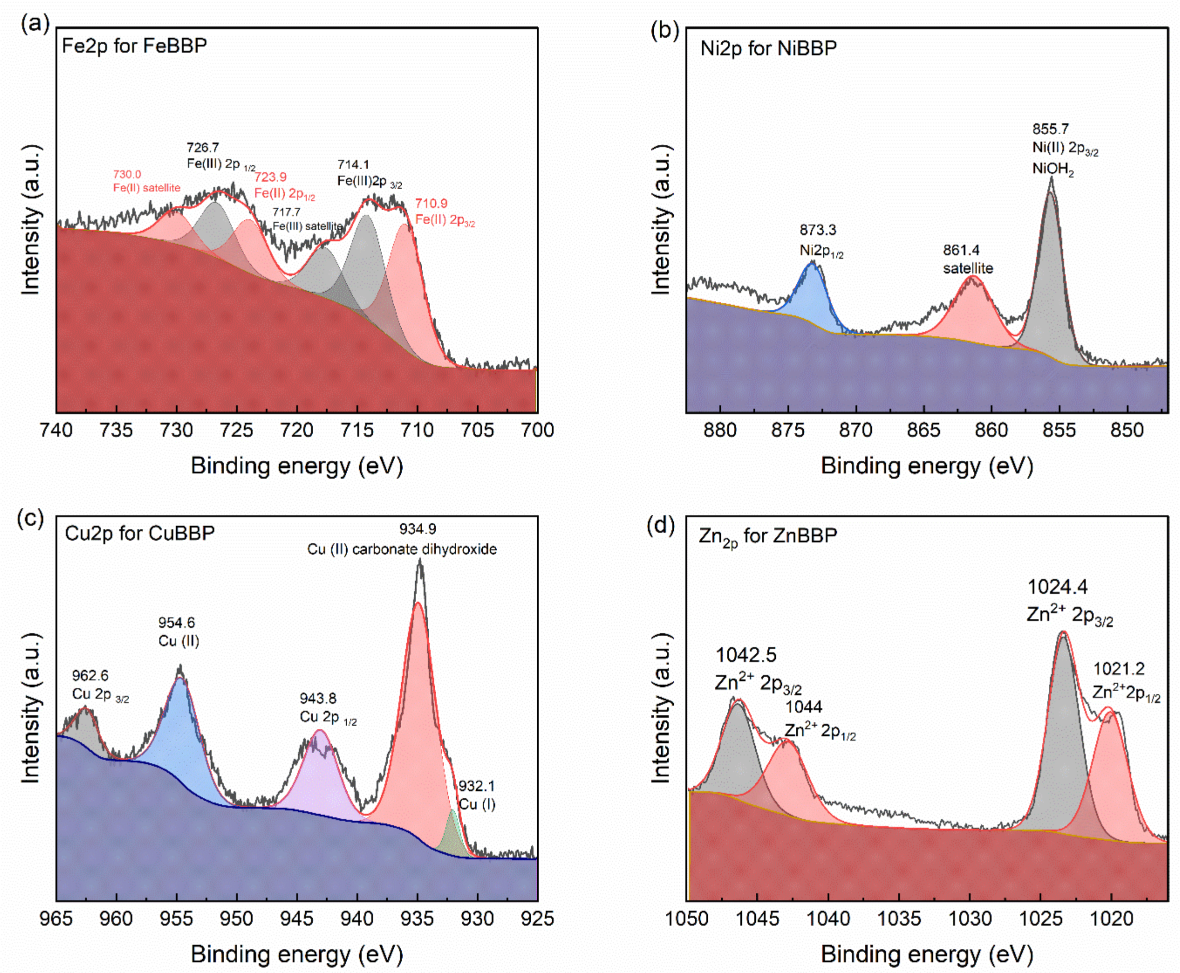

Fig. S6-8. The Metal ions spectra from XPS measurement of (a) Fe2p for FeBBP, (b) Ni2p for NiBBP, (c) Cu2p for CuBBP, and Zn2p for ZnBBP.

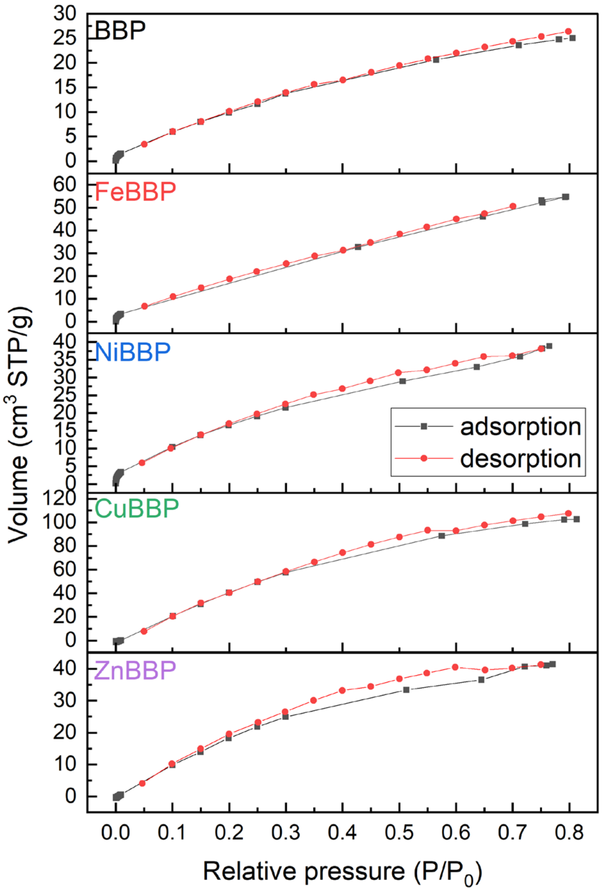

Fig. S6-9. N_2 isotherm of the BET analyses of MtBBP.

Chapter 7 Co-pyrolysis of MtBBP/PEI Carbon Molecular Sieve Membranes

In this chapter, we investigate the MtBBP/PEI membranes that was synthesized using CoBBP concentration between 0.5 and 10 w/w% (Section 7.1), and 1 w/w% of FeBBP and ZnBBP (Section 7.2) to demonstrate the MtBBP effect for preparing PEI-derived carbon molecular sieve membrane (CMSMs) for gas permeation and gas separation processes. In this chapter, due to the nature of CMSM, GPU permeance value is adopted due to convention and compared to the state-of-the-art CMSM literature. Before the investigation onto the additive performance onto the PEI membrane, four different pyrolysis temperatures were selected to determine the CMSMs performance. As shown in Table 7-1, increasing the pyrolysis temperature resulted in lower gas permeance due to pore densification within the CMS structure. The PEI-derived CMS membrane prepared at 600 °C exhibited an H_2 permeance of 108 GPU with the H_2/CH_4 permselectivity of 37.7, which were superior to those of the pristine polymeric PEI membrane and the membranes prepared at other pyrolysis temperatures. Therefore, a pyrolysis temperature of 600 °C was selected for further investigation.

Table 7-1. The gas permeance and permselectivity of the PEI derived carbon molecular sieve membrane with various temperature.

Membrane code	pyrolysis temperature (°C)	Gas permeance (GPU)				Permselectivity (α)		
		H_2	CO_2	N_2	CH_4	H_2/CO_2	H_2/CH_4	CO_2/CH_4
PEI_600	600	108	71.7	3.4	2.9	1.5	37.7	25.1
PEI_700	700	52.7	14.2	0.9	0.9	3.7	56.9	15.3
PEI_800	800	8.5	0.7	0.3	0.6	11.9	14.4	1.2
PEI_900	900	1.9	0.7	0.6	0.2	2.8	8.9	3.2

7.1. CoBBP concentration effect on the PEI carbon molecules sieve membrane

Section 7.1 is submitted to Carbon journal (under review).

7.1.1. Abstract

Carbon molecular sieve membranes (CMSM) have been extensively researched as potential membranes for industrial gas separation and purification owing to their molecular sieving mechanism with high permeance, tailored selectivity, and stability in corrosive and high-temperature environments. In recent years, CMSM development has focused the efforts on modifying the structure of the carbon precursor to further improve the gas separation performance and membrane stability with extended operation time. In this study, we focused on designing a new type of high performance, thin film CMSM with active gas facilitated moieties consisting of cobalt-2,6-bis(2-benzimidazolyl) pyridine (CoB) dopant within the polyetherimide (PEI) carbon precursor. CoB doped carbon molecular sieve membranes (CoB_CM) with systematic CoB concentrations (0-10 w/w %) were investigated to understand the co-pyrolysis effect of CoB on the PEI-derived CMSM microstructure and gas transport (single gas permeation and binary gas separation) over the course of 10 days. The CoB_CM membranes supported on alumina tubes were prepared using a vacuum-assisted, dip-coating process followed by vacuum pyrolysis at 600 °C. In single gas permeation, 1 wt% CoB_CM offered the highest H_2 permeability of 3280 ± 490 Barrer (325 ± 50 GPU) and H_2/CH_4 permselectivity of 259 ± 7 due to the tailored of ultramicropores sizes and distribution within the carbon molecular sieving thin film. Other gas pair permeability versus permselectivities also demonstrate that the CoB_CM membranes can surpass the 2015 and 2019 revisit Robeson upper bounds. 10-day binary gas separation (H_2/CH_4, 50/50 vol.%) tests further demonstrate the enhanced stability and separation performance of the 1CoB_CM membrane over the PEI_CM membrane, producing H_2 permeability of 2800 Barrer (282.2 ± 0.35 GPU) and

H_2/CH_4 selectivity of 234 ± 2. These results suggest that CoB can effectively tune the micropore architecture of the CMSMs, particularly further enhancing ultramicroporosity and gas transport of smaller gases, thereby offers a promising strategy of developing high-performance carbon molecular sieving membranes for challenging gas separations.

7.1.2. Introduction

Carbon molecular sieve membranes (CMSM) are particularly promising for gas separation applications due to their size-exclusion properties and high material stability [416, 417]. CMSM exhibit good thermal and chemical stability, enabling operation at high temperature gas separation (~600 °C) [418], making them suitable candidates for syngas purifications even in oil and tar entrained gas streams [419].

CMSMs are typically fabricated by pyrolyzing polymeric precursors or crosslinking of phenolic monomers followed by carbonization under controlled atmospheric conditions and temperatures, resulting in amorphous carbon structures with tailored pore characteristics. This process produces membranes with a bimodal pore size distribution, comprising micropores (7-20 Å) and ultramicropores (<7 Å) [420]. The micropores enhance sorption capacity and facilitate long penetrant jump lengths, enabling high gas permeance whilst the ultramicropores provide a tight molecular size-sieving effect, improving selectivity based on molecular dimensions of the penetrants [12, 335]. As illustrated in Fig. 7-1, the CMS structure is typically represented by a model composed of carbon plates, walls, and cells dispersed in amorphous carbon phase as proposed by Koros groups [86, 124, 421]. Fig. 7-1(b) represents the ideal individual cell forming interconnected ultramicropores between the aligned plates and micropores between the walls of aligned plates. The micropores within each cell are also randomly surrounded by a continuous phase of amorphous carbon strands, demonstrating the theoretically CMS framework. Additionally, Fig. 7-1(c) shows an ideal orphan carbon chain structure, which undergoes random or concerted packing to form the corresponding amorphous phase or a micropore cell during the pyrolysis. However, to date, it is difficult to characteristically distinguish the amorphous phase from the micropore cells in the CMS membrane bulk with modern techniques due to their identical elemental carbon compositions and similar physicochemical and morphological properties.

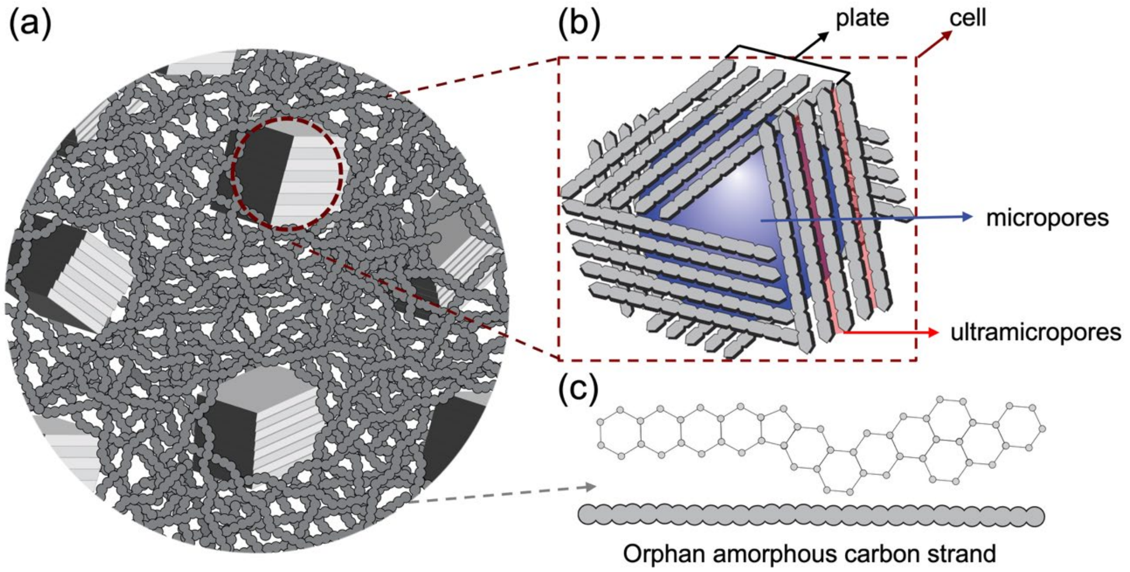

Fig. 7-1. The idealized schematic representation of hypothesized polyimide-based carbon molecular sieve (CMS) structures is depicted by (a) the overview for the carbon molecular sieving framework with microporous cells and the randomly-dispersed carbon chain (amorphous carbon), (b) the micropore cell featuring ultramicropores situated between the aligned carbon strands within the plate and (c) the orphan carbon chain. The figures were redrawn from the references [86, 124, 421].

Among the polymeric precursors for fabricating CMS membranes, polyetherimide (PEI), a subset of polyimide (PI), is recognised as a reliable source with a predictable membrane microstructure and separation performance [148, 159]. The PEI comprises of phthalimide and propylidene repeating segments, which are the aromatic groups of the polymer backbone. During the pyrolysis process, the polymer backbone may decompose into smaller aromatic fragments as the ether (Am-O-Am) or amide (O=C-N) followed by rearrangement into carbonaceous structure to form graphitic-like and/or amorphous carbon [422, 423]. Chemically, the carbon chains within the amorphous CMS membrane bulk consist of a combination of sp^3, sp^2 and sp hybridisation, with a small fraction (< 3 mol.%) of nitrogen and oxygen atoms covalently connected to the carbon backbone throughout the chains and plates [124, 424].

Tseng et al. [150-153] investigated a series of free-standing PEI derived carbon hollow fibres. A 25 wt.% PEI solution can form a CMS hollow fibre membrane with a H_2 permeability of 1140 Barrer and H_2/CH_4 of 293. Other PI-based or thermal rearranged (TR)-based CMS membranes are also widely investigated. Yerzhankyzy et al. [425] reported PI-derived CMS membranes using 1,7-diamino-6H,12H-5,11-methanodibenzo [1,5]diazocine-2,8-diol (hydroxyl-functionalized Tröger's base, HTB) modified 4,4-(hexafluoroisopropylidene) diphthalic anhydride (6FDA-HTB). After carbonisation at 600 °C, the CMS membranes exhibited a H_2 permeability of 4390 Barrer and H_2/CH_4 selectivity of 765. Lee et al. [426] synthesised CMS membranes using a 6FDA-based PI with the incorporation of 3,3’-dihydroxyl-4,4’-diaminobiphenyl (HAB) monomer, resulting in a H_2 permeability of 9130 Barrer and H_2/CH_4 of 83. Furthermore, Hou et al. [253] fabricated CMS membranes from 6FDA-based PI modified with 9,9-bis[4-(4-amino-3-hydroxyphenoxy)phenyl] fluorene (BAHPPF). At a pyrolysis temperature of 600 °C, these membranes demonstrated a H_2 permeability of 9291 Barrer and H_2/CH_4 of 17.6. In summary, despite these studies focused on the strategy of chemically modifying polymer backbone structure to control the free volume and separation performance of the CMS membranes, the synthesis is complicated and intensive, and the CMS membrane is somewhat prone to physical ageing [427, 428].

Mixed matrix membrane (MMM) fabrication has emerged as an effective strategy to enhance the gas separation performance of CMS membranes. By incorporating thermally stable porous fillers into polymer precursors, it is possible to tailor the pore structure and improve gas transport properties to overcome material instability. Thermally stable inorganic fillers, such as zeolites [101], metal organic frameworks [429], and silica oxide [152, 430], enhance membrane permeability via their intrinsic microporous structures, though excessive loading can cause significant interfacial defects and pore blockage. For example, Cai et al. [431] investigated the doping concentration of zeolite 10X in Matrimid® polyimide-based CMS membranes and found that 10 wt.% zeolite loading increased H_2 permeability from 1709 to 1934 Barrer whilst H_2/CH_4 permselectivity decreased by 20% compared to 7.5 wt.% zeolite loading membrane results. While most studies have focused on inorganic microporous fillers, the integration of biomimetic materials into CMS membranes may offer an augmented carbon-on-carbon framework via co-pyrolysis route leading to improved material stability. However, to our knowledge, this new strategy has not been reported. Akin to this, Zhang et al. [229] recently reported a cobalt-based biomimetic complex using cobalt-2,6-bis(2-benzimidazolyl)pyridine (CoB) with specific CO_2 binding affinity, which was systematically incorporated into a Pebax® polymer matrix to form CoB doped Pebax membranes (without co-pyrolysis). They found that with a loading of 1.33 wt.% CoB, the MMM demonstrated an improved CO_2 permeability (675 Barrer) and a CO_2/N_2 selectivity (62) by 5.6-fold and 1.2-fold, respectively, compared to the undoped membrane due to the enhanced CO_2 affinity conferred by the CoB moiety. These findings suggest that such biomimetic complexes with preferential gas conjugation can significantly enhance gas affinity and selectivity for specific gas separation in MMM.

In this work, CoB is systematically doped into polyetherimide (PEI) precursor to study the effect of the CoB on the MMM and its co-pyrolysis behaviour in forming the carbon-on-carbon membrane microstructure. The membrane performance was evaluated for single gas permeation and binary gas separation over a 10-day period. It is hypothesized that the aromatic conjugated CoB structure with good thermal stability may undergo high carbon conversion during co-pyrolysis to offer augmented molecular sieving microstructure that assists in the formation of CMS membrane with additional rigid carbon plates and micropore cells. This study represents a departure from conventional MMM systems and CMS systems, offering a new route for tailoring CMS structures through a single step, co-pyrolysis process. Therefore, to the best of our knowledge, this novel combination of CoB doped CMS membrane material has not been synthesized and investigated for gas separation applications.

7.1.3. Methodology

7.1.3.1. Membrane preparation

The experimental flowchart was shown in Fig, 7-2. Initially, the membrane was subjected to the process described in Section 3.2.5. Furthermore, the sample characteristics and the gas permeation tests also be shown in Section 3.3 and 3.4, respectively. In this section, a series of CoBBP was added to the PEI membrane via co-pyrolysis process to form the CMS membranes. Furthermore, to identify the concentration of the membrane, the membrane was named XCoB_CM to determine the effect of the CoBBP concentration, where X represents the added concentration of CoBBP (0.5, 1, 2.5, 5, and 10 w/w.%)

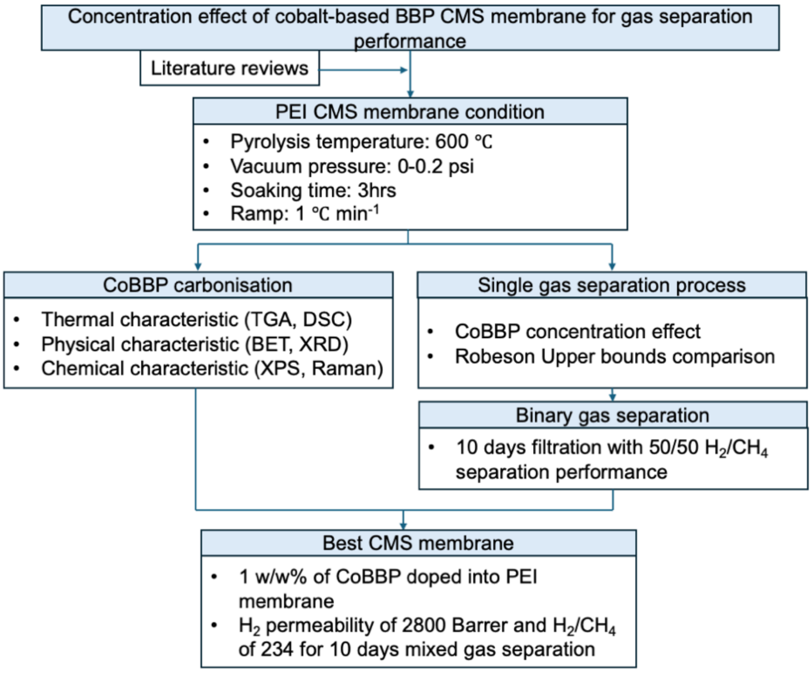

Fig. 7-2. The flow chart of the carbonisation with various CoBBP adding concentrations of PEI membranes.

7.1.4. Result and Discussion

7.1.4.1. BBP and CoB Carbonisation

The BBP and CoB powder samples were analysed by TGA-FTIR and DSC to evaluate the thermal stability and decomposition behaviour of BBP and CoB powder in nitrogen. As shown in Fig. 7-3(a), the TGA revealed that BBP underwent significant decomposition between 400-500 °C attributing to a 90% mass loss and reached a stable weight above 500 °C. In contrast, CoB displayed a multistep decomposition profile up to 800 °C. Two major weight-loss were observed between 200 to 300 °C (approximately 5%) and 300 to 400 °C (approximately 20%), after which the rate of decomposition was gradual, maintaining around 68% of the residual mass up to 700 °C. The third decomposition stage was observed between 700 and 800 °C. The weight change during the pyrolysis demonstrated that the CoB can maintained over 58 wt.%

even with temperature up to 800 °C, indicating its high thermal resistance and possible suitability for pyrolysis.

As shown in Fig. 7-3(b), the DSC analysis further highlights the differences in the early stages of the thermal behaviour between BBP and CoB. The DSC curve for BBP shows a sharp endothermic melting peak (T_m) at 118.8 °C, followed by a steady line during the second heating cycle, indicating the typical polymer melting behaviour. In contrast, CoB exhibited more complex thermal transitions. The first heating cycle reveals two endothermic peaks at 79.3 °C (T_{m1}) and 122.3 °C (T_{m2}), likely corresponding to softening and segmental transitions due to metal coordination-induced structural heterogeneity [432]. Notably, an exothermic transition appears at 296 °C (T_c) for CoB at the end of the first heating cycle, indicating the onset of irreversible thermal crosslinking. The behaviour of this exothermic event is not present in BBP. It indicates that cobalt coordination facilitated thermal crosslinking and structural reinforcement, which offers greater thermal resistance and carbon conversion.

To further elucidate the decomposition mechanisms between BBP and CoB, 2D contour spectral mapping from TGA-FTIR (gas phase) were conducted to monitor the gaseous products released during pyrolysis. As shown in Fig. 7-3(c), the FTIR spectral mapping of BBP decomposition gas products emitted during TGA analysis shows a broad peak appeared between 3100–3250 cm^{-1} at the onset of 150 °C, as attributed to the C-H and N-H bonding stretching for the BBP structure. These peaks continued to exist until 800 °C. The CO_2 peak at 2300 cm^{-1} appeared at 525 °C, indicating the BBP structure began to decompose its pyridine or benzimidazole by releasing small carbon dioxide molecules [433]. Comparing to the spectral mapping of CoB as shown in Fig. 7-3(d), peaks at 3750 and 1600 cm^{-1} corresponding to H_2O and 2350 cm^{-1} to CO_2 evolved between 300 and 400 °C concertedly with a small amount of C_2H_4 in isolation. This stage reflects the removal of water molecules and partial oxidation of the CoB structure giving rise to a 15 wt% weight loss. A second decomposition occurred between 700 and 800 °C, during which CO_2 peaks appeared again, which coincided with the last decomposition stage. However, there is no evidence of the C-H and N-H peaks in the CoB spectral map throughout the whole temperature profile, suggesting that thermal crosslinking between the carbonized pyridine and benzimidazole moieties are preserved. According to previous research, cobalt is recognised as a graphitization catalyst that can lower the pyrolysis temperature to produce graphite and amorphous carbons [434-436]. Furthermore, cobalt metal ions may be seen as a hard template to coordinate the small char fragments, resulting in a crosslinking effect with other char fragments [437].

Additionally, Fig. 7-3(e) provides a visual representation of the material's transformation. The precursor BBP (white powder) changes to a yellow CoB complex after cobalt coordination, and eventually forms a black, carbon-rich structure (CoB_C) after pyrolysis. This colour transition correlates directly with the thermal and chemical transitions observed in the TGA-FTIR and DSC analyses. The molecular diagrams illustrate the proposed chemical evolution, postulating the role of cobalt in stabilising the intermediate structures and in facilitating the formation of a crosslinked carbon network.

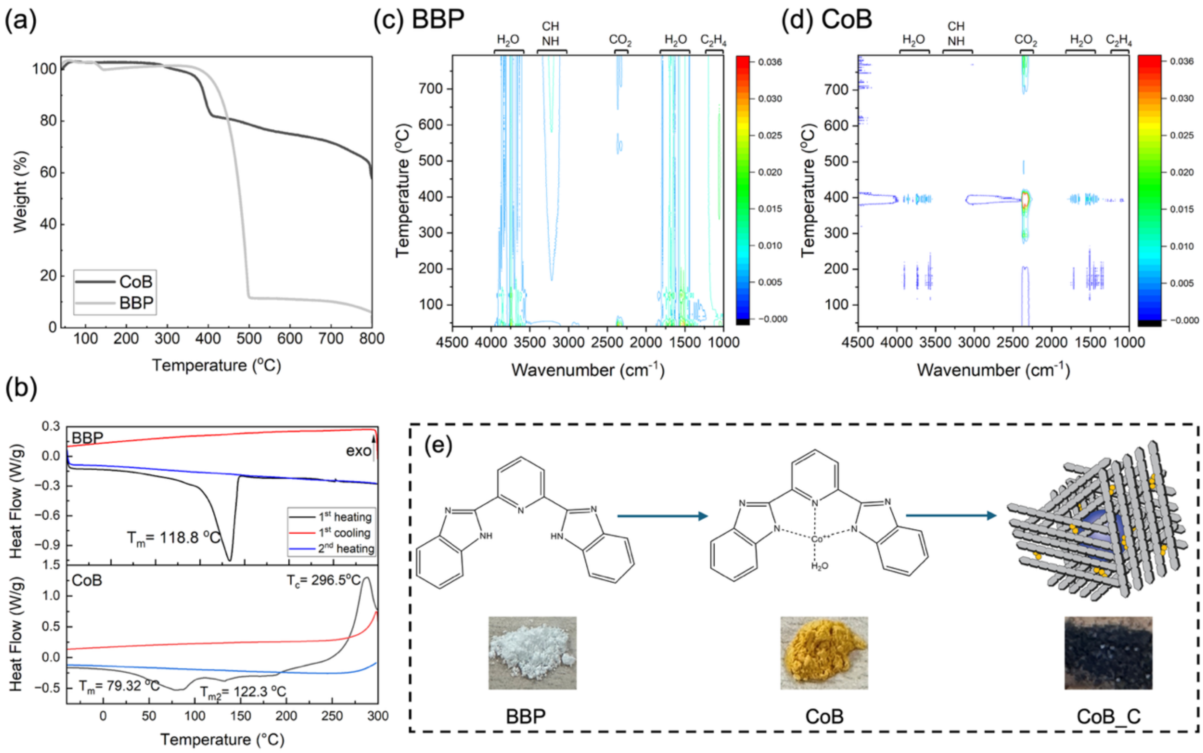

Fig. 7-3. The thermal and structural characterisation of BBP and CoB. (a) TGA analysis obtained from TGA-FTIR measurement, (b) DSC curves with two heating cycles, (c, d) 2D contour FTIR spectral mapping of (c) BBP and (d) CoB, and (e) schematic illustration of the material process, along with digital images of the corresponding materials.

The chemical structure of CoB_C was further evaluated using XRD, Raman spectroscopy, XPS and CO_2 physisorption techniques. At the outset, CoB was pyrolyzed under vacuum at 600 °C to form the CoB_C using the same thermal condition as the CMS membranes in this study. As shown in Fig. 7-4(a), a broad peak ranging from 15° to 35° 2θ, centred at 23.3° 2θ, corresponding to a d-spacing of 3.8 Å. This indicates a high composition of amorphous carbon derived from the CoB. Notably, no crystalline cobalt peaks were observed, suggesting that cobalt metals was not segregated or aggregated within the CoB_C structure [435].

Moreover, the degree of graphitisation of CoB_C was confirmed by Raman spectroscopy as shown in Fig. 7-4(b), which indicates three main deconvoluted peaks within the broad carbon peaks between 800 and 2000 cm^{-1}. The deconvoluted peaks at 1315 cm^{-1}, 1527 cm^{-1}, and 1592 cm^{-1} are assigned to be G, D_1, and D_3 bands, respectively [438, 439]. The Raman result indicates that the CoB_C structure can be described as a highly disordered graphitic structure [440]. The G band of CoB_C can be seen as the E_{2g}-symmetry vibration of the graphitic lattice, and the D_1 band is the A_{1g} symmetry vibration of the disordered graphitic lattice, such as the graphene layer edges. Moreover, the D_3 band is a typical amorphous carbon of CoB_C, such as pyrrolidine and fragments of benzimidazole [441]. By evaluating the D_1/G graphitic ratio, one can further appreciate the degree of the structural defect. The D_1/G ratio of CoB_C is 4.58, indicating numerous edges and defects in the carbon chain, and the structure could not be identified as ordered graphite. This finding concurs that the CoB_C carbon structure is amorphous, which is in good agreement with the XRD result.

Further insight into the chemical structure of CoB_C was obtained through XPS. The full survey spectra (Fig. S7-1(a)) revealed the atomic percentage of Co was only 1.22% in the amorphous carbon structure. Furthermore, high resolution C_{1s} spectra demonstrated sp^2 (C=C) and sp^3 (C-C) hybridised carbons with the sp^3/sp^2 ratio is approximately 1.5, which can be attributed to imperfect graphite stacking [442, 443]. For the Co_{2p} spectra (Fig. S7-1(d)) represented the Co-N binding peaks at 780 and 796 eV, indicating cobalt ions is coordinated to the nitrogen atoms [444]. The N_{1s} spectrum (Fig. 7-4c) confirmed the presence of N-pyridinic (397.7 eV) and N-pyrrolic (399.6 eV) species, with no significant signal corresponding to graphitic nitrogen due to the cobalt ion coordination [444]. These results are in good accord with the XRD and Raman evidencing that the CoB_C carbon sample is completely amorphous with a low percentage of cobalt-coordinated nitrogen group and nitrogen conserved in the carbon chain structure.

The textural property and pore size distribution (PSD) were determined by CO_2 physisorption technique (Fig. 7-4d), which shows a trimodal pore size distribution with pore sizes centred at 5.4, 6.3 and 7.5 Å. The PSD indicates that nearly 68% of the pore size was < 7 Å (ultramicropores), and 32% was in the range of 7 to 9 Å (micropores). For comparison, the PEI_C sample (Fig. S7-3(b)) exhibits a bimodal distribution at 5.7 Å and 7.8 Å, with an ultramicropore/micropore proportion of 51.1% and 48.9%, respectively. Notably, the pore sizes are relatively larger than those observed in the CoB_C samples. Additionally, both samples demonstrated comparable surface areas and pore volumes of approximately 77 m^2 g^{-1} and 0.027 cm^3 g^{-1}, respectively (Table S7-1). With a high percentage of ultramicropores, CoB_C is expected to be a promising dopant within the CMS membrane to further improve ultramicropore tailoring to confer high gas selectivity and separation.

In comparison, a detailed material characterization of the PEI_C is presented in Fig. S7-4 to S7–6. The corresponding results show PEI_C carbon sample have a similar amorphous nature whilst the D_1/G ratio of 1.76 suggesting a higher degree of graphitization. For the synthesis of CoB doped CMS membranes (CoB_CM), PEI membranes with 0.5 to 10 wt% CoB dopants were co-pyrolyzed at 600 °C to evaluate the dopant’s impact on the modified CMS membrane microstructure and its gas separation performance. For comparison, PEI-derived CMS membrane without CoB is included (PEI_CM).

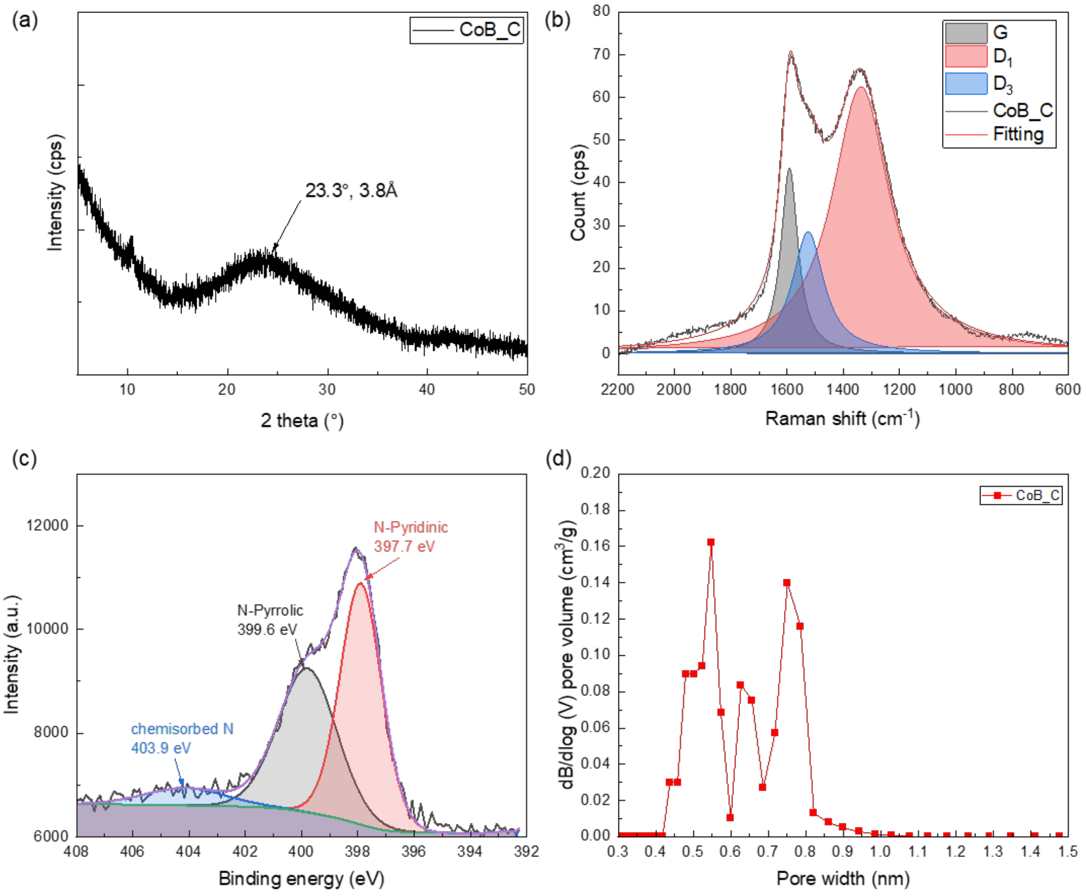

Fig. 7-4. The chemical characteristics of CoB_C samples showing (a) XRD, (b) Raman spectrum with the deconvoluted peaks and the overall fitting, (c) XPS narrow scan of N_{1s} spectrum with the deconvoluted peaks and the overall fitting, and (d) pore size distribution from CO_2 physisorption.

7.1.4.2. PEI_CM and CoB_CM Membrane Structure

To evaluate the microstructure and the physicochemical properties of the PEI_CM and CoB_CM membranes, a series of morphological and elemental analyses were conducted. As shown in Fig. 7-5(a), the cross-sectional SEM images of the PEI_CM sample revealed that the carbon membrane was successfully coated on the macroporous alumina substrates without any intermediate layer. Furthermore, elemental mapping via EDS confirmed a well-defined and continuous interface between the carbon top layer and the alumina support, with no evidence of collapse or infiltration into the porous structure of the support. The PEI_CM exhibited a thickness of approximately 10.6 ± 0.38 μm, while the 1CoB_CM (1 wt.% doped) sample displayed a comparable thickness of 9.9 ± 1.1 μm, which is also observed for the other CoB_CM samples with varying CoB concentration (Fig. S7-7). This suggests that CoB doping and co-pyrolysis does not compromise membrane top layer integrity and morphology. Furthermore, as shown in Fig. 7-5(c), high-resolution TEM (HRTEM) analysis of 1CoB_CM sample showed a homogeneous amorphous carbon structure without any evidence of crystallinity or cobalt aggregation, which is consistent with the DSC and XRD results. This is further demonstrated by Fig. S7-8. Additionally, the STEM-EDS mappings revealed that both the PEI_CM and 1CoB_CM samples exhibited very similar elemental composition, consisting predominantly of carbon and oxygen in the carbon membrane, with minor nitrogen components in both membranes (Fig. S7-9). Moreover, detecting cobalt atom in 1CoB_CM from TEM and STEM is challenging due to the extremely low CoB doping amount. Furthermore, the high-resolution C_{1s} and N_{1s} XPS spectra of the other CoB doped membranes are presented in Fig. S7-10, and the results are consistent with TEM analysis.

The pore size distribution (PSD) of all the carbon molecular sieve samples was determined via CO_2 physisorption process. As shown in Fig. 7-5(d), the calculated PSD revealed that all the membrane pore widths were below 9 Å, exhibiting a distinct bimodal distribution. Specifically, ultramicropores were centred at approximately 3.6 Å, while larger micropores were centred at around 7.5 Å, consistent with previously reported PEI-derived CMS membranes [159, 445, 446]. Notably, the relative proportion of ultramicropores and micropores shows that with increasing CoB loading, the proportion of ultramicropores increases, reaching 93.7 % for 1CoB_CM compared to 76.8 % for the PEI_CM sample. In contrast, the fraction of larger micropores decreased significantly from 23.2% (PEI_CM), and 6.3% (1CoB_CM), to

5.3% (5CoB_CM) and 3.3% (10CoB_CM). These findings indicate that carbonised CoB plays an important role in tailoring the micropore architecture, potentially enhancing the molecular size-sieving properties of the CoB doped membranes. The corresponding adsorption isotherms for each membrane are presented in Fig. S7-11, all of which exhibit a type I isotherm attributed to microporous structures.

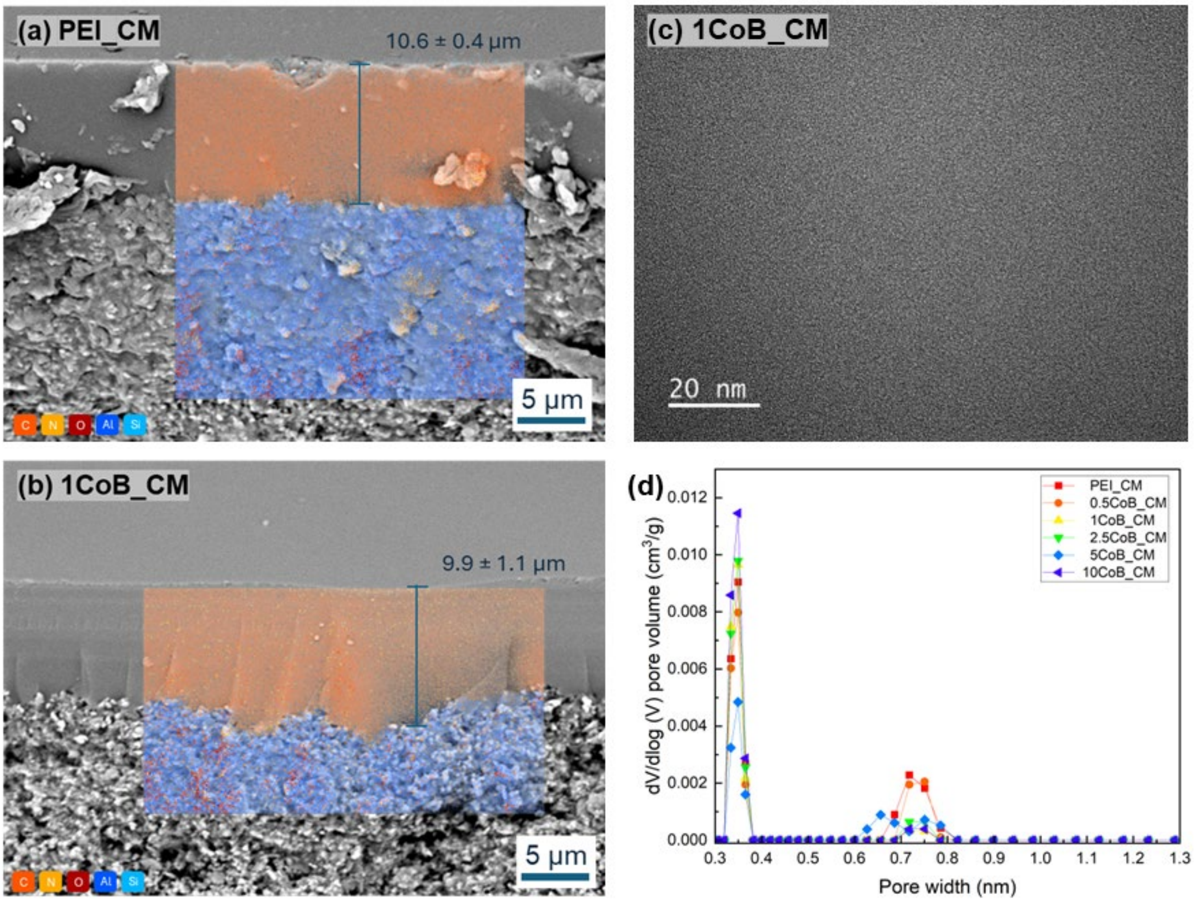

Fig. 7-5. The morphology and pore size distribution characteristic of the CMSM. (a)-(b) the cross-sectional SEM images of (a) PEI_CM, (b) 1CoB_CM, (c) HRTEM image of 1CoB_CM, and (d) pore size distribution from CO_2 physisorption for all the membranes.

7.1.4.3. Single gas permeation test

The single gas permeation evaluation of all the CM membranes using He, H_2, CO_2, O_2, N_2, and CH_4 at a temperature of 35 °C. Before co-pyrolysis process, the PEI and CoB doped PEI membranes were tested with H_2, CO_2, N_2, and CH_4 single gas permeations, and their H_2/CH_4 permselectivities lie in the range between 69 and 98 indicating all doped and non-doped PEI membranes are defect-free (Table S7-4). All the membranes were evaluated immediately after co-pyrolysis was completed to ensure consistency. Each dataset was collected from results of triplicate membranes, and each gas was tested three times to ensure data reproducibility and statistical robustness. As shown in Fig. 7-6(a), pure gas permeance as a function of gas type with respect to their kinetic diameters for the CM membranes were plotted. In the first instance, it is clear that gas transport occurs fastest for the H_2 gas while slowest for the CH_4 gas irrespective of membrane types as governed by the molecular sieving effect and the van der Waal interactions for the non-polar and polar molecules with the membrane pore wall. This trend was particularly evident between the H_2 (2.89 Å, non-polar), CO_2 (3.3 Å, polar) and N_2 (3.64 Å, non-polar) with gas permeance values of 328 ± 49, 118 ± 8.6 and 3.8 ± 0.3 GPU, respectively, for 1CoB_CM.

Secondly, CoB doping leads to significant gas permeance enhancement for He, H_2 and CO_2 but less noticeable for the larger O_2, N_2 and CH_4 gases. For example, PEI_CM exhibited moderate gas permeance, with H_2 and CH_4 permeances of 108 ± 5 and 3 ± 1.5 GPU, respectively, whereas doping the CM membrane with 1 wt.% CoB and higher leads to a two- to four-fold gas permeance enhancement for the corresponding gases. He and H_2 permeances rose with CoB concentration up to 5 wt.%, peaking at 408 ± 32 GPU for H_2 permeance, approximately 4 times higher than that of the PEI_CM. In contrast, CH_4 permeance maintained nearly unchanged (3 ± 1.2 GPU), suggesting that the increased proportion of the ultramicropore structure of the CoB doped membranes confer enhanced transport of smaller gases without significantly increasing the gas permeance of gases with larger kinetic diameter. However, this conjecture trended oppositely with higher CoB concentration up to 5 wt% as can be observed by the permselectivity values.

As shown in Fig. 7-6(b), gas permselectivities increase significantly with CoB doping compare to the PEI_CM. 1CoB_CM achieved the highest permselectivity across all gas pairs (O_2/N_2, CO_2/N_2, CO_2/CH_4, H_2/N_2, H_2/CH_4, and He/N_2), suggesting that 1 wt.% of CoB is an optimal concentration for enhancing the separation performance of the membranes. Although the 2.5CoB_CM and 5CoB_CM membranes also exhibited the high gas permeances, the slight rise in N_2 and CH_4 permeances compromised its potential gas selectivity, underscoring a trade-off between permeability and selectivity at higher CoB dopant levels.

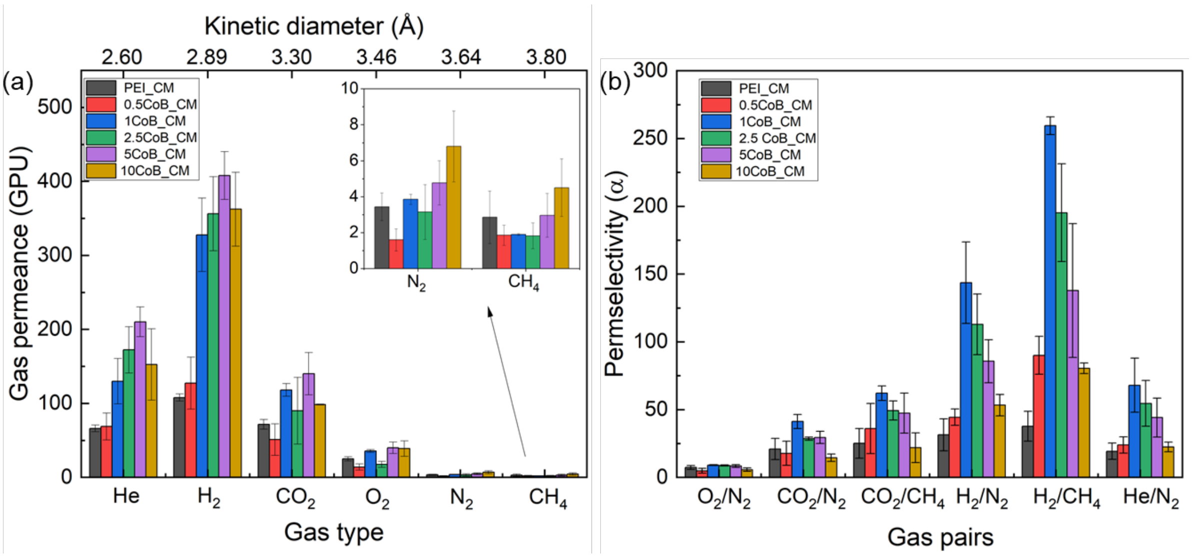

Fig. 7-6. The single gas permeance of the PEI_CM and CoB_CM membranes as a function of gas types showing (a) the gas permeance values and (b) the permselectivities for the respective gas pairs.

The gas permeation performance of the membranes produced in this work was benchmarked against the most recent revision of the Robeson upper bound plots [66-68]. While originally established for polymeric membranes, the Robeson upper bound remains a valuable reference for evaluating the trade-off performance of new CMS membranes, offering comparative insight into their separation efficiency relative to other membrane materials. As shown in Fig. 7, four Robeson's Upper Bound plots with the gas pairs He/N_2, H_2/CH_4, O_2/N_2, and CO_2/N_2, were selected, and the gas permeability unit expression of Barrer is used for direct comparison. These results were also compared with those of CMS membranes derived from various polymeric precursors, including cellulose [118, 173, 447], PEI [150-153], and 4,4'-(Hexafluoroisopropylidene) diphthalic anhydride (6FDA) [12, 253, 448-452]. Cellulose-based CMS membrane, due to their low cost, dense structure, and extensive hydrogen bonding, are known for their low permeability but high selectivity [28]. In contrast, 6FDA-based carbon membranes are characterised by high free volume [449, 453], which translates into superior gas permeability. To ensure meaningful comparisons, all literature data were selected from carbon membranes pyrolyzed using a temperature range of 550-650 °C similar to our work.

As shown in Fig. 7-7(a), the PEI_CM exhibited He/N_2 separation performance slightly below the 2008 revisited Robeson upper bound. However, upon CoB doping, the CoB_CM membranes surpassed the upper bound due to significantly improved helium permeability and He/N_2 permselectivity. Notably, the 5CoB_CM exhibited the highest He permeability (2100 ± 200 Barrer) with a permselectivity (αHe/N_2) of 44 ± 14. To the best of our knowledge, limited data exist for PEI-based CMS membranes for He/N_2 separation. These findings indicates that the CoB_CM membranes achieved higher gas permeability compared to cellulose-based CMS membranes, although still trailing behind 6FDA-based CMS membranes, attributable to lower intrinsic free volume of the PEI-derived CMS membranes even with the minimised trade-off via CoB doping and co-pyrolysis.

As shown in Fig. 7-7(b), it is observed that CoB concentrations above 1 wt.% enable the CoB_CM membrane trade-off performance to exceed the 2015 upper bound for H_2/CH_4 separation. The PEI_CM already exhibited comparable or slightly superior H_2 permeability relative to other PEI-based CMS membranes albeit permselectivity was modest. The incorporation of CoB further enhanced both H_2 permeability and $\alpha H_2/CH_4$. The 1CoB_CM offered the highest $\alpha H_2/CH_4$ at 259 ± 7 with H_2 permeability at 3280 ± 485 Barrer. However, with higher concentration of CoB, a lower permselectivity was obtained. Moreover, similar trends were observed for O_2/N_2 (Fig. 7-7(c)) and CO_2/N_2 (Fig. 7-7(d)) trade-off plots. The CoB dopant increased O_2 and CO_2 permeabilities while maintaining relatively modest permselectivity relative to N_2 gas. Overall, the 1CoB_CM membrane provided a balanced performance, delivering relatively high permselectivity across all four gas pairs. Meanwhile, the 5CoB_CM membrane exhibited the highest permeability, but with a slight modest permselectivity.

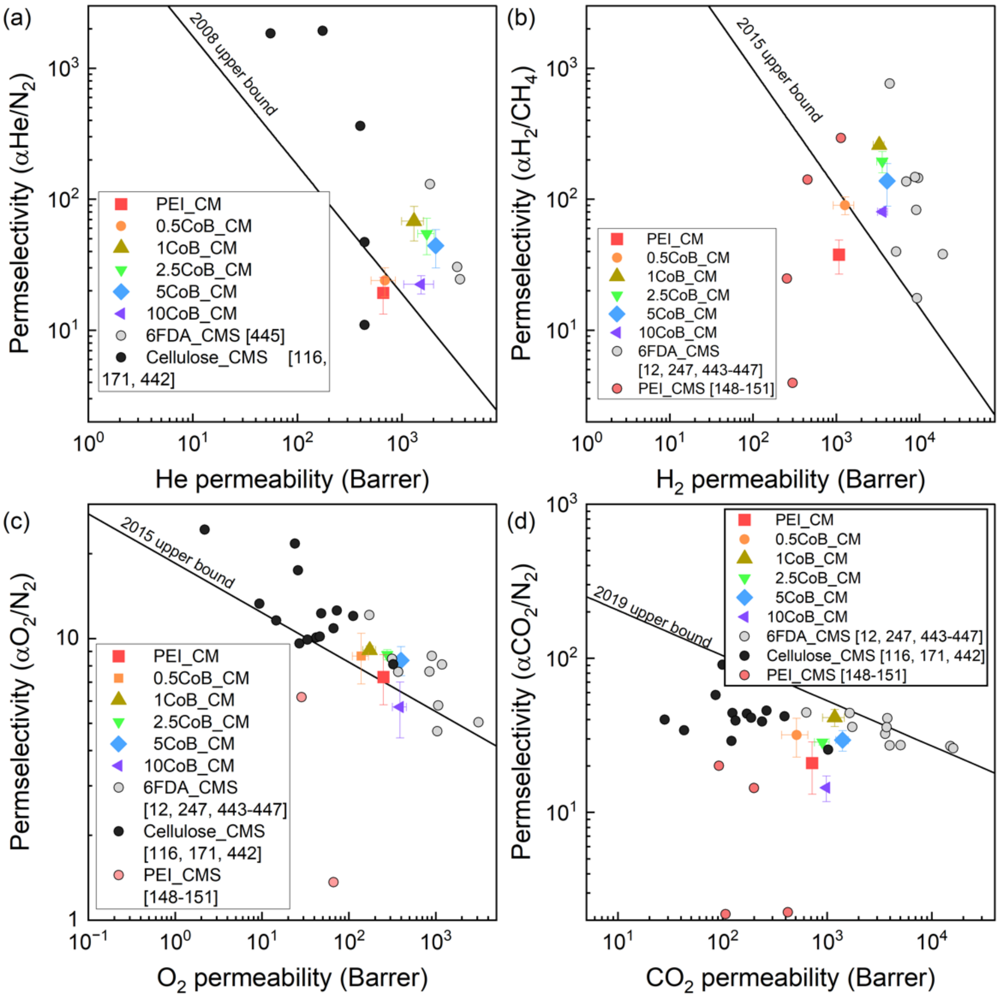

Fig. 7-7. The variety of CoB_C concentration membranes resulting in the state-of-the-art Robeson upper bound with of 6FDA and cellulose carbon membranes synthesis under 600 °C, (a) He/N_2, (b) H_2/CH_4, (c) O_2/N_2 and (d) CO_2/N_2.

7.1.4.4. Binary gas permeation test

The gas separation performance of the PEI_CM and 1CoB_CM membranes were evaluated using 50/50 vol.% H_2 and CH_4 binary gas mixture. As shown in Fig. 7-8, a 10-day continuous H_2/CH_4 separation was performed under a feed pressure of 2 bar gauge. For the PEI_CM, the initial H_2 and CH_4 permeabilities were 667 ± 4 and 54 ± 4 Barrer, respectively. Over the 10-day testing period, both gas permeabilities declined by approximately 17% for H_2 and 22% for CH_4 resulting in a 14% increase of H_2/CH_4 selectivity. This result is on par with Sedigh et al. who also showed H_2 permeability and H_2/CH_4 selectivity of the Poly(furfuryl alcohol)-derived CMS membrane decline over 4 days [454]. In contrast, 1CoB_CM maintained a sustained separation performance over the 10 days period. Although there are marginal variations of gas permeability across the test period, the overall H_2 permeability of 2752 ± 46 Barrer and CH_4 permeability of 13.3 ± 3.0 Barrer led to a steady H_2/CH_4 selectivity of 207 ± 43, which is comparable to the H_2 permeability and $\alpha H_2/CH_4$ permselectivity derived from the single gas permeation. Interestingly, the H_2/CH_4 selectivity dropped to 152 ± 1 on day 4 followed by a gradual rebound to 234 ± 2 by day 10, which showed the membrane performance is consistently and considerably stable.

These results illustrated that the incorporation of co-pyrolysis of CoB in PEI-derived CMS membrane augmented the molecular sieving structure that helps to mitigate the loss of hydrogen permeability and selectivity. The formation of a highly ultramicroporous structure in 1CoB_CM membrane offers enhanced hydrogen transport while hindered CH_4 permeability. This structural tuning not only improves the durability of hydrogen permeation but also maintains high separation performance stability over time.

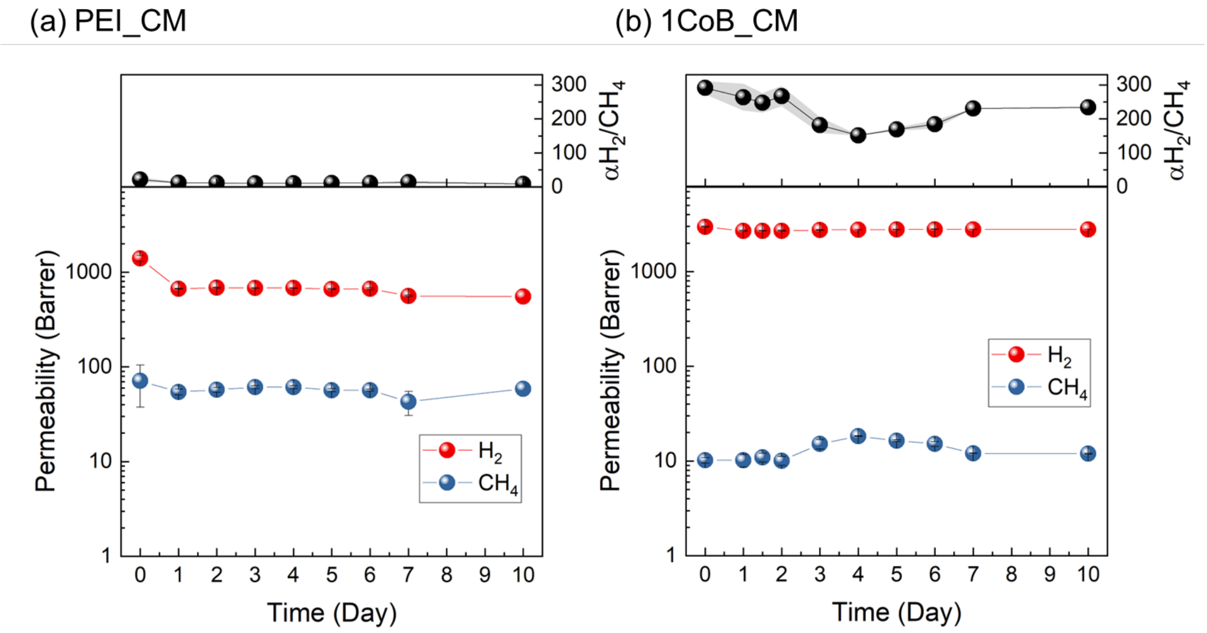

Fig. 7-8. The binary gas (H_2/CH_4) separation performance for the (a) PEI_CM and (b) 1CoB_CM membranes. The membrane testing under 2 barg of mixed gas under with 20 sccm Ar sweep gas with 35 °C operation temperature.

7.1.4.5. Cobalt-coordination modifier reinforces CMS microporous

In this study, the incorporation of a cobalt-based (CoB) dopant into a PEI polymer through co-pyrolysis significantly enhanced the ultramicroporous structure leading to improved gas permeation and separation stability performance. The observed enhancement can be attributed to the thermally crosslinking and thermally stable properties of the CoB material at temperature of approximately 300 °C. As schematically illustrated in Fig. 7-9, PEI_C structure shows similar CMS microstructure with a bimodal pore size distribution (Fig. S7-6(b)). In contrast, CoB_C structure features short-chains of CoB carbon embedded within the CMS bulk as orphan chains or integrated cell structures. The CoB chains may undergo self-crosslinking (orphan chain) or crosslinking with the aligned carbon strands (within the cells) through cobalt-nitrogen coordination, thus forming a more interconnected and rigid carbon network leading to a new ultramicropore type (green pore size population) and a trimodal pore size distribution (Fig. 7-4(d)). During the co-pyrolysis process of CoB and PEI, it is postulated that the initial degradation of PEI involves the loss of bisphenol A and –CH_3 side groups [433], creating new reactive sites that CoB species may bind with the partially pyrolyzed PEI chains, which results in interstrand carbon-carbon crosslinking within the micropore cells. As shown in Fig. 7-5d, the 1CoB_CM's pore size distribution revealed a significant 22% increase of the relative ultramicroporous volume reaching to a total of 93.7% (Fig. 7-5(d)), giving rise to a 17-fold increase in gas permselectivities without compromising the gas permeability of the smaller gas (Fig. 7-6(b) H_2/CH_4), and a stable gas permeability and H_2/CH_4 selectivity over a 10-day test.

The co-pyrolysis approach introduces a novel concept by utilizing cobalt coordination biomimetic materials in tandem with polymer pyrolysis to strategically tailor membrane microstructures and advance gas separation performance. To our knowledge, this is the first reported application of such CoB additives in CMS membrane fabrication through co-pyrolysis.

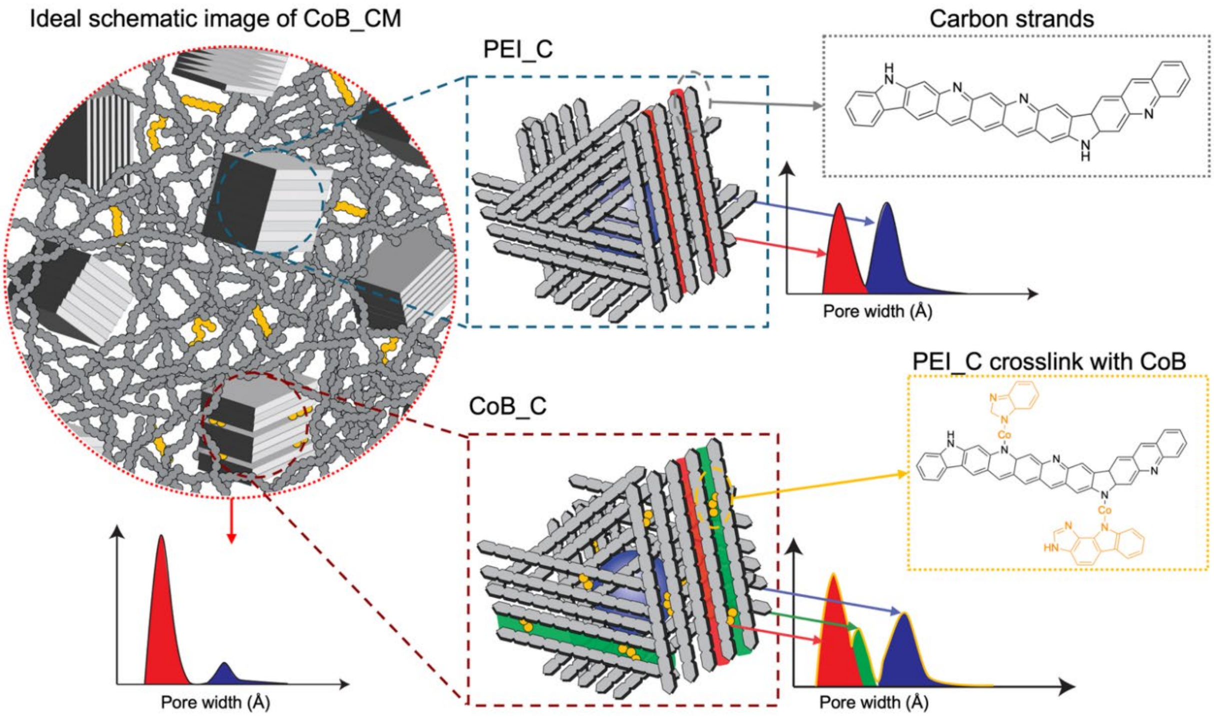

Fig. 7-9. The idealized schematic representation of hypothesized PEI-based carbon molecular sieve structures with and without CoB co-pyrolysis.

7.1.5. Conclusion

In this study, the gas separation properties of CoB doped carbon molecular sieve membranes were investigated via co-pyrolysis to enhance the ultramicroporous structure of PEI-derived CMS membrane. The effect of CoB concentration on material-membrane properties and gas separation performance relationship was elucidated. CoB showed excellent thermal stability and high carbon yield (75%) during pyrolysis due to the cobalt-nitrogen coordination-induced effect. Pore size distribution demonstrated that the CoB_C is microporous texture containing 68% of ultramicropores (< 7Å). Upon CoB incorporation, the relative degree of ultramicropores in 1CoB_CM increased to 93.7% compared to only 76.8% in the PEI_CM (undoped) membrane. Under single gas permeation tests, 1CoB_CM membrane demonstrated an excellent balance between H_2 permeability (3280 ± 490 Barrer) and H_2/CH_4 permselectivity (259 ± 6) surpassing the Robeson upper bound, similarly observed for the He/N_2 and O_2/N_2 trade-off performance. A 10-day H_2/CH_4 binary gas separation demonstrated 1CoB_CM maintained H_2 permeability with approximately 2700 Barrer and a stable H_2/CH_4 selectivity of 222 over the whole testing period, whereas the PEI_CM separation performance was significantly lower by 17-fold albeit performance stability was comparable. The findings of this work represent a new strategy to explore co-pyrolysis of biomimetic moiety with CMS membranes and the potential of CoB as an effective structural modifier of ultramicroporous membranes for gas separation applications.

7.2. Metal BBP effect on the PEI carbon molecular sieving membranes

7.2.1. Introduction

In Section 7.1, we showed that CoBBP demonstrates high thermal stability, enabling crosslinking of BBP structure and facilitating the formation of a new carbon molecule sieve framework, thereby enhancing H_2 separation performance. To further explore other metal-ion-effect, FeBBP and ZnBBP were studied using 1 w/w% in PEI membranes and co-pyrolysis was carried out to produce the FeB_CM and ZnB_CM to assess their gas permeation behaviour and separation efficiency.

In this study, BBP, FeBBP and ZnBBP were independently incorporated into polyetherimide (PEI) membranes to examine the increase in gas permeability in PEI CMS membranes for gas separation processes. A comprehensive analysis of the impact of thermally resistant additives on the physical, chemical, and gas separation properties of the membrane demonstrated the potential of modifying the blending method to produce high-performance gas separation membranes. Furthermore, the mixed CO_2/CH_4 (10/90) under a high RH (~100%) feed stream was also evaluated to assess the feasibility of a CMSM separating the simulated wet-biogas process.

7.2.2. Methodology

7.2.2.1. Materials and experimental setup

The polymeric membrane blended with various MtBBP was pyrolysed to be CMS membrane to investigate the MtBBP performance. As shown in Fig. 7-10, the carbonisation process was assessed for 1FeBBP and 1ZnBBP. Before assessing the gas separation performance, the membranes underwent pyrolysis at 600 °C under conditions of 0–0.2 psi for 3 h to form carbon molecular sieve membranes. Initially, MtBBP powder samples were pyrolyzed under the same conditions as the CMS membrane synthesis temperature. Subsequently, the carbonized samples (MtB_C) were subjected to a series of thermal (TGA and DSC), physical (BET and XRD), and chemical (XPS and Raman) analyses to determine their material properties. The methodologies for these synthesis and characterizations are detailed in Chapter 3. After confirming the additive material characteristics, the morphology (SEM) and the physical (BET) and chemical properties (Raman and XPS) of the membrane were observed to elucidate the pyrolysis mechanism and membrane properties. Additionally, the carbon membrane was tested with various single gases with kinetic diameters less than 3.8 Å. Furthermore, the BBP_C (BBP_CM) and ZnB_C (ZnB_CM) membranes were selected to evaluate the CO_2/CH_4 mixture under 100% relative humidity (RH) for long-term separation, in order to analysed the membrane properties after exposure to RH conditions and during the heat regeneration process.

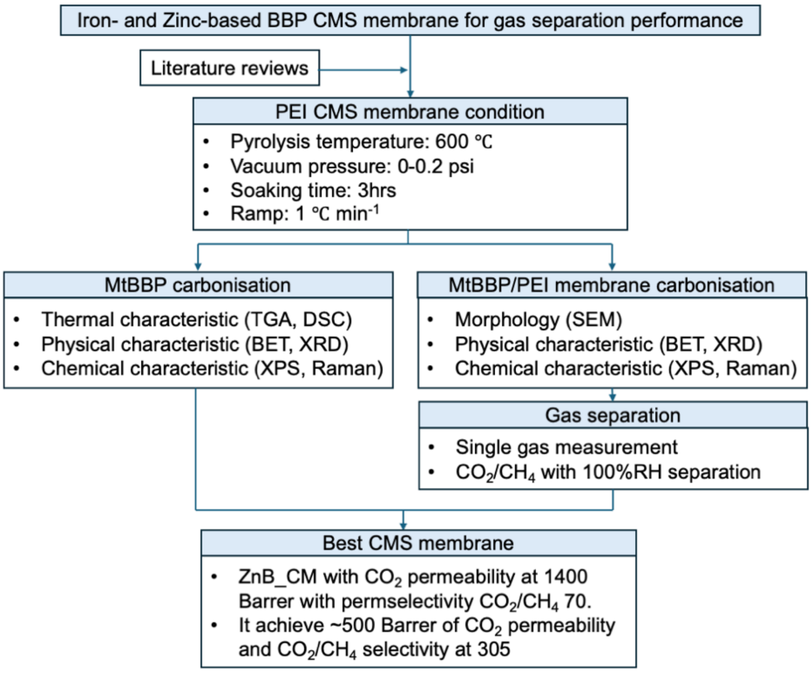

Fig. 7-10. Experimental flow chart for the metal based BBP CMS membranes.

7.2.3. Results and Discussion

7.2.3.1. FeBBP and ZnBBP characteristics

The FeBBP and ZnBBP samples were analysed using TGA and DSC to assess their thermal stability and phase transition behaviour during pyrolysis in a N_2 atmosphere. As shown in Fig. 7-11(a), the weight changes of BBP, FeBBP, and ZnBBP during heating were evaluated by TGA to determine their thermostability. BBP underwent complete decomposition when the pyrolysis temperature exceeded 450 °C. In contrast, FeBBP and ZnBBP exhibited significantly improved thermal stability, retaining 81.9% and 75.0% of their char weight, respectively, at 650 °C. This occurrence indicates that metal doping enhances the thermal resistance of the BBP structure and demonstrates the potential performance of CMS additives as CoBBP materials.

As shown in Fig. 7-12(b), the DSC analysis further demonstrates the differences in initial thermal transitions among BBP, FeBBP and ZnBBP. Analysis further demonstrates the differences in initial thermal transitions among BBP, FeBBP, and ZnBBP. Pristine BBP exhibits a sharp endothermic peak at 118.8 °C, corresponding to its melting point. Upon metal doping, the thermal transitions shift significantly. FeBBP displays a major endothermic peak at 57.2 °C, distinct from both pristine BBP and $FeCl_3$ (FeBBP precursors), indicating strong chelation between Fe ions and the BBP backbone. For ZnBBP, two endothermic peaks are observed at 54.5 °C (T_{m1}) and 114.7 °C (T_{m2}), corresponding to a eutectic melting event and the primary melting point, respectively. The appearance of the eutectic peak and the slight shift in the main melting point suggest successful structural modification of BBP through Zn coordination. Notably, no thermal signals corresponding to free $ZnCl_2$ (ZnBBP precursor) were detected, confirming the formation of a new ZnBBP complex [455].

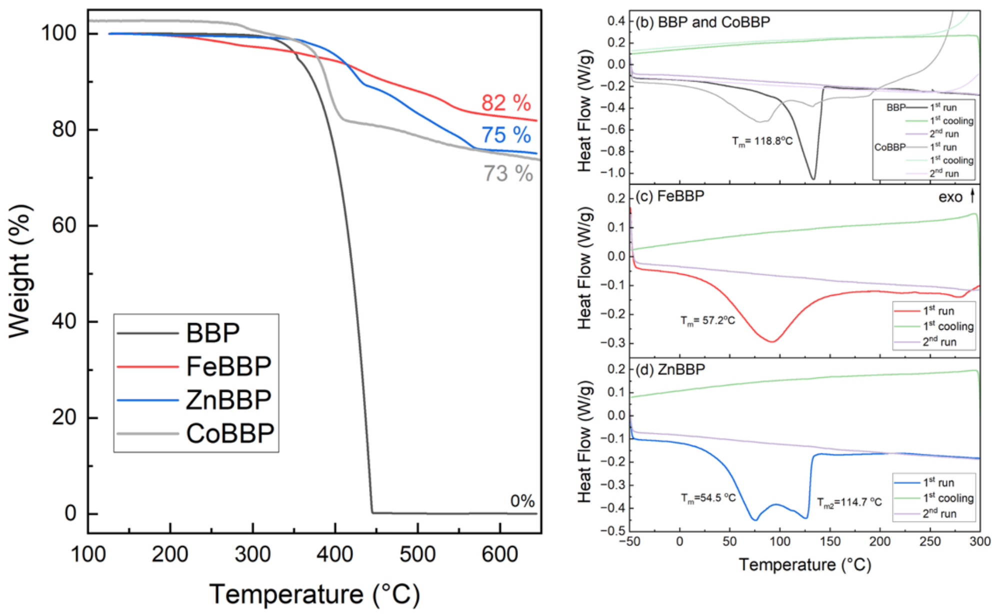

Fig. 7-11. Thermostability of BBP and MtBBP, (a) TG diagram and (b) DSC analysis. Data for BBP and CoBBP is reproduced from Fig. 7 3 in Section 7.1.4.1.

The graphitisation and structural disorder of carbonised MtBBP derivatives were analysed using a series of characteristics. As shown in Fig. 7-13(a), the Raman spectra of FeB_C and ZnB_C exhibited the typical D and G bands of carbon-based materials. The G bands, located at 1580 cm^{-1}, corresponds to the E_{2g} vibration of sp^2-bonded carbon atoms in graphitic materials, while the D bands (D_1, D_2, D_3) are associated with various forms of structurally disordered carbon [438]. In the FeB_C sample, spectral deconvolution revealed the presence of the D_1 band (disordered graphitic edges), D_2 (graphitic surface defects), and D_3 (amorphous carbon), all indicative of the amorphous carbon structure. The high D_1/G intensity ratio of 3.07 for FeB_C suggests a significantly higher degree of disorder carbon compared to the PEI_C sample, which exhibited a D_1/G ratio of 1.69. This indicates that Fe coordination promotes more extensive structural disorder during carbonisation. For ZnB_C, a D_1/G ratio of 4.99 and a strong D_3 contribution were observed, suggesting a structure that combines ordering.

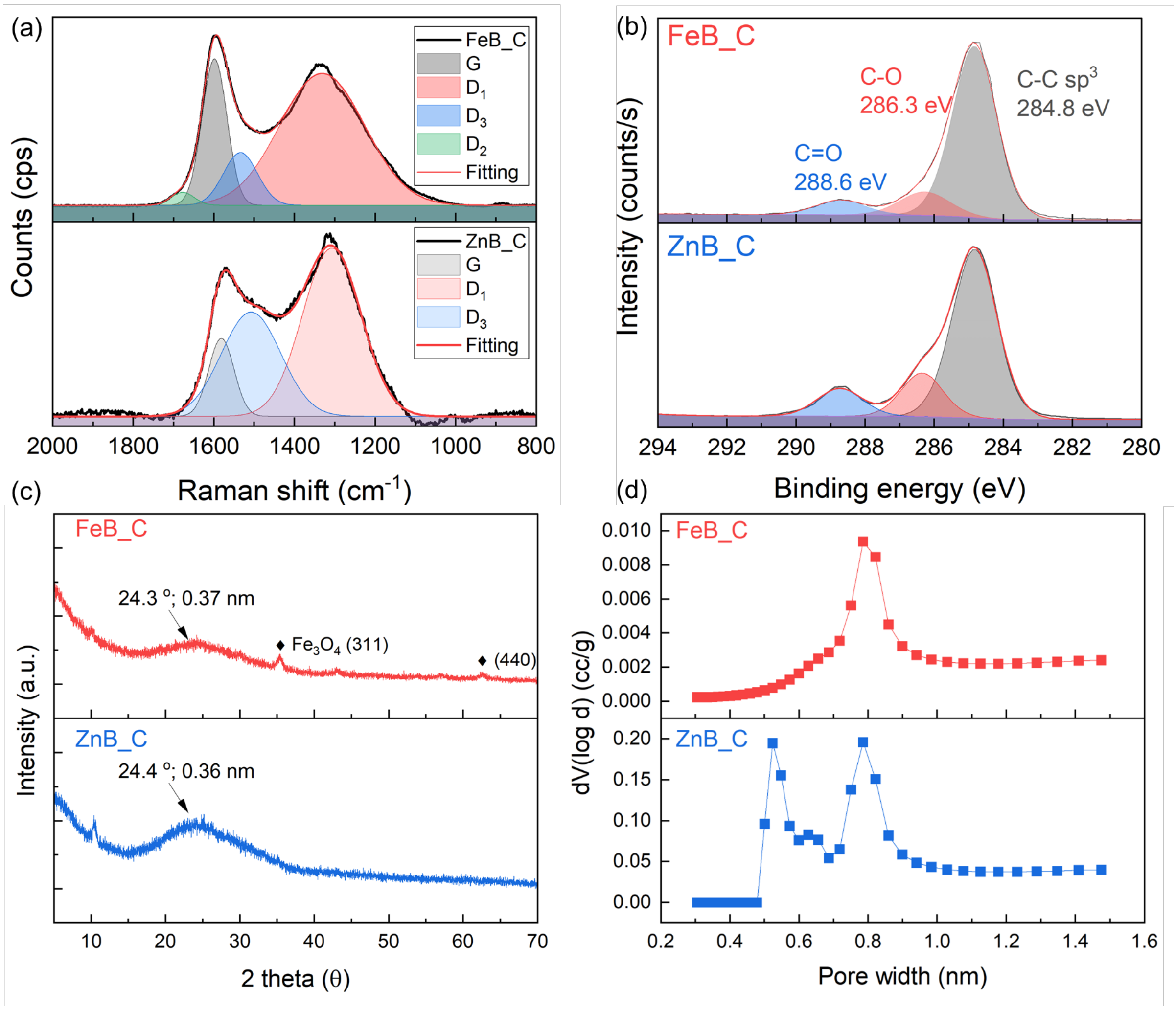

Fig. 7-12. The chemical characteristic of the FeB_C and ZnB_C samples showing (a) the Raman spectrum with the deconvoluted peaks and the overall fitting, (b) high-resolution C_{1s} spectra of the XPS analysis, (c) the XRD pattern, and (d) pore size distribution from CO_2 physisorption. Data for CoBBP can be found in Fig. 7-4 in Section 7.1.4.1.

The surface chemical composition of the FeB_C and ZnB_C was analysed by XPS full survey (Fig. S7-12). As shown in Table 7-1, all samples contained a high carbon content, ranging from approximately 76-80 at. %, confirming effective carbonisation. The N content increased marginally for ZnB_C (14.9 at. %) compared with that of the ZnBBP (12.6 at. %), and no N was observed in FeB_C compared with the FeBBP (10.2 at. %). This reduction suggests partial or completely decomposition of nitrogen-containing moieties, such as the benzimidazole and pyrrolidine units, during the pyrolysis. Furthermore, ZnB_C contained 3.2 at. % of Zn metal and no Fe metal was measured in FeB_C, which could be attributed to FeB_C sample inhomogeneity and ferromagnetic nature as a result of Fe_3O_4 aggregation (Fig. 7-13c). As shown in Fig. S7-13, the high-resolution Zn_{2p} spectrum indicated that Zn metal was contained within zinc oxide (ZnO) in the structure, thereby suggesting that oxidation occurred on the metal ions and they transformed into the metal oxide during the pyrolysis process. These observations highlight the different thermal stability and coordination behaviour of metal ions, which directly affect their retention post-carbonisation.

Table 7-2. Atomic percentage of MtB_C obtained using XPS analysis.

Sample	C (at. %)	N (at. %)	O (at. %)	Metal (at. %)
FeB_C	80.3		19.7	
ZnB_C	76.6	14.9	5.4	3.2

High-resolution C_{1s} spectra (Fig. 7-12b) provided further insight into the surface bonding states. In all the samples, the main peak normalised at 284.8 eV corresponding to sp^3 C–C bonds, which are characteristic of amorphous carbon structures. Additional peaks at 286.3 eV and 288.6 eV were assigned to C–O and O–C=O functional groups, respectively. These oxygenated species likely originate from the adsorbed water molecules in FeBBP and ZnBBP (Fig. S6-6) interacting with the carbon structure during pyrolysis. Overall, the XPS results confirm that while the bulk carbonisation efficiency remained consistent across the samples, the surface chemistry and metal integration varied significantly depending on the metal type, which affected the disordered carbon formation.

As shown in Fig. 7-12(c), the FeB_C and ZnB_C samples exhibit a broad amorphous peak with centre located between 24.3° 2θ and 24.4° 2θ, respectively, consistent with amorphous carbon structure and confirming that the amorphous carbon was retained in the structure. This corresponds to a d-spacing of 0.36–0.39 nm, indicating that the BBP backbone was uniformly converted into a disordered carbon matrix regardless of the coordinating metal ion. Metal coordination significantly influences the fate of the dopant species during pyrolysis. For FeB_C, the appearance of additional peaks at 35.5°, 43.1°, and 62.6° 2θ can be indexed to the (311), (400), and (440) planes of magnetite (Fe_3O_4), respectively, suggesting in situ oxidation of iron under the trace O_2 present in chelated water. In contrast, ZnB_C exhibited no crystalline ZnO peaks, implying ZnO remains amorphous or highly dispersed within the carbon matrix. Due to the different probing depths of XPS (~5–10 nm) and XRD (~25 μm), Fe_3O_4 was detected only by XRD, indicating it was embedded deeper within the FeB_C structure, probably serving as a structural core. The strong Zn signal in ZnB_C from XPS, despite the absence of crystalline ZnO in XRD, suggests Zn is surface-enriched and exists as dispersed or amorphous ZnO. This surface localisation may affect both pore formation and surface functionality, distinguishing ZnB_C from FeB_C in terms of carbonisation mechanisms.

The pore size distributions of the FeB_C and ZnB_C samples, as determined by CO_2 physisorption at 273 K, are shown in Fig. 7-12(d). FeB_C displayed a relatively narrow and sharp PSD centred at approximately ~0.75 nm, indicating a uniform microporous network, with 79% of micropores retained in FeB_C. ZnB_C revealed a clear bimodal pore structure at 0.52 and 0.78 nm under CO_2 adsorption, with the ratio of ultramicropores to micropores being approximately 43:57. Overall, the carbonisation of different MtB_C clearly influenced pore development and pore size distribution.

Overall, FeB_C formed a N-free amorphous carbon matrix with embedded Fe_3O_4, contributing to uniform microporosity. In comparison, ZnB_C retained N-component and exhibited no crystalline ZnO, suggesting a surface-dispersed amorphous ZnO phase. Its bimodal pore architecture and heteroatom content offer a distinct mechanism for CMS formation, also suitable for gas separation applications.

7.2.3.2. Carbon membrane characteristic

The membrane thickness and EDS mapping results were determined using SEM with EDS analysis. As shown in Fig. 7-13(a-c), the 1 wt.% of BBP, FeB and ZnB co-pyrolysis carbon membranes (BBP_CM, FeB_CM, and ZnB_CM) show a clear boundary between the CMSMs and alumina substrates. In the EDS analysis, the membranes exhibited low infiltration of the PEI membrane into the alumina substrates. The membrane thickness of PEI_C was 10.6 ± 0.2 µm, which decreased by approximately 16.3% when 1 wt.% BBP was doped into the membrane bulk. Similarly, FeB_CM and ZnB_CM decreased by 26% and 41%, respectively, with the membrane thickness at 7.8 ± 0.5 µm and 6.2 ± 0.6 µm, respectively. Interestingly, FeB_CM and ZnB_CM exhibited clear Fe and Zn accumulation near the interface between the alumina substrates and CMSMs as observed by the EDS analyse. During polymer carbonisation, volumetric shrinkage of FeB_CM and ZnB_CM leads to the redistribution of metal particles. Moreover, capillary effects can drive the migration of metal particles along pores or toward low-energy regions such as the alumina substrates [456].

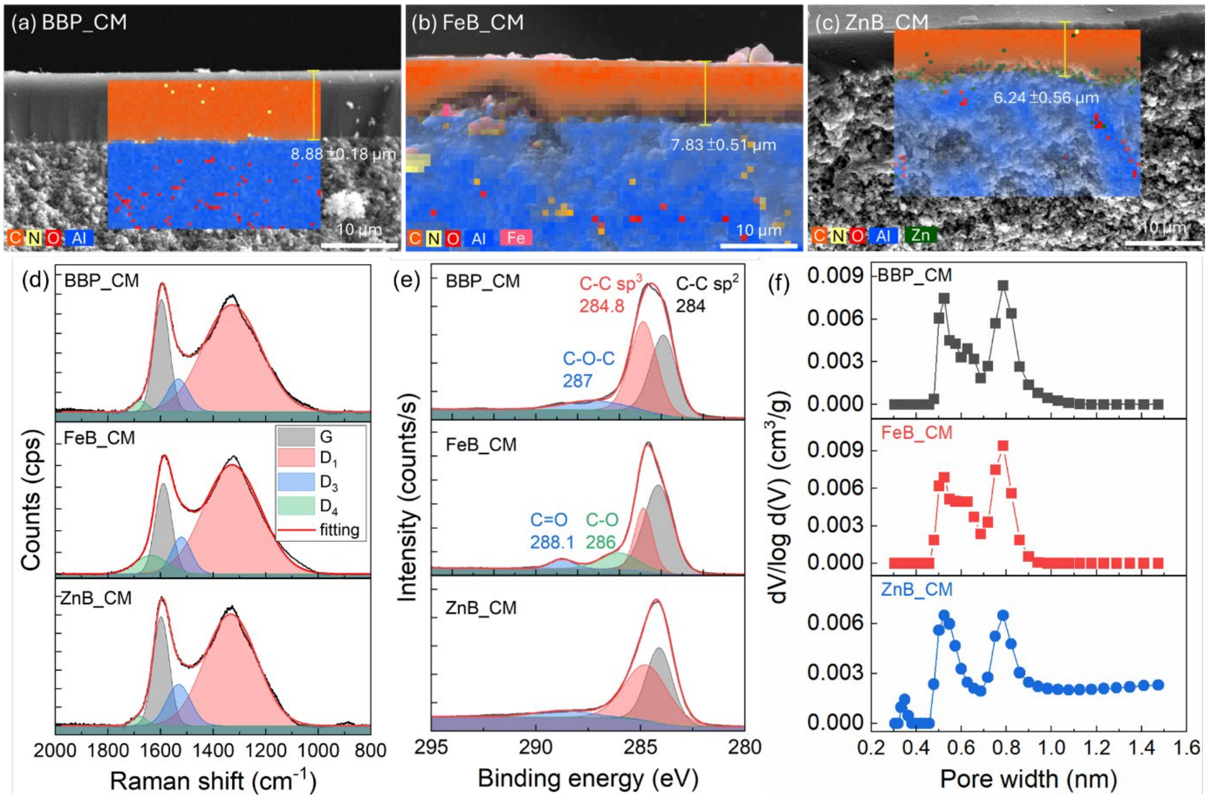

Fig. 7-13. Cross-section images with EDS analysis, (a) BBP_CM, (b) FeB_CM, and (c) ZnB_CM. All membranes were measured under 5000x magnification with over 300,000 counts of EDS mapping. The colour represnting each atom is displayed in the left-bottom of each image. (d) Raman spectra, (e) high resolution C_{1s} of XPS spectra and (f) pore size distribution from the CO_2 physisorption. Data for CoBBP can be found in Fig. 7-5 in Section 7.1.4.2.

As shown in Fig. 7-13(d), the amorphous carbon structures were analysed using Raman spectroscopy to determine the carbon structure. Upon deconvolution of the Raman spectra, all CMSMs exhibited four types of carbon structures. The G band represented the ideal graphitic lattice (E_{2g}-symmetry) vibration, while the defect band was identified with D_1 (1350 cm^{-1}), D_2 (1620 cm^{-1}), and D_3 (1500 cm^{-1}) bands, corresponding to the graphene layer edges, surface graphene layers, and amorphous carbon, respectively. Notably, all CMS membranes displayed a prominent D_1 band compared with the other defect bands, indicating their classification as

CMS membranes. In comparison to the pure PEI_CM discussed in the previous section, which had a D_1/G ratio of 1.67, the ratio increased significantly after doping various MtBBP into the PEI CMS membrane. The MtB_C additive potentially enhanced the disordered carbon in the PEI_C membrane, thereby increasing the intensity of the D_1, D_2 and D_3 bands. The highest ratio was observed for FeB_CM (4.12), followed by BBP_CM (3.48), and ZnB_CM (3.27).

As shown in Fig. 7-13(e), the high-resolution C_{1s} spectra provide insights into the surface bonding environment of the CMS membranes. The sp^2/sp^3 ratio in BPP_CM was approximately 48: 42, while FeB_CM and ZnB_CM exhibited sp^2/sp^3 ratios 25: 56 and 51: 41, respectively. This indicates that FeB_CM contains a higher proportion of sp^3–hybridised carbon, reflecting a more disordered, amorphous structure. Additionally, the spectrum of FeB_CM contained prominent peaks at 286.3 eV and 288.6 eV, corresponding to C-O and C=O functionalities, suggesting increased surface defects. In contrast, ZnB_CM exhibited a C=O peak but no detectable C-O contribution. Overall, all three membranes displayed a low sp^2/sp^3 ratio, indicative of high structural disorder, consistent with Raman spectroscopy findings.

The pore size distributions (PSD) of BBP_CM, FeB_CM, and ZnB_CM were analysed using CO_2 physisorption. As shown in Fig. 7-13(f), the pore widths of BBP_CM and FeB_CM were below 9 Å and exhibited a clear bimodal distribution, while the pore widths of ZnB_CM remained up to 15 Å. In particular, ultramicropores with pore width of approximately 5.2 Å, while the larger micropores were centred near 7.8 Å, aligning with the previously reported characteristics of PEI-derived CMS membranes [159, 445, 446]. Notably, the relative proportion of ultramicropores and micropores varied depending on dopant type. BBP_CM exhibited a ratio of 55:45, FeB_CM displayed a ratio of 59:41, and ZnB_CM presented a reversed distribution of 44:56. These results suggest that the incorporation of these additives leads to a nearly 1:1 ratio of ultramicropores to micropores in the CMS membranes, compared to PEI_CM, which shows a dominant microporous structure (74:26). The increased proportion of larger micropores in the doped membranes may influence gas permeability performance. The corresponding CO_2 adsorption isotherms of each membrane are shown in Fig. S7-14, all of which display type-I isotherms that are characteristic of microporous materials.

7.2.3.3. Single gas permeance test

Single gas permeation tests were conducted on all CMS membranes using He (2.6 Å), H_2 (2.89 Å), CO_2 (3.3 Å), O_2 (3.4Å), N_2 (3.64 Å) and CH_4 (3.8Å) at an operating temperature of 35 °C. As shown in Fig. 7-14(a), PEI_CM exhibited higher gas permeance than that of the previously reported PEI-derived CMS membranes, with H_2, CO_2, and O_2 permeances of approximately 107 ± 5, 72 ± 7, and 25 ± 3 GPU, respectively, surpassing that of earlier reports, which typically showed CO_2 permeances in the range of 50–60 GPU [151, 153]. N_2 and CH_4 permeance values were significantly lower at 3.43 ± 0.77 and 2.9 ± 1.5 GPU, respectively. These results indicate that gas transport in the PEI_CM exhibits a molecular sieving effect, allowing faster transport of smaller gases such as He, H_2, and CO_2, while restricting the movement of larger gas molecules such as N_2 and CH_4.

BBP_CM demonstrated a considerable improvement in the He, H_2 and CO_2 permeance, with 150%, 260%, and 50% higher permeance, respectively, than those of PEI_CM. By contrast, N_2 and CH_4 permeances showed slight decreases of 7.3% and 46.4%, respectively. This performance improvement is attributed to the decomposition of thermally labile BBP moieties during carbonisation, which promoted the formation of additional micropores and expanded the microporous network within the CMS structure, particularly enhancing the transport of smaller, more diffusible gases. Further enhancement was observed for FeB_CM and ZnB_CM, where the incorporation of FeB and ZnB led to more improvements in gas transport. FeB_CM exhibited the highest He, H_2, and CO_2 permeance reaching 193 ± 7, 454 ±

4, and 184 ± 6 GPU, respectively. The N_2 and CH_4 permeance also slightly increased to 5.6 ± 2.9 and 2.5 ± 1.2 GPU, respectively. Moreover, ZnB_CM followed closely, exhibiting permeances of 211 ± 9.5, 450 ± 10, and 179 ± 38 GPU. Conversely, the N_2 and CH_4 permeances of ZnB_CM decreased by 8% and 46%, respectively, compared with those of PEI_CM.

As shown in Fig. 7-14(b), the permselectivities for PEI_CM were evaluated using five different gas pairs: 21 ± 8 (CO_2/N_2), 25 ± 11 (CO_2/CH_4), 31 ± 12 (H_2/CH_4), 37 ± 11 (H_2/N_2), and 7 ± 2 (O_2/N_2). The BBP_CM membrane exhibited significantly higher values of 43%, 163%, 437%, 214%, and 18%, respectively, for the same gas pairs. Additionally, the FeB_CM and ZnB_CM membranes demonstrated significant increases in permselectivities across all gas pairs. Specifically, the most improvement was observed in $\alpha H_2/CH_4$, reaching 184 ± 3 for FeB_CM and 270 ± 20 for ZnB_CM, representing approximately six-fold and nine-fold increases, respectively, compared with that of PEI_CM. Furthermore, $\alpha H_2/N_2$ rose by 115% and 180%, respectively, and $\alpha CO_2/CH_4$ increased by 137% and 208%, respectively, for FeB_CM and ZnB_CM. By contrast, $\alpha O_2/N_2$ exhibited a marginal increase of approximately 20% compared with that of PEI_CM.

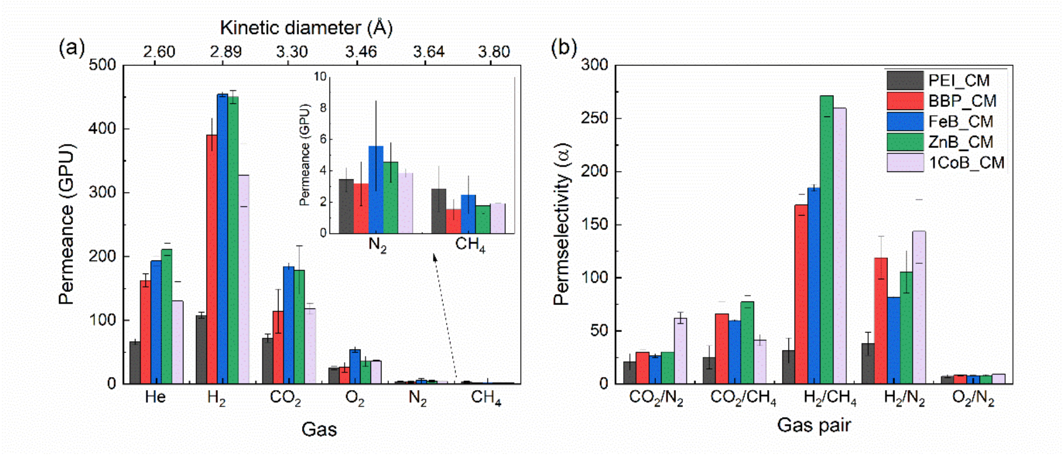

Fig. 7-14. Gas permeance and permselectivity for CMSMs produced using BBP, FeBBP, and ZnBBP co-pyrolysis fabrication. (a) gas permeance of various kinetic diameter gas molecules

and (b) permselectivity of various gas pairs. Data of 1CoB_CM is reproduced from Fig. 7-6 in Section 7.1.4.3.

The gas separation performance of all membranes prepared in this study was evaluated using He/N_2, H_2/CH_4, O_2/N_2, and CO_2/CH_4, as reported in the 2008, 2015 and 2019 revisited Robeson upper bounds [66, 67, 70]. However, these upper bounds were originally established based on polymeric membranes and may not serve as direct comparable benchmarks for CMSMs [457]. To enable a more meaningful comparison, CMSM derived from various polymer precursors, including PEI [150-153], PPO [31, 191], cellulose [118, 173, 447], polyimide-based materials (e.g. BTDA- or 6FDA-derived polymers) [12, 125, 253, 448-453, 458, 459], and high-performance polymers such as PBI and Torlon® polyamide-imide based membranes [191, 457, 460], were also included in Fig. 7-15. Only the data points produced at temperatures between 550 °C and 650 °C were considered to minimise the influence of pyrolysis temperature.

As shown in Fig. 7-15(a), He/N_2 separation is key for recovering helium from natural gas by-products. He permeability of FeB_CM reached 1490 ± 120 Barrer compared with 900 ± 60 Barrer for PEI_CM. Additionally, He/N_2 permselectivity also increased from 19 to 44. These modified membranes surpassed the 2008 Robeson upper bound and outperformed most PBI-based and cellulose-derived CMSMs, performing comparably to 6FDA-based CMSMs. As shown in Fig. 7-15(b), the H_2/CH_4 separation performance of PEI_CM showed noticeable differences compared to that of previously reported PEI-based CMS membranes [150-153], which exhibited H_2 permeabilities ranging from 250 to 1140 Barrer, and H_2/CH_4 permselectivities between approximately 3 and 294. Variations in membrane fabrication methods and structural features often lead to substantial differences in gas separation performance, even among membranes derived from the same precursor [26]. In this context, PEI_CM demonstrated a higher H_2 permeability of approximately 1460 ± 65 Barrer, albeit with a lower H_2/CH_4 permselectivity of 31 ± 12. Upon incorporation of BBP into, both H_2 permeability and H_2/CH_4 permselectivity increased to 3470 ± 230 Barrer and 169 ± 10, demonstrating the effectiveness of the modification. Notably, the FeB_CM achieved higher H_2 permeability and H_2/CH_4 permselectivity with 3560 ± 30 Barrer and 185 ± 3, whilst the ZnB_CM showed a slight reduce on H_2 permeability with 2800 ± 65 Barrer and higher H_2/CH_4 permselectivity of 271 ± 20.

Furthermore, the O_2/N_2 permeation performance of all membranes in this report surpassed the 2015 upper bound, as shown in Fig. 7-15(c). PEI_CM exhibited an O_2 permeability of 340 Barrer with $\alpha O_2/N_2$ of 7.3. BBP_CM, FeB_CM and ZnB_CM demonstrated an 8 – 18% increase in $\alpha O_2/N_2$, while the O_2 permeability decreased by approximately 20 − 30%, compared with that of PEI_CM. Furthermore, PEI_CM fabricated in this study was better than that of other PEI CMS membranes. However, it was still lower than that of the polyimides-based CMS membranes for O_2 permeability. Furthermore, the CO_2/CH_4 separation performance was compared with the 2019 Robeson upper bound. As shown in Fig. 7-15(d), PEI_CM achieved a CO_2 permeability of 970 ± 90 Barrer with $\alpha CO_2/CH_4$ of 25 ± 11. Moreover, the CO_2 permeability of BBP_CM, FeB_CM, and ZnB_CM improved approximately from 3% to 44%, in the range between 1000 and 1400 Barrer, with α CO_2/CH_4 of approximately 60 – 70. Adding the FeBBP and ZnBBP co-pyrolysis with PEI membrane can improve the CO_2 permeability and permselectivity over most of cellulose-based and PEI-based CMSM based on the CO_2 permeability. Moreover, the modification ensured a higher CO_2/CH_4 permselectivity compared with that of polyimide-based CMS membranes.

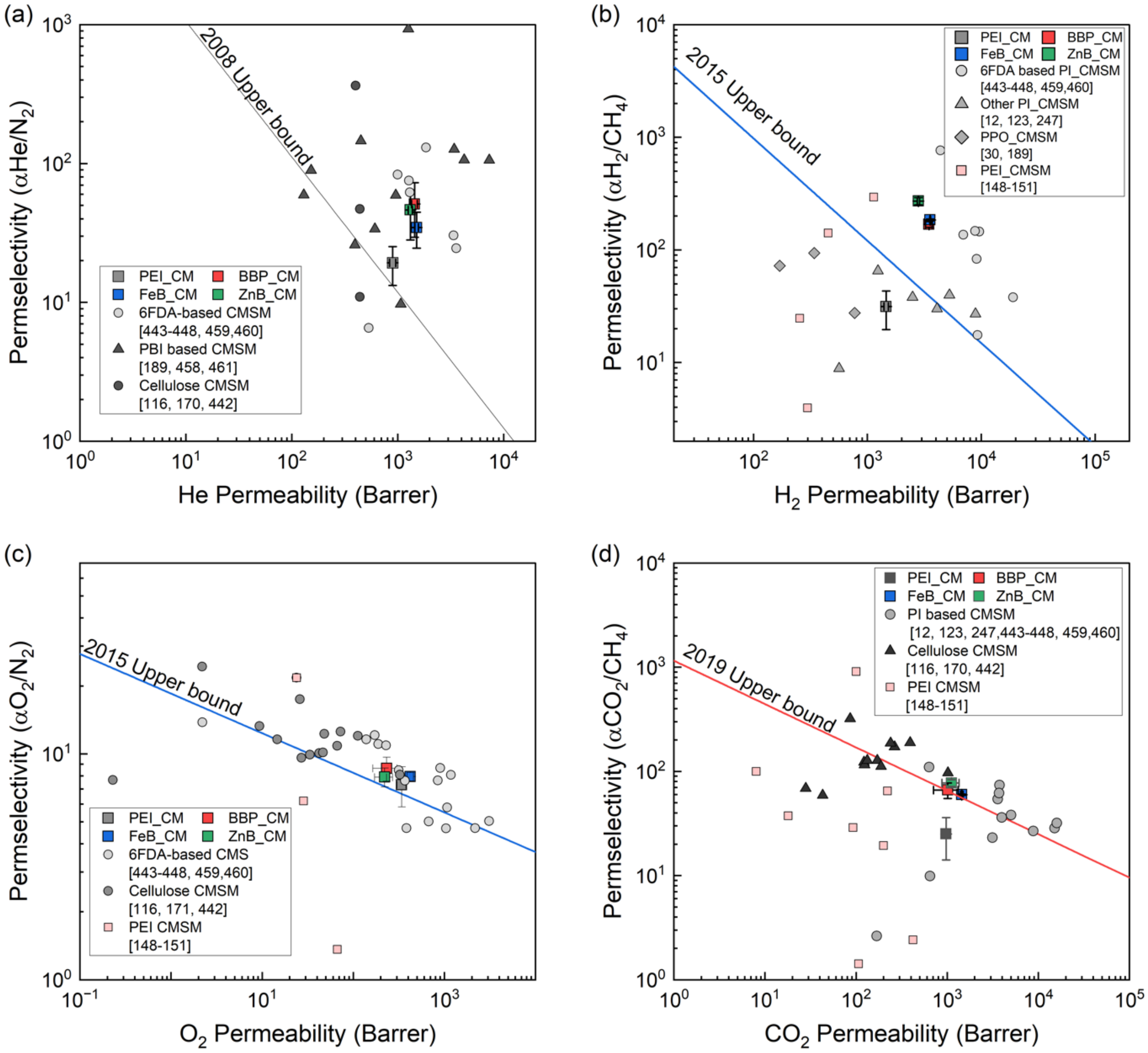

Fig. 7-15. CMS results plotted on the Robeson upper bounds compared with that of other polymer-based CMS membranes. (a) He/N$_2$, (b) H$_2$/CH$_4$, (c) O$_2$/N$_2$, and (d) CO$_2$/CH$_4$. Data for CoB_CM can be found in Fig. 7-7 in Section 7.1.4.3.

7.2.3.4. Mixed gas separation experiment under 100% relatively humidity (RH)

FeB_CM exhibited lower CO$_2$/CH$_4$ permselectivity compared to ZnB_CM and BBP_CM, suggesting it may not be the suitable membrane for humidified mixed gas separation testing. Furthermore, the 1CoB_CM was new fabricated to evaluate the MtBBP performance after the co-pyrolysis process under humidity CO$_2$/CH$_4$ gas separation. The PEI_CM, BBP_CM, 1CoB_CM, and ZnB_CM membranes were evaluated using a 10/90 CO_2/CH_4 gas mixture under 100% RH at 4 bar and 80 °C. Initially, the membranes were tested with dried (0% RH) mixed gas (10/90) for 1 h, followed by exposure to humidified (100% RH) gas mixture for 48 h. Post regeneration (P. Re.) steps were interspersed throughout the process using a 5/95 H_2/Ar mixture at 150 °C for 24 h to reactivate the CMS pore structure. Subsequently, repeat these processes again to determine the 2nd cycle performance of the membranes.

As shown in Fig. 7-16(a), under dry condition the PEI_CM membrane exhibited initial CO_2 and CH_4 permeability of 1130 ± 168 and 135 ± 23 Barrer, respectively, corresponding to $\alpha CO_2/CH_4$ of 8 ± 1. Upon exposure to 100% RH, CO_2 and CH_4 initial permeability significantly decreased to 644.5 ± 20 Barrer and 114 ± 4 Barrer, respectively, with a slightly increased $\alpha CO_2/CH_4$ of 15 ± 1. The observed reduction in permeability was attributed to the strong water adsorption within the CMS structure, which blocked the pores and hindered gas transport [461, 462]. This effect continued over time, with the permeability stabilising after 24 h. After 48 h of humid gas permeation, the CO_2 and CH_4 permeability dropped to 342 ± 66 and 0.45 ± 0.25 Barrer, respectively, representing reductions of 53% and 98% from the initial values. Consequently, the CO_2/CH_4 selectivity increases to 744 ± 145. Following 1st P. Re. step, the CO_2 permeability increased to 1390 ± 6 Barrer, while the CH_4 permeability reduced to 19.6 ± 4 Barrer. Indicating that the adsorbed water molecules had been removed. The 2nd cycle of exposure to 100% RH followed a similar trend. CO_2 and CH_4 permeability dropped from 800 ± 53 Barrer and 0.4 ± 0.3 Barrer to 374 ± 28 Barrer and 0.013 ± 0.001 Barrer, respectively. After 2nd P. Re., CO_2 and CH_4 permeabilities recovered to 1190 ± 0.6 and 1.2 ± 0.5 Barrer.

As shown in Fig. 7-16(b), the BBP_CM membrane initially exhibited a CO_2 and CH_4 permeability of 2015 ± 281 and 148 ± 9.8 Barrer, respectively, under dry condition, corresponding with $\alpha CO_2/CH_4$ is 14 ± 2. Upon exposure to 100% RH, CO_2 permeability increased to 3220 ± 336 Barrer, while CH_4 permeability decreased to 81 ± 1 Barrer, resulting in a significantly improved selectivity of 40 ± 5. After 48 h of humid gas permeation, the CO_2 and CH_4 permeability dropped to 568 ± 1 and 3 ± 1 Barrer, respectively, representing reductions of 82 % and 99.7%. Following 1st P. Re. process, CO_2 permeability partially recovered to 68 % of its initial value, while CH_4 permeability surprisingly increased to 264 ± 20 Barrer, suggesting possible changes in the pore structure or residual moisture retention. During 2nd RH cycle, a similar degradation trend was observed, with CO_2 and CH_4 permeabilities decreasing by 71% and 99%, respectively. After 2nd P. Re. process, the CO_2 and CH_4 permeabilities recovered to 1081 ± 140 and 204 ± 26 Barrer. The BBP_CM demonstrated a significant aging after the high RH environment.

As shown in Fig. 7-16(c). Under dry conditions, 1CoB_CM displayed a CO_2 permeability of 1125 ± 273 Barrer and CH_4 permeability of 295 ± 30 Barrer, resulting in a low CO_2/CH_4 selectivity of 4 ± 1. During the 1st RH cycle, the initial CO_2 and CH_4 permeability slightly decreased to 858 ± 1 and 132 ± 1 Barrer, respectively. After 48 hours separation, CO_2 and CH_4 permeabilities declined by 13% and 65%, respectively. Compared to the PEI_CM and BBP_CM, the CO_2 permeability of 1CoB_CM was less affected by moisture. However, its CO_2/CH_4 selectivity remained relatively low, fluctuating between 10 and 30 throughout the cycle. Following this, the CO_2 and CH_4 permeabilities recovered to 1085 and 182 Barrer, respectively, representing a 97% recovery of the CO_2 permeability after 1st P. Re. process. However, during the 2nd cycle of humidified gas separation, a significant reduction in permeability was observed. CO_2 and CH_4 permeabilities decreased by 66% and 100%, similar to the behaviour of the PEI_CM. After the 2nd P. Re. step, CO_2 and CH_4 permeabilities increased to 1480 and 344 Barrer, respectively.

As shown in Fig. 7-16(d), Under dry conditions, it displayed a CO_2 permeability of 1885 ± 315 Barrer and CH_4 permeability of 31 ± 6 Barrer, yielding a high CO_2/CH_4 selectivity of 63 ± 11, which is 280% higher than that of BBP_CM. Under the initial 1st RH testing, $\alpha CO_2/CH_4$

further increased to 206 ± 34, while CH_4 permeability decreased to 16 ± 10 Barrer. After 48 hours, CO_2 and CH_4 permeabilities declined by 74% and 89%, respectively. Compared to the BBP_CM, it determined a slower gas permeabilities dropping. Following the 1st P. Re. process, CO_2 permeability recovered to 1713 Barrer, with 90% CO_2 permeability recovery, whilst the $\alpha CO_2/CH_4$ declined to 23 ± 1. Interestingly, during the 2nd RH testing, ZnB_CM demonstrated an extraordinary increase in CO_2/CH_4 selectivity to ~28,000, driven by an ultra-low CH_4 permeability of 0.02 ± 0.01 Barrer. Even after 2nd P. Re. process, the selectivity remained high at 305 ± 20. However, the CO_2 and CH_4 permeability dropped to 400 ± 50 and 1.3 ± 0.2 Barrer, suggesting that the CMS structure changed after the permeation testing.

These investigations revealed the aging effects of CMS membranes in high-moisture environments during gas separation processes. Water vapour can cause fouling of membrane pores through physisorption and oxidation. This aging effect significantly reduces CO_2 permeability while increased CO_2/CH_4 selectivity due to pore structure blockage. To address this issue, a hydrogen regeneration process can be applied [463]. However, our observations indicate that in-line hydrogen regeneration may result in more uniform membrane performances. In the second cycle of humidified gas separation, CO_2 permeability declined by approximately 50 – 70%, showing a consistent trend across all membranes. This suggests that structural changes occurred during regeneration, leading to more uniform gas separation performance.

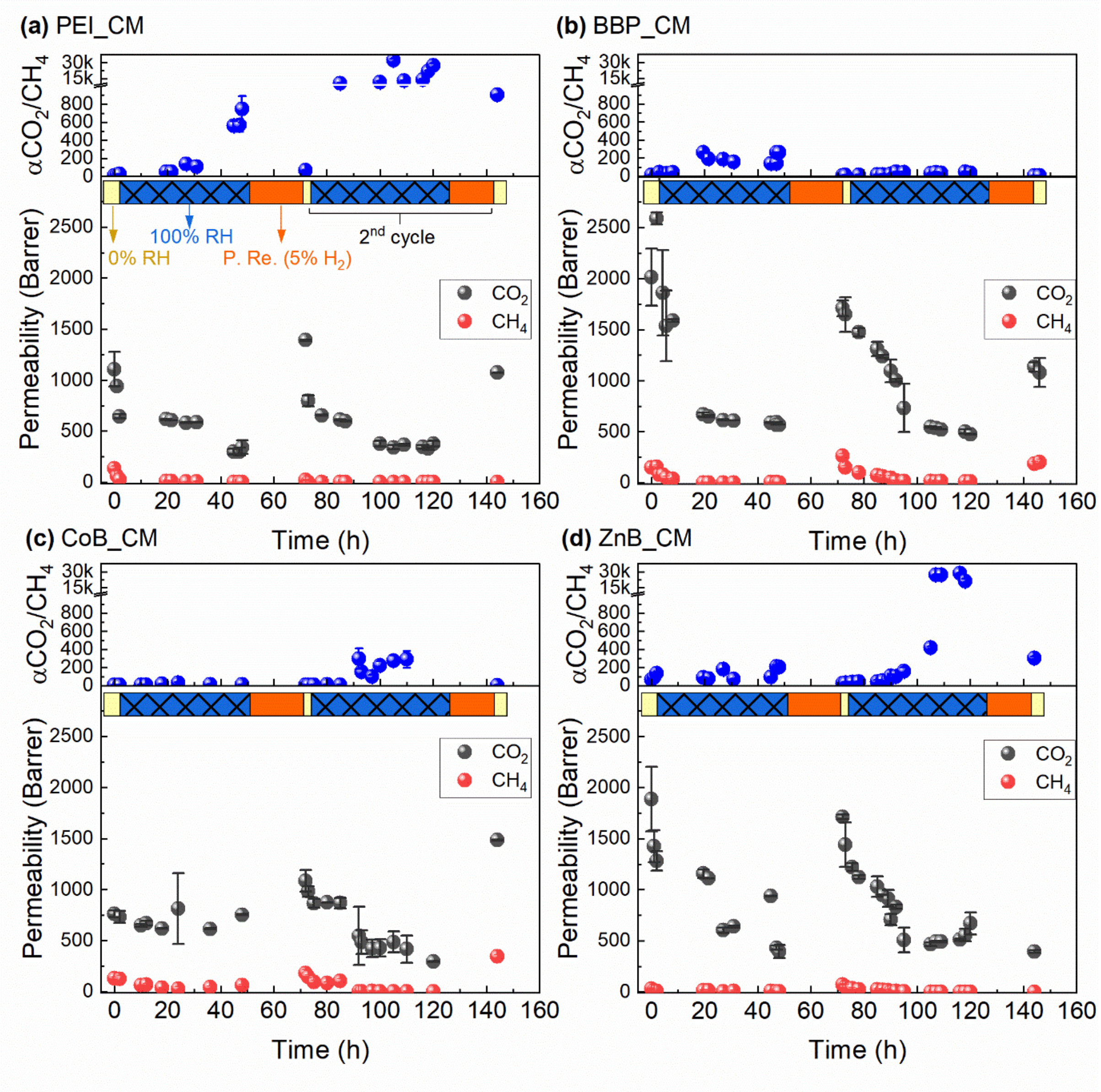

Fig. 7-16. Cycling test of CO_2/CH_4 (10/90) mixed gas separation with 100% relative humidity and post-regeneration (P. Re.) (a) PEI_CM, (b)BBP_CM, (c) CoB_CM, and (b) ZnB_CM.

To understand the structural changes in the CMS membrane, PSD and XPS analyses of BBP_CM and ZnB_CM were conducted to evaluate the effects of heat treatment and moisture aging on the membrane pore size. These analyses may be able to identify structural alterations in CMSM and the efficiency of in-situ heat regeneration. As shown in Fig. 7-17(a), the PSD distribution changed marginally after exposure to humidity and thermal processing. The ratio of ultramicropores and micropores changed to 54:46 for BBP_CM and 61:39 for ZnB_CM.

Compared with the PSD of original CMS (Fig 7-12f), the membrane pore size distribution changed toward the ultramicroporous structure after permeation, which may explain the observed decrease in gas permeability and increase in $\alpha CO_2/CH_4$.

Furthermore, the high resolution of C_{1s} XPS spectra, along with the total elemental composition of BBP_CM and ZnB_CM, are shown in Fig. 7-17(b). BBP_CM exhibited a higher oxygen content in the membrane bulk after the permeation, increasing from 9.8 at. % to 15.2 at. %. This suggests that inefficient heat regeneration may reduce the performance of gas permeation. Similarly, the ZnB_CM membrane also showed an increase in oxygen content, from 5.4 at. % to 13.4 at. %. These findings indicate that the post-regeneration process may not completely remove chemisorbed oxygen species from the CMS structure, potentially resulting in the formation of a denser pore network that restricts gas transport.

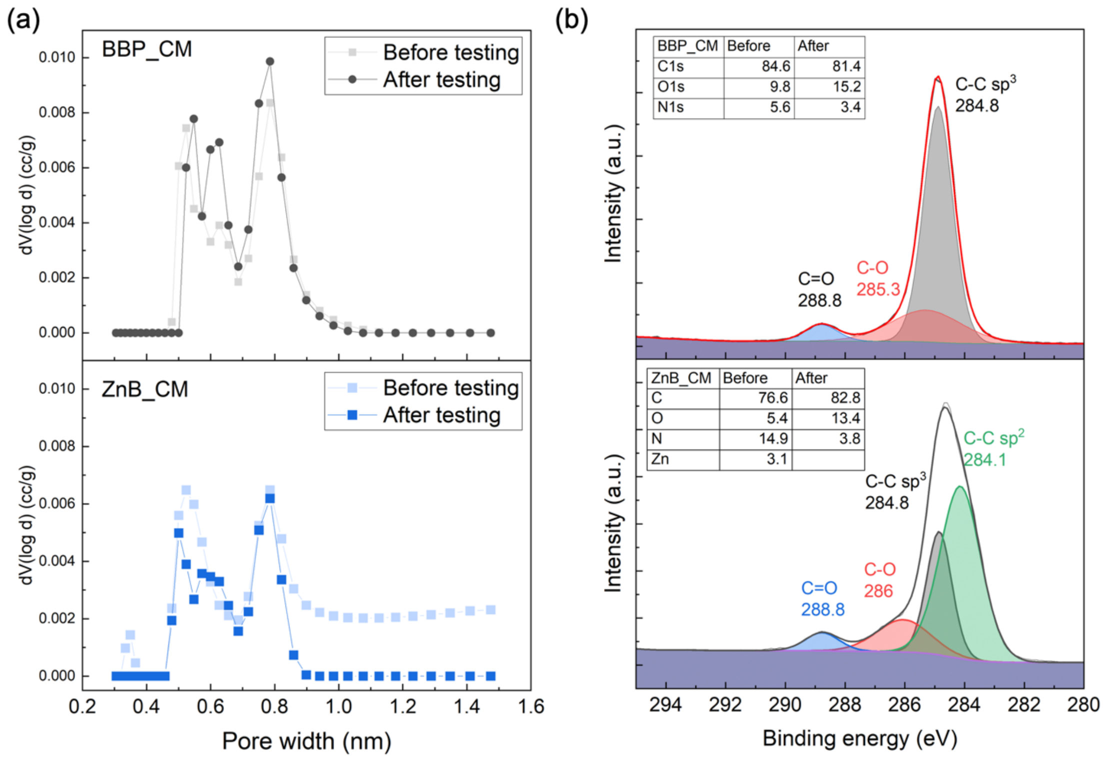

BBP_CM	Before	After
C1s	84.6	81.4
O1s	9.8	15.2
N1s	5.6	3.4

ZnB_CM	Before	After
C	76.6	82.8
O	5.4	13.4
N	14.9	3.8
Zn	3.1	

Fig. 7-17. The characteristic of BBP_CM and ZnB_CM after the cycling mixed gas separation. (a) PSD and (b) XPS.

As shown in Fig. 7-18, ZnB_CM exhibited superior CO_2/CH_4 permeability and selectivity, exceeding the upper bounds for mixed gas established in 2015 and 2018 [464, 465], and outperformed the CMSM reference result [156, 466-471]. By contrast, PEI_CM, BBP_CM, and CoB_CM displayed lower gas separation performance, all falling below the 2018 mixed gas upper bounds. Notably, ZnB_CM and PEIC_CM maintained high selectivity even after 2nd P. Re., despite a reduction in CO_2 permeability compared to its original performance. In comparison, the BBP_CM membrane fell below the 2018 upper bound and experienced further performance decline following the post-regeneration process after moisture exposure.

These results highlight the excellent CO_2/CH_4 separation performance of ZnB_CM, even under conditions of moisture aging. If further strategies are developed to enhance its resistance to humidity-induced degradation, ZnB_CM has strong potential for even greater performance in practical gas separation applications.

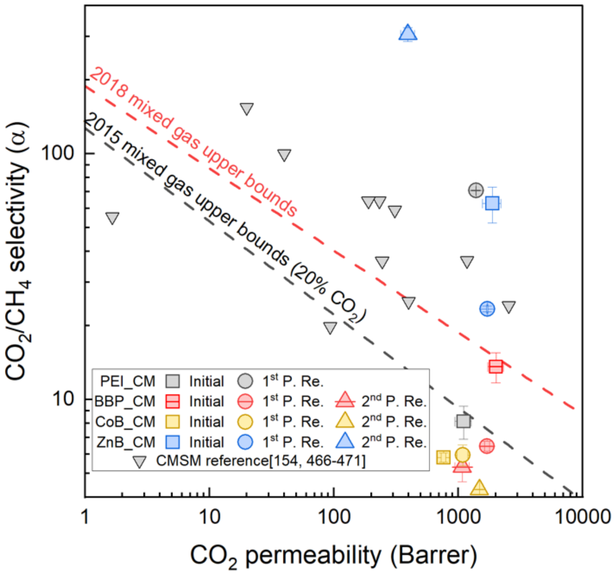

Fig. 7-18. A comparison of CO_2/CH_4 separation performance for CMSMs. The CO_2/CH_4 mixed gas upper bound was presented from [464, 465], along with data collected from [156, 466-471].

7.2.4. Conclusion

The BBP_CM, FeB_CM, and ZnB_CM membranes demonstrated significant improvements in gas permeability following the co-pyrolysis process compared to the PEI_CM membrane. This enhancement is attributed to the higher proportion of micropores relative to PEI_CM and CoB_CM, as discussed in Section 7.1. Notably, H_2 permeability increased to approximately 3560 ± 30 Barrer for FeB_CM and 2800 ± 65 Barrer for ZnB_CM. Among them, ZnB_CM exhibited the highest H_2/CH_4 permselectivity, reaching 271 ± 20, which was nearly nine times greater than that of PEI_CM. This superior performance might be supported by the balanced distribution of ultramicropores and micropores of ZnB_CM, which contributes to its high permeability and selectivity, making it a promising modifier for PEI-based CMS membranes. In the dried CO_2/CH_4 (10/90) condition, the ZnB_CM surpassed the mixed gas upper bounds with 1885 ± 315 Barrer and CO_2/CH_4 selectivity of 62.7 ± 10.5. Further investigated the membrane under humidified mixed CO_2 and CH_4 with 10/90 condition, the ZnB_CM membrane exhibited a performance trend similar to that of PEI_CM, although with a notably higher CO_2 permeability. After two cycles of post-regeneration and humidified mixed-gas separation, CO_2 permeability reached 400 ± 50 Barrer, and CO_2/CH_4 selectivity increased to 305 ± 20. These findings suggest that moisture exposure compromised the pore structure of the membrane, while hydrogen regeneration further reduced the micropore content by approximately 17.3%, potentially contributing to the observed performance decline. To address these issues, further research on process design optimisation and long-term stability under humid conditions is strongly recommended.

7.3. Supporting information

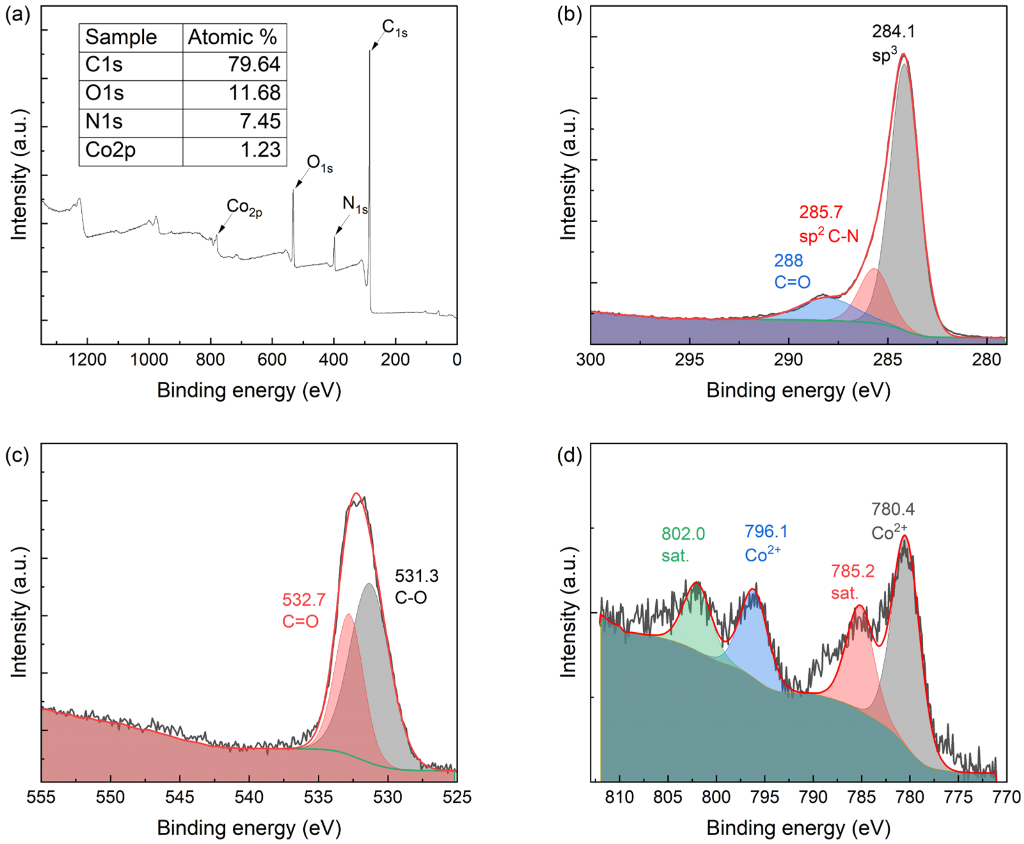

Sample	Atomic %
C1s	79.64
O1s	11.68
N1s	7.45
Co2p	1.23

Fig. S7-1. The XPS spectrum of CoB_C (a) full survey spectra, (b) C_{1s}, (c) O_{1s} and (d) Co_{2p}.

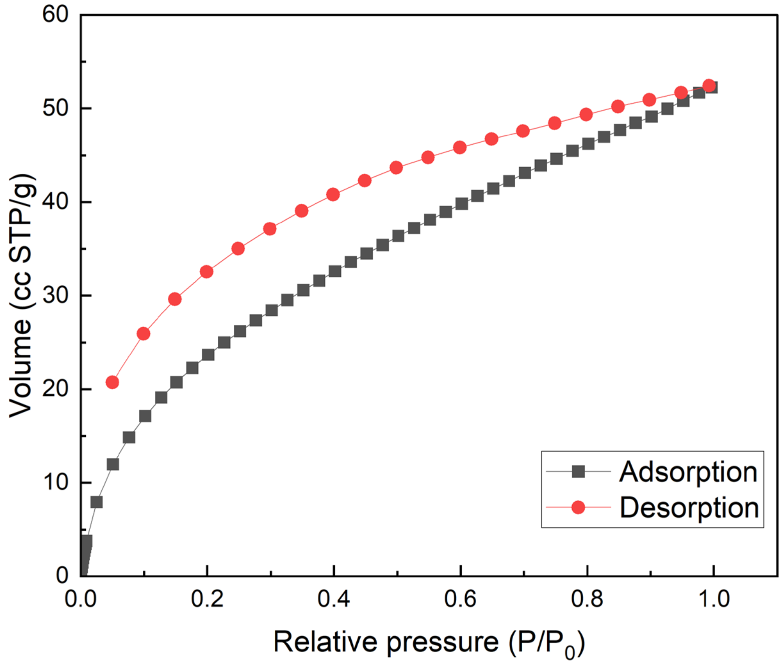

Fig. S7-2. The CO_2 isotherm of the CoB_C samples.

As shown in Fig. S7-3(b), the pore size distribution of the PEI_C determined a bimodal pore structure within the carbonised network. The total pore volume is concentrated in pores smaller than 10 Å, with prominent peaks at approximately 5.7 Å and 7.8 Å. Quantitatively, ultramicropores (<7 Å) and micropores (> 7 Å) constitute 51.1% and 49.9% of the total pore volume, respectively, indicating an almost equal distribution between two pore types.

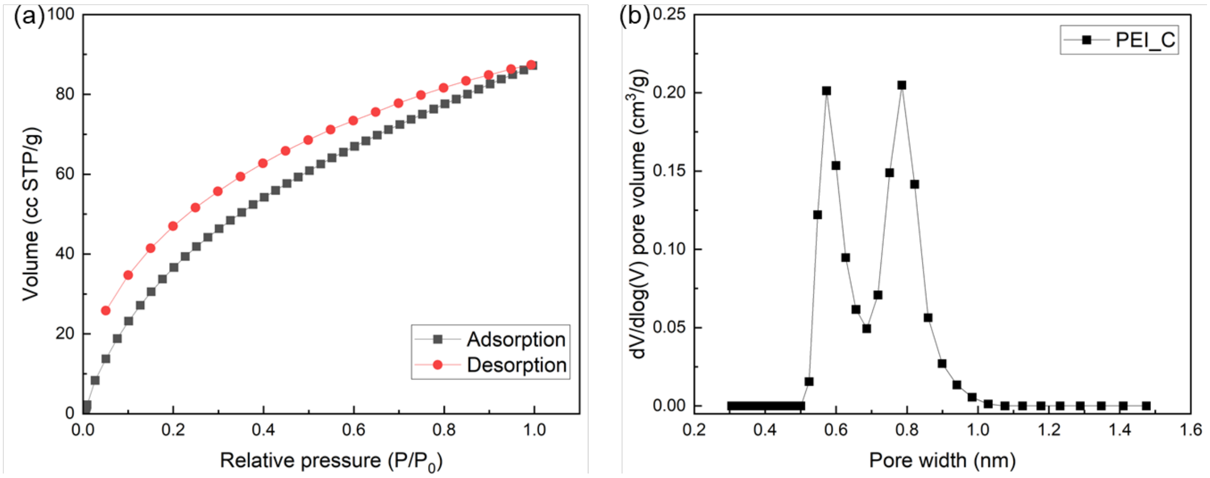

Fig. S7-3. The CO_2 physisorption of the PEI_C (a) isotherms and (b) the pore size distribution from DFT theory calculation.

Table S7-1. The comparison of between PEI_C and CoB_C samples in the BET analyse result.

Sample	Surface area (m^2/g)	Pore volume (cm^3/g)	Average Pore width (nm)
PEI_C	77.305	0.027	0.785
CoB_C	75.607	0.022	0.508

As shown in Fig. S7-4, the TGA-FTIR analysis of the PEI pellet revealed weight changes and evolving gases during the pyrolysis process. Specifically, Fig. S7-4(a) shows the primary decomposition of the PEI occurred at 500 °C, resulting in an approximate 40% weight loss. This observation is corroborated by the DSC analysis and Gram-Schmidt results, which is similar with the previous report on the PEI CMS membranes [204, 446]. Additionally, the gases emitted by PEI during pyrolysis were detectable at the selected temperature (Fig. S4(b)). Upon increasing the temperature to 500 °C, CO_2 and CH_4 were generated because the bisphenol A group and the -CH_3 groups decomposed [433, 472]. As the temperature rose to 600 °C, the appearance of CO and C_6H_6 peaks indicated that PEI began to rearrange, producing more significant emission gases. Stronger peaks were also noted at 700 and 800 °C for CH_4, C_6H_6 and HCN peaks, suggesting that higher temperatures promote the rearrangement of the carbon chain, forming a specific structure in the carbon membrane [433]. As depicted in Fig. S4(c), a comprehensive survey of the FTIR spectra during the pyrolysis of the PEI precursor shows a significant increase in emission gas intensity after 400 °C.

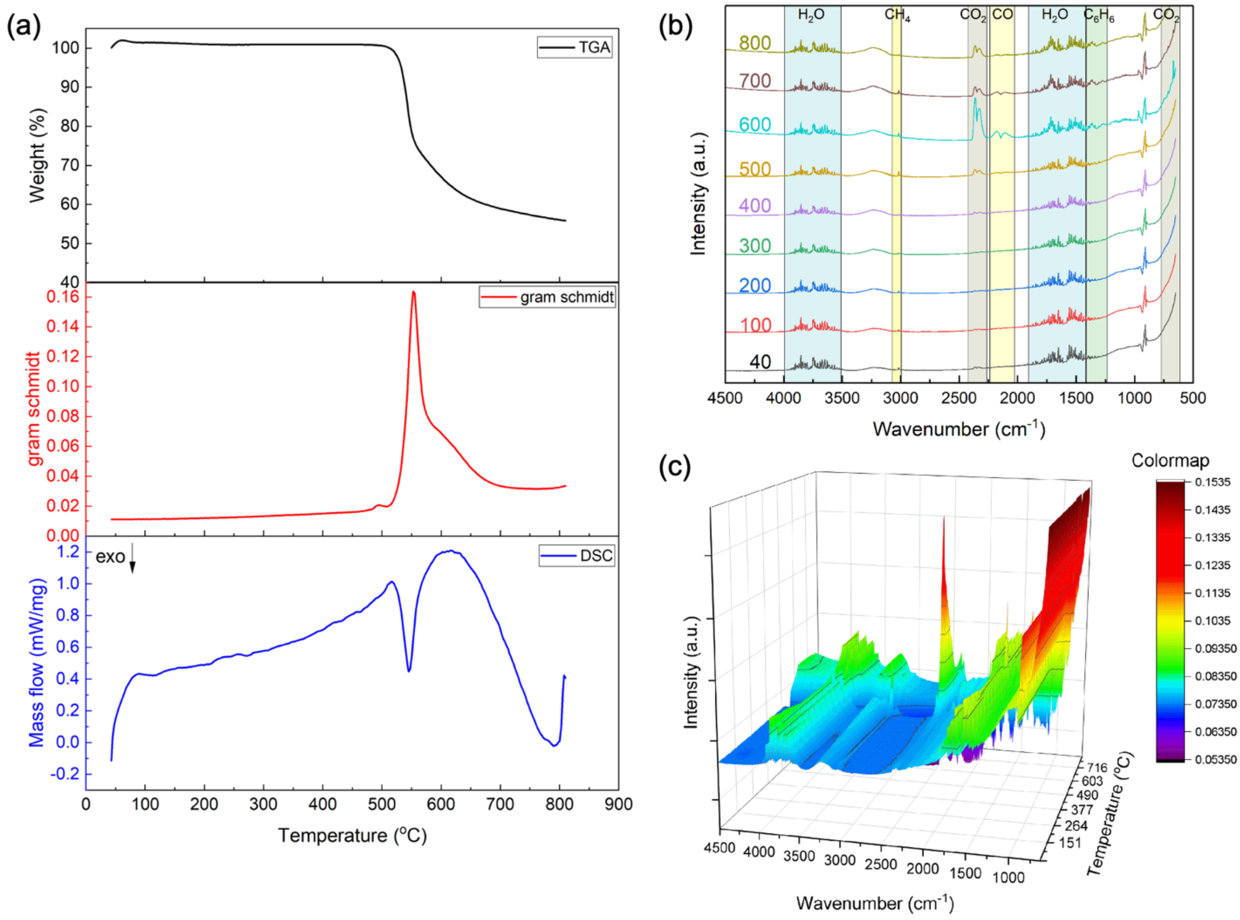

Fig. S7-4. The Thermogravimetric combined FTIR analyse for the PEI precursor. (a) the TGA, gram Schmidt, DSC analyse, (b) FTIR spectra of specific temperature during the pyrolysis process, and (c) full survey of the FTIR spectra of PEI pyrolysis.

The PEI pellet was carbonised (PEI_C) to analyse the chemical structure. As shown in Fig. S7-5, the XRD analysis of PEI_C revealed an amorphous carbon structure. The specific peaks at 22.9° which can be used to calculate the d-spacing of the CMS, yielding a value of 3.9 Å for the PEI_C.

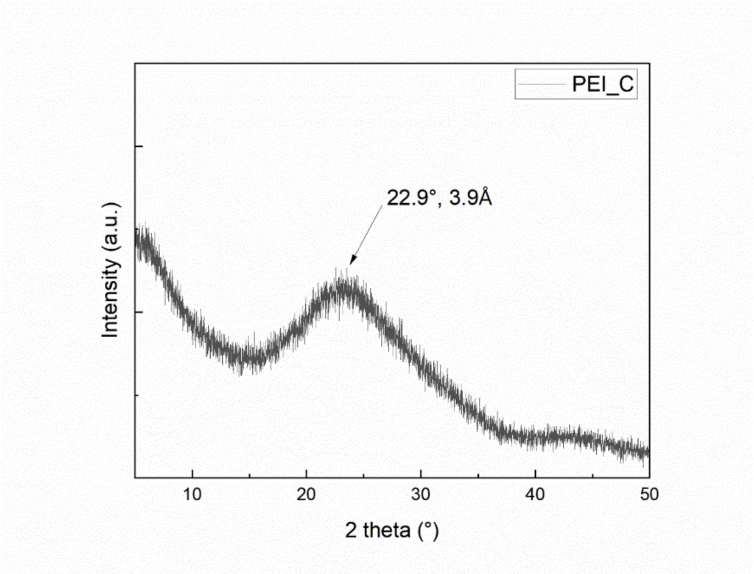

Fig. S7-5. The XRD spectra of the PEI_C structure.

As shown in Fig. S7-6, the Raman spectra of PEI_C exhibited a board peak profile characteristic of carbonaceous materials. The spectrum was deconvoluted to evaluate the carbonisation behaviour, revealing four distinct carbon-related bands at 1590, 1484, 1340 and 1227 cm^{-1}, corresponding to the G, D_3, D_1, and D_4 respectively. Compared to CoB_C, PEI_C exhibited the D_4 peak in the carbonised structure, representing a disordered graphitic lattice (A_{1g} symmetry) of the PEI_C chain structures. Furthermore, the intensity ratio of D1 to G bands (I_{D1}/I_G) for PEI_C was calculated to be 1.76, significantly lower than that of CoB_C, suggesting a higher degree of graphitization in PEI_C.

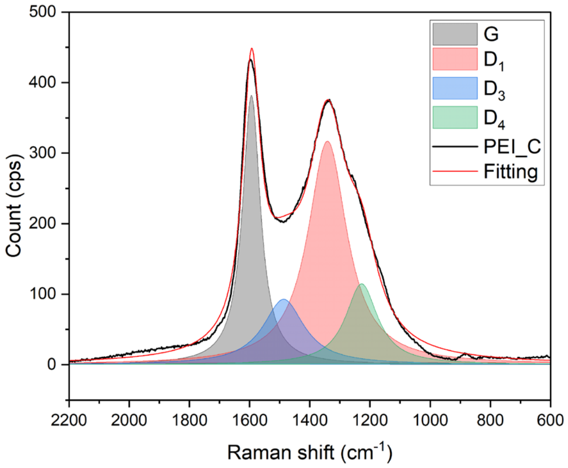

Fig. S7-6. The Raman spectra of the PEI_C.

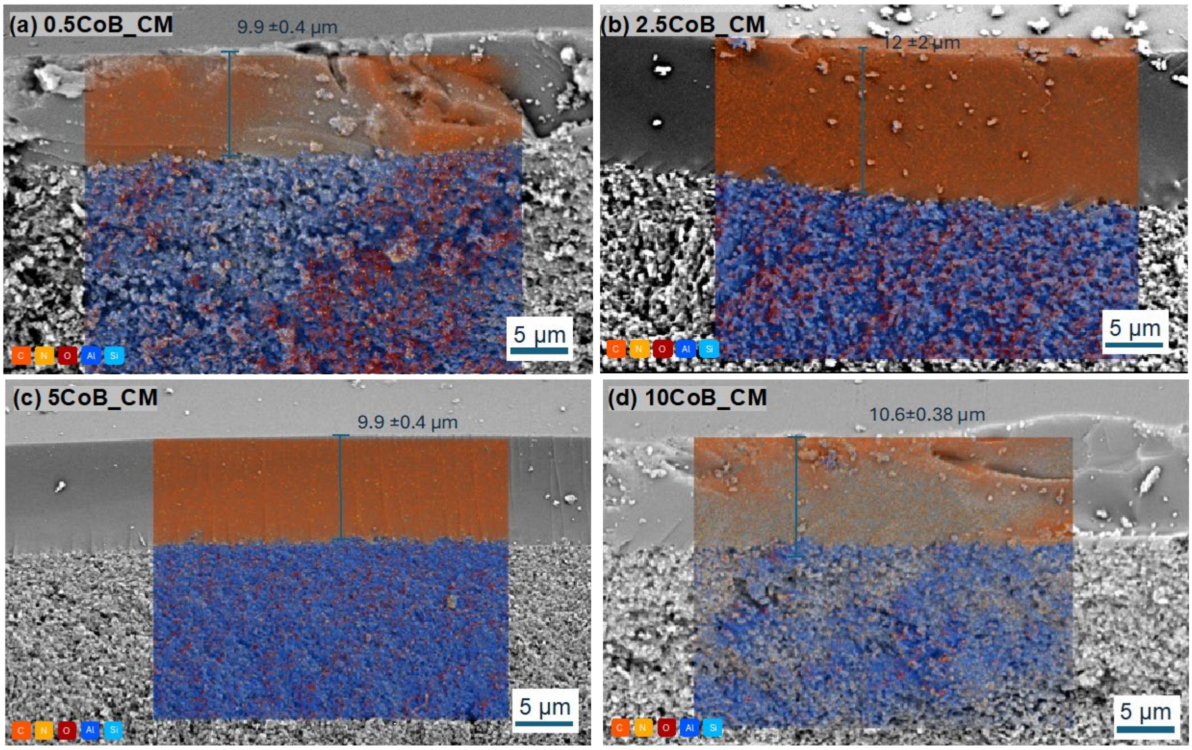

Fig. S7-7. The SEM/EDS mapping for the carbon membranes (a) 0.5CoB_CM, (b) 2.5CoB_CM, (c) 5CoB_CM and (d) 10CoB_CM.

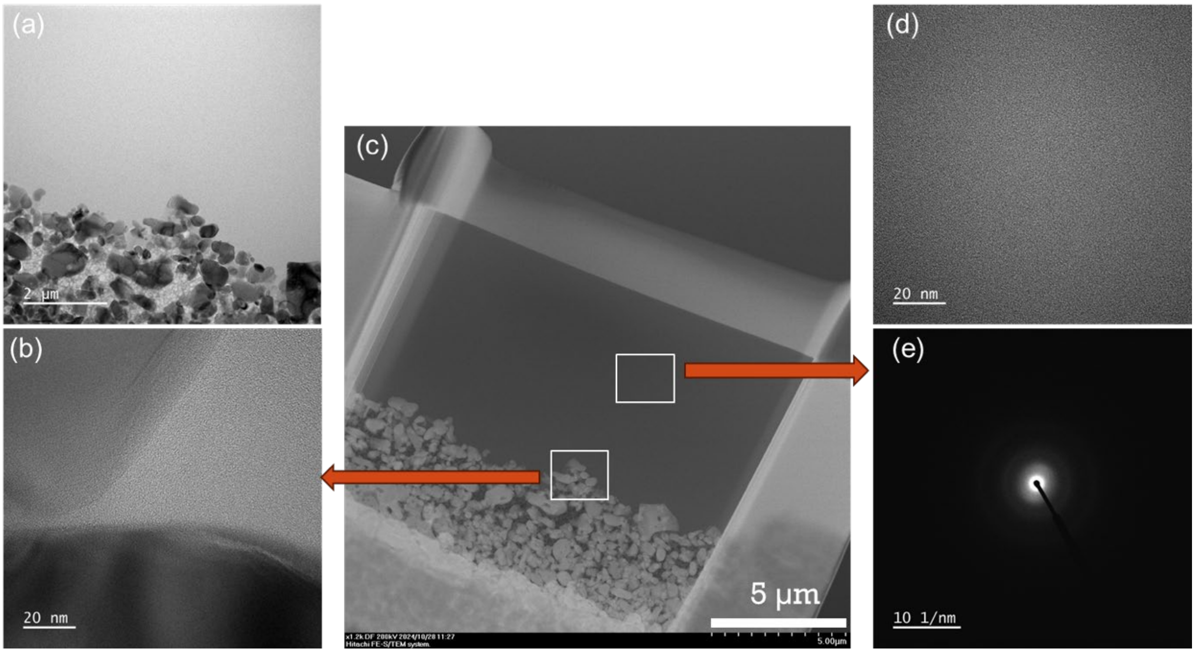

Fig. S7-8. The TEM cross-sectional analysis of the 1CoB_CM membrane. The CoB_CM and alumina substrate boundary at (a) 6000x magnification and (b) 400kX magnification. (c) The annular dark field (ADF)-STEM image of the FIB lamella consisting of the 1CoB_CM. (d) The HRTEM image of 1CoB_CM at 400kX magnification, and (e) the selected area electron diffraction (SAED) pattern of amorphous carbon.

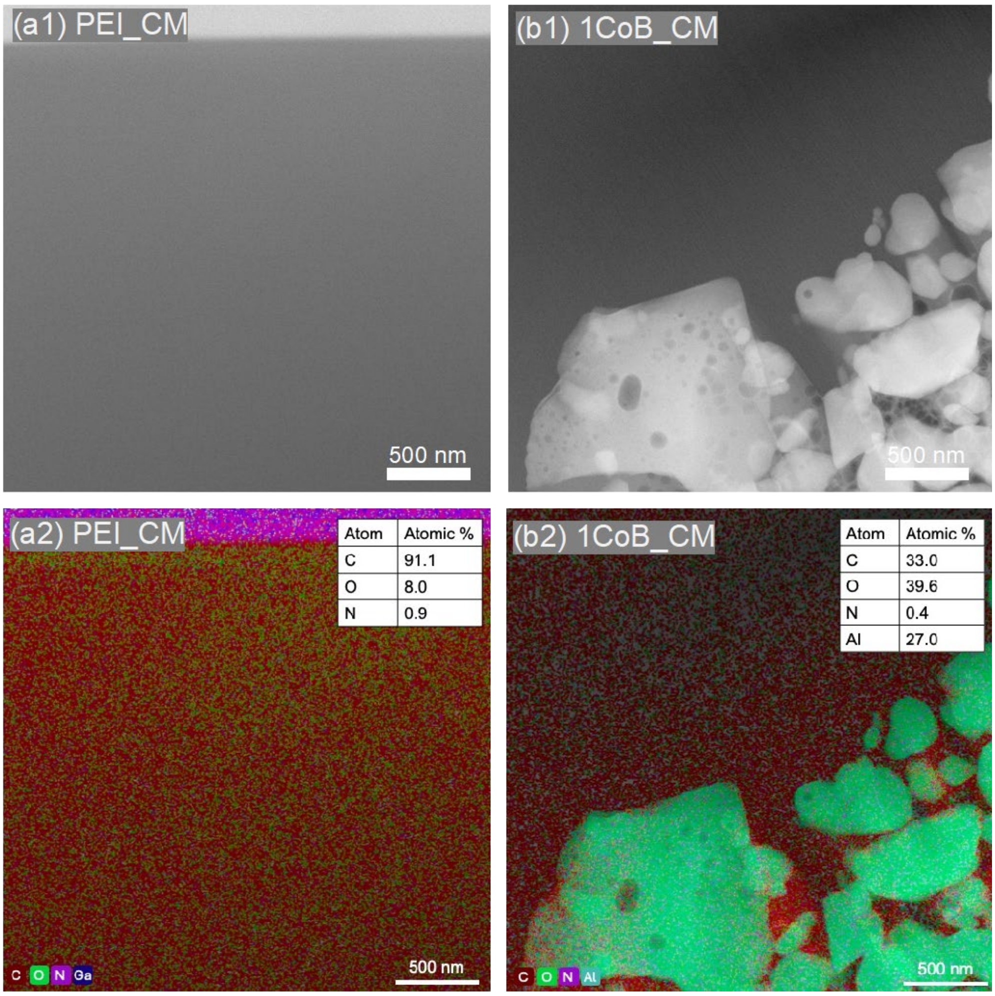

(a2) PEI_CM

Atom	Atomic %
C	91.1
O	8.0
N	0.9

(b2) 1CoB_CM

Atom	Atomic %
C	33.0
O	39.6
N	0.4
Al	27.0

Fig. S7-9. STEM-EDS analysis of (a) PEI_CM and (b) 1CoB_CM. (1) STEM images captured at 8000× magnification reveal the membrane microstructure; (2) corresponding EDS elemental mappings illustrate the spatial distribution of constituent elements within the membrane cross-section.

As shown in Table S7-2, the high-resolution C_{1s} spectra reveal a clear trend in carbon hybridisation as a function of CoB doping. Specifically, the sp^3/sp^2 carbon ratio decreases from 2.93 in the PEI_CM membrane to 1.42 in the 10CoB_CM, indicating that increasing the CoB concentration promotes the formation of sp^2-hybridised carbon structures. This observation is further supported by the shift in the sp^2 carbon peak from 283.8 eV (non-doped CM) to 284.1

eV in 1CoB_CM, as depicted in Fig. S10(a). The enhanced presence of sp^2 carbon suggests a transition towards a more graphitic configuration within the carbon matrix. Ma et al. [176] established a relationship between the sp^3/sp^2 ratio and gas permeability, proposing that sp^2-hybridised carbon might be a planar configuration that encourages the development of compact ultramicropores. In contrast, sp^3-hybridised carbon contributes to a more three-dimensional (3D) porous structure, which can support higher gas permeability [417]. Thus, the reduction in sp^3 content with increasing CoB_C loading implies a shift toward a more selective membrane structure. The sp^3/sp^2 ratio of the 10CoB_CM sample (~1.42) closely matched that of the pure CoB_C powder (~1.5), suggesting that the carbon environment became increasingly similar to that of the dopant itself.

Table. S7-2. The peak area percentage and the sp^3/sp^2 ratio of the XPS C_{1s} spectra.

Membrane	sp^3 284.8 eV	sp^2 283.8 eV	sp^3/sp^2
PEI_CM	57.9	19.8	2.93
1 CoB_CM	39.1	36.7	1.06
5 CoB_CM	42.8	46.8	0.91
10 CoB_CM	40.6	28.5	1.42

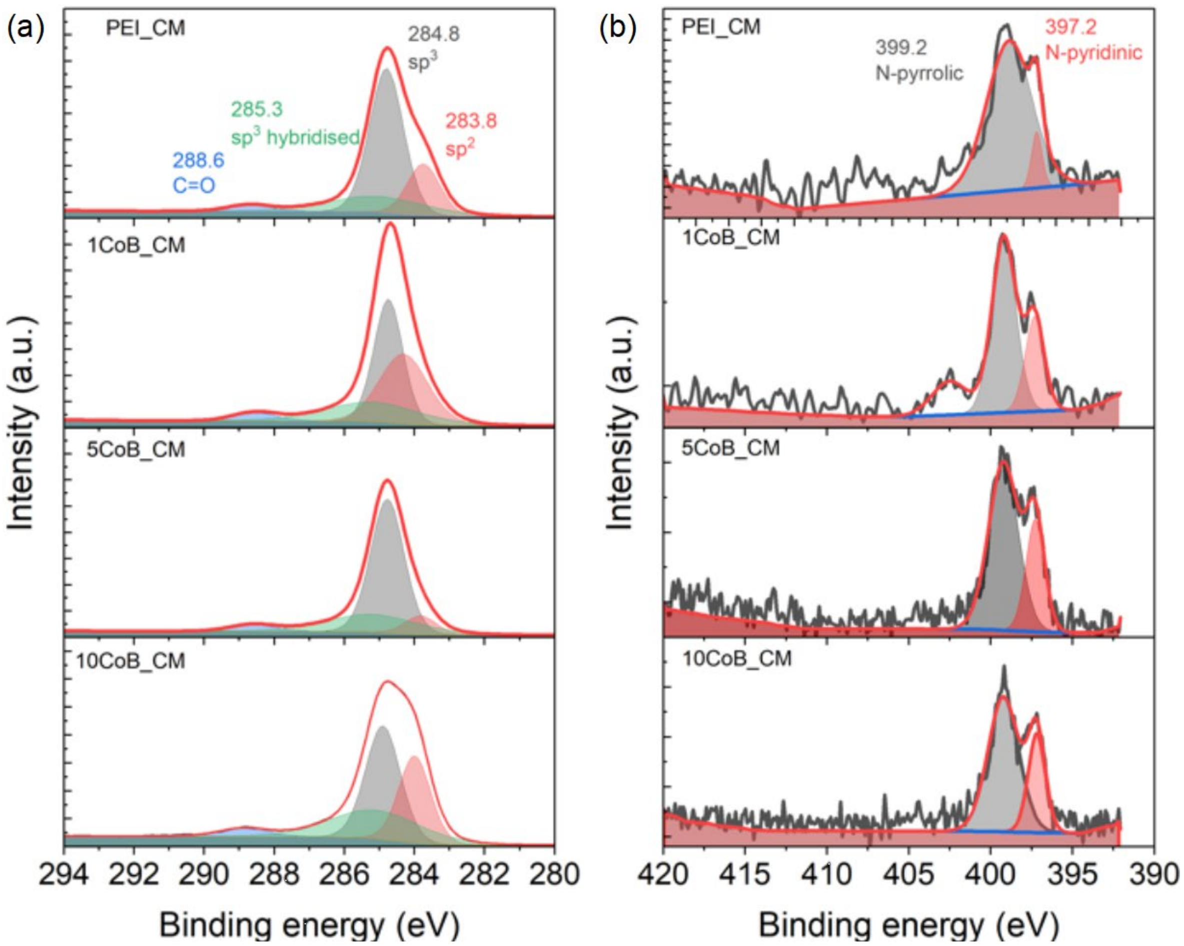

Fig. S7-10. The XPS analysis for the different concentrations of PEI_CM and CoB_CM membrane samples (a) C_{1s} and (b) N_{1s} figure.

In addition, Table S7-3 presents the ratio of N-pyrrolic/N-pyridinic ratio, which was deconvoluted from N_{1s} spectra (Fig S7-9(b)), which provide further evidence of structural modification. The N-pyrrolic/N-pyridinic ratio decreased markedly from 22.85 in the PEI_CM to approximately 2.4 in the 10CoB_CM. This trend parallels the reduction in sp^3/sp^2 ratio and highlights a shift in nitrogen speciation. Pyridinic nitrogen, typically associated with five adjacent sp^2 carbon atoms, is not a native structure in the PEI backbone. Therefore, its emergence in CoB -doped membranes strongly suggests that CoB_C facilitates the reconfiguration of nitrogen bonding environments during pyrolysis. The incorporation of pyridinic nitrogen is often linked to increased structural order and graphitisation, consistent with the observed XPS trends.

Table S7-3. The N_{1s} ratio of the different concentration of the CoB_C membranes.

Membrane	N-pyrrolic 399.2 eV	N-pyridinic 397.2 eV	N-pyrrolic/ N-pyridinic
PEI_CM	91.9	8.2	22.85
1 CoB_CM	57.8	25.3	2.28
5 CoB_CM	70	30	2.34
10 CoB_CM	58.3	24.3	2.40

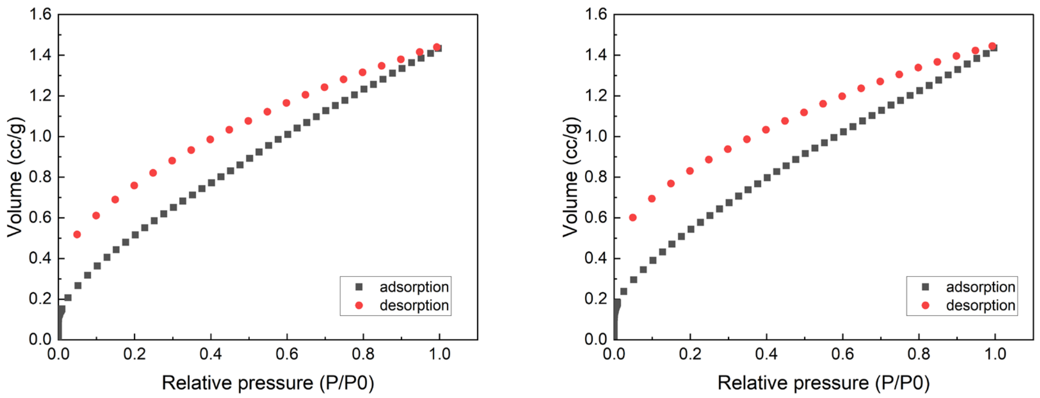
(a) PEI_CM (b) 0.5CoB_CM

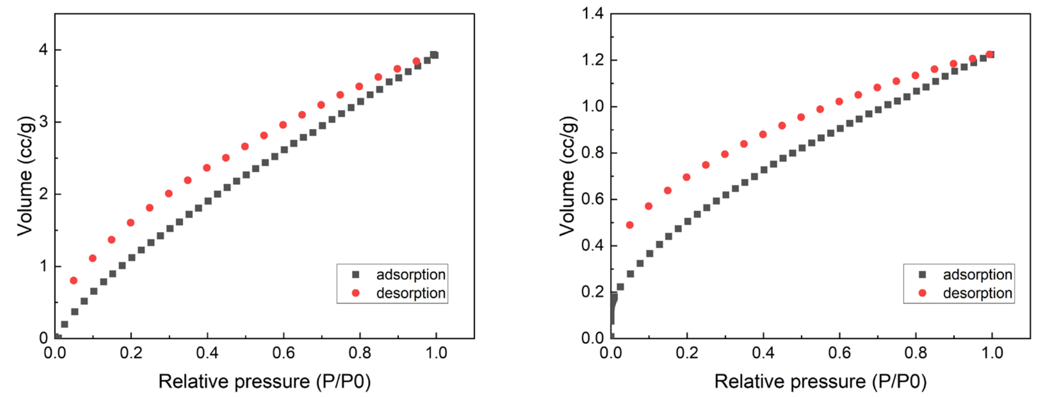
(c) 1CoB_CM (d) 2.5CoB_CM

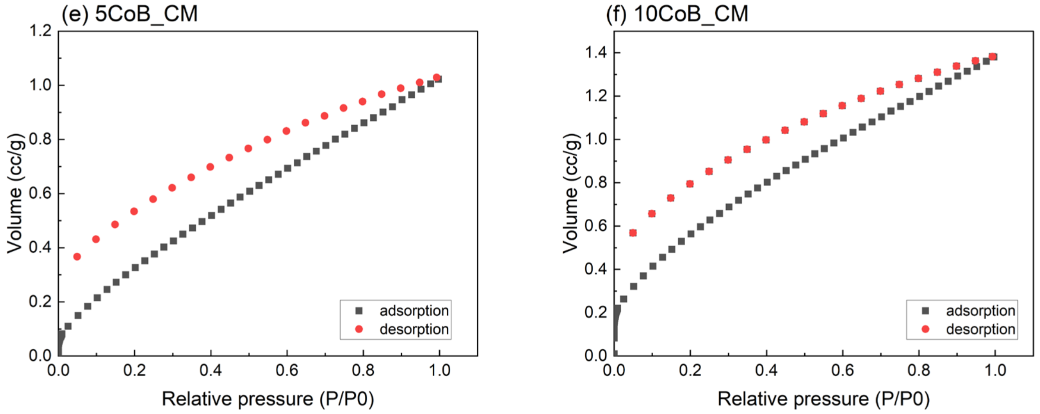
(e) 5CoB_CM (f) 10CoB_CM

Fig. S7-11. The CO_2 physisorption isotherm of the CMS membrane. (a) PEI_CM, (b) 0.5CoB_CM, (c) 1CoB_CM, (d) 2.5CoB_CM, (e) 5CoB_CM, and (f) 10CoB_CM.

Table S7-4. The gas permeance and permselectivities of the polymeric membrane with various CoB concentration dopant into PEI membranes.

Polymeric membrane	Permeance (GPU)[a]				Permselectivity ($\alpha_{X/Y}$)	
	H_2	CO_2	N_2	CH_4	H_2/CH_4	CO_2/N_2
PEI	0.346	0.098	0.006	0.005	76.6	17.7
0.5CoB	0.456	0.105	0.006	0.005	90.2	19.0
1CoB	0.398	0.087	0.006	0.006	68.8	12.7
2.5CoB	0.375	0.086	0.005	0.005	81.0	18.0
5CoB	0.372	0.099	0.006	0.005	72.8	17.5
10CoB	0.312	0.076	0.004	0.003	98.1	21.1

[a] GPU (gas permeance unit) = 3.35×10^{-10} [mol m^{-2} s^{-1} Pa^{-1}]

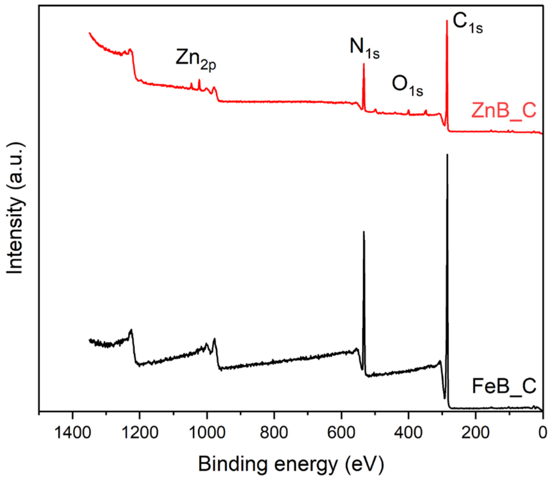

Fig. S7-12. XPS spectra of full survey of ZnB_C and FeB_C.

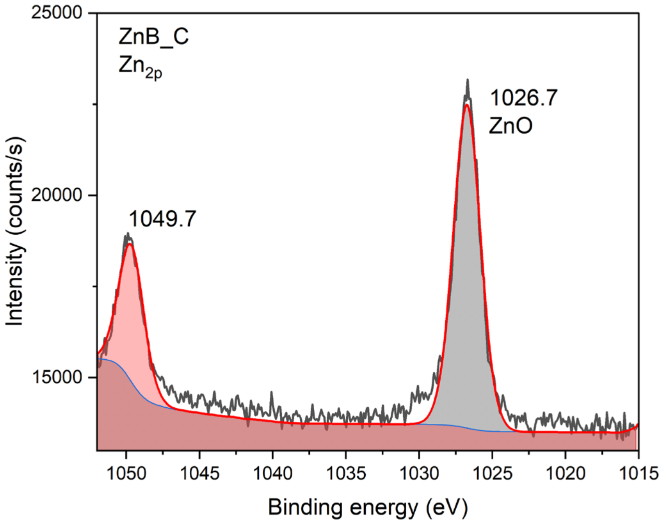

Fig. S7-13. High-resolution Zn_{2P} XPS spectrum of ZnB_C sample.

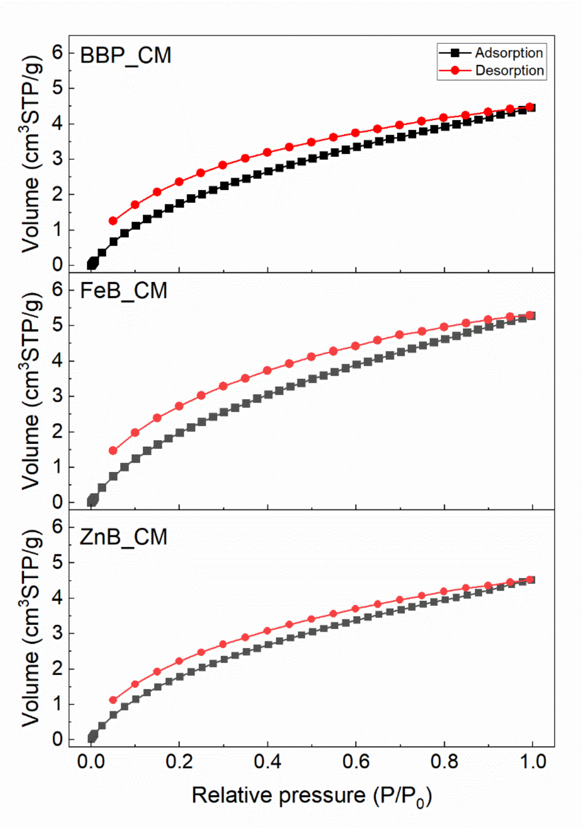

Fig. S7-14. The CO_2 physisorption isotherm of the BBP_CM, FeB_CM and ZnB_CM.

Chapter 8 Conclusion and Future Outlook

8.1. Conclusion

This thesis presents a systematic investigation into the development and optimisation of PEI-based composite membranes and MtBBP-derived CMSMs for gas separation applications. In chapter 4, a novel polishing process for tubular alumina substrates was established using a lab-scale automatic polishing machine. Polishing significantly improved surface uniformity, enabling the deposition of defect-free polymeric membranes directly onto the substrate without the need for a gutter layer. The enhanced surface compatibility facilitated the formation of robust PEI membranes.

Chapter 5 explored the optimisation of the vacuum-assisted dip-coating process for PEI membranes. A three-layer membrane structure using 12 wt.% PEI and a vacuum pressure of -1 bar significantly enhanced the separation performance. Notably, the CO_2/N_2 selectivity increased from 0 to 21.1 as the vacuum pressure was applied, confirming the role of the vacuum pressure as a driving force in reducing the coating defects. Additionally, thermal treatment studies revealed that the residual NMP solvent adversely affects separation by increasing the free volume. Complete solvent removal at 195 °C restored ideal performance, aligning with the results observed in classical PEI membrane systems.

Furthermore, in chapter 6, MtBBP was incorporated into PEI composites to evaluate the effects of metal-base coordination and concentration on membrane performance. A 1 wt.% doping of CoBBP yielded an H_2/CH_4 selectivity of 102 ± 5, a 62% improvement over the unmodified PEI membrane. Furthermore, ZnBBP and FeBBP significantly improved CO_2 permeability (approximately 1.88 Barrer), a 73% increase relative to the pristine membrane.

These findings highlight the role of metal coordination in enhancing the separations of specific gas pairs.

Chapter 7 focused on the co-pyrolysis behaviour of MtBBP-containing PEI membranes. A systematic study evaluated the influence of various metal centres (Co, Fe, Zn) on the structure and gas transport properties of CMS membranes. The resulting CMS membranes outperformed both PEI- and cellulose-derived CMS membranes in H_2/CH_4 and CO_2/CH_4 separations. Notably, ZnB_CM achieved a CO_2 permeability of 500 Barrer and CO_2/CH_4 selectivity of 305 after two regeneration cycles under humid conditions. Although CO_2 permeability declined by approximately 60%, selectivity increased fivefold, likely due to partial pore blockage that restricted gas flow while improving molecular discrimination.

To benchmark membrane performance, gas separation data were compared with the Robeson upper bounds for H_2/CH_4 (2015) and CO_2/CH_4 (2019), as shown in Fig. 8.1. Two performance regimes were identified: (1) polymeric membranes (e.g., PEI, BBP, MtBBP), which showed moderate permeability (~10 Barrer) with enhanced permselectivities via metal coordination (e.g., CoBBP $\alpha H_2/CH_4 = 102 \pm 5$, ZnBBP $\alpha = 83 \pm 1$); and (2) CMS membranes, which demonstrated significantly increased permeability. Post-carbonisation, MtBBP-based CMSMs reached H_2 permeability of 2000 – 3000 Barrer. Among these, CoB_CM exhibited the highest H_2/CH_4 selectivity (~200), indicating superior suitability for H_2 purification. Although FeB_CM and ZnB_CM achieved high permeability, their selectivity was comparatively lower, suggesting a trade-off influenced by the specific metal coordination. As shown in Fig. 8.1(b), a similar trend was observed in the CO_2/CH_4 separation. CoB_CM achieved the highest permselectivity ((~156 ± 5), while the 5CoB_CM variant demonstrated enhanced CO_2 permeability (~1400 Barrer) at the cost of reduced permselectivity ($\alpha = 77 \pm 6$). Both FeB_CM and ZnB_CM exceeded the 2019 Robeson upper bound, outperforming many reported polymeric and CMS membranes [12, 69].

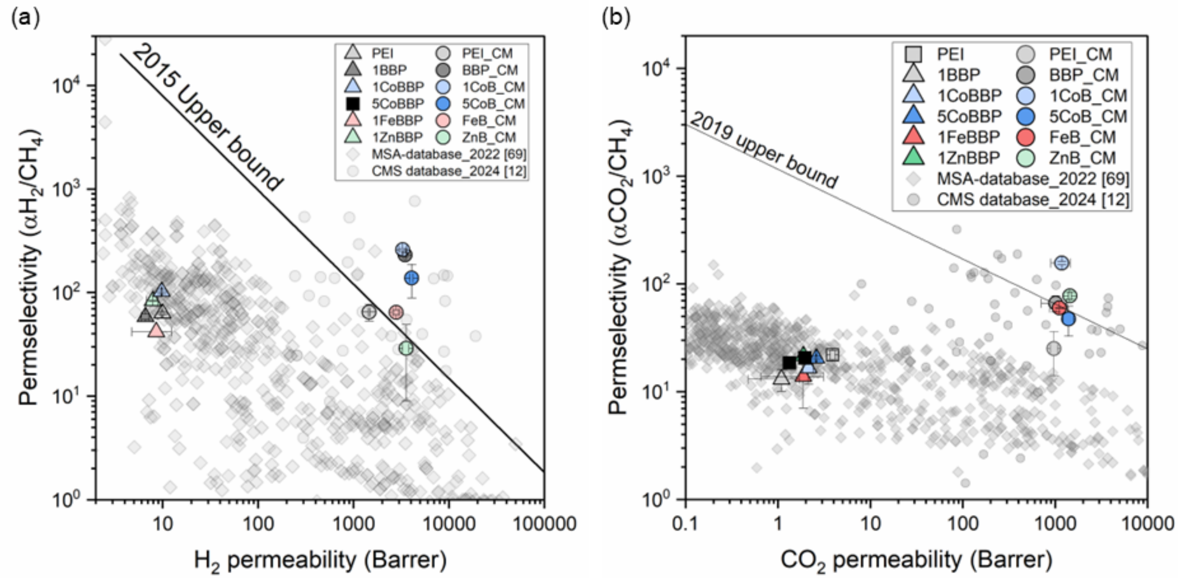

Fig. 8-1. Robeson upper bounds for H_2/CH_4 and CO_2/CH_4 gas pairs, including the representative data obtained in this thesis. Reference data were selected from sources [12, 69].

Table 8-1 benchmarks post-2022 literature and commercial CMS membranes against the best-performing condition in this study. Two flat-sheet CMS membranes were selected to illustrate that thicker films (50-100 μm) can achieve high permselectivities, while at the expense of gas permeance [473, 474]. For example, a fluorinated, modified polyimide (6FDA-TMPD) membrane pyrolyzed at 550 °C with 60 s of fluorination step achieved an H_2 permeance of 18.4 GPU with an extremely high H_2/CH_4 permselectivity of 1508 [474]. Nevertheless, the inherent brittleness of flat-sheet CMS films complicates module fabrication and scale up. In contrast, one-step hollow fibre fabrication has produced excellent gas separation [470, 475]. The representative cellulose-based membrane showed H_2 permeance of 148 GPU and H_2/CH_4 selectivity of 5700 [475]. However, similar to flat sheets, CMS hollow fibres can be fragmented under high operating pressures. To address mechanical limitations, commercial suppliers such as Media and Process Technology Inc. (MPT) and the Fraunhofer Institute for Ceramic Technologies and Systems (IKTS) employ ceramic-supported tubular composite fabrication

[476, 477], which mitigate brittleness and enable operation at higher pressures. Notably, MPT has demonstrated stable performance for >100 h under mid-temperature (~300 °C) and moderate-pressure (120-140 psig) conditions. Compared with the data reported by these manufacturers, our membrane exhibited a higher permselectivity but a slightly lower gas permeance. This difference is mainly attributed to the thicker CMS layer (~6–10 μm), which is approximately four times thicker than that of the reference membranes. Reducing the membrane thickness is therefore necessary to further enhance gas permeance while maintaining high selectivity. Future work will focus on fabricating thinner membranes with improved overall performance.

Table 8-1. Benchmarking of post-2022 literature and commercial CMS membranes with high hydrogen permeance and associated permselectivities

Membrane	Permeance (GPU)			Permselectivities (α)		Membrane type	Ref
	H_2	CO_2	CH_4	H_2/CH_4	CO_2/CH_4		
PI-GO-1.0%-550	149.3	15	0.7	210	21.3	Flat sheet	[473]
FCMS_550-60	18.4	1.58	0.01	1508	111.2	Flat sheet	[474]
Cellulose_850	148	1.76	0.03	5700	70.4	Hollow fibre	[475]
6FDA-DAM_675	-	233	3.6	-	64.3	Hollow fibre	[470]
M&PT_CMS	550	-	-	~100	-	Tubular composite	[476]
IKTS_CMS	1950	408	25.6	75	15.9	Tubular composite	[477]
1CoB_CM	**328**	**118**	**3.8**	**259**	**41.3**	**Tubular composite**	**This work**
ZnB_CM	**450**	**211**	**2.0**	**271**	**77.3**		

8.2. Future Outlook

Based on the membrane synthesis and characterisation described in the preceding chapters, several directions for future research and development are proposed to deepen the understanding and broaden the applicability of MtBBP-derived CMS membranes. CMS membranes prepared by a co-pyrolysis route under vacuum at 600 °C exhibit H_2 and CO_2 permeances comparable to conventional PEI-derived CMS membranes, while delivering higher selectivity. This suggests co-pyrolysis as a viable alternative precursor-modification pathway for CMS fabrication. Due to membrane scalability is yet to be demonstrated, we have not yet evaluated the pathway towards demonstration- or pilot-scale. Future work should assess multi-element CMS modules with larger active area and robust, high-flux packaging, and validate performance under process-relevant conditions (e.g., biogas upgrading and flue-gas CO_2 separation), including long-term stability, impurity tolerance, and start–stop operation [12, 478].

Scaling up the polishing process for industrial applications

In this study, alumina substrates were polished at lengths of 5 – 8 cm using a laboratory-scale automatic polishing system. For industrial-scale production, it is critical to assess the feasibility of polishing longer substrates while maintaining uniform surface quality. Developing or adapting polishing technologies for large-scale substrates would significantly improve the scalability and commercial viability of the membrane fabrication process.

Exploring Metal-based BBP for CO_2 conversion applications

Although the synthesis and gas separation performance of MtBBP-derived membranes have been successfully demonstrated, the potential for CO_2 conversion remains largely unexplored. Future investigations should focus on evaluating the reactivity of MtBBP powders in CO2-rich environments, particularly the mechanisms of carbonate formation. This line of research could enable the development of integrated systems that combine gas separation and catalytic conversion within a single platform.

Optimising carbonisation conditions

The carbonisation process in this work was performed at 600 °C under high vacuum. However, key membrane properties, such as porosity, surface chemistry, and gas selectivity, are highly sensitive to pyrolysis parameters, including temperature, gas atmosphere (e.g., argon, helium, nitrogen), and heating ramp rate. A systematic study of these variables on MtB_CM-modified CMSMs could yield further improvements in membrane performance and tailorability for specific gas separation targets.

Simulative analysis of the mechanisms of metal-based BBP carbonisation

Although experimental results have indicated structural transformations during carbonisation, computational methods, such as molecular dynamics or Monte Carlo simulations, could provide valuable insights into the crosslinking dynamics and structural evolution of metal-based BBPs. These simulations would support the elucidation of amorphous carbon network formation and clarify the role of metal coordination in tuning pore morphology and selectivity.

Long-term moisture stability and advanced testing modules

This study demonstrated the promising regeneration behaviour of CMS membranes under high-humidity conditions. However, the current testing module is limited to environments with 100% relative humidity. Future work should focus on the development of advanced testing systems capable of simulating variable humidity levels and elevated regeneration temperatures. Such capabilities are essential for assessing membrane performance under realistic operation conditions, such as those encountered in biogas upgrading or flue gas treatment, where moisture content may fluctuate significantly.

Chapter 9 Reference

1. Chen, W., Z. Huang, and K.J. Chua, *Sustainable energy recovery from thermal processes: a review.* Energy, Sustainability and Society, 2022. **12**(1): p. 46.
2. Brueske, S., C. Kramer, and A. Fisher, *Bandwidth Study on Energy Use and Potential Energy Saving Opportunities in U.S. Petroleum Refining*, U.D.o. Energy, Editor. 2015, Advanced Manufacturing Office.
3. United Nations. *Paris Agreement*. Paris Agreement 2015; Available from: https://unfccc.int/process-and-meetings/the-paris-agreement/the-paris-agreement.
4. Obotey Ezugbe, E. and S. Rathilal, *Membrane Technologies in Wastewater Treatment: A Review.* Membranes (Basel), 2020. **10**(5): p. 89.
5. Matsukata, M., et al., *Chapter 8 - Review on Prospects for Energy Saving in Distillation Process with Microporous Membranes*, in *Membrane Science and Technology*, S.T. Oyama and S.M. Stagg-Williams, Editors. 2011, Elsevier. p. 175-193.
6. Koros, W.J. and C. Zhang, *Materials for next-generation molecularly selective synthetic membranes.* Nature Materials, 2017. **16**(3): p. 289-297.
7. Lau, W.J., et al., *A recent progress in thin film composite membrane: A review.* Desalination, 2012. **287**: p. 190-199.
8. Liang, C.Z., T.-S. Chung, and J.-Y. Lai, *A review of polymeric composite membranes for gas separation and energy production.* Progress in Polymer Science, 2019. **97**: p. 101141.
9. Baker, R.W. and B.T. Low, *Gas Separation Membrane Materials: A Perspective.* Macromolecules, 2014. **47**(20): p. 6999.
10. Dai, Z., L. Ansaloni, and L. Deng, *Recent advances in multi-layer composite polymeric membranes for CO_2 separation: A review.* Green Energy & Environment, 2016. **1**(2): p. 102-128.
11. Salleh, W.N.W., et al., *Precursor Selection and Process Conditions in the Preparation of Carbon Membrane for Gas Separation: A Review.* Separation & Purification Reviews, 2011. **40**(4): p. 261-311.
12. Genduso, G., et al., *Carbon molecular sieve gas separation materials and membranes: A comprehensive review.* Journal of Membrane Science, 2024. **699**: p. 122533.
13. Feng, C., et al., *Thin-Film-Composite Carbon Molecular Sieve Membranes for Efficient Helium and Hydrogen Separation.* Industrial & Engineering Chemistry Research, 2024. **63**(1): p. 594-606.
14. Zhang, G. and H. Lin, *Indispensable gutter layers in thin-film composite membranes for carbon capture.* Green Energy & Environment, 2024. **9**(8): p. 1220-1238.
15. Kattula, M., et al., *Designing ultrathin film composite membranes: the impact of a gutter layer.* Scientific Reports, 2015. **5**(1): p. 15016.
16. Tang, X. and X. Yan, *Dip-coating for fibrous materials: mechanism, methods and applications.* Journal of Sol-Gel Science and Technology, 2017. **81**: p. 378-404.
17. Yoo, M.J., et al., *Defect control for large-scale thin-film composite membrane and its bench-scale demonstration.* Journal of Membrane Science, 2018. **566**: p. 374-382.
18. Hao, L., P. Li, and T.-S. Chung, *PIM-1 as an organic filler to enhance the gas separation performance of Ultem polyetherimide.* Journal of Membrane Science, 2014. **453**: p. 614-623.

19. Yong, W.F., et al., *Molecular interaction, gas transport properties and plasticization behavior of cPIM-1/Torlon blend membranes.* Journal of Membrane Science, 2014. **462**: p. 119-130.
20. Swaidan, R., et al., *Pure- and mixed-gas CO2/CH4 separation properties of PIM-1 and an amidoxime-functionalized PIM-1.* Journal of Membrane Science, 2014. **457**: p. 95-102.
21. Park, H.B., et al., *Thermally rearranged (TR) polymer membranes for CO2 separation.* Journal of Membrane Science, 2010. **359**(1): p. 11-24.
22. Han, S.H., et al., *Thermally Rearranged (TR) Polybenzoxazole: Effects of Diverse Imidization Routes on Physical Properties and Gas Transport Behaviors.* Macromolecules, 2010. **43**(18): p. 7657-7667.
23. Shamsipur, H., et al., *Thermally Rearrangeable PIM-Polyimides for Gas Separation Membranes.* Macromolecules, 2014. **47**(16): p. 5595-5606.
24. Baker, R.W., *Future Directions of Membrane Gas Separation Technology.* Industrial & Engineering Chemistry Research, 2002. **41**(6): p. 1393-1411.
25. Jones, C.W. and W.J. Koros, *Carbon molecular sieve gas separation membranes-I. Preparation and characterization based on polyimide precursors.* Carbon, 1994. **32**(8): p. 1419-1425.
26. Ismail, A.F. and L.I.B. David, *A review on the latest development of carbon membranes for gas separation.* Journal of Membrane Science, 2001. **193**(1): p. 1-18.
27. Koresh, J.E. and A. and Soffer, *The Carbon Molecular Sieve Membranes. General Properties and the Permeability of CH_4/H_2 Mixture.* Separation Science and Technology, 1987. **22**(2-3): p. 973-982.
28. Araújo, T., G. Bernardo, and A. Mendes, *Cellulose-Based Carbon Molecular Sieve Membranes for Gas Separation: A Review.* Molecules, 2020. **25**(15): p. 3532.
29. Hamm, J.B.S., et al., *Recent advances in the development of supported carbon membranes for gas separation.* International Journal of Hydrogen Energy, 2017. **42**(39): p. 24830-24845.
30. Tseng, H.-H., et al., *Enhanced H_2/CH_4 and H_2/CO_2 separation by carbon molecular sieve membrane coated on titania modified alumina support: Effects of TiO_2 intermediate layer preparation variables on interfacial adhesion.* Journal of Membrane Science, 2016. **510**: p. 391-404.
31. Tseng, H.-H., S.-H. Chang, and M.-Y. Wey, *A carbon gutter layer-modified α-Al_2O_3 substrate for PPO membrane fabrication and CO_2 separation.* Journal of Membrane Science, 2014. **454**: p. 51-61.
32. Ismail, N.H., et al., *Effect of intermediate layer on gas separation performance of disk supported carbon membrane.* Separation Science and Technology, 2017. **52**(13): p. 2137-2149.
33. Sazali, N., et al., *Influence of intermediate layers in tubular carbon membrane for gas separation performance.* International Journal of Hydrogen Energy, 2019. **44**(37): p. 20914-20923.
34. Hamelinck, C.N. and A.P.C. Faaij, *Future prospects for production of methanol and hydrogen from biomass.* Journal of Power Sources, 2002. **111**(1): p. 1-22.
35. He, J., et al., *Molecular simulations of organic solvent transport in dense polymer membranes: Solution-diffusion or pore-flow mechanism?* Journal of Membrane Science, 2024. **708**: p. 123055.
36. Ismail, A.F., K.C. Khulbe, and T. Matsuura, *Fundamentals of Gas Permeation Through Membranes*, in *Gas Separation Membranes: Polymeric and Inorganic*, A.F. Ismail, K. Chandra Khulbe, and T. Matsuura, Editors. 2015, Springer International Publishing: Cham. p. 11-35.

37. Wu, A.X., et al., *Revisiting group contribution theory for estimating fractional free volume of microporous polymer membranes.* Journal of Membrane Science, 2021. **636**: p. 119526.
38. Wijmans, J.G. and R.W. Baker, *The solution-diffusion model: a review.* Journal of Membrane Science, 1995. **107**(1): p. 1-21.
39. Kumins, C. and T. Kwei, *Diffusion in polymers.* Academic Press, New York, NY, 1968.
40. Frisch, H.L. and S. Alexander Stern, *Diffusion of small molecules in polymers.* Critical Reviews in Solid State and Materials Sciences, 1983. **11**(2): p. 123-187.
41. Frisch, H.L., D. Klempner, and T.K. Kwei, *Modified Free-Volume Theory of Penetrant Diffusion in Polymers.* Macromolecules, 1971. **4**(2): p. 237-238.
42. Ganesh, K., R. Nagarajan, and J.L. Duda, *Rate of gas transport in glassy polymers: a free volume based predictive model.* Industrial & Engineering Chemistry Research, 1992. **31**(3): p. 746-755.
43. Paul, D.R. and W.J. Koros, *Effect of partially immobilizing sorption on permeability and the diffusion time lag.* Journal of Polymer Science Part A-2: Polymer Physics, 1976. **14**(4): p. 675-685.
44. Koros, W.J., D.R. Paul, and G.S. Huvard, *Energetics of gas sorption in glassy polymers.* Polymer, 1979. **20**(8): p. 956-960.
45. Lee, W.M., *Selection of barrier materials from molecular structure.* Polymer Engineering & Science, 1980. **20**(1): p. 65-69.
46. Pace, R.J. and A. Datyner, *Model of sorption of simple molecules in polymers.* Journal of Polymer Science: Polymer Physics Edition, 1980. **18**(5): p. 1103-1124.
47. Hu, C.-C., et al., *Effect of free volume and sorption on membrane gas transport.* Journal of Membrane Science, 2003. **226**(1): p. 51-61.
48. Zheng, W., et al., *Dual-function biomimetic carrier based facilitated transport mixed matrix membranes with high stability for efficient CO_2/N_2 separation.* Separation and Purification Technology, 2022. **285**: p. 120371.
49. Tong, Z. and W.S.W. Ho, *New sterically hindered polyvinylamine membranes for CO_2 separation and capture.* Journal of Membrane Science, 2017. **543**: p. 202-211.
50. Rea, R., M.G. De Angelis, and M.G. Baschetti, *Models for Facilitated Transport Membranes: A Review.* Membranes, 2019. **9**(2): p. 26.
51. Guo, H., et al., *Facilitated transport membranes for CO_2/CH_4 separation - State of the art.* Advanced Membranes, 2022. **2**: p. 100040.
52. Sidhikku Kandath Valappil, R., N. Ghasem, and M. Al-Marzouqi, *Current and future trends in polymer membrane-based gas separation technology: A comprehensive review.* Journal of Industrial and Engineering Chemistry, 2021. **98**: p. 103-129.
53. Chiwaye, N., T. Majozi, and M.O. Daramola, *Optimisation of post-combustion carbon dioxide capture by use of a fixed site carrier membrane.* International Journal of Greenhouse Gas Control, 2021. **104**: p. 103182.
54. Hanioka, S., et al., *CO_2 separation facilitated by task-specific ionic liquids using a supported liquid membrane.* Journal of Membrane Science, 2008. **314**(1): p. 1-4.
55. Fu, W. and W. Zhang, *Measurement of the surface hydrophobicity of engineered nanoparticles using an atomic force microscope.* Physical Chemistry Chemical Physics, 2018. **20**(37): p. 24434-24443.
56. Sandru, M., T.-J. Kim, and M.-B. Hägg, *High molecular fixed-site-carrier PVAm membrane for CO_2 capture.* Desalination, 2009. **240**(1): p. 298-300.
57. *Membrane solutions for natural gas treatment*. 2018; Available from: https://advancedseparations.airliquide.com/sites/alas/files/2016/11/28/alas_ng_brochure_final.pdf.

58. *GENERON® nitrogen membrane system*. 2023; Available from: https://www.generon.com/product_type/nitrogen-generator-containerized-mobile-systems/#:~:text=GENERON%C2%AE%20Membrane%20separation%20systems,met%20and%20your%20expectations%20exceeded.
59. Song, C., et al., *Tri-reforming of Methane over Ni Catalysts for CO_2 Conversion to Syngas With Desired H_2/CO Ratios Using Flue Gas of Power Plants Without CO_2 Separation*, in *Studies in Surface Science and Catalysis*, S.-E. Park, J.-S. Chang, and K.-W. Lee, Editors. 2004, Elsevier. p. 315-322.
60. Larocca, N.M. and L.A. Pessan, *Effect of antiplasticisation on the volumetric, gas sorption and transport properties of polyetherimide.* Journal of Membrane Science, 2003. **218**(1): p. 69-92.
61. *Nitrogen Membranes*. 2019; Available from: https://oxair.com.au/oxair-products/nitrogen-membrane/?gad_source=1&gad_campaignid=10866508251&gbraid=0AAAAD_p57vxp43Equyrryd5o69d9nh6l&gclid=CjwKCAjw24vBBhABEiwANFG7y96L9g17-MotRGDHv6arZ5Y_l1_TNYMz2D_-oSgMqlxgskzoJC0oBRoCJX8QAvD_BwE.
62. *How does the VaporSep® process work?* 2025; Available from: https://www.mtrinc.com/faqs/how-does-the-vaporsep-process-work/.
63. *UBE CO_2 Separator for Biogas Upgrading*. 2025; Available from: https://ube.es/products/.
64. markets, A.s.r., *Standard Test Method for Determining Gas Permeability Characteristics of Plastic Film and Sheeting1*. 2023: United State.
65. Robeson, L.M., *Correlation of separation factor versus permeability for polymeric membranes.* Journal of Membrane Science, 1991. **62**(2): p. 165-185.
66. Robeson, L.M., *The upper bound revisited.* Journal of Membrane Science, 2008. **320**(1): p. 390-400.
67. Swaidan, R., B. Ghanem, and I. Pinnau, *Fine-tuned intrinsically ultramicroporous polymers redefine the permeability/selectivity upper bounds of membrane-based air and hydrogen separations.* ACS Macro Letters, 2015. **4**(9): p. 947-951.
68. Comesaña-Gándara, B., et al., *Redefining the Robeson upper bounds for CO_2/CH_4 and CO_2/N_2 separations using a series of ultrapermeable benzotriptycene-based polymers of intrinsic microporosity.* Energy & Environmental Science, 2019. **12**(9): p. 2733-2740.
69. A. W. Thornton, B.D.F., L. M. Robeson. *Polymer gas separation membrane database (2012)*. 2012; Available from: https://membrane-australasia.org/polymer-gas-separation-membrane-database/.
70. Comesana-Gandara, B., et al., *Redefining the Robeson upper bounds for CO_2/CH_4 and CO_2/N_2 separations using a series of ultrapermeable benzotriptycene-based polymers of intrinsic microporosity.* Energy & Environmental Science, 2019. **12**(9): p. 2733-2740.
71. Freeman, B.D., *Basis of permeability/selectivity tradeoff relations in polymeric gas separation membranes.* Macromolecules, 1999. **32**: p. 375-380.
72. Robeson, L.M., et al., *An empirical correlation of gas permeability and permselectivity in polymers and its theoretical basis.* Journal of Membrane Science, 2009. **341**(1-2): p. 178-185.
73. Breck, D.W., *Zeolite molecular sieves: structure, chemistry, and use.* Journal of Chromatographic Science, 1974. **13**(4): p. 18A.
74. Pandey, P. and R.S. Chauhan, *Membranes for gas separation.* Progress in Polymer Science, 2001. **26**(6): p. 853-893.

75. Keizer, K., et al., *Gas separation mechanisms in microporous modified γ-Al_2O_3 membranes.* Journal of Membrane Science, 1988. **39**(3): p. 285-300.
76. Jazani, O., M.A. Elharati, and S. Liguori, *Effects of porous supports and binary gases on hydrogen permeation in Pd–Ag–Y alloy membrane.* Journal of Membrane Science, 2025. **713**: p. 123327.
77. Karimi, M.B., S. Hassanajili, and G. Khanbabaei, *Capillary condensation mechanism for gas transport in fiber reinforced poly (ether-b-amide) membranes.* Chemical Engineering Research and Design, 2019. **148**: p. 180-190.
78. Greil, S., et al., *Gas Transport Selectivity of Ultrathin, Nanoporous, Inorganic Membranes Made from Block Copolymer Templates.* Chemistry of Materials, 2017. **29**(21): p. 9572-9578.
79. Yang, G., et al., *Capillary Condensation of Single- and Multicomponent Fluids in Nanopores.* Industrial & Engineering Chemistry Research, 2019. **58**(41): p. 19302-19315.
80. Rao, M.B. and S. Sircar, *Nanoporous carbon membranes for separation of gas mixtures by selective surface flow.* Journal of Membrane Science, 1993. **85**(3): p. 253-264.
81. Uhlhorn, R.J.R., K. Keizer, and A.J. Burggraaf, *Gas and surface diffusion in modified γ-alumina systems.* Journal of Membrane Science, 1989. **46**(2): p. 225-241.
82. Kiyono, M., P.J. Williams, and W.J. Koros, *Effect of pyrolysis atmosphere on separation performance of carbon molecular sieve membranes.* Journal of Membrane Science, 2010. **359**(1): p. 2-10.
83. Jenkins, G.M. and K. Kawamura, *Polymeric carbons: carbon fibre, glass and char.* 1976: Cambridge University Press.
84. Steel, K.M. and W.J. Koros, *Investigation of porosity of carbon materials and related effects on gas separation properties.* Carbon, 2003. **41**(2): p. 253-266.
85. Steel, K.M. and W.J. Koros, *An investigation of the effects of pyrolysis parameters on gas separation properties of carbon materials.* Carbon, 2005. **43**(9): p. 1843-1856.
86. Sanyal, O., et al., *A Self-Consistent Model for Sorption and Transport in Polyimide-Derived Carbon Molecular Sieve Gas Separation Membranes.* Angewandte Chemie International Edition, 2020. **59**(46): p. 20343-20347.
87. Yoon, Y.H., et al., *Direct evidence of the ultramicroporous structure of carbon molecular sieves.* Carbon, 2023. **210**: p. 118002.
88. David, L.I.B. and A.F. Ismail, *Influence of the thermastabilization process and soak time during pyrolysis process on the polyacrylonitrile carbon membranes for O2/N2 separation.* Journal of Membrane Science, 2003. **213**(1): p. 285-291.
89. Lie, J.A. and M.-B. Hägg, *Carbon membranes from cellulose and metal loaded cellulose.* Carbon, 2005. **43**(12): p. 2600-2607.
90. Lie, J.A. and M.-B. Hägg, *Carbon membranes from cellulose: Synthesis, performance and regeneration.* Journal of Membrane Science, 2006. **284**(1): p. 79-86.
91. Rao, M. and S. Sircar, *Nanoporous carbon membranes for separation of gas mixtures by selective surface flow.* Journal of Membrane Science, 1993. **85**(3): p. 253-264.
92. Centeno, T.A. and A.B. Fuertes, *Carbon molecular sieve gas separation membranes based on poly(vinylidene chloride-co-vinyl chloride).* Carbon, 2000. **38**(7): p. 1067-1073.
93. Pierson, H., *Vitreous carbon.* Handb. Carbon Graph. Diam. Fuller., Noyes, 1993. **533**: p. 122-140.
94. Teixeira, M., et al., *Composite phenolic resin-based carbon molecular sieve membranes for gas separation.* Carbon, 2011. **49**(13): p. 4348-4358.

95. Centeno, T.A., J.L. Vilas, and A.B. Fuertes, *Effects of phenolic resin pyrolysis conditions on carbon membrane performance for gas separation.* Journal of Membrane Science, 2004. **228**(1): p. 45-54.
96. Fuertes, A.B., *Adsorption-selective carbon membrane for gas separation.* Journal of Membrane Science, 2000. **177**(1-2): p. 9-16.
97. Fuertes, A.B. and I. Menendez, *Separation of hydrocarbon gas mixtures using phenolic resin-based carbon membranes.* Separation and purification technology, 2002. **28**(1): p. 29-41.
98. Donnet, J.-B. and R.C. Bansal, *Carbon fibers*. 1998: Crc Press.
99. Schindler, E. and F. Maier, *Manufacture of porous carbon membranes.* US4919860A, 1990.
100. Yoneyama, H. and Y. Nishihara, *Porous hollow carbon fiber film and method of manufacturing the same.* EP Patent 0,394,449, 1990.
101. Smith, S.P.J., et al., *Preparation of hollow-fibre composite carbon-zeolite membranes.* Microporous Materials, 1995. **4**(5): p. 385-390.
102. Linkov, V.M., R.D. Sanderson, and E.P. Jacobs, *Carbon membranes from precursors containing low-carbon residual polymers.* Polymer international, 1994. **35**(3): p. 239-242.
103. Song, C., et al., *Effect of carbonization atmosphere on the structure changes of PAN carbon membranes.* Journal of Porous Materials, 2009. **16**(2): p. 197-203.
104. Lamond, T., J. Metcalfe Iii, and P. Walker Jr, *6Å molecular sieve properties of saran-type carbons.* Carbon, 1965. **3**(1): p. 59-63.
105. Dacey, J.R. and R.G. Barradas, *STRUCTURE OF PYROLYZED POLYVINYLIDENE CHLORIDE.* Canadian Journal of Chemistry, 1963. **41**(1): p. 180-190.
106. Liu, J., et al., *Self-standing permselective CMS membrane from melt extruded PVDC.* Journal of Membrane Science, 2020. **615**: p. 118554.
107. Song, C., et al., *Gas separation performance of C/CMS membranes derived from poly(furfuryl alcohol) (PFA) with different chemical structure.* Journal of Membrane Science, 2010. **361**(1): p. 22-27.
108. Acharya, M. and H.C. Foley, *Spray-coating of nanoporous carbon membranes for air separation.* Journal of Membrane Science, 1999. **161**(1): p. 1-5.
109. Shiflett, M.B. and H.C. Foley, *Reproducible production of nanoporous carbon membranes.* Carbon, 2001. **39**(9): p. 1421-1425.
110. Shiflett, M.B. and H.C. Foley, *On the preparation of supported nanoporous carbon membranes.* Journal of Membrane Science, 2000. **179**(1): p. 275-282.
111. Shiflett, M.B. and H.C. Foley, *Ultrasonic Deposition of High-Selectivity Nanoporous Carbon Membranes.* Science, 1999. **285**(5435): p. 1902-1905.
112. Detlefsen, W.D., *Chapter 20 - Phenolic resins: some chemistry, technology, and history*, in *Adhesion Science and Engineering*, D.A. Dillard, A.V. Pocius, and M. Chaudhury, Editors. 2002, Elsevier Science B.V.: Amsterdam. p. 869-945.
113. Borah, M. and S. Dhakate, *Expanded Graphite Composite Based Bipolar Plate for PEM Fuel Cell: Development of Low Density and Low Cost Composite Bipolar Plate for Proton Exchange Membrane Fuel Cell.* 2016.
114. Zhou, W., et al., *Preparation and gas permeation properties of carbon molecular sieve membranes based on sulfonated phenolic resin.* Journal of Membrane Science, 2003. **217**(1): p. 55-67.
115. Abd Jalil, S.N., et al., *Vacuum-assisted tailoring of pore structures of phenolic resin derived carbon membranes.* Journal of Membrane Science, 2017. **525**: p. 240-248.

116. Wu, Y., et al., *A simple one-step drop-coating approach on fabrication of supported carbon molecular sieve membranes with high gas separation performance.* Asia-Pacific Journal of Chemical Engineering, 2018. **13**(6): p. e2251.
117. Ho, N.A.D. and C.P. Leo, *A review on the emerging applications of cellulose, cellulose derivatives and nanocellulose in carbon capture.* Environmental Research, 2021. **197**: p. 111100.
118. Lei, L., et al., *Spinning cellulose hollow fibers using 1-ethyl-3-methylimidazolium acetate–dimethylsulfoxide co-solvent.* Polymers, 2018. **10**(9): p. 972.
119. Sazali, N., et al., *Effect of heating rates on the microstructure and gas permeation properties of carbon membranes.* Malaysian Journal of Fundamental and Applied Sciences, 2018. **14**(3): p. 378-381.
120. Sazali, N., et al., *Impact of stabilization environment and heating rates on P84 co-polyimide/nanocrystaline cellulose carbon membrane for hydrogen enrichment.* International Journal of Hydrogen Energy, 2019. **44**(37): p. 20924-20932.
121. Sazali, N., et al., *Incorporation of thermally labile additives in carbon membrane development for superior gas permeation performance.* Journal of Natural Gas Science and Engineering, 2018. **49**: p. 376-384.
122. Hatori, H., et al., *Carbon molecular sieve films from polyimide.* Carbon, 1992. **30**(2): p. 305-306.
123. Dasgupta, S., et al., *Influence of chain length on structural properties of carbon molecular sieving membranes and their effects on CO_2, CH_4 and N_2 adsorption: A molecular simulation study.* Journal of Membrane Science, 2022. **664**: p. 121044.
124. Rungta, M., et al., *Carbon molecular sieve structure development and membrane performance relationships.* Carbon, 2017. **115**: p. 237-248.
125. Park, H.B., S.Y. Lee, and Y.M. Lee, *Pyrolytic carbon membranes containing silica: morphological approach on gas transport behavior.* Journal of Molecular Structure, 2005. **739**(1): p. 179-190.
126. Kim, Y.K., H.B. Park, and Y.M. Lee, *Preparation and characterization of carbon molecular sieve membranes derived from BTDA–ODA polyimide and their gas separation properties.* Journal of Membrane Science, 2005. **255**(1): p. 265-273.
127. Zhuang, Y., et al., *Intrinsically Microporous Soluble Polyimides Incorporating Tröger's Base for Membrane Gas Separation.* Macromolecules, 2014. **47**(10): p. 3254-3262.
128. Gunawan, T., et al., *Zeolite templated carbon: Preparation, characterization and performance as filler material in co-polyimide membranes for CO_2/CH_4 separation.* Malaysian Journal of Fundamental and Applied Sciences, 2019. **15**(3): p. 407-413.
129. Widiastuti, N., et al., *P84/ZCC Hollow Fiber Mixed Matrix Membrane with PDMS Coating to Enhance Air Separation Performance.* Membranes, 2020. **10**(10): p. 267.
130. Park, H.B., et al., *Relationship between chemical structure of aromatic polyimides and gas permeation properties of their carbon molecular sieve membranes.* Journal of Membrane Science, 2004. **229**(1): p. 117-127.
131. Itta, A.K. and H.-H. Tseng, *Hydrogen separation performance of CMS membranes derived from the imide-functional group of two similar types of precursors.* International Journal of Hydrogen Energy, 2011. **36**(14): p. 8645-8657.
132. Tin, P.S., et al., *Novel approaches to fabricate carbon molecular sieve membranes based on chemical modified and solvent treated polyimides.* Microporous and Mesoporous Materials, 2004. **73**(3): p. 151-160.
133. Sazali, N., et al., *Matrimid-based carbon tubular membranes: The effect of the polymer composition.* Journal of Applied Polymer Science, 2015. **132**(33): p. 42394.

134. Sazali, N., et al., *Matrimid-based carbon tubular membrane: Effect of carbonization environment.* Journal of Industrial and Engineering Chemistry, 2015. **32**: p. 167-171.
135. Xiao, Y., et al., *Effects of Brominating Matrimid Polyimide on the Physical and Gas Transport Properties of Derived Carbon Membranes.* Macromolecules, 2005. **38**(24): p. 10042-10049.
136. Sim, Y.H., et al., *High performance carbon molecular sieve membranes derived from hyperbranched polyimide precursors for improved gas separation applications.* Carbon, 2013. **53**: p. 101-111.
137. Kiyono, M., P.J. Williams, and W.J. Koros, *Effect of polymer precursors on carbon molecular sieve structure and separation performance properties.* Carbon, 2010. **48**(15): p. 4432-4441.
138. Li, J.-Y., et al., *Uniformity control and ultra-micropore development of tubular carbon membrane for light gas separation.* AIChE Journal, 2020. **66**(6): p. e16226.
139. Li, J.-Y., H.-H. Tseng, and M.-Y. Wey, *Tuning thermal expansion behavior and surface roughness of tubular Al_2O_3 substrates for fabricating high-performance carbon molecular sieving membranes for H_2 separation.* International Journal of Hydrogen Energy, 2019. **44**(45): p. 24746-24758.
140. Lin, Y.-T., et al., *Orientation of the microstructure of free-standing carbon hollow fiber membranes modulated by carbonization condition triggers aging-resistant properties.* Journal of Environmental Chemical Engineering, 2022. **10**(6): p. 108941.
141. Lin, Y.-T., et al., *Engineered pinhole-stitching process of PEI-based hollow fiber membrane enables preferred performance toward light gas separation.* International Journal of Hydrogen Energy, 2024. **50**: p. 400-408.
142. Wey, M.-Y., et al., *Interfacial interaction between CMS layer and substrate: Critical factors affecting membrane microstructure and H_2 and CO_2 separation performance from CH_4.* Journal of Membrane Science, 2019. **580**: p. 49-61.
143. Tseng, H.-H., et al., *Influence of support structure on the permeation behavior of polyetherimide-derived carbon molecular sieve composite membrane.* Journal of Membrane Science, 2012. **405-406**: p. 250-260.
144. Wang, K.Y., M. Weber, and T.-S. Chung, *Polybenzimidazoles (PBIs) and state-of-the-art PBI hollow fiber membranes for water, organic solvent and gas separations: a review.* Journal of Materials Chemistry A, 2022. **10**(16): p. 8687-8718.
145. Omidvar, M., et al., *Unexpectedly Strong Size-Sieving Ability in Carbonized Polybenzimidazole for Membrane H_2/CO_2 Separation.* ACS Applied Materials & Interfaces, 2019. **11**(50): p. 47365-47372.
146. Hosseini, S.S. and T.S. Chung, *Carbon membranes from blends of PBI and polyimides for N_2/CH_4 and CO_2/CH_4 separation and hydrogen purification.* Journal of Membrane Science, 2009. **328**(1): p. 174-185.
147. Zainal, W.N.H.W., S.H. Tan, and M.A. Ahmad, *Carbon Membranes Prepared from a Polymer Blend of Polyethylene Glycol and Polyetherimide.* Chemical Engineering & Technology, 2017. **40**(1): p. 94-102.
148. Fuertes, A.B. and T.A. Centeno, *Carbon molecular sieve membranes from polyetherimide.* Microporous and Mesoporous Materials, 1998. **26**(1): p. 23-26.
149. Salleh, W.N.W. and A.F. Ismail, *Effect of Stabilization Condition on PEI/PVP-Based Carbon Hollow Fiber Membranes Properties.* Separation Science and Technology, 2013. **48**(7): p. 1030-1039.
150. Tseng, H.-H. and A.K. Itta, *Modification of carbon molecular sieve membrane structure by self-assisted deposition carbon segment for gas separation.* Journal of Membrane Science, 2012. **389**: p. 223-233.

151. Lin, Y.-T., et al., *Insights into the Role of Polymer Conformation on the Cutoff Size of Carbon Molecular Sieving Membranes for Hydrogen Separation and Its Novel Pore Size Detection Technology.* ACS Applied Materials & Interfaces, 2021. **13**(4): p. 5165-5175.
152. Tseng, H.-H., P.-T. Shiu, and Y.-S. Lin, *Effect of mesoporous silica modification on the structure of hybrid carbon membrane for hydrogen separation.* International Journal of Hydrogen Energy, 2011. **36**(23): p. 15352-15363.
153. Tseng, H.-H., et al., *The influence of matrix structure and thermal annealing-hydrophobic layer on the performance and durability of carbon molecular sieving membrane during physical aging.* Journal of Membrane Science, 2015. **495**: p. 294-304.
154. Hazazi, K., et al., *Ultra-selective carbon molecular sieve membranes for natural gas separations based on a carbon-rich intrinsically microporous polyimide precursor.* Journal of Membrane Science, 2019. **585**: p. 1-9.
155. Li, H., et al., *Molecular simulation of the adsorption and diffusion characteristics of CH_4 in coal subjected to N-Methylpyrrolidone treatment.* Fuel, 2023. **352**: p. 129060.
156. Salleh, W.N.W. and A.F. Ismail, *Carbon hollow fiber membranes derived from PEI/PVP for gas separation.* Separation and Purification Technology, 2011. **80**(3): p. 541-548.
157. Wan Nurul Huda, W.Z. and M.A. Ahmad, *Effect of the Pyrolysis Soaking Time on CO_2 Separation of Polyetherimide/Polyethylene Glycol-Based CMS Membranes*, in *Developments in Sustainable Chemical and Bioprocess Technology*, R. Pogaku, A. Bono, and C. Chu, Editors. 2013, Springer US: Boston, MA. p. 329-335.
158. Setnickova, K., et al., *Realizing the impact of the intermediate layer structure on the CO_2/CH_4 separation performance of carbon molecular sieving membranes: Insights from experimental synthesis and molecular simulation.* Separation and Purification Technology, 2021. **269**: p. 118627.
159. Sedigh, M.G., et al., *Transport and Morphological Characteristics of Polyetherimide-Based Carbon Molecular Sieve Membranes.* Industrial & Engineering Chemistry Research, 1999. **38**(9): p. 3367-3380.
160. Hayashi, J.-i., et al., *Separation of Ethane/Ethylene and Propane/Propylene Systems with a Carbonized BPDA−pp'ODA Polyimide Membrane.* Industrial & Engineering Chemistry Research, 1996. **35**(11): p. 4176-4181.
161. Suda, H. and K. Haraya, *Alkene/alkane permselectivities of a carbon molecular sieve membrane.* Chemical Communications, 1997(1): p. 93-94.
162. Salleh, W.N.W. and A.F. Ismail, *Effects of carbonization heating rate on CO_2 separation of derived carbon membranes.* Separation and Purification Technology, 2012. **88**: p. 174-183.
163. Su, J. and A.C. Lua, *Effects of carbonisation atmosphere on the structural characteristics and transport properties of carbon membranes prepared from Kapton® polyimide.* Journal of Membrane Science, 2007. **305**(1): p. 263-270.
164. Zainal, W., S.H. Tan, and M.A. Ahmad, *Controlled Carbonization Heating Rate for Enhancing CO_2 Separation Based on Single Gas Studies.* Periodica Polytechnica-Chemical Engineering, 2021. **65**(1): p. 97-104.
165. Norazlianie, S., *The Influence of Carbonization Temperature and Heating Rate Towards Carbon Membrane Performance: A Review.* Journal of Advanced Research in Fluid Mechanics and Thermal Sciences, 2019. **62**(2): p. 151-158.
166. Suda, H. and K. Haraya, *Gas Permeation through Micropores of Carbon Molecular Sieve Membranes Derived from Kapton Polyimide.* The Journal of Physical Chemistry B, 1997. **101**(20): p. 3988-3994.

167. Hosseini, S.S., et al., *Enhancing the properties and gas separation performance of PBI–polyimides blend carbon molecular sieve membranes via optimization of the pyrolysis process.* Separation and Purification Technology, 2014. **122**: p. 278-289.
168. Geiszler, V.C. and W.J. Koros, *Effects of Polyimide Pyrolysis Conditions on Carbon Molecular Sieve Membrane Properties.* Industrial & Engineering Chemistry Research, 1996. **35**(9): p. 2999-3003.
169. Vu, D.Q., W.J. Koros, and S.J. Miller, *High Pressure CO_2/CH_4 Separation Using Carbon Molecular Sieve Hollow Fiber Membranes.* Industrial & Engineering Chemistry Research, 2002. **41**(3): p. 367-380.
170. Ismail, N.H., et al., *Disk supported carbon membrane via spray coating method: Effect of carbonization temperature and atmosphere.* Separation and Purification Technology, 2018. **195**: p. 295-304.
171. Bordas-Nagy, J., D. Despeyroux, and K.R. Jennings, *Comparison of helium and argon as collision gases in the high energy collision-induced decomposition of MH^+ ions of peptides.* Journal of the American Society for Mass Spectrometry, 1992. **3**(5): p. 502-514.
172. Dubinin, M., *Chemistry and physics of carbon*. Vol. 2. 1966, Arnold in London: Arnold. 51.
173. Campo, M.C., F.D. Magalhães, and A. Mendes, *Carbon molecular sieve membranes from cellophane paper.* Journal of Membrane Science, 2010. **350**(1): p. 180-188.
174. Kim, H.J., et al., *A Carbonaceous Membrane based on a Polymer of Intrinsic Microporosity (PIM-1) for Water Treatment.* Scientific Reports, 2016. **6**(1): p. 36078.
175. Yoon, Y.H., et al., *Structure–Transport Relationships of Water–Organic Solvent Co-transport in Carbon Molecular Sieve (CMS) Membranes.* Industrial & Engineering Chemistry Research, 2023. **62**(44): p. 18647-18661.
176. Ma, Y., et al., *Creation of Well-Defined "Mid-Sized" Micropores in Carbon Molecular Sieve Membranes.* Angewandte Chemie International Edition, 2019. **58**(38): p. 13259-13265.
177. Llosa Tanco, M.A. and D.A. Pacheco Tanaka, *Recent Advances on Carbon Molecular Sieve Membranes (CMSMs) and Reactors.* Processes, 2016. **4**(3): p. 29.
178. Campo, M.C., et al., *Influence of Pyrolysis Parameters on the Performance of CMSM.* International Journal of Chemical Engineering, 2009. **2009**(1): p. 147879.
179. Xu, L., M. Rungta, and W.J. Koros, *Matrimid® derived carbon molecular sieve hollow fiber membranes for ethylene/ethane separation.* Journal of Membrane Science, 2011. **380**(1): p. 138-147.
180. Salleh, W.N.W. and A.F. Ismail, *1.13 Preparation of Carbon Membranes for Gas Separation*, in *Comprehensive Membrane Science and Engineering (Second Edition)*, E. Drioli, L. Giorno, and E. Fontananova, Editors. 2017, Elsevier: Oxford. p. 330-357.
181. Scott, K., *Introduction to membrane separations*, in *Handbook of Industrial Membranes*, K. Scott, Editor. 1995, Elsevier Science: Amsterdam. p. 3-185.
182. Zhao, G., et al., *Sprayed separation membranes: A systematic review and prospective opportunities.* Green Energy and Environment, 2022. **7**(6): p. 1143-1160.
183. Dong, S., et al., *Scaling up of defect-free flat membrane with ultra-high gas permeance used for intermediate layer of multi-layer composite membrane and oxygen enrichment.* Separation and Purification Technology, 2020. **239**: p. 116580.
184. Xie, K., et al., *Continuous assembly of a polymer on a metal–organic framework (CAP on MOF): a 30 nm thick polymeric gas separation membrane.* Energy & Environmental Science, 2018. **11**(3): p. 544-550.
185. Fernández-Hernán, J.P., et al., *Influence of roughness and grinding direction on the thickness and adhesion of sol-gel coatings deposited by dip-coating on AZ31*

magnesium substrates. A Landau–Levich equation revision. Surface and Coatings Technology, 2021. **408**: p. 126798.

186. Moore, T.T. and W.J. Koros, *Non-ideal effects in organic–inorganic materials for gas separation membranes.* Journal of Molecular Structure, 2005. **739**(1): p. 87-98.
187. Moore, T.T., et al., *Characterization of low permeability gas separation membranes and barrier materials; design and operation considerations.* Journal of Membrane Science, 2004. **245**(1): p. 227-231.
188. Bastani, D., N. Esmaeili, and M. Asadollahi, *Polymeric mixed matrix membranes containing zeolites as a filler for gas separation applications: A review.* Journal of Industrial and Engineering Chemistry, 2013. **19**(2): p. 375-393.
189. Han, S., C. Kim, and D. Kwon, *Thermal degradation of poly(ethyleneglycol).* Polymer Degradation and Stability, 1995. **47**(2): p. 203-208.
190. Peniche, C., et al., *Study of the thermal degradation of poly(N-vinyl-2-pyrrolidone) by thermogravimetry–FTIR.* Journal of Applied Polymer Science, 1993. **50**(3): p. 485-493.
191. Itta, A.K., H.-H. Tseng, and M.-Y. Wey, *Fabrication and characterization of PPO/PVP blend carbon molecular sieve membranes for H_2/N_2 and H_2/CH_4 separation.* Journal of Membrane Science, 2011. **372**(1): p. 387-395.
192. Lee, H.-J., et al., *Gas permeation properties of carbon molecular sieving membranes derived from the polymer blend of polyphenylene oxide (PPO)/polyvinylpyrrolidone (PVP).* Journal of Membrane Science, 2007. **296**(1): p. 139-146.
193. Hatori, H., et al., *Mesoporous carbon membranes from polyimide blended with poly (ethylene glycol).* Journal of applied polymer science, 2001. **79**(5): p. 836-841.
194. Zhang, X., et al., *Carbon molecular sieve membranes derived from phenol formaldehyde novolac resin blended with poly (ethylene glycol).* Journal of membrane science, 2007. **289**(1-2): p. 86-91.
195. Briceño, K., R. Garcia-Valls, and D. Montané, *State of the art of carbon molecular sieves supported on tubular ceramics for gas separation applications.* Asia-Pacific Journal of Chemical Engineering, 2010. **5**(1): p. 169-178.
196. Chua, M.L., Y.C. Xiao, and T.-S. Chung, *Effects of thermally labile saccharide units on the gas separation performance of highly permeable polyimide membranes.* Journal of Membrane Science, 2012. **415-416**: p. 375-382.
197. Chua, M.L., Y.C. Xiao, and T.-S. Chung, *Modifying the molecular structure and gas separation performance of thermally labile polyimide-based membranes for enhanced natural gas purification.* Chemical Engineering Science, 2013. **104**: p. 1056-1064.
198. Zhang, B., et al., *Preparation and characterization of carbon and carbon/zeolite membranes from ODPA–ODA type polyetherimide.* Journal of Membrane Science, 2015. **474**: p. 114-121.
199. Zhang, B., et al., *Preparation and gas permeation of composite carbon membranes from poly(phthalazinone ether sulfone ketone).* Separation and Purification Technology, 2008. **60**(3): p. 259-263.
200. Tin, P.S., et al., *Carbon-zeolite composite membranes for gas separation.* Carbon, 2005. **43**(9): p. 2025-2027.
201. Aroon, M.A., et al., *Performance studies of mixed matrix membranes for gas separation: A review.* Separation and Purification Technology, 2010. **75**(3): p. 229-242.
202. Zagho, M.M., et al., *A review on recent advances in CO_2 separation using zeolite and zeolite-like materials as adsorbents and fillers in mixed matrix membranes (MMMs).* Chemical Engineering Journal Advances, 2021. **6**: p. 100091.

203. Li, W., et al., *Mixed-matrix carbon molecular sieve membranes using hierarchical zeolite: A simple approach towards high CO_2 permeability enhancements.* Journal of Membrane Science, 2019. **588**: p. 117220.
204. Rao, P.S., et al., *A comparison of carbon/nanotube molecular sieve membranes with polymer blend carbon molecular sieve membranes for the gas permeation application.* Microporous and Mesoporous Materials, 2008. **113**(1): p. 499-510.
205. Wang, X., et al., *Reversed thermo-switchable molecular sieving membranes composed of two-dimensional metal-organic nanosheets for gas separation.* Nature Communications, 2017. **8**: p. 14460.
206. Zhao, X., et al., *Metal–Organic Frameworks for Separation.* Advanced Materials, 2018. **30**(37): p. 1705189.
207. Shan, M., et al., *Metal- and covalent-organic framework mixed matrix membranes for CO2 separation: A perspective on stability and scalability.* Journal of Membrane Science, 2024. **691**: p. 122258.
208. Healy, C., et al., *The thermal stability of metal-organic frameworks.* Coordination Chemistry Reviews, 2020. **419**: p. 213388.
209. Czakis-Sulikowska, D., A. Malinowska, and J. Radwańska-Doczekalska, *Synthesis, properties and thermal decomposition of bipyridine-oxalato complexes with Mn (II), Co (II), Ni (II) and Cu (II).* Polish Journal of Chemistry, 2000. **74**(5): p. 607-614.
210. Li, H., et al., *Enhanced Hydrostability in Ni-Doped MOF-5.* Inorganic Chemistry, 2012. **51**(17): p. 9200-9207.
211. Katz, M.J., et al., *A facile synthesis of UiO-66, UiO-67 and their derivatives.* Chemical Communications, 2013. **49**(82): p. 9449-9451.
212. Mustafa, D., et al., *Stability improvement of $Cu_3(BTC)_2$ metal–organic frameworks under steaming conditions by encapsulation of a Keggin polyoxometalate.* Chemical Communications, 2011. **47**(28): p. 8037-8039.
213. Wang, Y., et al., *Hybrid carbon molecular sieve membranes having ordered Fe_3O_4@ZIF-8-derived microporous structure for gas separation.* Journal of Membrane Science, 2023. **666**: p. 121127.
214. Diercks, C.S. and O.M. Yaghi, *The atom, the molecule, and the covalent organic framework.* Science, 2017. **355**(6328): p. eaal1585.
215. Biswal, B.P., et al., *Chemically Stable Covalent Organic Framework (COF)-Polybenzimidazole Hybrid Membranes: Enhanced Gas Separation through Pore Modulation.* Chemistry – A European Journal, 2016. **22**(14): p. 4695-4699.
216. Zou, C., et al., *Mechanical Synthesis of COF Nanosheet Cluster and Its Mixed Matrix Membrane for Efficient CO_2 Removal.* ACS Applied Materials & Interfaces, 2017. **9**(34): p. 29093-29100.
217. Evans, Austin M., et al., *Trends in the thermal stability of two-dimensional covalent organic frameworks.* Faraday Discussions, 2021. **225**(0): p. 226-240.
218. Zhang, J., X. Sheng, and L. Jiang, *The dewetting properties of lotus leaves.* Langmuir, 2009. **25**(3): p. 1371-1376.
219. Bixler, G.D. and B. Bhushan, *Bioinspired rice leaf and butterfly wing surface structures combining shark skin and lotus effects.* Soft matter, 2012. **8**(44): p. 11271-11284.
220. Wang, N., et al., *Bioinspired one-step construction of hierarchical superhydrophobic surfaces for oil/water separation.* Journal of Colloid and Interface Science, 2018. **531**: p. 300-310.
221. Rahmah, W., et al., *Advancing carbon capture with bio-inspired membrane materials: A review.* Carbon Capture Science & Technology, 2024. **13**: p. 100318.

222. Widakdo, J., et al., *Bioinspired ionic liquid-graphene based smart membranes with electrical tunable channels for gas separation.* Applied Materials Today, 2022. **27**: p. 101441.
223. Feng, Q.L., et al., *Crystal orientation, toughening mechanisms and a mimic of nacre.* Materials Science and Engineering: C, 2000. **11**(1): p. 19-25.
224. Mishra, N. and B. and Kandasubramanian, *Biomimetic Design of Artificial Materials Inspired by Iridescent Nacre Structure and Its Growth Mechanism.* Polymer-Plastics Technology and Engineering, 2018. **57**(15): p. 1592-1606.
225. Dai, Y., et al., *1D-2D intercalated network CMC@g-C_3N_4/IL membrane with high permeability and selectivity for the CO_2 capture.* Journal of Membrane Science, 2023. **686**: p. 122019.
226. Supuran, C.T., *Carbonic anhydrases: from biomedical applications of the inhibitors and activators to biotechnological use for CO_2 capture.* Journal of Enzyme Inhibition and Medicinal Chemistry, 2013. **28**(2): p. 229-230.
227. Kim, J.K., et al., *Elucidating the role of metal ions in carbonic anhydrase catalysis.* Nature Communications, 2020. **11**(1): p. 4557.
228. Fu, Y., et al., *Ultra-thin enzymatic liquid membrane for CO_2 separation and capture.* Nature Communications, 2018. **9**(1): p. 990.
229. Zhang, Y., et al., *Biomimetic material functionalized mixed matrix membranes for enhanced carbon dioxide capture.* Journal of Materials Chemistry A, 2018. **6**(32): p. 15585-15592.
230. Wankat, P.C., *Separation Process Engineering*. 2007: Prentice Hall.
231. Lee, S., *Performance Comparison of Spiral-Wound and Plate-and-Frame Forward Osmosis Membrane Module.* Membranes, 2020. **10**(11): p. 318.
232. Yang, X., et al., *Membrane module design and dynamic shear-induced techniques to enhance liquid separation by hollow fiber modules: a review.* Desalination and Water Treatment, 2013. **51**(16): p. 3604-3627.
233. Li, F.Y., et al., *Development and positron annihilation spectroscopy (PAS) characterization of polyamide imide (PAI)–polyethersulfone (PES) based defect-free dual-layer hollow fiber membranes with an ultrathin dense-selective layer for gas separation.* Journal of Membrane Science, 2011. **378**(1): p. 541-550.
234. Takahashi, S. and D.R. Paul, *Gas permeation in poly(ether imide) nanocomposite membranes based on surface-treated silica. Part 1: Without chemical coupling to matrix.* Polymer, 2006. **47**(21): p. 7519-7534.
235. Koros, W.J., et al., *Polymeric membrane materials for solution-diffusion based permeation separations.* Progress in Polymer Science, 1988. **13**(4): p. 339-401.
236. Vu, D.Q., W.J. Koros, and S.J. Miller, *Mixed matrix membranes using carbon molecular sieves: II. Modeling permeation behavior.* Journal of Membrane Science, 2003. **211**(2): p. 335-348.
237. Shamsabadi, A.A., et al., *Role of critical concentration of PEI in NMP solutions on gas permeation characteristics of PEI gas separation membranes.* Journal of Industrial and Engineering Chemistry, 2013. **19**(2): p. 677-685.
238. Alqaheem, Y., et al., *Preparation of polyetherimide membrane from non-toxic solvents for the separation of hydrogen from methane.* Chemistry Central Journal, 2018. **12**(1): p. 80.
239. López-González, M.M., et al., *Effect of the upstream pressure on gas transport in poly (ether-imide) films.* Journal of membrane science, 2005. **253**(1-2): p. 175-181.
240. Wang, Y., et al., *Investigation of the fundamental differences between polyamide-imide (PAI) and polyetherimide (PEI) membranes for isopropanol dehydration via pervaporation.* Journal of Membrane Science, 2008. **318**(1): p. 217-226.

241. Wang, D., K. Li, and W.K. Teo, *Preparation and characterization of polyetherimide asymmetric hollow fiber membranes for gas separation.* Journal of Membrane Science, 1998. **138**(2): p. 193-201.

242. Peng, N., et al., *Evolution of ultra-thin dense-selective layer from single-layer to dual-layer hollow fibers using novel Extem® polyetherimide for gas separation.* Journal of Membrane Science, 2010. **360**(1): p. 48-57.

243. Eiras, D., Y. Labreche, and L.A. Pessan, *Ultem®/ZIF-8 Mixed Matrix Membranes for Gas Separation: Transport and Physical Properties.* Materials Research, 2016. **19**(1): p. 220-228.

244. Hamidavi, F., A. Kargari, and A. Eliassi, *Sorption and permeation study of polyetherimide/hydrophobic silica nanocomposite membrane for effective syngas ($H_2/CO/CO_2$) separation.* Separation and Purification Technology, 2021. **279**: p. 119774.

245. Duan, C., et al., *Enhanced gas separation properties of metal organic frameworks/polyetherimide mixed matrix membranes.* Journal of Applied Polymer Science, 2014. **131**(17): p. 40719.

246. Husain, S. and W.J. Koros, *Mixed matrix hollow fiber membranes made with modified HSSZ-13 zeolite in polyetherimide polymer matrix for gas separation.* Journal of Membrane Science, 2007. **288**(1): p. 195-207.

247. Maqsood, K., et al., *Effect of TiO_2 on Thermal, Mechanical, and Gas Separation Performances of Polyetherimide–Polyvinyl Acetate Blend Membranes.* Membranes, 2023. **13**(8): p. 734.

248. Zhu, H., et al., *Effect of MIL-53 on phase inversion and gas separation performance of mixed matrix hollow fiber membranes.* RSC Advances, 2016. **6**(73): p. 69124-69134.

249. Dai, Y., et al., *Ultem®/ZIF-8 mixed matrix hollow fiber membranes for CO_2/N_2 separations.* Journal of Membrane Science, 2012. **401-402**: p. 76-82.

250. Belhaj Messaoud, S., et al., *Mixed matrix membranes using SAPO-34/polyetherimide for carbon dioxide/methane separation.* Separation and Purification Technology, 2015. **148**: p. 38-48.

251. Sarrigani, G.V., et al., *Interfacially-confined polyetherimide tubular membranes for H_2, CO_2 and N_2 separations.* Journal of Membrane Science, 2022. **655**: p. 120596.

252. Wang, D.K., et al., *High Selectivity Gas Separation by Interfacial Diffusion Membranes.* Advanced Materials Interfaces, 2019. **6**(1): p. 1801273.

253. Hou, M., et al., *High-performance carbon molecular sieving membrane derived from a novel hydroxyl-containing polyetherimide precursor for CO_2 separations.* Journal of Membrane Science, 2022. **656**: p. 120639.

254. Salleh, W.N.W. and A.F. Ismail, *Fabrication and characterization of PEI/PVP-based carbon hollow fiber membranes for CO_2/CH_4 and CO_2/N_2 separation.* AIChE Journal, 2012. **58**(10): p. 3167-3175.

255. Lin, Y.-T., M.-Y. Wey, and H.-H. Tseng, *Highly Permeable Mixed Matrix Hollow Fiber Membrane as a Latent Route for Hydrogen Purification from Hydrocarbons/Carbon Dioxide.* Membranes, 2021. **11**(11): p. 865.

256. Lin, Y.-C., H.-H. Tseng, and D.K. Wang, *Uncovering the effects of PEG porogen molecular weight and concentration on ultrafiltration membrane properties and protein purification performance.* Journal of Membrane Science, 2021. **618**: p. 118729.

257. Liao, K.-S., et al., *Determination of Free-Volume Properties in Polymers Without Orthopositronium Components in Positron Annihilation Lifetime Spectroscopy.* Macromolecules, 2011. **44**(17): p. 6818-6826.

258. Kansy, J., *Microcomputer program for analysis of positron annihilation lifetime spectra.* Nuclear Instruments and Methods in Physics Research Section A, Accelerators, Spectrometers, Detectors and Associated Equipment, 1996. **374**(2): p. 235-244.
259. Cumming, G., F. Fidler, and D.L. Vaux, *Error bars in experimental biology.* Journal of cell Biology, 2007. **177**(1): p. 7-11.
260. Asif, M.B. and Z.H. Zhang, *Ceramic membrane technology for water and wastewater treatment: A critical review of performance, full-scale applications, membrane fouling and prospects.* Chemical Engineering Journal, 2021. **418**: p. 129481.
261. Li, C., et al., *Ceramic nanocomposite membranes and membrane fouling: A review.* Water Research, 2020. **175**: p. 115674.
262. Leenaars, A.F.M., K. Keizer, and A.J. Burggraaf, *The preparation and characterization of alumina membranes with ultra-fine pores - Part 1 Microstructural investigations on non-supported membranes.* Journal of Materials Science, 1984. **19**(4): p. 1077-1088.
263. Saleh, T.A. and V.K. Gupta, *Synthesis and characterization of alumina nano-particles polyamide membrane with enhanced flux rejection performance.* Separation and Purification Technology, 2012. **89**: p. 245-251.
264. Lakshmi, B.B., C.J. Patrissi, and C.R. Martin, *Sol−Gel Template Synthesis of Semiconductor Oxide Micro- and Nanostructures.* Chemistry of Materials, 1997. **9**(11): p. 2544-2550.
265. Das, N. and H.S. Maiti, *Ceramic membrane by tape casting and sol–gel coating for microfiltration and ultrafiltration application.* Journal of Physics and Chemistry of Solids, 2009. **70**(11): p. 1395-1400.
266. Shang, R., et al., *Hydraulically irreversible fouling on ceramic MF/UF membranes: Comparison of fouling indices, foulant composition and irreversible pore narrowing.* Separation and Purification Technology, 2015. **147**: p. 303-310.
267. Abdallah, H., et al., *Fabrication of ceramic membranes from nano–rosette structure high alumina roller kiln waste powder for desalination application.* Ceramics International, 2018. **44**(7): p. 8612-8622.
268. Li, J., M. Wei, and Y. Wang, *Substrate matters: The influences of substrate layers on the performances of thin-film composite reverse osmosis membranes.* Chinese Journal of Chemical Engineering, 2017. **25**(11): p. 1676-1684.
269. Zhu, H., et al., *Recycle of ceramic substrate of PDMS/ceramic composite membranes towards alcohol-permselective pervaporation.* Journal of Membrane Science, 2021. **640**: p. 119835.
270. Deng, B., et al., *High-surface-area corundum nanoparticles by resistive hotspot-induced phase transformation.* Nature Communications, 2022. **13**(1): p. 5027.
271. Kholodkova, A.A., et al., *The Direct Cold Sintering of α-Al_2O_3 Ceramics in a Pure Water Medium.* Ceramics, 2024. **7**(3): p. 1030-1042.
272. Wang, B., *Alumina Membranes*, in *Encyclopedia of Membranes*, E. Drioli and L. Giorno, Editors. 2015, Springer Berlin Heidelberg: Berlin, Heidelberg. p. 1-2.
273. Cheng, L.-T., et al., *Boehmite coating on θ-Al_2O_3 particles via a sol–gel route.* Ceramics International, 2008. **34**(2): p. 337-343.
274. Xi, X., et al., *The fabrication of mesoporous η-Al_2O_3 nanofiber with tunable pore size by template-induced strategy.* Materials Today Communications, 2023. **36**: p. 106743.
275. Cortes-Vega, F.D., et al., *Room-temperature synthesis of χ-Al_2O_3 and ruby (α-Cr:Al_2O_3).* CrystEngComm, 2018. **20**(25): p. 3505-3511.

276. Ray, M., et al., *Preparation and characterization of macroporous pure alumina capillary membrane using boehmite as binder for filtration application.* Journal of Porous Materials, 2015. **22**(4): p. 1043-1052.
277. Owens, G.J., et al., *Sol–gel based materials for biomedical applications.* Progress in Materials Science, 2016. **77**: p. 1-79.
278. Nisticò, R., D. Scalarone, and G. Magnacca, *Sol-gel chemistry, templating and spin-coating deposition: A combined approach to control in a simple way the porosity of inorganic thin films/coatings.* Microporous and Mesoporous Materials, 2017. **248**: p. 18-29.
279. Lin, C.-H., *Surface roughness effect on the metallic bipolar plates of a proton exchange membrane fuel cell.* Applied Energy, 2013. **104**: p. 898-904.
280. Guazzato, M., et al., *Influence of grinding, sandblasting, polishing and heat treatment on the flexural strength of a glass-infiltrated alumina-reinforced dental ceramic.* Biomaterials, 2004. **25**(11): p. 2153-2160.
281. Ahn, J., T. Ryu, and J. Park, *Composite membranes with ultrathin and conformal passivation for universal microfiltration compatible with organic solvents.* Journal of Membrane Science, 2022. **651**: p. 120455.
282. Poodt, P., et al., *(Invited) Ultrafast Atomic Layer Deposition of Alumina Layers for Solar Cell Passivation.* ECS Transactions, 2010. **33**(2): p. 419.
283. Dingemans, G. and W.M.M. Kessels, *Status and prospects of Al_2O_3-based surface passivation schemes for silicon solar cells.* Journal of Vacuum Science & Technology A, 2012. **30**(4): p. 040802.
284. Ryi, S.K., et al., *Ultra-thin Ni dense membrane prepared by polishing treatment of porous nickel support for high-temperature H_2 separation.* Korean Journal of Chemical Engineering, 2016. **33**(9): p. 2699-2702.
285. Ryi, S.K., et al., *Repair of Pd-based composite membrane by polishing treatment.* International Journal of Hydrogen Energy, 2011. **36**(21): p. 13776-13780.
286. Barbari, T., W. Koros, and D. Paul, *Polymeric membranes based on bisphenol-A for gas separations.* Journal of membrane science, 1989. **42**(1-2): p. 69-86.
287. Usman, M., et al., *Controlled Covalent Functionalization of ZIF-90 for Selective CO_2 Capture & Separation.* Membranes, 2022. **12**(11): p. 1055.
288. Alqaheem, Y. and A. Alomair, *Recent developments in polyetherimide membrane for gas separation.* Journal of the Chinese Chemical Society, 2019. **66**(12): p. 1738-1744.
289. Zhu, Z., et al., *A phase-inversion casting process for preparation of tubular porous alumina ceramic membranes.* Journal of the European Ceramic Society, 2015. **35**(11): p. 3187-3194.
290. Bissett, H., J. Zah, and H.M. Krieg, *Manufacture and optimization of tubular ceramic membrane supports.* Powder Technology, 2008. **181**(1): p. 57-66.
291. Levänen, E. and T. Mäntylä, *Effect of sintering temperature on functional properties of alumina membranes.* Journal of the European Ceramic Society, 2002. **22**(5): p. 613-623.
292. Rahimian, M., et al., *The effect of particle size, sintering temperature and sintering time on the properties of Al-Al_2O_3 composites, made by powder metallurgy.* Journal of Materials Processing Technology, 2009. **209**(14): p. 5387-5393.
293. de la Rocha, M.R., et al., *Preparation of alumina based tubular asymmetric membranes incorporated with coal fly ash by centrifugal casting.* Ceramics International, 2021. **47**(3): p. 4187-4196.
294. (FEPA), T.F.o.E.P.o.A., *Grains of fused aluminium oxide,silicon carbide and other abrasive materials for coated abrasives*, in *Grains for coated abrasives P240 to P5000*. 2017.

295. Yang, G., et al., *The influence of surface treatment on the tensile properties of carbon fiber-reinforced epoxy composites-bonded joints.* Composites Part B: Engineering, 2019. **160**: p. 446-456.

296. Woo, S.H., B.R. Min, and J.S. Lee, *Change of surface morphology, permeate flux, surface roughness and water contact angle for membranes with similar physicochemical characteristics (except surface roughness) during microfiltration.* Separation and Purification Technology, 2017. **187**: p. 274-284.

297. Mahato, B.K. and L.W. Shemilt, *Effect of surface roughness on mass transfer.* Chemical Engineering Science, 1968. **23**(2): p. 183-185.

298. Poulson, B., *Mass transfer from rough surfaces.* Corrosion Science, 1990. **30**(6): p. 743-746.

299. Ramon, G.Z. and E.M.V. Hoek, *Transport through composite membranes, part 2: Impacts of roughness on permeability and fouling.* Journal of Membrane Science, 2013. **425-426**: p. 141-148.

300. Woo, S.H., J. Park, and B.R. Min, *Relationship between permeate flux and surface roughness of membranes with similar water contact angle values.* Separation and Purification Technology, 2015. **146**: p. 187-191.

301. Khan, M.Y., et al., *Biomass derived carboxylated carbon nanosheets blended polyetherimide membranes for enhanced CO_2/CH_4 separation.* Journal of Natural Gas Science and Engineering, 2020. **75**: p. 103156.

302. Budd, P.M., et al., *Gas separation membranes from polymers of intrinsic microporosity.* Journal of Membrane Science, 2005. **251**(1): p. 263-269.

303. Zou, X. and G. Zhu, *Microporous Organic Materials for Membrane-Based Gas Separation.* Advanced Materials, 2018. **30**(3): p. 1700750.

304. Okamoto, Y., H.-C. Chiang, and T. Merkel, *Chapter 5 - Perfluoropolymers for gas separation membrane applications*, in *Fascinating Fluoropolymers and Their Applications*, B. Ameduri and S. Fomin, Editors. 2020, Elsevier. p. 143-155.

305. Yavari, M., et al., *Dioxolane-Based Perfluoropolymers with Superior Membrane Gas Separation Properties.* Macromolecules, 2018. **51**(7): p. 2489-2497.

306. White, L.S., et al., *Properties of a polyimide gas separation membrane in natural gas streams.* Journal of Membrane Science, 1995. **103**(1): p. 73-82.

307. Sanaeepur, H., et al., *Polyimides in membrane gas separation: Monomer's molecular design and structural engineering.* Progress in Polymer Science, 2019. **91**: p. 80-125.

308. Eastmond, G.C., et al., *Poly(ether imide)s with hindering substituents in the anhydride moiety: synthesis, properties and gas permeabilities.* Polymer, 1994. **35**(19): p. 4215-4227.

309. Eastmond, G.C. and J. Paprotny, *Synthesis of bulky bis(ether anhydride)s and poly(ether imide)s with bulky main-chain units.* Journal of Materials Chemistry, 1997. **7**(4): p. 589-592.

310. Kim, I.-C. and K.-H. Lee, *Effect of poly(ethylene glycol) 200 on the formation of a polyetherimide asymmetric membrane and its performance in aqueous solvent mixture permeation.* Journal of Membrane Science, 2004. **230**(1): p. 183-188.

311. Kanagaraj, P., et al., *Effects of Polyvinylpyrrolidone on the Permeation and Fouling-Resistance Properties of Polyetherimide Ultrafiltration Membranes.* Industrial & Engineering Chemistry Research, 2015. **54**(17): p. 4832-4838.

312. Li, J.-Y., M.-Y. Wey, and H.-H. Tseng, *Low-temperature Cu/Zn/SBA-16 integrating carbon membrane reactor for hydrogen production and high CO conversion through water-gas shift reaction.* International Journal of Hydrogen Energy, 2022.

313. Barbari, T.A., W.J. Koros, and D.R. Paul, *Polymeric membranes based on bisphenol-A for gas separations.* Journal of Membrane Science, 1989. **42**(1): p. 69-86.

314. Nematolahi, K., et al., *CO_2 separation of a novel Ultem-based mixed matrix membrane incorporated with Ni^{2+}-exchanged zeolite X.* Greenhouse Gases: Science and Technology, 2022. **12**(1): p. 48-66.

315. Dai, Z. and L. Deng, *Membranes for CO_2 capture and separation: Progress in research and development for industrial applications.* Separation and Purification Technology, 2024. **335**: p. 126022.

316. Yang, W.J., et al., *Polymer brush coatings for combating marine biofouling.* Progress in Polymer Science, 2014. **39**(5): p. 1017-1042.

317. Zhou, F., et al., *Ultrathin graphene oxide-based hollow fiber membranes with brush-like CO_2-philic agent for highly efficient CO_2 capture.* Nature Communications, 2017. **8**(1): p. 2107.

318. Jiang, X., et al., *A facile direct spray-coating of Pebax® 1657: Towards large-scale thin-film composite membranes for efficient CO_2/N_2 separation.* Journal of Membrane Science, 2021. **638**: p. 119708.

319. Wei, W., et al., *Preparation of non-oxide SiC membrane for gas purification by spray coating.* Journal of Membrane Science, 2017. **540**: p. 381-390.

320. Car, A., et al., *Pebax®/polyethylene glycol blend thin film composite membranes for CO_2 separation: Performance with mixed gases.* Separation and Purification Technology, 2008. **62**(1): p. 110-117.

321. Liu, S., et al., *Preparation of PDMSvi–Al_2O_3 composite hollow fibre membranes for VOC recovery from waste gas streams.* Separation and Purification Technology, 2005. **46**(1): p. 110-117.

322. Sridhar, S., et al., *Matrimid polyimide membranes for the separation of carbon dioxide from methane.* Journal of Applied Polymer Science, 2007. **106**(3): p. 1585-1594.

323. Formela, K., *Strategies for compatibilization of polymer/waste tire rubber systems prepared via melt-blending.* Advanced Industrial and Engineering Polymer Research, 2024. **7**(4): p. 466-481.

324. Okazaki, J., et al., *In situ high-temperature X-ray diffraction study of thin palladium/α-alumina composite membranes and their hydrogen permeation properties.* Journal of Membrane Science, 2009. **335**(1): p. 126-132.

325. Feret, F.R., D. Roy, and C. Boulanger, *Determination of alpha and beta alumina in ceramic alumina by X-ray diffraction.* Spectrochimica Acta Part B: Atomic Spectroscopy, 2000. **55**(7): p. 1051-1061.

326. Wolinska-Grabczyk, A., et al., *Structure and properties of new highly soluble aromatic poly(etherimide)s containing isopropylidene groups.* Polymer Journal, 2013. **45**(12): p. 1202-1209.

327. Amancio-Filho, S.T., et al., *Thermal degradation of polyetherimide joined by friction riveting (FricRiveting). Part I: Influence of rotation speed.* Polymer Degradation and Stability, 2008. **93**(8): p. 1529-1538.

328. Dlubek, G., et al., *Local free volumes in boron-bombarded Kapton polyimide: A positron lifetime study.* Journal of Polymer Science Part B: Polymer Physics, 1999. **37**(17): p. 2539-2543.

329. Fraga, S.C., et al., *A novel time lag method for the analysis of mixed gas diffusion in polymeric membranes by on-line mass spectrometry: Method development and validation.* Journal of Membrane Science, 2018. **561**: p. 39-58.

330. Shishatskii, A.M., Y.P. Yampol'skii, and K.V. Peinemann, *Effects of film thickness on density and gas permeation parameters of glassy polymers.* Journal of Membrane Science, 1996. **112**(2): p. 275-285.

331. Scherillo, G., et al., *Weak Interactions between Poly(ether imide) and Carbon Dioxide: A Multiscale Investigation Combining Experiments, Theory, and Simulations.* Macromolecules, 2022. **55**(24): p. 10773-10787.
332. Firpo, G., et al., *Permeability thickness dependence of polydimethylsiloxane (PDMS) membranes.* Journal of Membrane Science, 2015. **481**: p. 1-8.
333. Kocherlakota, L.S., et al., *Enhanced gas transport properties and molecular mobilities in nano-constrained poly[1-(trimethylsilyl)-1-propyne] membranes.* Polymer, 2012. **53**(12): p. 2394-2401.
334. Mensitieri, G., et al., *The effect of film thickness on oxygen sorption and transport in dry and water-saturated Kapton® polyimide.* Journal of Membrane Science, 1994. **89**(1): p. 131-141.
335. Ogieglo, W., et al., *Gas separation performance and physical aging of tubular thin-film composite carbon molecular sieve membranes based on a polyimide of intrinsic microporosity precursor.* Journal of Membrane Science, 2022. **652**: p. 120497.
336. Lin, H., et al., *High-Performance Polymer Membranes for Natural-Gas Sweetening.* Advanced Materials, 2006. **18**(1): p. 39-44.
337. Liemberger, W., et al., *Experimental analysis of membrane and pressure swing adsorption (PSA) for the hydrogen separation from natural gas.* Journal of Cleaner Production, 2017. **167**: p. 896-907.
338. Lin, R.-B., et al., *Microporous Metal-Organic Framework Materials for Gas Separation.* Chem, 2020. **6**(2): p. 337-363.
339. Bridge, A.T., et al., *Preparation of defect-free asymmetric gas separation membranes with dihydrolevoglucosenone (CyreneTM) as a greener polar aprotic solvent.* Journal of Membrane Science, 2022. **644**: p. 120173.
340. Pesek, S.C. and W.J. Koros, *Aqueous quenched asymmetric polysulfone membranes prepared by dry/wet phase separation.* Journal of Membrane Science, 1993. **81**(1): p. 71-88.
341. Berghmans, S., H. Berghmans, and H.E.H. Meijer, *Spinning of hollow porous fibres via the TIPS mechanism.* Journal of Membrane Science, 1996. **116**(2): p. 171-189.
342. Wu, F., et al., *Membrane-based air separation for catalytic oxidation of isolongifolene.* Chemical Engineering Journal, 2010. **158**(3): p. 426-430.
343. Widjojo, N., T.S. Chung, and W.B. Krantz, *A morphological and structural study of Ultem/P84 copolyimide dual-layer hollow fiber membranes with delamination-free morphology.* Journal of Membrane Science, 2007. **294**(1): p. 132-146.
344. Zeman, L. and T. Fraser, *Formation of air-cast cellulose acetate membranes. Part I. Study of macrovoid formation.* Journal of Membrane Science, 1993. **84**(1): p. 93-106.
345. Zeman, L. and T. Fraser, *Formation of air-cast cellulose acetate membranes Part II. Kinetics of demixing and microvoid growth.* Journal of Membrane Science, 1994. **87**(3): p. 267-279.
346. Dong, X., et al., *Polymers and Solvents Used in Membrane Fabrication: A Review Focusing on Sustainable Membrane Development.* Membranes (Basel), 2021. **11**(5): p. 309.
347. Pagliero, M., et al., *Novel hydrophobic PVDF membranes prepared by nonsolvent induced phase separation for membrane distillation.* Journal of Membrane Science, 2020. **596**: p. 117575.
348. Choi, O., P.G. Ingole, and C.H. Park, *Precision-aiming tuning of membranes prepared by NIPS and its performance enhancement.* Journal of Cleaner Production, 2022. **365**: p. 132858.

349. Lin, Y.-C., H.-H. Tseng, and D.K. Wang, *Uncovering the effects of PEG porogen molecular weight and concentration on ultrafiltration membrane properties and protein purification performance.* Journal of Membrane Science, 2020.
350. Lin, Y.-C., et al., *Enhancing the antifouling properties of a PVDF membrane for protein separation by grafting branch-like zwitterions via a novel amphiphilic SMA-HEA linker.* Journal of Membrane Science, 2021. **624**: p. 119126.
351. van't Hof, J.A., et al., *Preparation of asymmetric gas separation membranes with high selectivity by a dual-bath coagulation method.* Journal of Membrane Science, 1992. **70**(1): p. 17-30.
352. Bernardo, P., et al., *Effect of physical aging on the gas transport and sorption in PIM-1 membranes.* Polymer, 2017. **113**: p. 283-294.
353. Fu, Y.-J., et al., *Effects of residual solvent on gas separation properties of polyimide membranes.* Separation and Purification Technology, 2008. **62**(1): p. 175-182.
354. Joly, C., et al., *Residual solvent effect on the permeation properties of fluorinated polyimide films.* Separation and Purification Technology, 1999. **16**(1): p. 47-54.
355. Macchione, M., et al., *Experimental analysis and simulation of the gas transport in dense Hyflon® AD60X membranes: Influence of residual solvent.* Polymer, 2007. **48**(9): p. 2619-2635.
356. Choi, S.-S., et al., *Formation of interfiber bonding in electrospun poly(etherimide) nanofiber web.* Journal of Materials Science, 2004. **39**(4): p. 1511-1513.
357. Wang, D., et al., *Theoretical and experimental study on the pyrolysis of N-methylpyrrolidone.* Journal of Analytical and Applied Pyrolysis, 2024. **183**: p. 106751.
358. Christmann, A.M. and A.R. Muniz, *Analysis of the effect of temperature and density on polyetherimide pyrolysis toward carbon molecular sieve membrane formation.* Carbon, 2023. **205**: p. 97-111.
359. McKeen, L.W., *6 - Solvent Systems*, in *Fluorinated Coatings and Finishes Handbook (Second Edition)*, L.W. McKeen, Editor. 2016, William Andrew Publishing: Oxford. p. 107-118.
360. Sharma, D., et al., *Surfactant enhanced drying of waterbased poly(vinyl alcohol) coatings.* Progress in Organic Coatings, 2018. **125**: p. 443-452.
361. Tin, P.S., Y. Xiao, and T.S. Chung, *Polyimide-Carbonized Membranes for Gas Separation: Structural, Composition, and Morphological Control of Precursors.* Separation & Purification Reviews, 2006. **35**(4): p. 285-318.
362. Cai, M.F. and R.B. Smart, *Quantitative analysis of N-methyl-2-pyrrolidinone in coal extracts by TGA-FTIR.* Energy & Fuels, 1993. **7**(1): p. 52-56.
363. Mariwala, R.K. and H.C. Foley, *Evolution of ultramicroporous adsorptive structure in poly (furfuryl alcohol)-derived carbogenic molecular sieves.* Industrial & engineering chemistry research, 1994. **33**(3): p. 607-615.
364. Pramoda, K.P., et al., *Characterization and thermal degradation of polyimide and polyamide liquid crystalline polymers.* Polymer Degradation and Stability, 2000. **67**(2): p. 365-374.
365. Kurdi, J. and A. Kumar, *Structuring and characterization of a novel highly microporous PEI/BMI semi-interpenetrating polymer network.* Polymer, 2005. **46**(18): p. 6910-6922.
366. Technology, N.I.o.S.a., *2-Pyrrolidinone, 1-methyl-*, in *Infrared Spectrum*. 2018, NIST Mass Spectrometry Data Center, William E. Wallace, director: NIST Standard Reference Database 69: NIST Chemistry WebBook.
367. Shiva Prasad, N., et al., *Residual solvent induced physical morphology and gas permeation in polyamide-imide membrane: Experimental investigation and molecular simulations.* European Polymer Journal, 2022. **165**: p. 111012.

368. Barbari, T.A., W.J. Koros, and D.R. Paul, *Gas sorption in polymers based on bisphenol-A.* Journal of Polymer Science Part B: Polymer Physics, 1988. **26**(4): p. 729-744.
369. Barbari, T.A., W.J. Koros, and D.R. Paul, *Gas transport in polymers based on bisphenol-A.* Journal of Polymer Science Part B: Polymer Physics, 1988. **26**(4): p. 709-727.
370. López-González, M.M., et al., *Effect of the upstream pressure on gas transport in poly(ether-imide) films.* Journal of Membrane Science, 2005. **253**(1): p. 175-181.
371. Chirkov, S.V., et al., *The influence of uniform deformation of Ultem-1000 polyetherimide films on their mechanical and gas transport characteristics.* Petroleum Chemistry, 2016. **56**(11): p. 1074-1084.
372. Ronova, I.A., et al., *Influence of swelling in supercritical carbon dioxide of Ultem and polyhexafluoropropylene thin films on their gas separation properties: comparative analysis.* Structural Chemistry, 2018. **29**(2): p. 457-466.
373. Yáñez, M., et al., *Comparative performance of commercial polymeric membranes in the recovery of industrial hydrogen waste gas streams.* International Journal of Hydrogen Energy, 2021. **46**(33): p. 17507-17521.
374. Checchetto, R., et al., *Mixed gas diffusion and permeation of ternary and quaternary CO2/CO/N2/O2 gas mixtures in Matrimid®, polyetherimide and poly(lactic acid) membranes for CO2/CO separation.* Journal of Membrane Science, 2022. **659**: p. 120768.
375. Alentev, A.Y., et al., *Correlation between the transport behavior of polyimides and the conformational rigidity of their chains.* Polymer Science Series A, 2007. **49**(2): p. 217-226.
376. Vogel, S., *Life's devices: the physical world of animals and plants*. 2025: Princeton University Press.
377. Bencharit, S., *History of progress and challenges in structural biology.* J Pharmacogenom Pharmacoproteomics S, 2012. **4**: p. 2153-0645.
378. Shen, Y.-x., et al., *Biomimetic membranes: A review.* Journal of Membrane Science, 2014. **454**: p. 359-381.
379. Min, K., et al., *Enzyme immobilization on carbon nanomaterials: Loading density investigation and zeta potential analysis.* Journal of Molecular Catalysis B: Enzymatic, 2012. **83**: p. 87-93.
380. Zhang, Y., et al., *Carbonic anhydrase membranes for carbon capture and storage.* Journal of Membrane Science Letters, 2022. **2**(2): p. 100031.
381. Wu, H., et al., *Synthesis, Crystal Structure and DNA-binding Properties of a Nickel (II) Complex with 2, 6-Bis (2-benzimidazolyl) pyridine.* Zeitschrift für Naturforschung B, 2010. **65**(11): p. 1334-1340.
382. Wu, H., et al., *A V-shaped ligand 2, 6-bis (2-benzimidazolyl) pyridine and its picrate Mn (II) complex: synthesis, crystal structure and DNA-binding properties.* European journal of medicinal chemistry, 2010. **45**(11): p. 5324-5330.
383. Renuka Maldepalli, K. and G. Virupaiah, *A polymer-anchored cobalt (II) complex as a reusable catalyst for oxidation of benzene, ethylbenzene and cyclohexane.* Transition Metal Chemistry, 2017. **42**: p. 25-34.
384. Sahoo, P.C., Y.N. Jang, and S.W. Lee, *Enhanced biomimetic CO_2 sequestration and $CaCO_3$ crystallization using complex encapsulated metal organic framework.* Journal of crystal growth, 2013. **373**: p. 96-101.
385. Badiei, A., et al., *A novel fluorescent chemosensor assembled with 2, 6-bis (2-benzimidazolyl) pyridine-functionalized nanoporous silica-type SBA-15 for*

recognition of Hg^{2+} ion in aqueous Media. International Journal of Environmental Research, 2018. **12**: p. 109-115.

386. Allahbakhsh, A., *20 - High barrier graphene/polymer nanocomposite films*, in *Food Packaging*, A.M. Grumezescu, Editor. 2017, Academic Press. p. 699-737.
387. Robeson, L.M., *The upper bound revisited.* Journal of membrane science, 2008. **320**(1-2): p. 390-400.
388. Yampolskii, Y., et al., *Intermolecular interactions: New way to govern transport properties of membrane materials.* Industrial & engineering chemistry research, 2010. **49**(23): p. 12031-12037.
389. Gonzo, E.E., M.L. Parentis, and J.C. Gottifredi, *Estimating models for predicting effective permeability of mixed matrix membranes.* Journal of Membrane Science, 2006. **277**(1): p. 46-54.
390. Chiew, Y.C. and E.D. Glandt, *The effect of structure on the conductivity of a dispersion.* Journal of Colloid and Interface Science, 1983. **94**(1): p. 90-104.
391. Wu, H., et al., *Gas Permeation Model of Mixed-Matrix Membranes with Embedded Impermeable Cuboid Nanoparticles.* Membranes, 2020. **10**(12): p. 422.
392. Kyrychenko, A., et al., *Partitioning of 2,6-Bis(1H-Benzimidazol-2-yl)pyridine fluorophore into a phospholipid bilayer: Complementary use of fluorescence quenching studies and molecular dynamics simulations.* Biophysical Chemistry, 2011. **154**(1): p. 8-17.
393. Chetia, B. and P.K. Iyer, *2,6-Bis(2-benzimidazolyl)pyridine receptor for urea recognition.* Tetrahedron Letters, 2006. **47**(46): p. 8115-8117.
394. Correa, A., et al., *A Molecular Interpretation of the Dynamics of Diffusive Mass Transport of Water within a Glassy Polyetherimide.* International Journal of Molecular Sciences, 2021. **22**(6): p. 2908.
395. Baldanza, A., et al., *Modelling relative humidity and temperature effects on CO_2 gas transport in polyetherimide.* Polymer, 2024. **291**: p. 126595.
396. Kitajima, N., et al., *Fixation of atmospheric carbon dioxide by a series of hydroxo complexes of divalent metal ions and the implication for the catalytic role of metal ion in carbonic anhydrase. Synthesis, characterization, and molecular structure of [LM(OH)]n (n = 1 or 2) and LM(.mu.-CO_3)ML (M(II) = Mn, Fe, Co, Ni, Cu, Zn; L = HB(3,5-iso-$Pr_2pz)_3$).* Journal of the American Chemical Society, 1993. **115**(13): p. 5496-5508.
397. Barzetti, T., et al., *Pyridine and ammonia as probes for FTIR analysis of solid acid catalysts.* Journal of the Chemical Society, Faraday Transactions, 1996. **92**(8): p. 1401-1407.
398. Boča, M., R.F. Jameson, and W. Linert, *Fascinating variability in the chemistry and properties of 2,6-bis-(benzimidazol-2-yl)-pyridine and 2,6-bis-(benzthiazol-2-yl)-pyridine and their complexes.* Coordination Chemistry Reviews, 2011. **255**(1): p. 290-317.
399. Fujimoto, A., et al., *Origins of sp^3C peaks in C1s X-ray Photoelectron Spectra of Carbon Materials.* Analytical Chemistry, 2016. **88**(12): p. 6110-6114.
400. Smith, M., et al., *Improving the deconvolution and interpretation of XPS spectra from chars by ab initio calculations.* Carbon, 2016. **110**: p. 155-171.
401. Stoch, J. and J. Gablankowska-Kukucz, *The effect of carbonate contaminations on the XPS O_{1s} band structure in metal oxides.* Surface and Interface Analysis, 1991. **17**(3): p. 165-167.
402. Rojas, J.V., et al., *Facile radiolytic synthesis of ruthenium nanoparticles on graphene oxide and carbon nanotubes.* Materials Science and Engineering: B, 2016. **205**: p. 28-35.

403. Lazar, P., R. Mach, and M. Otyepka, *Spectroscopic Fingerprints of Graphitic, Pyrrolic, Pyridinic, and Chemisorbed Nitrogen in N-Doped Graphene.* The Journal of Physical Chemistry C, 2019. **123**(16): p. 10695-10702.

404. Cychosz, K.A. and M. Thommes, *Progress in the Physisorption Characterization of Nanoporous Gas Storage Materials.* Engineering, 2018. **4**(4): p. 559-566.

405. Sun, Y., et al., *Effect of metal ion intercalation on the gas diffusion confined in two-dimensional MXene nanosheets.* Materials Today Communications, 2024. **38**: p. 107897.

406. Inukai, M., et al., *Storage of* CO_2 *into Porous Coordination Polymer Controlled by Molecular Rotor Dynamics.* Angewandte Chemie International Edition, 2018. **57**(28): p. 8687-8690.

407. Kogut, K.A. and R.S. Rowlett, *A comparison of the mechanisms of* CO_2 *hydration by native and* Co^{2+}*-substituted carbonic anhydrase II.* Journal of Biological Chemistry, 1987. **262**(34): p. 16417-16424.

408. Gu, J., et al., *Atomically dispersed* Fe^{3+} *sites catalyze efficient* CO_2*electroreduction to CO.* Science, 2019. **364**(6445): p. 1091-1094.

409. Zhang, X., et al., *Electrocatalytic carbon dioxide reduction: from fundamental principles to catalyst design.* Materials Today Advances, 2020. **7**: p. 100074.

410. Lu, T., et al., *Competitive adsorption in* CO_2 *enhancing shale gas: Low-field NMR measurement combined with molecular simulation for selectivity and displacement efficiency model.* Chemical Engineering Journal, 2022. **440**: p. 135865.

411. Loianno, V., et al., *Unveiling the competitive diffusion of binary gas mixtures in polymers: The case of carbon dioxide and alkanes in nanoporous-crystalline polyphenylene oxide.* Separation and Purification Technology, 2024. **341**: p. 126953.

412. Liu, Y., et al., *Enhanced* CO_2/CH_4 *Separation Performance of a Mixed Matrix Membrane Based on Tailored MOF-Polymer Formulations.* Advanced Science, 2018. **5**(9): p. 1800982.

413. Guo, A., et al., *Metal-organic framework-based mixed matrix membranes: Synergetic effect of adsorption and diffusion for* CO_2/CH_4 *separation.* Journal of Membrane Science, 2018. **562**: p. 76-84.

414. Wiesenburg, D.A. and N.L. Guinasso, Jr., *Equilibrium solubilities of methane, carbon monoxide, and hydrogen in water and sea water.* Journal of Chemical & Engineering Data, 1979. **24**(4): p. 356-360.

415. Mohammadian, E., et al., *Probing Solubility and pH of* CO_2 *in aqueous solutions: Implications for* CO_2 *injection into oceans.* Journal of CO2 Utilization, 2023. **71**: p. 102463.

416. Araújo, T., G. Bernardo, and A. Mendes, *High-performance hydrogen separation using cellulose-based carbon molecular sieve membranes.* Journal of Membrane Science, 2024. **693**: p. 122337.

417. Lei, L., et al., *Carbon membranes for* CO_2 *removal: Status and perspectives from materials to processes.* Chemical Engineering Journal, 2020. **401**: p. 126084.

418. Liu, L., D. Liu, and C. Zhang, *High-temperature hydrogen/propane separations in asymmetric carbon molecular sieve hollow fiber membranes.* Journal of Membrane Science, 2022. **642**: p. 119978.

419. Parsley, D., et al., *Field evaluation of carbon molecular sieve membranes for the separation and purification of hydrogen from coal- and biomass-derived syngas.* Journal of Membrane Science, 2014. **450**: p. 81-92.

420. Thommes, M., et al., *Physisorption of gases, with special reference to the evaluation of surface area and pore size distribution (IUPAC Technical Report).* Pure and Applied Chemistry, 2015. **87**(9-10): p. 1051-1069.

421. Qiu, W., et al., *Key Features of Polyimide-Derived Carbon Molecular Sieves.* Angewandte Chemie International Edition, 2021. **60**(41): p. 22322-22331.
422. Carroccio, S., C. Puglisi, and G. Montaudo, *Thermal degradation mechanisms of polyetherimide investigated by direct pyrolysis mass spectrometry.* Macromolecular Chemistry and Physics, 1999. **200**(10): p. 2345-2355.
423. Hamm, J.B.S., et al., *Experimental and computational analysis of carbon molecular sieve membrane formation upon polyetherimide pyrolysis.* Carbon, 2017. **119**: p. 21-29.
424. Lascovich, J.C., R. Giorgi, and S. Scaglione, *Evaluation of the* sp^2/sp^3 *ratio in amorphous carbon structure by XPS and XAES.* Applied Surface Science, 1991. **47**(1): p. 17-21.
425. Yerzhankyzy, A., et al., *Structural evolution and gas separation properties of thermally rearranged polybenzoxazole (TR-PBO), polymer-carbon transition (PCT) and early-stage carbon (ESC) membranes derived from a 6FDA-hydroxyl-functionalized Tröger's base polyimide.* Journal of Membrane Science, 2023. **683**: p. 121764.
426. Lee, W.H., et al., *Energy and time efficient infrared (IR) irradiation treatment for preparing thermally rearranged (TR) and carbon molecular sieve (CMS) membranes for gas separation.* Journal of Membrane Science, 2020. **613**: p. 118477.
427. Huang, C., et al., *Research progress and challenges in polyimide and polyimide-derived gas separation membranes: A review.* Advanced Membranes, 2025. **5**: p. 100154.
428. Kim, S.-J., et al., *A Review on Polymer Precursors of Carbon Molecular Sieve Membranes for Olefin/Paraffin Separation.* Membranes, 2021. **11**(7): p. 482.
429. Yin, L., et al., *High-performance carbonized ZIF-8-doped hybrid carbon molecular sieve membrane for* CO_2/N_2 *separation.* Journal of Membrane Science, 2022. **655**: p. 120610.
430. Wang, F., et al., *Investigation of the attapulgite hybrid carbon molecular sieving membranes for permanent gas separation.* Chemical Engineering Research and Design, 2019. **151**: p. 146-156.
431. Cai, M., et al., *Excellent gas separation performance of hybrid carbon molecular sieve membrane derived from polyimide/10X zeolite for hydrogen purification.* Microporous and Mesoporous Materials, 2024. **365**: p. 112889.
432. Gill, P., T.T. Moghadam, and B. Ranjbar, *Differential scanning calorimetry techniques: applications in biology and nanoscience.* Journal of Biomolecular Techniques, 2010. **21**(4): p. 167-93.
433. Lisa, G., et al., *Thermal and thermo-oxidative stability and probable degradation mechanism of some polyetherimides.* Journal of Analytical and Applied Pyrolysis, 2016. **118**: p. 144-154.
434. Yang, Q., et al., *Iron–cobalt mixed oxide nanocatalysts: Heterogeneous peroxymonosulfate activation, cobalt leaching, and ferromagnetic properties for environmental applications.* Applied Catalysis B: Environmental, 2009. **88**(3): p. 462-469.
435. Hamonnet, J., et al., *Influence of Carbon Support on the Pyrolysis of Cobalt Phthalocyanine for the Efficient Electroreduction of* CO_2*.* ACS Catalysis, 2022. **12**(23): p. 14571-14581.
436. Cho, D.-W., et al., *Reduction of Bromate by Cobalt-Impregnated Biochar Fabricated via Pyrolysis of Lignin Using* CO_2 *as a Reaction Medium.* ACS Applied Materials & Interfaces, 2017. **9**(15): p. 13142-13150.

437. Chen, Q., et al., *Biomass-derived porous graphitic carbon materials for energy and environmental applications.* Journal of Materials Chemistry A, 2020. **8**(12): p. 5773-5811.
438. Sadezky, A., et al., *Raman microspectroscopy of soot and related carbonaceous materials: Spectral analysis and structural information.* Carbon, 2005. **43**(8): p. 1731-1742.
439. Ferrari, A.C., *Raman spectroscopy of graphene and graphite: Disorder, electron–phonon coupling, doping and nonadiabatic effects.* Solid State Communications, 2007. **143**(1): p. 47-57.
440. Homann, K.H., *Fullerenes and soot formation - New pathways to large particles in flames.* Angewandte Chemie - International Edition, 1998. **37**(18): p. 2434-2451.
441. Jawhari, T., A. Roid, and J. Casado, *Raman spectroscopic characterization of some commercially available carbon black materials.* Carbon, 1995. **33**(11): p. 1561-1565.
442. Araújo, T., et al., *Cellulose-based carbon membranes for gas separations - Unraveling structural parameters and surface chemistry for superior separation performance.* Carbon, 2023. **204**: p. 398-410.
443. Liu, W., et al., *Tuning the atomic configuration of Co-N-C electrocatalyst enables highly-selective H_2O_2 production in acidic media.* Applied Catalysis B: Environmental, 2022. **310**: p. 121312.
444. Su, L., et al., *Co, N-doped carbon dot nanozymes with acid pH-independence and substrate selectivity for biosensing and bioimaging.* Sensors and Actuators B: Chemical, 2022. **353**: p. 131150.
445. Fu, Y.-J., et al., *Adjustable microstructure carbon molecular sieve membranes derived from thermally stable polyetherimide/polyimide blends for gas separation.* Carbon, 2017. **113**: p. 10-17.
446. Sedigh, M.G., et al., *Structural characterization of polyetherimide-based carbon molecular sieve membranes.* AIChE Journal, 2000. **46**(11): p. 2245-2255.
447. Rodrigues, S.C., et al., *Preparation of carbon molecular sieve membranes from an optimized ionic liquid-regenerated cellulose precursor.* Journal of Membrane Science, 2019. **572**: p. 390-400.
448. Hou, M., et al., *Polyimide-derived carbon molecular sieve membranes for high-efficient hydrogen purification: The development of a novel phthalide-containing polyimide precursor.* Separation and Purification Technology, 2022. **301**: p. 121982.
449. Deng, G., et al., *Structure evolution in carbon molecular sieve membranes derived from binaphthol-6FDA polyimide and their gas separation performance.* Journal of Industrial and Engineering Chemistry, 2021. **94**: p. 489-497.
450. Li, H., et al., *Simultaneously enhanced gas permeability, selectivity and aging stability of carbon molecular sieve membranes by the molecule doping of silicon.* Carbon, 2023. **203**: p. 47-58.
451. Shao, L., T.-S. Chung, and K.P. Pramoda, *The evolution of physicochemical and transport properties of 6FDA-durene toward carbon membranes; from polymer, intermediate to carbon.* Microporous and Mesoporous Materials, 2005. **84**(1): p. 59-68.
452. Liang, J., et al., *Effects on carbon molecular sieve membrane properties for a precursor polyimide with simultaneous flatness and contortion in the repeat unit.* ChemSusChem, 2020. **13**(20): p. 5531-5538.
453. Fu, S., et al., *Temperature dependence of gas transport and sorption in carbon molecular sieve membranes derived from four 6FDA based polyimides: Entropic selectivity evaluation.* Carbon, 2015. **95**: p. 995-1006.

454. Sedigh, M.G., et al., *Experiments and Simulation of Transport and Separation of Gas Mixtures in Carbon Molecular Sieve Membranes.* The Journal of Physical Chemistry A, 1998. **102**(44): p. 8580-8589.
455. Lucas, P., et al., *Structure of $ZnCl_2$ Melt. Part II: Fragile-to-Strong Transition in a Tetrahedral Liquid.* The Journal of Physical Chemistry B, 2017. **121**(49): p. 11210-11218.
456. Wang, L., et al., *Influence of ceramic substrate porosity and glass phase content on the microstructure and mechanical properties of metallized ceramics via an activated Mo-Mn method.* Ceramics International, 2020. **46**(6): p. 8244-8254.
457. Pérez-Francisco, J.M., et al., *CMS membranes from PBI/PI blends: Temperature effect on gas transport and separation performance.* Journal of Membrane Science, 2020. **597**: p. 117703.
458. Kim, Y.K., H.B. Park, and Y.M. Lee, *Gas separation properties of carbon molecular sieve membranes derived from polyimide/polyvinylpyrrolidone blends: effect of the molecular weight of polyvinylpyrrolidone.* Journal of Membrane Science, 2005. **251**(1): p. 159-167.
459. Pirouzfar, V., et al., *Modeling and optimization of gas transport characteristics of carbon molecular sieve membranes through statistical analysis.* Polymer Engineering & Science, 2014. **54**(1): p. 147-157.
460. Jiao, Y., et al., *Coordination enhancement of hydrogen and helium recovery in polybenzimidazole-based carbon molecular sieve membranes.* Separation and Purification Technology, 2023. **315**: p. 123691.
461. Moon, J.D., et al., *Impact of humidity on gas transport in polybenzimidazole membranes.* Journal of Membrane Science, 2021. **639**: p. 119758.
462. Lopez-Marques, H., et al., *Water vapor sorption and transport in carbon molecular sieve membranes.* Journal of Membrane Science, 2024. **691**: p. 122170.
463. Ma, X., et al., *Propylene/Propane Mixture Separation Characteristics and Stability of Carbon Molecular Sieve Membranes.* Industrial & Engineering Chemistry Research, 2015. **54**(40): p. 9824-9831.
464. Wang, Y., et al., *Polymers of intrinsic microporosity for energy-intensive membrane-based gas separations.* Materials Today Nano, 2018. **3**: p. 69-95.
465. Lin, H. and M. Yavari, *Upper bound of polymeric membranes for mixed-gas CO_2/CH_4 separations.* Journal of Membrane Science, 2015. **475**: p. 101-109.
466. Bhuwania, N., et al., *Engineering substructure morphology of asymmetric carbon molecular sieve hollow fiber membranes.* Carbon, 2014. **76**: p. 417-434.
467. Yang, R., M.Y. Chen, and P. Li, *Carbon molecular sieve hollow fiber composite membrane derived from PMDA-ODA polyimide for gas separation.* High Performance Polymers, 2022. **34**(4): p. 444-454.
468. Jue, M.L., Y. Ma, and R.P. Lively, *Streamlined Fabrication of Asymmetric Carbon Molecular Sieve Hollow Fiber Membranes.* ACS Applied Polymer Materials, 2019. **1**(8): p. 1960-1964.
469. Zhang, C., R. Kumar, and W.J. Koros, *Ultra-thin skin carbon hollow fiber membranes for sustainable molecular separations.* AIChE Journal, 2019. **65**(8): p. e16611.
470. Cao, Y., et al., *Appealing sheath-core spun high-performance composite carbon molecular sieve membranes.* Angewandte Chemie International Edition, 2023. **62**(27): p. e202303915.
471. Cao, Y., Z. Liu, and W.J. Koros, *Above-Tg Annealing Benefits in Nanoparticle-Stabilized Carbon Molecular Sieve Membrane Pyrolysis for Improved Gas Separation.* Angewandte Chemie International Edition, 2024. **63**(8): p. e202317864.

472. Corres, M.A., et al., *Thermal and thermo-oxidative degradation of poly(hydroxy ether of bisphenol-A) studied by TGA/FTIR and TGA/MS.* Journal of Analytical and Applied Pyrolysis, 2011. **92**(2): p. 407-416.
473. He, W., et al., *Nanoarchitectonics of carbon molecular sieve membranes with graphene oxide and polyimide for hydrogen purification.* RSC Advances, 2023. **13**(15): p. 10168-10181.
474. Liu, L., et al., *Ultrahigh He enrichment property of carbon molecular sieve membranes by direct fluorination.* Journal of Membrane Science, 2025. **717**: p. 123647.
475. Lei, L., et al., *Carbon hollow fiber membranes for a molecular sieve with precise-cutoff ultramicropores for superior hydrogen separation.* Nature Communications, 2021. **12**(1): p. 268.
476. Inc., M.a.P.T. *Carbon Molecular Sieve Membranes*. 2025; Available from: https://www.mediaandprocess.com/process/carbon_molecular.html.
477. Kämnitz, S., et al., *Hydrogen Conditioning Using Nanoporous Inorganic Membranes.* Chemie Ingenieur Technik, 2022. **94**(1-2): p. 49-55.
478. Rahimalimamaghani, A., et al., *Carbon Molecular Sieve Membranes for Selective CO2/CH4 and CO2/N2 Separation: Experimental Study, Optimal Process Design, and Economic Analysis.* Industrial & Engineering Chemistry Research, 2023. **62**(45): p. 19116-19132.